Ceské vysoké ucení technické v Praze

Fakulta strojní

Ing. Martin Laub

Development of opto-mechanical tools and procedures for the new generation of RICH-detectors at CERN

Disertacní práce

Studijní obor: Presná mechanika a optika

Školitel: Doc.Ing. Josef Zicha, CSc.
Školitel specialista: Dr. Carmelo D'Ambrosio

Praha, zárí 2001

Disertacní práce vznikla v Evropském stredisku pro nukleární fyziku (CERN) v Ženeve.

Abstract

This thesis is focused on development of opto-mechanical tools and procedures, which would contribute to the achievement of the best possible performance of new Ring Imaging Cherenkov (RICH) detectors.

On the base of requirements, given by the physics objective of the LHCb detector, and an analysis of the detector opto-mechanical system, specifications of individual opto-mechanical components were determined. Spherical mirrors, planar mirrors and mirror adjustable mounts were the components of interest. Next, their parameters to be characterised were defined. Possible measurement methods were studied and relevant set ups based on suitable methods were developed. Meanwhile, available modern metrology technologies, like laser operated instruments or digital image processing, were applied with an attempt to innovate them and to increase their achievable performance limits. When applicable, the set ups were automated in order to make the measurements fast and reliable. An optical laboratory, devoted to the characterisation of the RICH opto-mechanical components, was established.

Collaboration with industry was started. A number of prototypes of mirrors and of mirror mounts for both the LHCb and COMPASS RICH detectors was tested, and a feedback to manufacturers was provided. The quality of the whole production of the COMPASS RICH 1 mirrors was tested. The laboratory and its facilities are being applied for optimisation of the LHCb RICH opto-mechanical component parameters and they will be used for the quality tests of the final products.

Anotace

Tato disertacní práce je zamerena na vývoj optomechanických zarízení a metod, jejichž aplikace prispeje k dosažení optimální funkce Ring Imaging Cherenkov (RICH) detektoru.

S tímto cílem byla na základe požadavku daných zamerením LHCb detektoru provedena analýza jeho optomechanického systému a urceny parametry jednotlivých optomechanických komponent. Tato práce se zabývá sférickými, prípadne rovinnými zrcadly a jejich justážními mechanikami. Dále byly definovány parametry, které bude úcelné merit, spolu s požadovanou merící presností. Dostupné merící metody byly analyzovány a príslušné merící aparatury, založené na vybraných principech, vyvinuty. Pri jejich vývoji byly aplikovány moderní merící technologie, jako zarízení pracující s laserovým zárením nebo zpracování digitální obrazové informace, se zámerem je inovovat a posunout hranice jejich maximálních možností. Pokud to bylo možné a vhodné, merící zarízení byla automatizována, aby byla zajištena jejich maximální efektivita a objektivita získaných výsledku. Aparatury byly instalovány v optické laboratori založené k tomuto úcelu.

Byla navázána spolupráce s prumyslem a v jejím rámci testováno množství prototypu zrcadel a jejich justážních mechanik pro LHCb a COMPASS RICH

detektory. V optické laboratori TA2 byla testována kvalita celé produkce zrcadel pro COMPASS RICH 1 detektor. Merící aparatury byly použity pro nalezení optimálních parametru optomechanických komponent LHCb RICH detektoru a počítá se s nimi také pro merení kvality finálních komponent.

Contents

Glossary

a	granularity of the photodetector
A	atomic weight of the transferred material
B	magnetic field strength
c	speed of light in vacuum ($2.998 \cdot 10^8$ m s^{-1})
d	mirror diameter, diameter of the beam on the Ronchi grating
d'	diameter of the mirror image
dx	movement in co-ordinate x
dy	movement in co-ordinate y
dS_{lim}	limit value
dS_D	relative increment of the amount of light inside diameter D
D	spot diameter, microlens pitch
D_{diff}	diffraction limited spot diameter
D_{max}	maximum processed diameter
D_s	spot diameter
D_0	diameter of the smallest circle containing 95 % of reflected light
D_{0ref}	parameter D_0 of the reference mirror
E	Young's Modulus of the material
E_c	critical energy
f	focal length, coefficient of friction
$f/\#$	f-number of the mirror
F	force
h	height of the mirror reflective surface above the ideal surface, height of the CCD active area
$\hbar$	Planck constant ($6.626 \cdot 10^{-34}$ J s)
I	CCD pixel signal
I_{max}	maximum signal
I_{r}	electrical charge
I_{F}	forward current
J_1	Bessel function of the first order
k_{abs}	coefficient
K	rigidity of the mirror substrate
l	distance of Ronchi ruling from the mirror
l_1	distance point source – planar mirror
l_2	distance planar mirror – reference mirror
L	length of radiator
m	rest mass of the particle
M	image magnification, number of pixels
$M_{b\,\mathrm{max}}$	maximum moment of deflection
n	refraction index of the medium, number of irradiated pixels

N	number of photoelectrons, number of wavelength, number of pixels, dynamic range of the CCD, number of subapertures, number of iterations
N_{cf}	number of combination fringes
N_m	number of mirrors
N_{pe}	expected number of detected photoelectrons
N_{ph}	number of emitted photons
N_A	Avogadro's number ($6.022 \cdot 10^{23}$ /mole)
N_0	detector response parameter
$N.A.$	numerical aperture of the mirror
$N.A._{ps}$	numerical aperture of the point source
p	momentum of the particle
p'	distance objective – microlens array
p_a	resulting momentum from multiple scattering and magnetic deflection
p_c	probability of having a ring imaged by a single mirror
p_{ma}	momentum from magnetic deflection
p_{ms}	momentum from multiple scattering
p_{th}	threshold momentum for emission of Cherenkov photons
P	pitch of the Ronchi ruling
P_{loc}	local pitch of combination fringes
P_{ps}	optical power output of the point source
P_D	percentage of light inside diameter D
$P(x)$	density of the Gaussian function
Q	photodetector quantum efficiency
r	radius of the mirror aperture, reflectivity
r_c	maximum base radius of the Cherenkov cone
$r_{c\ im}$	radius of the Cherenkov ring-image
r_e	electron radius ($2.818 \cdot 10^{-13}$ cm)
r_m	maximum acceptable mirror radius
r_l	spectral reflectivity
R	mirror reflectivity, radius of curvature of the mirror
R_a	roughness
R_{loc}	local radius of curvature
R_{ref}	radius of curvature of the reference mirror
R_D	radius of the spherical detector
R_M	radius of the spherical mirror
s	distance mirror – object, pitch of the screw
s'	distance mirror – image
S_{tot}	total light integrated on the CCD
S_D	amount of light inside diameter D
t	mirror thickness, exposure time
t_m	maximum acceptable mirror thickness
T	transmission, temperature
v_p	velocity of the particle
w	width of the CCD active area
w_j	fraction by weight
W_i	weight constant ($i=$ A, B, C)

$W(x,y)$	local deviation of the wavefront from the reference spherical surface
X_0, X_j	radiation length
$X_{0\ mount}$	radiation length of the mirror mount
z	charge of a particle
Z	atomic number of the transferred material
a	fine structure constant ($\approx 1/137$), coefficient of thermal expansion
a_{max}	maximum measurable wavefront slope
a_h, a_v	tilt of the mirror horizontal, vertical
b	relative speed of the particle, wedge angle
d	angular range
$d(x,y)$	displacement of Hartmann spot
e	energy average, crosstalk
e_A	coverage of the photodetector active area
e_x, e_y	transverse ray aberration in co-ordinate x,y
g	angular position of a screw
h	single photoelectron detection efficiency
l	wavelength of radiation
m	mean of the Gaussian distribution
q, q_i, q_c	Cherenkov angle
q_{ma}	angle between particle direction and magnetic field direction
q_{max}	maximum Cherenkov angle
q_n	angular deviation of the n-th diffraction order
q_x, q_y	components of the local slope in co-ordinate x,y
$q(x,y)$	local slope of the wavefront
s	rms value of the Gaussian distribution
s_{comp}	intrinsic precision of optical or mechanical component of the RICH opto-mechanical system
s_d	photodetector resolution
s_m	centroid finding precision
s_{max}	maximum stress in the material
s_n	rms value of noise
s_{oms}	precision of the RICH opto-mechanical system
s_p	rms value of the point source size, angular positioning precision
s_{part}	precision of the part of the RICH opto-mechanical system
s_{res}	angular resolution
s_s	rms value of the Gaussian distribution, angular stability
s_{Do}	precision of the spot size measurement
s_G	rms value of the spot intensity distribution
s_R	precision of the radius of curvature of the mirror
s_a	resolution of the slope determination
$s_q^{chromatic}$	contribution of chromatic aberration to the total resolution of the Cherenkov angle
$s_q^{emission}$	contribution of emission point to the total resolution of the Cherenkov angle

s_q^{pixel}	contribution of photodetector granularity to the total resolution of the Cherenkov angle
s_q^{total}	total angular resolution of the Cherenkov angle
s_q^{track}	contribution of tracking errors to the total resolution of the Cherenkov angle
s_{sJ}	fluctuation of the parameter s_J
s_J	average angular precision of the mirror reflective surface
DD	diameter increment
ΔE	energy bandwidth
Dx	pixel size
Δb	velocity acceptance
Δq	directional acceptance
W	area

1   Introduction

Correct particle identification is one of the crucial tasks of particle detectors. With rapid progress of the knowledge of matter in the last decades and with increasing technological skills, requirements on precision of the positive particle identification are higher and higher. Ring Imaging Cherenkov (RICH) technique is presently one of the most popular techniques in this field.

The RICH detector is in principle an optical instrument. The requirement of its high precision means that all components, creating the opto-mechanical system of the detector, have to be made to a high precision and correctly adjusted. Small deviations from the maximum admissible tolerances can result in an unacceptably low performance of the instrument. Therefore, it is essential to determine correct specifications of the individual opto-mechanical components, which would guarantee good performance of the instrument and which, at the same time, are technologically feasible. It is also necessary to be able to test the specified characteristics of the components. A feedback to manufacturers should be provided in a stage of the iterative development process. Then, when final components are manufactured, their quality and performance should be tested as well.

At CERN, two of four prepared detectors on the Large Hadron Collider (LHC), ALICE and LHCb, will contain RICH detectors. The new accelerator will replace the Large Electron Positron collider (LEP), which was after more than ten years of successful function stopped in November 2000. The preparation will be completed in 2005. Apart from this, another two RICH detectors are being prepared for the COMPASS experiment at the Super Proton Synchrotron (SPS) at CERN.

The author of this thesis participated in the preparation of the LHCb RICH detector and collaborated with the COMPASS experiment. The author was responsible for development of opto-mechanical tools and procedures for the new generation of RICH-detectors. Main results are summarised in the presented thesis.

The thesis is outlined as follows. Chapter 2 introduces briefly modern particle physics and the subject of particle detectors. Chapter 3 deals with RICH detectors. First at large about their principle and features, and then with focus on basic parameters of the LHCb RICH counters. In the context of the given analysis, the significance of the work of the author is suggested. Chapter 4 describes the work of the author and achieved results. Finally, conclusions are given in chapter 5.

1.1   Objectives

In the framework for research and development of new RICH detectors at CERN, the author followed these objectives:

- To study and to understand the detector under preparation and its proposed opto-mechanical system.

- To determine specifications of detector opto-mechanical components.

- To decide which characteristics of the opto-mechanical components should be tested.

- To analyse convenient methods and to develop facilities for characterisation of the opto-mechanical components.

- To establish an optical laboratory for this purpose.

- To establish a collaboration with industry.

- To provide feedback to manufacturers and to optimise initial specifications of the opto-mechanical components.

2   Particle physics today and tomorrow

An intense work in the field of theoretical and experimental particle physics in the past has allowed scientists to make many important discoveries and to penetrate deeper into a mystery of matter. A dramatic progress in the research during the last decades has led to the construction of the Standard Model, which theoretically describes the elementary particles and their interactions.

2.1   The Standard Model

The Standard Model [2.1] is a very successful description of interactions between the smallest particles of matter. It claims that matter consists of four fundamental particles [2.2, 2.3, 2.4]: two leptons and two quarks. Its quantum field theory predicts the interactions of quarks and leptons with agreement at level of ~ 0.1 % with experimental observations. Four types of interaction are recognized: the electromagnetic, the weak, the strong and the gravitational. The Standard Model neglects the gravitational interaction because it is very weak in particle scale. Other three interactions are explained by existence of particles called gauge bosons. Unified electroweak theory describes the electromagnetic interaction caused by the photon, and the weak interaction caused by W^+, W^- and Z^0 bosons. The strong interaction is mediated by gluons. Masses[1] of the gauge bosons are explained by Higgs mechanism, which expects a new particle – the Higgs boson. It is the last particle in the Standard Model that has not been observed yet. More information about fundamental particles and their interactions can be found in Appendix A.

Although the Standard Model is a consistent theoretical framework, it cannot explain adequately some phenomena. New theories beyond the Standard Model are trying to explain them [2.5] (see Appendix B). Essential data for building, confirmation or rejection of these theories are acquired experimentally by means of particle accelerators and detectors.

2.2   LHC and what was before

Particle accelerators and detectors are experimental devices designed to study properties of elementary particles. Accelerated particles collide either head-on with each other or with a fixed target. The value of energy of accelerated particles is

---

[1] The energy unit of particle physics is the electron volt (eV), the energy gained by one electron in crossing a potential difference of one volt. Masses are given in GeV/c^2 ($E = mc^2$). The mass of the proton is 0.938 GeV/c^2 = 1.67 x 10^{-27} kg.

proportional to the energy of particles produced by collision. In order to observe highly energetic particles, accelerators have to be able to accelerate particles at very high energies. Accelerators with the highest energies are the following:

- LEP[2] at CERN (Geneva, Switzerland) with maximum achieved energies up to 209 GeV in 2000. Colliding particles are electrons and positrons. The accelerator was primarily designed to measure the weak interaction by production of large amounts of $W^{\pm}$ and Z^0 bosons and for the discovery of the Higgs boson.

- HERA at DESY[3] (Hamburg, Germany) with electrons and protons colliding at energies up to 314 GeV to study mainly protons.

- TEVATRON at Fermilab[4] (Batavia, Illinois, USA) can achieve energy around 1.8 TeV at proton – antiproton collisions, mainly to study $W^{\pm}$ and Z^0 bosons.

These and a few other accelerators with their detectors have verified well the Standard Model. LEP was stopped in November 2000, after the four LEP experiments had produced a number of collisions compatible with the production of Higgs particles with a mass of around 115 GeV/c^2. These events were also compatible with other known processes. The question of Higgs bosons has not been solved yet.

A new accelerator, the Large Hadron Collider, LHC [2.6], is under preparation at CERN. The installation of the superconducting LHC machine in the 26.6 km circumference tunnel of LEP [2.7] is planned to be completed in 2005. It will produce proton – proton collisions at energies up to 14 TeV to study the fundamental interactions at effective energies around 1 TeV. At these energies, never reached before, questions related to the Higgs bosons, the supersymmetry theory, the spontaneous symmetry-breaking theory and other questions could be answered. Four detectors will be placed at LHC: ALICE, ATLAS, CMS and LHCb. In the following, we will focus mainly on the LHCb detector.

2.3   LHCb

LHCb [2.8] is a single-arm spectrometer devoted to CP-violation measurements (see Appendix B). The spectrometer will be installed in the intersection point 8, recently used by the DELPHI experiment. It is designed to exploit the large number of b-hadrons produced at the LHC in order to make precision studies of CP asymmetries and of rare decays in the B-meson systems. A fundamental requirement of the LHCb experiment resides in positive particle identification. Especially distinguishing between pions (π) and kaons (K) in a variety of final states is crucial for measurement of CP asymmetries in various B-meson decays. For example, without separating kaons from pions, reconstructed $B_d \rightarrow \pi^+\pi^-$ decays are heavily

---

[2] Large Electron Positron collider.
[3] Deutsches Elektronen-Synchrotron.
[4] Fermilab is a national high-energy physics laboratory near Chicago.

contaminated by $B_d \to K^{\pm} \pi^{\Upsilon}$, $B_s \to K^{\Upsilon} \pi^{\pm}$ and $B_s \to K^{\pm} K^{\Upsilon}$ decays. These introduce unknown systematic errors in the measured CP asymmetry in $B_d \to \pi^+ \pi^-$ decays, since these decay modes may well have asymmetries too. The ability to distinguish kaons from pions is also essential for the reconstruction of $B_s \to D_s^{\pm} K^{\Upsilon}$, where the main background comes from $B_s \to D_s^{\pm} \pi^{\Upsilon}$ decays. Particle identification is also needed for the reconstruction of $B_d \to DK^*$ decays, to reduce combinatoric background. Particle identification will be discussed in Chapter 3.
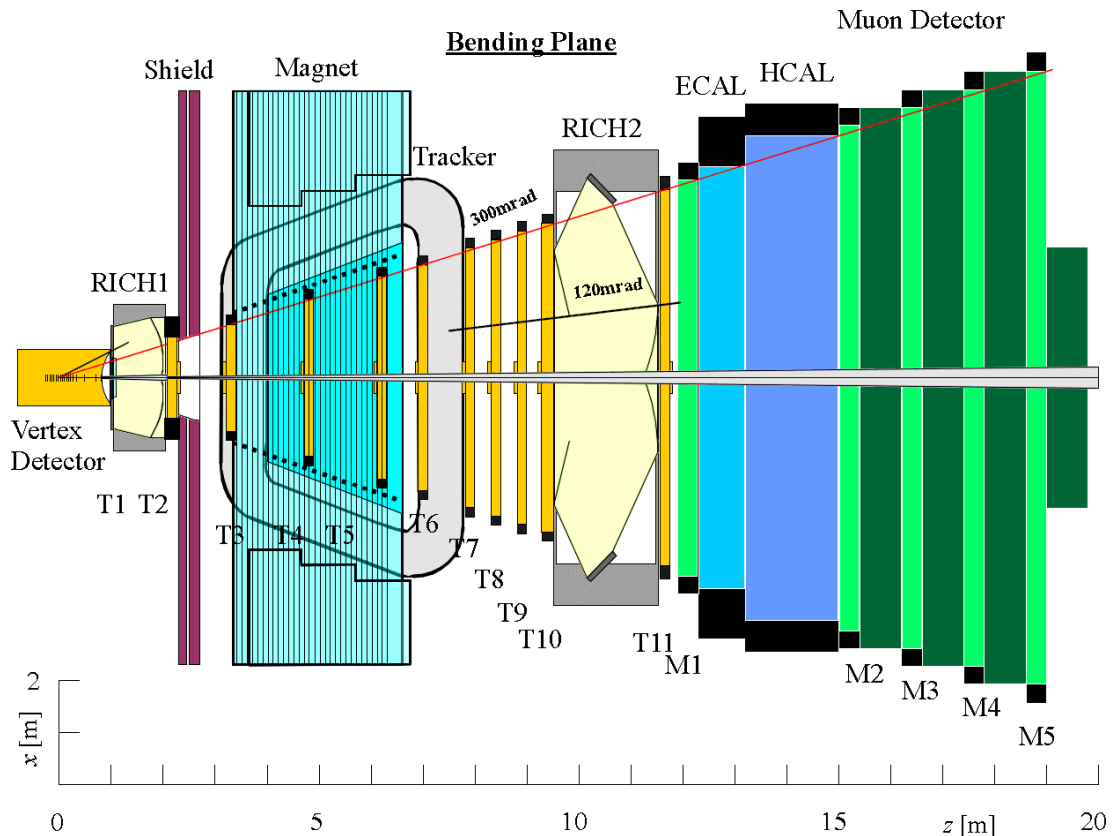

Fig. 2.1: The LHCb spectrometer seen from above (cut in the bending plane). It consists of following subdetectors: vertex detector, RICH 1, tracker, RICH 2, two calorimeters and moun detector. From [2.8].

The detector consists of several subdetectors as shown in Fig. 2.1. The detected event initiates in middle of the vertex detector, where two accelerated protons collide (pp interaction). The vertex detector determines trajectories of produced particles, which are in its detection range. It consists of a silicon detector and pile-up veto counter. A resolution on the impact of high-momentum tracks in the vertex detector is around 40 μm. The vertex detector provides information on the production and decay vertices of b-hadrons for the level-1 and level-0 triggers. The RICH 1 detector identifies different types of charged particles by measurement of their velocity. Trajectories of charged particles are bent in magnetic field of the big superconducting magnet and their radiuses of curvature are measured in tracker. This measurement gives information about the momentum of charged particles. The magnetic field is oriented vertically and has a maximum value of 1.1 T. The magnet coil is designed to

maximise the field homogeneity. An iron shield upstream of the magnet reduces the stray field in the vicinity of the vertex detector and of RICH 1. The tracker is based on gas chamber technology. It provides also information for higher-level triggers. The hit resolution of Inner Tracker is better than 65 μm, in the case of Outer Tracker it is < 200 μm. Particles with higher momentum are identified in the RICH 2 detector. Mass of particles can be determined from known momentum and velocity. Energies of electrons and hadrons are measured in the electromagnetic and hadron calorimeters. In the last part of the LHCb detector, in the muon filter, muons are detected.

Interactions of particles with matter of detector

In general, any particle detector must be as transparent as possible for transferring particles going to following parts of the detector. This means that the amount of material used to build components of the detector system has to be minimised because of particle interactions with matter. Particles interacting with material are losing their energy by electromagnetic shower. Bremsstrahlung and electron pair production are the dominant processes for high-energy electrons and photons. Their cross-sections become nearly independent of energy above 1 GeV. Fig. 2.2 shows for example hadronic interactions in the DELPHI detector and their comparison with electromagnetic interactions of photons. All these considerations are related to the LHCb system too.

In dealing with particles at high energies, it is convenient to measure the cross-section of the material in units of a scaling variable, radiation length X_0. This is the mean distance over which a high-energy electron loses all but 1/e of its energy by bremsstrahlung, ionisation and scattering. Bremsstrahlung is a German word for 'braking radiation'. The energy emitted by an accelerated particle is proportional to $1/m^2$, with m the rest mass of the particle. Bremsstrahlung therefore plays a particularly important role for light particles. Up to energies of 100 GeV, bremsstrahlung contributes substantially to energy loss in matter only for electrons. At the critical energy E_c, for electrons approximately given by $E_c \approx 550/Z$ MeV, the average energy loss by radiation and by ionisation are equal (Z is the atomic number of the traversed material). For high-energy photons, the dominant effect causing energy loses is pair production. The attenuation length due to pair production is 9/7 times the radiation length. The radiation length is given by:

$$\frac{1}{X_0} = \frac{4a\ N_A Z(Z+1)r_e^2 \log(183\ Z^{-1/3})}{A} , \qquad (2.1)$$

where a is fine structure constant ($\approx 1/137$), N_A is Avogadro's number (6.022×10^{23}/mole), Z is atomic number of the traversed material, A is atomic weight of the traversed material, r_e is electron radius (2.818×10^{-13} cm). For practical calculation of X_0 the following formula can be used [2.9]:

$$X_0 = \frac{716.4 \ g \ cm^{-2} \ A}{Z(Z+1) \ln(287/\sqrt{Z})} \qquad\qquad (2.2)$$
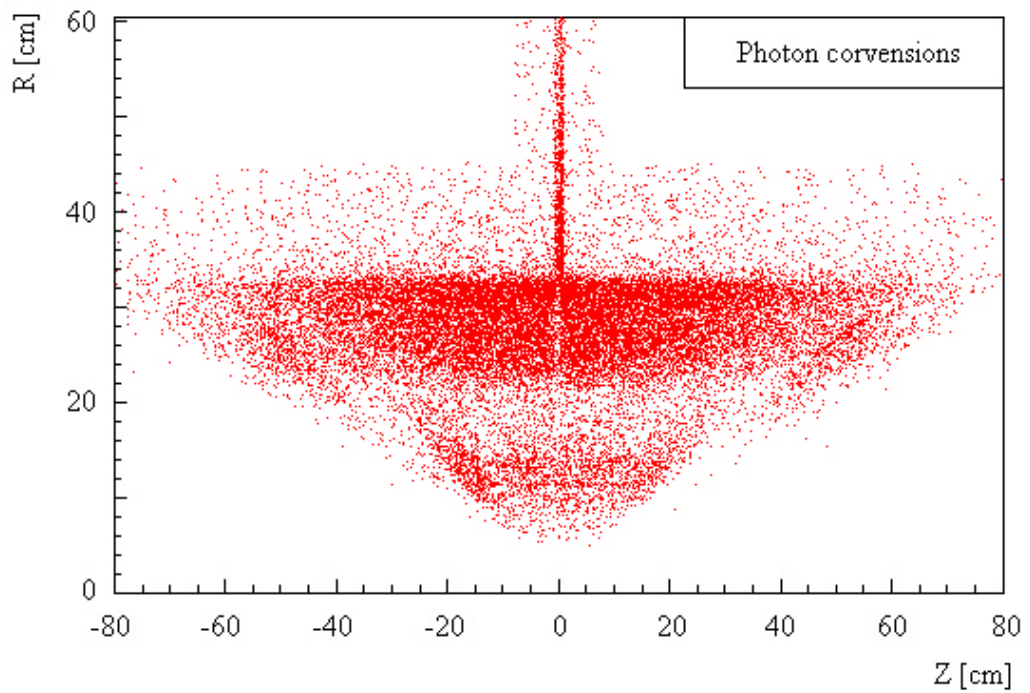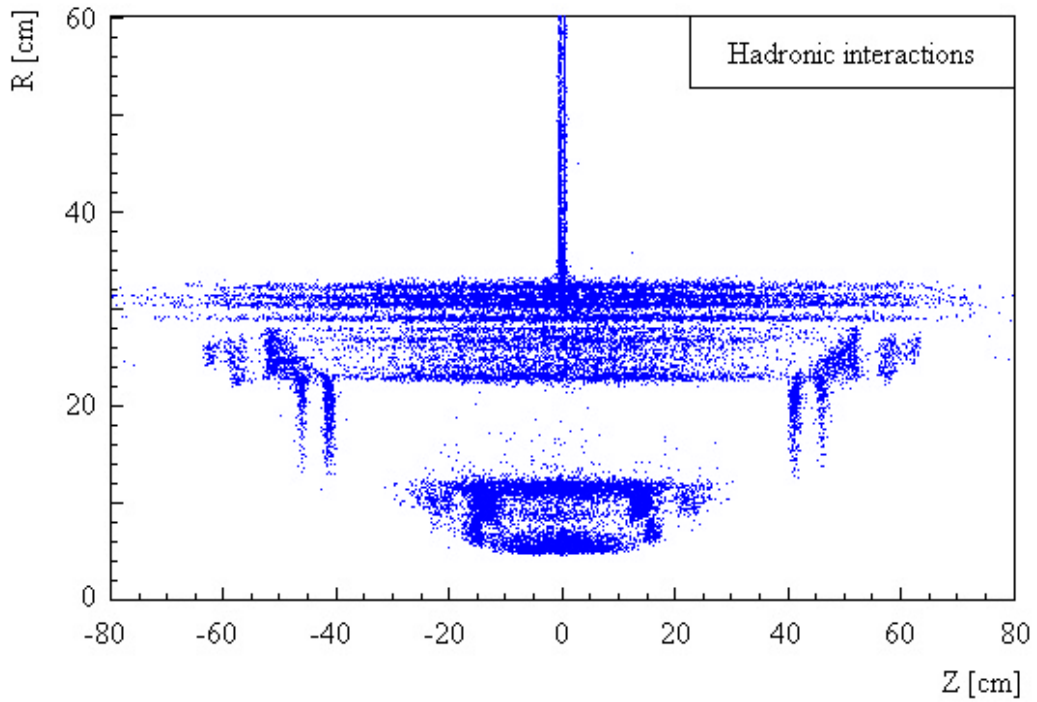

Fig. 2.2: Comparison of hadronic interactions with electromagnetic interactions of photons, simulated for the Delphi detector. Hadronic interactions show the distribution of material inside the detector, while photon conversions are much more scattered.

Radiation length in a mixture or compound may be approximated by:

$$X_0 = \frac{\sum w_j}{\sum w_j / X_j},$$

(2.3)

where w_j and X_j are the fraction by weight and the radiation length for the j-th element.

Later in this thesis (see Chapter 4), the importance of the previous arguments will be shown in the context of RICH opto-mechanical components specification.

3 RICH detectors

3.1 Principle of Cherenkov detectors

Ring Imaging CHerenkov (RICH) detector identifies charged particles by measurement of their velocity. From a known momentum of a detected particle, measured in another detector, it is possible to get information about the mass of the particle. It is important to understand that the RICH subdetector is part of a complex system and cannot perform particle identification without the information provided by the tracking subdetectors.

The measurement of a charged particle velocity is based on Cherenkov effect: a charged particle travelling in a dielectric medium faster than light, i.e. $v_p > c/n$, causes polarisation of the medium atoms. Polarised atoms, see Fig. 3.1, then emit Cherenkov radiation, which creates conical wavefronts with vertex angle q because of interference, see Fig. 3.2. The angle q is given by formula:

$$\cos q = \frac{1}{n(l)b}, \text{ where } b = \frac{v_p}{c} \qquad (3.1),(3.2)$$
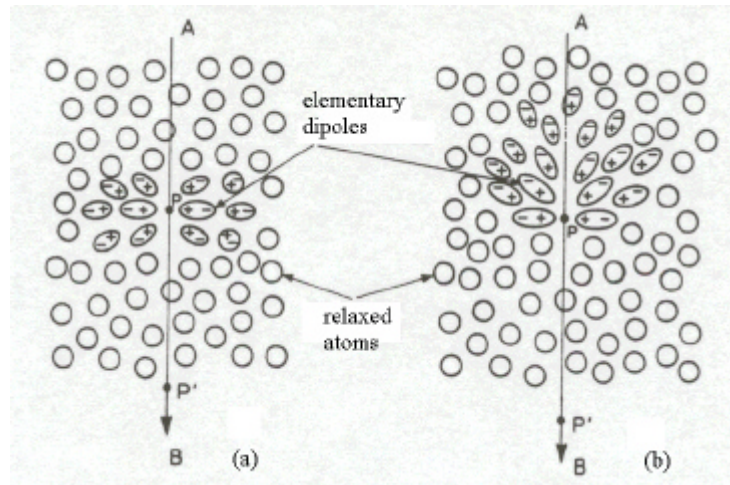

Fig. 3.1: Principle of polarisation of a dielectric medium by negatively charged particle (a) at low velocity, (b) at high velocity. From [3.1].

It depends on velocity of the particle v_p and on index of refraction n of the dielectric medium, which is a function of wavelength l of the emitted radiation. Angle q can have value between 0 ($b_{min} = 1/n$) and $q_{max} = \arccos(1/n)$ ($b_{max} = 1$). The intensity and spectrum of the radiation is given by the Frank-Tamm relation:

$$\frac{dN_{ph}}{dE} = \left(\frac{a}{\hbar c}\right) z^2 L \sin^2 q \tag{3.3}$$
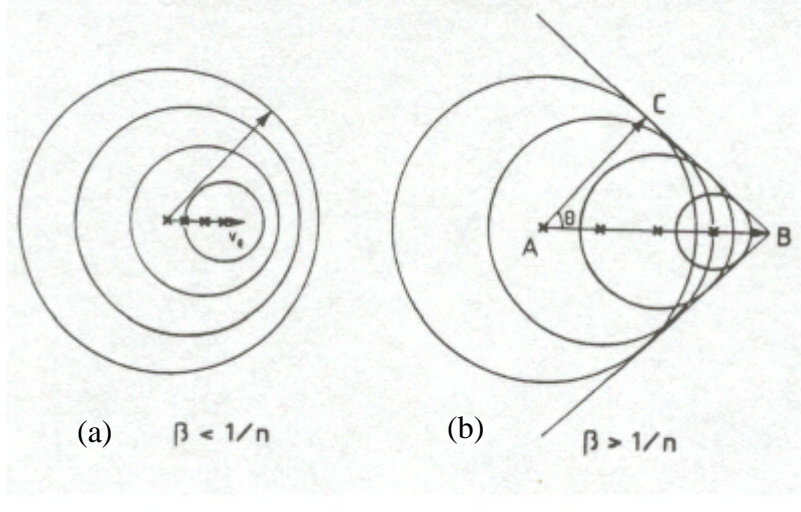

Fig. 3.2: Huygens principle applied on wavefronts emitted due to a charged particle travelling (a) at low velocity, (b) faster than light. From [3.1].

A number of emitted photons is a function of the charge z of the particle , Cherenkov radiator length L, the angle q as given by formula [3.2]:

$$N = N_0 z^2 L \sin^2 q , \tag{3.4}$$

where $N_0 \propto \dfrac{1}{l^2}$ is the detector response parameter. Its dependence on wavelength of the emitted radiation l is shown in Fig 3.3. Number of emitted photons increases with their energy. N_0 is expressed in following formula:

$$N_0 = \left(\frac{\alpha}{\hbar c}\right) \varepsilon \, \Delta E , \tag{3.5}$$

where $$\varepsilon \Delta E = \int (QRT)\, dE \tag{3.6}$$

e is the energy average of detector efficiencies (Q is quantum, T is transmission, R is mirror reflectivity) over the energy bandwidth ΔE. As the charged particle passes the radiator medium, Cherenkov conical wavefronts are emitted along the whole trajectory of the particle inside the radiator.

In the most cases, the Cherenkov ring-image is formed from conical wavefronts in focal plane of a focusing mirror (see Fig. 3.4) and photons are detected by high sensitive photodetectors. In the case of a spherical mirror, the radius of the Cherenkov ring-image $r_{c\,im}$ is given by:

$$r_{c\,im} = \frac{R \tan q}{2},$$ (3.7)

where R is a radius of curvature of the mirror.

Particle identification is limited by the resolution of the Cherenkov angle measurement. The minimum difference in Cherenkov angle Dq_{m_1,m_2} necessary for separation of two particles with masses m_1 and m_2 and at momentum p with number of sigmas n_s is given by:

$$Dq_{m_1,m_2} = \frac{m_2^2 - m_1^2}{2n_s} \frac{\sqrt{N_0 L}}{p^2}$$ (3.8)

Required resolution in Db/b is then:

$$\left(\frac{Db}{b}\right)_{m_1,m_2} = \frac{m_2^2 - m_1^2}{2p^2}$$ (3.9)

For given Cherenkov angle q, single photon resolution s_q and number of detected photons N, two particles can be separated with n_s sigmas if their momentum is:

$$p_{m_1,m_2} \leq \frac{1}{\sqrt{n_s}} \sqrt{\frac{\left(m_2^2 - m_1^2\right)\sqrt{N}}{2\tan q \cdot s_q}}$$ (3.10)

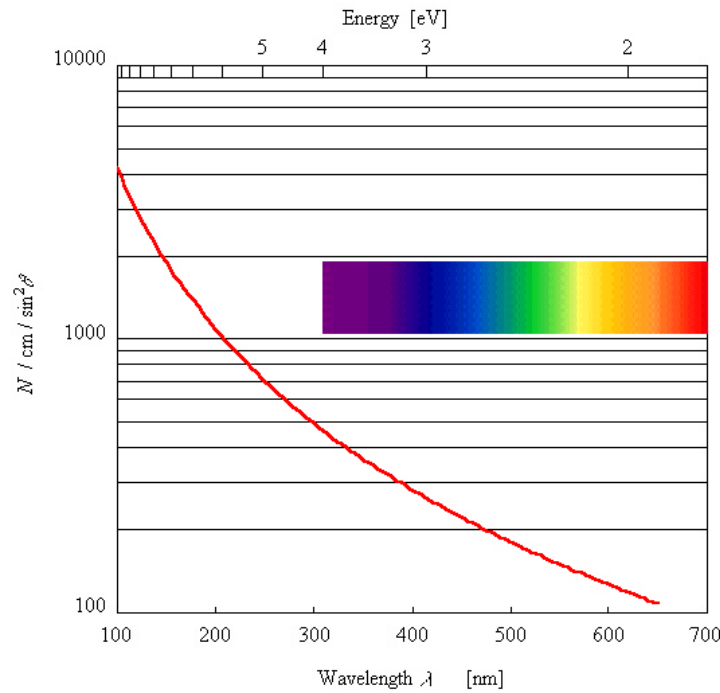**Fig. 3.3**: Number of Cherenkov photons emitted per cm and divided by $\sin^2 q$ (or $N_0 z^2$) as a function of their wavelength l. The wavelength range is also scaled in eV energy units.
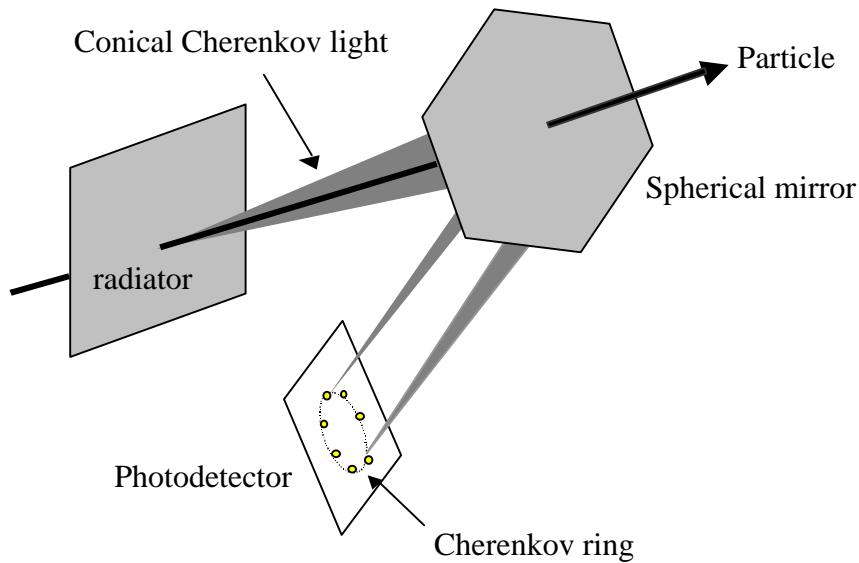
Fig. 3.4: Scheme of the principle of a RICH detector with a spherical focusing mirror. Conical wavefronts of Cherenkov light are transformed in ring images, which are detected by photodetectors in mirror focal plane.

3.2   History of Cherenkov detectors

RICH detectors are based on the process of the Cherenkov radiation. The radiation was researched by Cherenkov [3.4] between 1934 and 1944. For the characterisation of the radiation, Cherenkov, Frank and Tamm were awarded the Nobel Prize in 1958. The development of the photomultiplier (PM) allowed using this radiation for the first particle physics experiments.

The first system was proposed by Getting and built by Dicke [3.5] in 1947. It consisted of lucite cylindrical radiator which was extended to a cone, a focusing lens
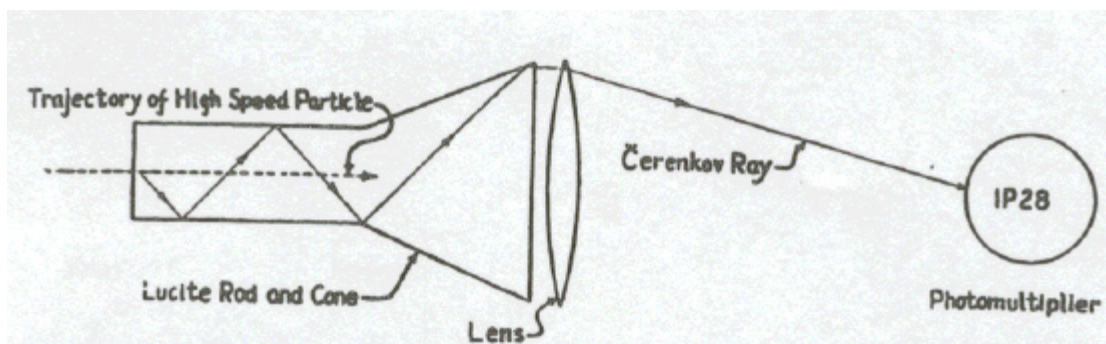

Fig. 3.5: The focusing Cherenkov counter proposed by Getting and Dicke. Axial particles produce Cherenkov rays in the Lucite radiator which are focused by the lens. From [3.2].

and a PM, see Fig. 3.5. Cherenkov light produced by a charged particle in the radiator was totally reflected inside the lucite cylinder and cone. Only a beam with Cherenkov
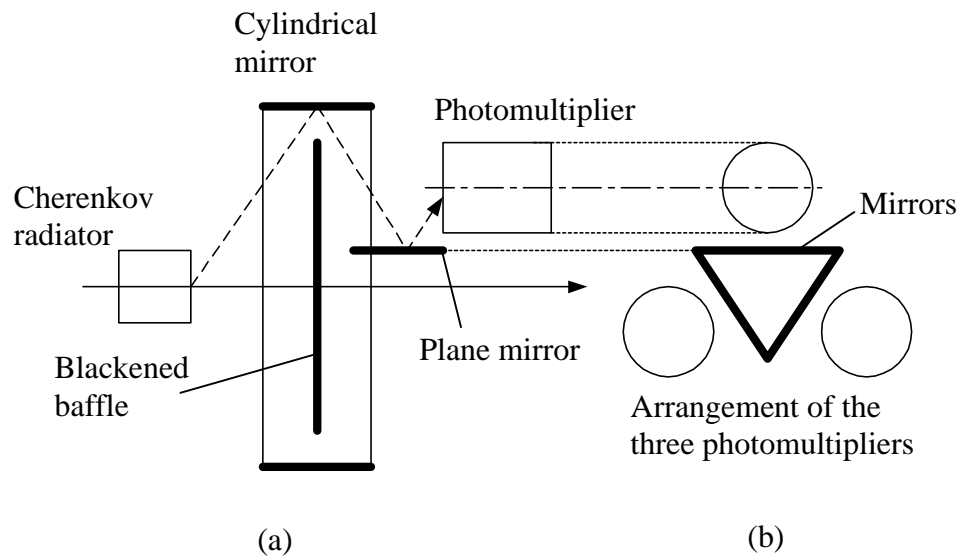
Fig. 3.6: The differential Cherenkov counter used in the antiproton discovery experiment: (a) side view, (b) end view.

angle exactly double of the cone angle was focused to a point on the PM. This system belongs to a group of differential counters with ability to measure precisely velocity but with only small range acceptance in velocity and direction of a charged particle. Another type of counters is called threshold counter. It will be described later in this section. The differential Cherenkov counter, shown in Fig. 3.6, was used by Segre, Chamberlain, Wiegand and Ypsilantis to discover the antiproton in 1955 [3.6]. The radiator was made of a quartz cylinder. Cherenkov light was reflected by a cylindrical mirror and a reflective triangle equally onto the three PMs. The range of selected bs was given by the limited axial length of the cylindrical mirror with possibility of variation by moving the mirror relatively to the radiator. It detected approximately axial particles with b between 0.75 and 0.78, $s_b/b = 0.011$.

Another improvement was done in 1962 by Meunier et al. [3.7], who placed a correction prism in front of an annular slid, viewed by PMs, to reduce the chromatic aberrations, see Fig. 3.7. This system, called differential isochronous self-collimating (DISC) counter covered the range of b between 0.85 and 0.96 by variation the position of the prism and had resolution $s_b/b = 0.006$ and $s_q = 0.003$. Differential gas counters reached the extreme resolution s_b/b in order of 10^{-6} in 1960s.

In comparison with differential counters, threshold counters have large velocity acceptance Δb and directional acceptance Δq but the resolution of b measurement is low. The first threshold counter was build by Jelley [3.8] in 1951. Because of their large phase space acceptance, threshold counters were convenient for detection of secondary particles emanating from an interaction vertex. A very efficient system formed by two threshold counters was built in Fermilab in the framework of the tagged photon spectrometer experiment. Threshold counters C_1 and C_2 attained $N_0 = 70$/cm, respectively $N_0 = 123$/cm with the resolution $s_b/b = 7.7 \times 10^{-5}$ and 2.3×10^{-5}, respectively [3.9]. This is only a factor six lower resolution than in case of the best differential counter but with large phase space acceptance. Since they are
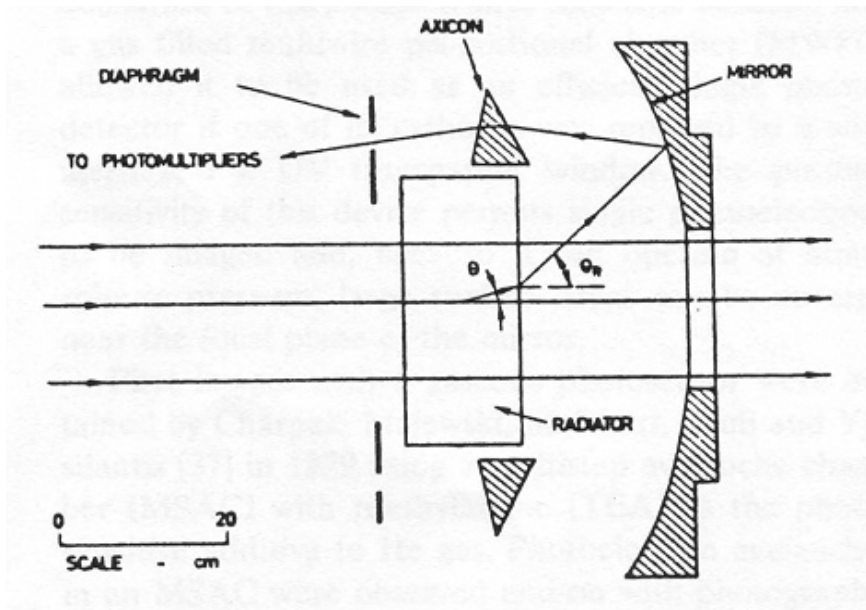
Fig. 3.7: The differential isochronous self-collimating (DISC) Cherenkov counter proposed by Meunier et al. From [3.2].

relatively long (3.8 and 6.6 m), they are convenient for fixed target spectrometers but not for colliding beam experiments.

The intense development has led to construction of RICH counters, which have decoupled the acceptance and the resolution. A RICH counter can achieve high **b** resolution of differential counters together with large phase space acceptance of threshold counters. The first system was proposed by Roberts [3.10] in 1960, see Fig. 3.8. A focusing lens formed Cherenkov ring on the surface of an image intensifier. Its angular acceptance was limited only by the size of the lens and intensifier. Construction of one of the first efficient RICH detector, built by Sequinot and Ypsilantis [3.11] in 1977, was allowed by replacement of the PM by gas phase photoionization photon detector with large surface area. A gas filled multiwire proportional chamber (MWPC) with admixture of the photosensitive molecule benzene, and with one of its cathodes replaced by a wire mesh and a UV transparent window, made possible to use it as an efficient single photon detector. First ring images were observed by means of a gaseous photodetector by Charpak, Majewski, Melchart, Sauli and Ypsilantis [3.12] in 1979. They used a multistep avalanche chamber (MSAC) with triethylamine (TEA) as a photosensitive additive to He gas. A photographic film detected an unambiguous two-dimensional image, this means that detection was possible only for very low rates ≈ 1 Hz. Value of $N_0 = 27$/cm was achieved with a low quality mirror. A value of $N_0 = 56$/cm was obtained with the same type of photodetector and with a better mirror by Ekelof et al. [3.13] in 1980. They also developed MPWC with a methane + TEA gas mixture with > 95 % single photoelectron counting efficiency. Next, they proposed a long drift time projection chamber (TPC) coupled to MWPC for unambiguous two-dimensional imaging with electronic readout. A lower threshold molecule, tetrakis-dimethyl-amino-ethylene (TMAE), suitable for use with fused quartz windows, was proposed by Anderson [3.14] in 1980. A MPWC-TPC detector with TMAE gas and a quartz window, used by Barrelet et al. [3.15] in 1981, had $N_0 = 56$/cm and unambiguous two-dimensional
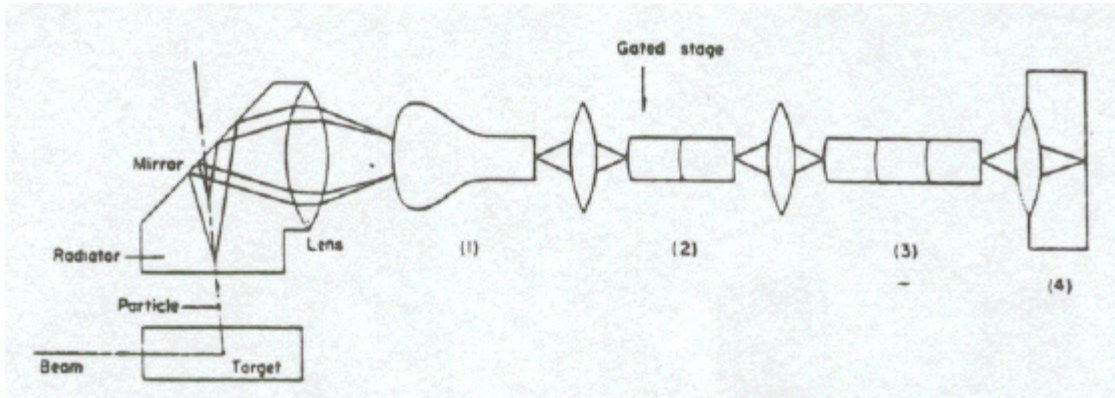
Fig. 3.8: The ring imaging counter proposed by Roberts: (1) an image intensifier, (2) a gated intensifier, (3) an intensifier, (4) a camera. From [3.2].

imaging with electronic readout. Thanks to the described development, large devices like Ω-RICH, DELPHI RICH and SLD CRID with up to 30 m^2 of detector based on the MWPC-TPC + TMAE + quartz technology have been built. In the recent past, new technologies for single photon detectors have allowed construction of more efficient and precise devices. They are described in the following section.

3.3   Overview of existing RICHes

Resolution of the Cherenkov angle q measurement depends on several parameters of the RICH detectors. In the following, RICH detectors, already working or under preparation, are classified according to different parameters. Table 3.1 summarises their parameters.

The resolution s_b/b of a RICH detector depends on the number of photoelectrons N:

$$\frac{s_b}{b} = \tan q \, \frac{s_q}{\sqrt{N}} \tag{3.11}$$

For the same particle momentum, the number of produced photoelectrons is given by the type of radiator and its length. In general, liquid and solid radiators can be long only $L \leq 10$ cm, and gas radiators require a length $L \geq 1$ m. RICH detectors can be divided according to the number of photoelectrons per ring into three generations [3.16]:

- 1st generation: OMEGA, DELPHI, SLD CRID, CERES, JETSET, CAPRICE, etc. with typically $N = 8$ to 16.
- 2nd generation: ALICE, HADES and CLEO with $N = 18$ to 24.
- 3rd generation: HERA-B, LHCb, COMPASS, HERMES and BaBar DIRC with $N = 30$ to 60.

Table 3.1: Overview of existing and being prepared RICH detectors. The table lists some of their basic parameters.

Detector		Radiator	Photodetector	N_0	N	L [m]	Focussing optics	s_q [mrad]
ALICE		C_6F_{14}	CsI	44	17		No (proximity foc.)	
CAPRICE		NaF	TPCs with TMAE					
CERES		CH_4	TPCs with TMAE				Spherical mirrors	
CLEO		LiF	TEA	34	18-19			
COMPASS	RICH 1	C_4F_{10}	CsI			3	Spherical m. $R = 6.6$ m	0.9
	RICH 2	$C_2F_6 + Ne$				8	Spherical m. $R = 16$ m	0.4
DELPHI	Forward	C_6F_{14}	TPCs with TMAE					13
		C_4F_{10}						2.9
	Barrel	C_6F_{14}						13.9
		C_5F_{12}						4.5
DIRC		quartz	PMTs	31	28			
HADES		C_4F_{10}	CsI	109			Spherical m. $R = 0.87$ m	
HERA-B		C_4H_{10}	PMTs	45	32		Sph. $R = 11.5$ m + planar m.	7.0
HERMES		Aerogel (SiO_2)	PMTs			0.4÷0.7		
		C_4F_{10}						
JETSET								
LHCb	RICH 1	Aerogel	PMTs	58	16	0.05	Spherical m. $R = 1.7$ m	2.0
		C_4F_{10}		181	46	0.85	Spherical m. $R = 8.0$ m	1.5
	RICH 2	CF_4	PMTs	174	29	1.7	+ planar m.	0.6
OMEGA		$C_2F_6 + N_2$	TPCs with TMAE	49	16			
SLD CRID		C_6F_{14}	TPCs with TMAE		10		Spherical m. $R = 10$ m	1.0
		$C_5F_{12} + N_2$						

The RICH detectors from the 1st generation proved that it was possible to build successfully big devices. They used gaseous detectors. Many related problems had to be solved, like the purity of a large UV system for a long period, the purity of gases to drift single electrons over distances in order of metres etc. The problem of the TMAE wire ageing was recognised as serious for higher rate applications.

For the 2nd generations of the RICH detectors, development in field of electronics allowed to replace high gas gain ($2\text{-}5 \times 10^5$), short charge integration constant (10-100 ns) and drift time measurement by low gas gain ($\sim 5 \times 10^4$), long charge integration constant (600-1000 ns), low noise electronics (< 500 e$^-$ rms) and geometrical pixelization. In principle, TMAE, TEA and CsI photocathodes can be used for these detectors. The first CsI solid photocathodes are being used on a very large scale in the ALICE and HADES RICH [3.17] detectors.

For the 3rd generation of the RICH detectors, wire aging excluded TMAE to be used at LHC or HERA-B [3.18] high-luminosities. Also, detectors used in the 2nd generation were not adequate for the highest rates applications of the LHC or HERA-B RICH detectors, where short shaping times and a high gas gain operation are required. In LHC detectors, charge integration constant of 10-20 ns is needed. Vacuum operated PMTs or HPDs operating with bi-alcali photocathodes are used instead of the gaseous photon detectors, except for COMPASS, where MWPCs equipped with CsI photocathodes were chosen. The new photodetectors moved the devices of the 3rd generation in the visible light region to reduce chromatic errors, and to simplify their operation.
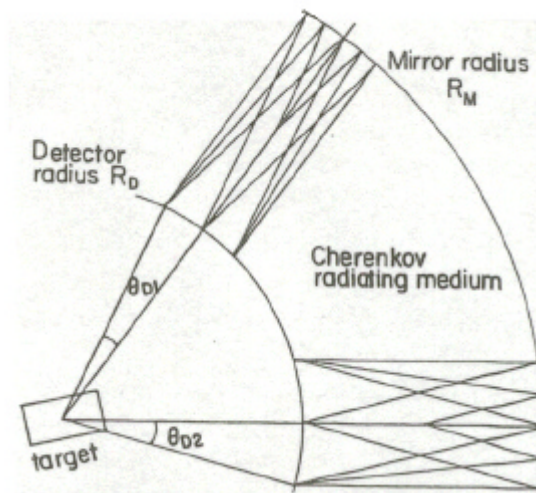

Fig. 3.9: Scheme of the classical spherical RICH optics. Particles emerge from a target or interaction region with zero impact parameter. From [3.2].

Another factor that has influence on the obtained results is the detector optical layout. We can find a variety of optical arrangements because each detector has a specific goal. The classical spherical RICH optics scheme is shown in Fig. 3.9. A radiator gas fills the space between the mirror and the detector. The spherical mirror with radius R_M focuses Cherenkov light on the spherical detector with radius

$R_D = R_M/2$. Parallel tracks form an identical image. A similar optical scheme was used in the Omega RICH, see Fig. 3.10, and in the DELPHI RICH, Fig. 3.11. The Ω-RICH [3.19] had a 5 m long radiator and an array of 7×4 m^2 spherical mirrors. With angular acceptance ± 400 mrad horizontally and ± 200 mrad vertically, the Ω-RICH
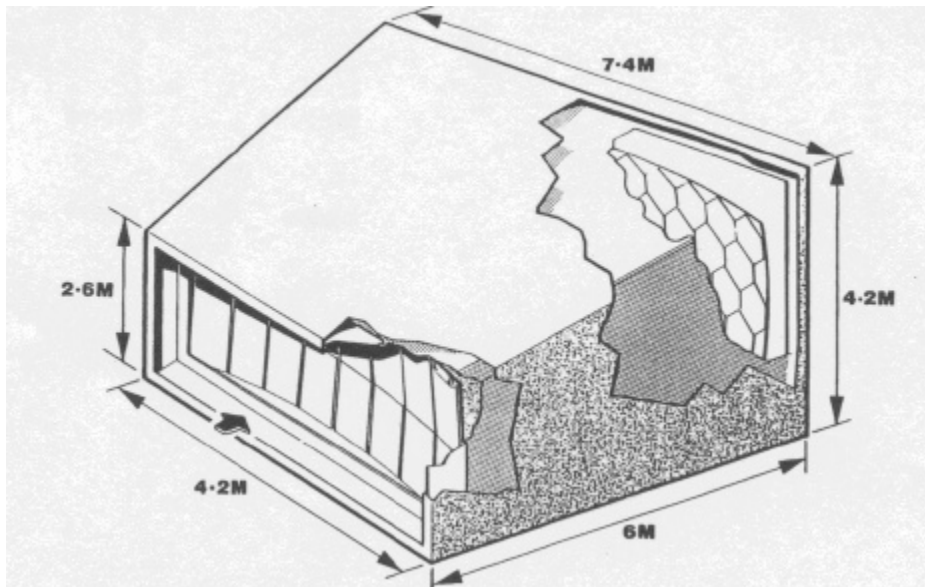

Fig. 3.10: Overview of the Omega RICH. At the back, part of the mirror mosaic is visible. At the front, two rows of 8 chambers each form the photon detector. From [3.19].

identified particles with momenta down to 5 GeV/c. The detector achieved $N_0 = 30$/cm. After a change of drift chambers and central part of mirrors, N_0 was increased to 49/cm. Cherenkov angle resolution was $s_q = 1$ mrad. The DELPHI RICH [3.20] consisted of two subsystems with total photosensitive area 36.5 m^2: Barrel RICH and Forward RICH. Photons emitted in 1 cm thick C_6F_{14} liquid radiators were detected directly by TPC photodetectors with $N_0 = 32$/cm respectively 39/cm, and $s_q = 13.9$ mrad respectively 13 mrad for the Barrel respectively Forward RICH. This approach is called the proximity focusing technique, Fig. 3.12 shows the principle. In the Forward RICH, spherical mirrors focused Cherenkov light, generated in the C_4F_{10} gas volume, on the same TPC detectors. The Barrel RICH used the C_5F_{12} gas and parabolic mirrors, see Fig. 3.13 [3.21]. Gas radiators achieved values of $N_0 = 50$/cm respectively 33/cm with $s_q = 4.5$ mrad respectively 2.9 mrad for the Barrel respectively Forward RICH. The reconstructed Cherenkov angle q in the Barrel RICH is shown in Fig. 3.14. Fig. 3.15 shows π/K/p separation in the large momentum range $0.7 - 45$ GeV/c of the same RICH [3.22].

In several RICH systems, mirrors are tilted to bring the image out of the detector angular acceptance, so that the material of the photodetectors does not degrade the tracking. As an example, Figs. 3.16–20 show optical schemes of several RICH detectors, each with its specific arrangement. The solid LiF radiator plate (refractive index $n = \sqrt{2}$) of the CLEO RICH detector (Fig. 3.19) has a saw-tooth profile to overcome problem of the total internal reflection and to enable escape all tracks from
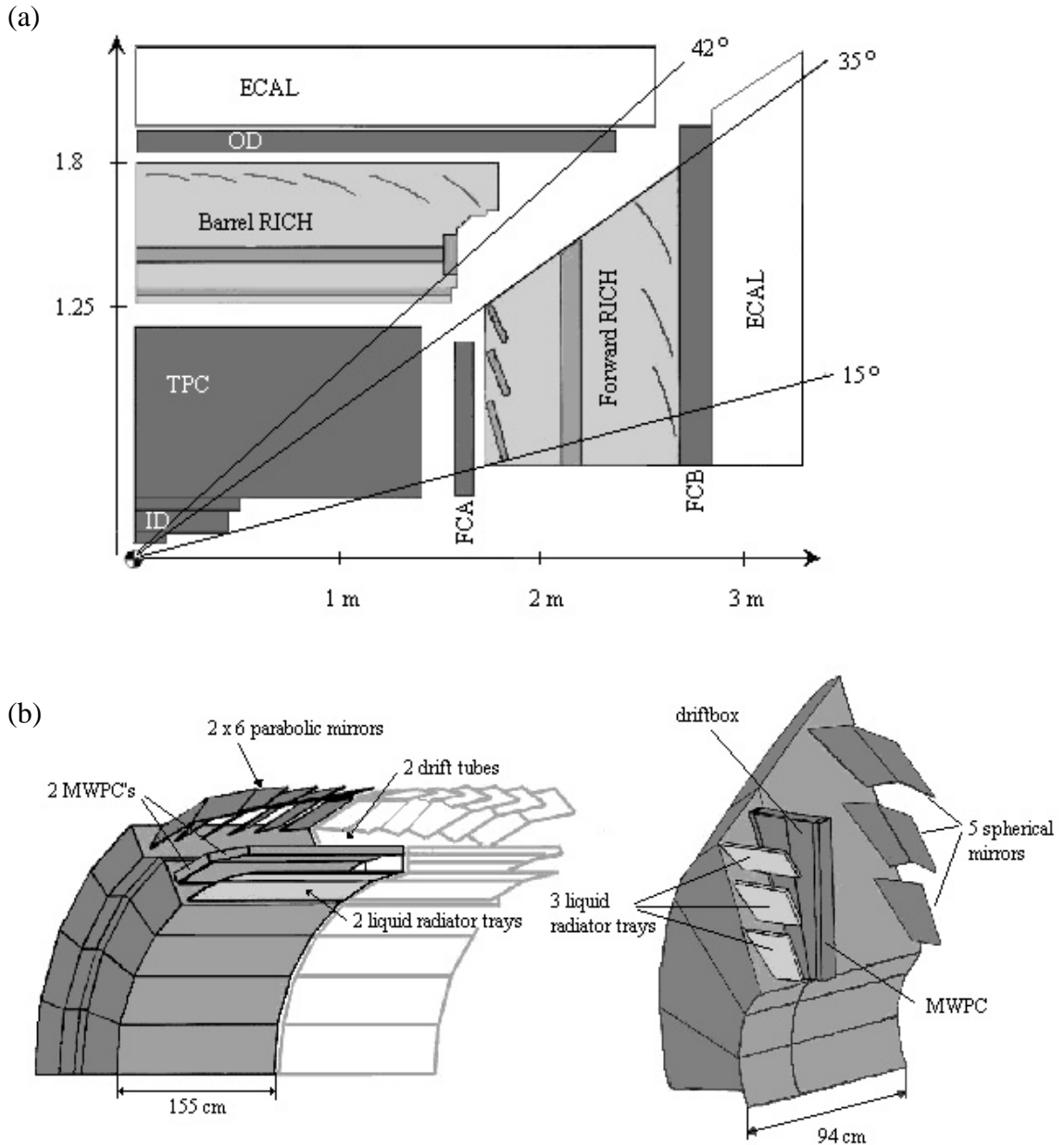
(a)

(b)

Fig. 3.11: (a): Scheme of the DELPHI detector. (b) 3-D view of the Barrel RICH (left) and the Forward RICH (right).From [3.20].

the radiator. Contrary, DIRC optical arrangement (Fig. 3.20) [3.23] uses total internal reflection in the quartz radiator to transmit Cherenkov light towards a photodetector surface.

At present, three new detectors containing the RICH detectors are under preparation at CERN: ALICE, COMPASS and LHCb. The ALICE RICH detector uses the proximity focusing technique. RICH detectors at COMPASS and LHCb focus Cherenkov light by means of tilted spherical mirrors. Their optical schemes are shown in Fig. 3.21, 3.22 and 3.23. The requirement for the Cherenkov angle resolution is, in case of these new detectors higher than ever before, especially in the case of LHCb RICH 2 detector, see Table 3.1
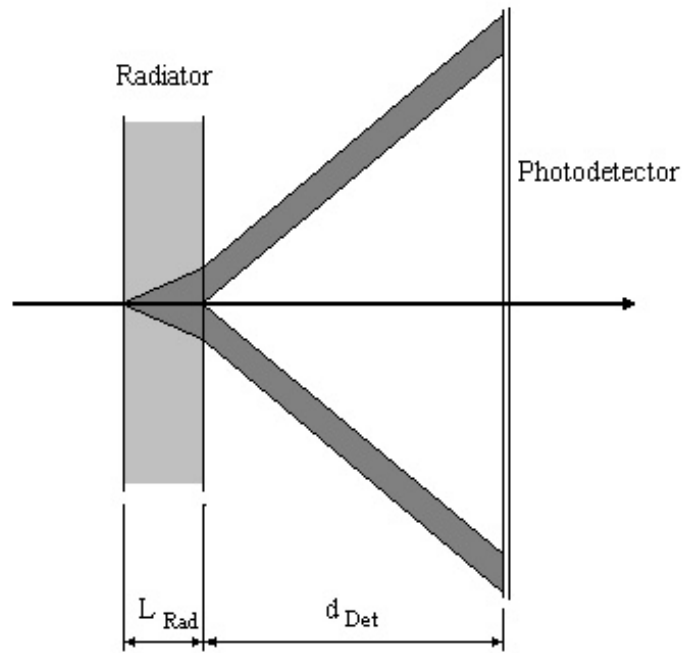
Fig. 3.12: Principle of the proximity focusing technique. Cherenkov photons, emitted in a thin radiator, are directly detected by a photodetector. From [3.3].
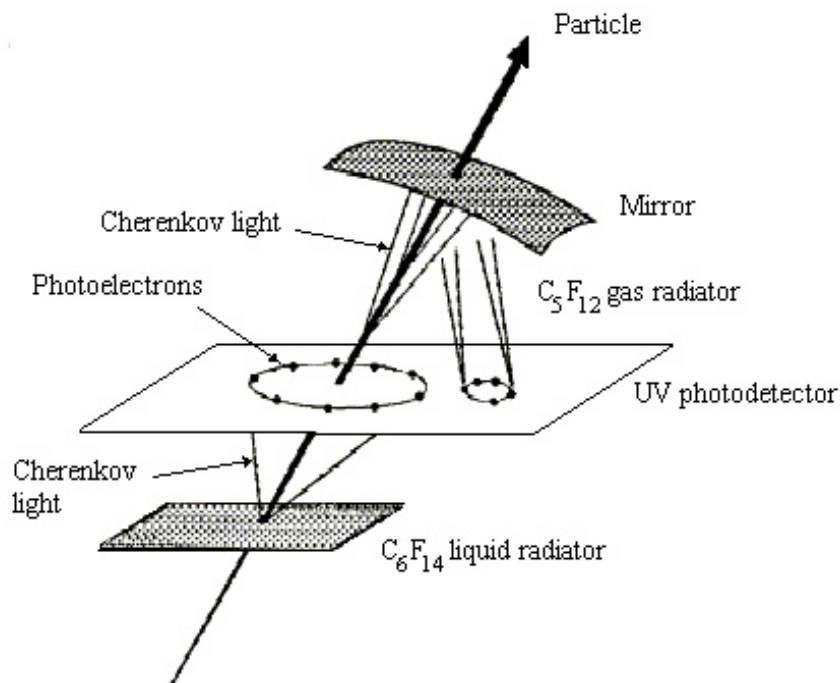

Fig. 3.13: The optical scheme of the Barrel RICH, equipped with parabolic mirrors. The same photodetectors are used for both photon emitted in the liquid and gas radiators. From [3.21].
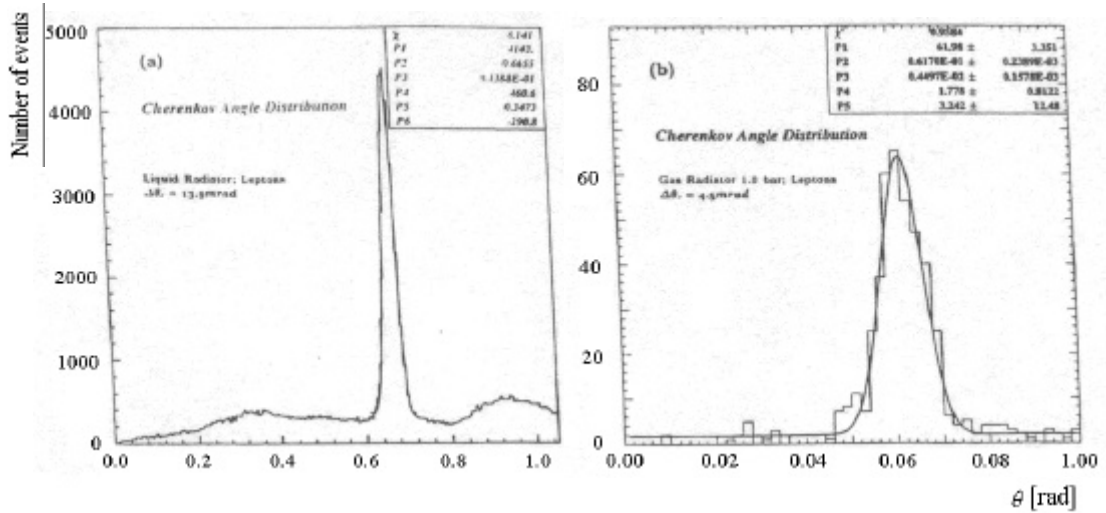
Fig. 3.14: The reconstructed Cherenkov angle q in DELPHI Barrel RICH from $p > 40$ GeV/c muons from Z^0 decays: (a) in the liquid C_6F_{14} radiator, (b) from the C_5F_{12} gas radiator. From [3.22].
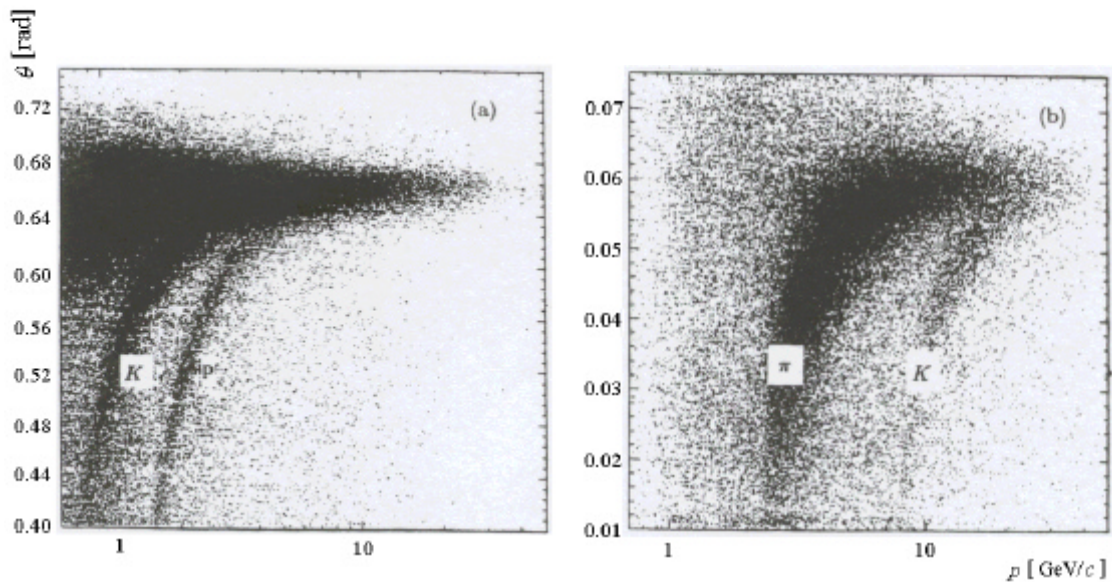

Fig. 3.15: Scatter plots of the reconstructed Cherenkov angle q versus track momentum p from hadrons as seen by DELPHI Barrel RICH: (a) from the liquid C_6F_{14} radiator, (b) from the C_5F_{12} gas radiator. From [3.22].

(a)   **(b)**
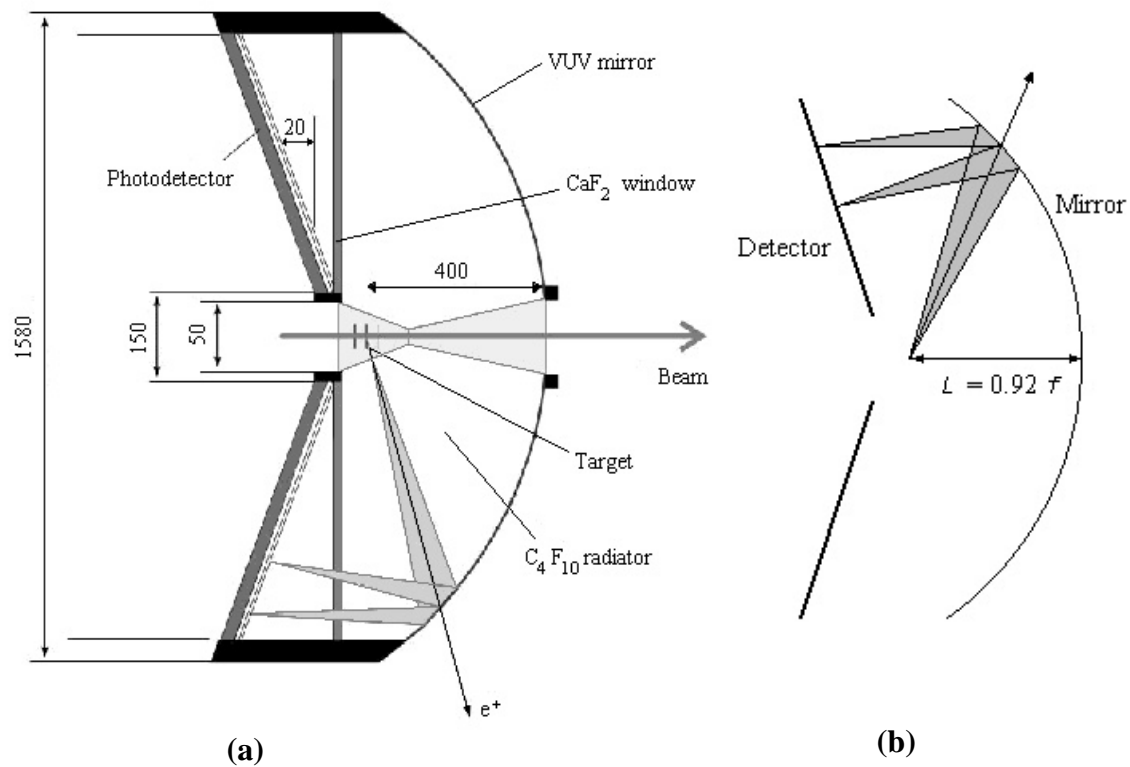
Fig. 3.16: (a): Schematic cross section of the HADES (High Acceptance DiElectron Spectrometer) RICH detector. The spectrometer is installed at GSI Darmstadt. (b): Simplified sketch of the corresponding optical principle. It features a very large acceptance angle. The spherical VUV mirror has diameter 1450 mm and $R = 870$ mm. It is segmented into 18 trapezoidal mirror elements. The requirement on geometry was: angular precision better than 0.6 mrad and $\Delta R < \pm 3$ mm. From [3.3],[3.17].
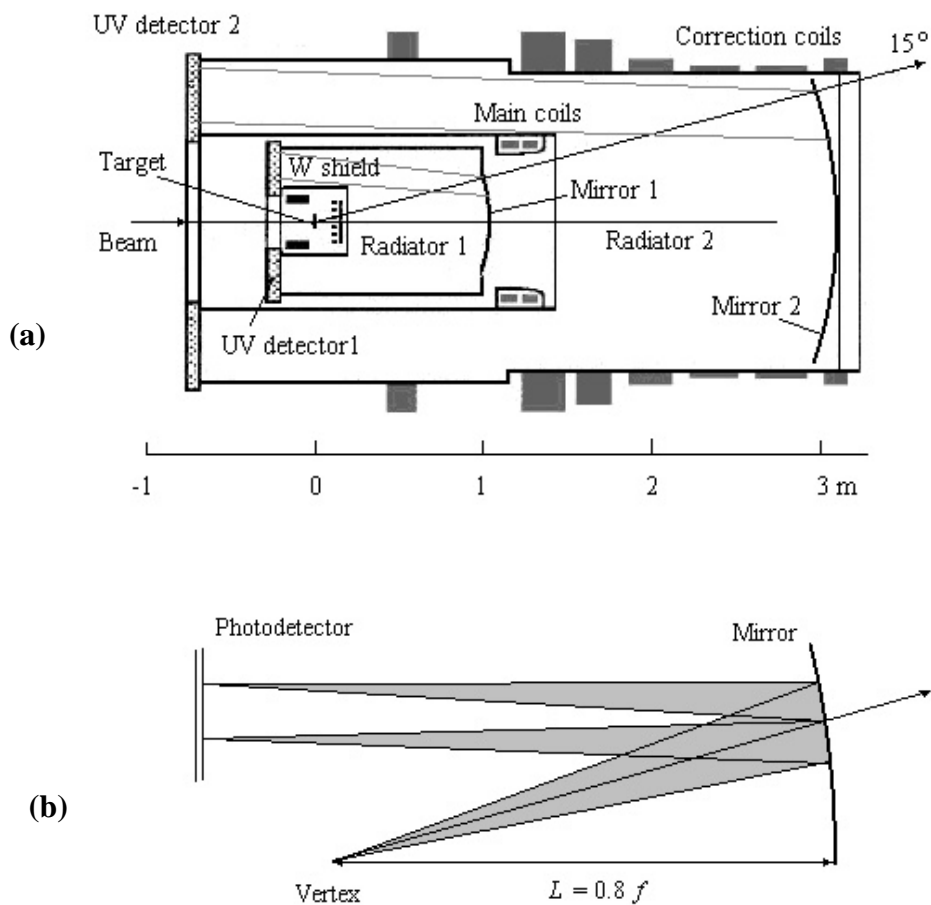
Fig. 3.17: (a): Schematic cross section of the CERES RICH detector. (b): Corresponding optical scheme. In comparison with the HADES RICH, it has much lower angular acceptance. On the other hand, it has an advantage of a flat focal surface. From [3.3], [3.21].
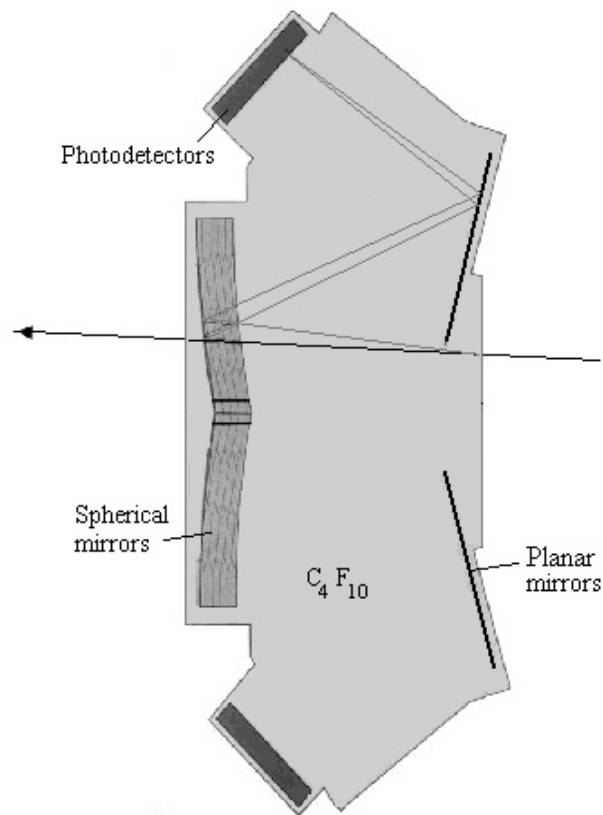
Fig. 3.18: Cross-sectional view of the HERA-B RICH detector. Spherical mirrors with R = 11.5 m are formed from 80 mirror elements. Plane mirrors are used to direct the Cherenkov photons to the photodetectors. From [3.18].
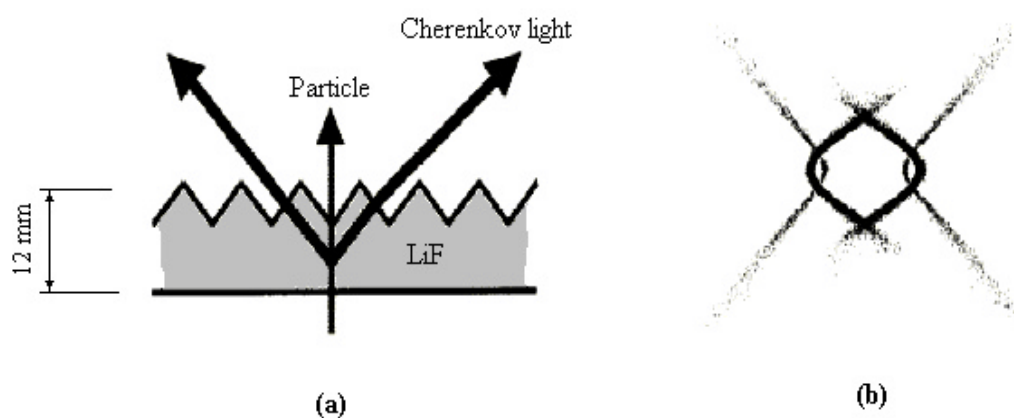

Fig. 3.19: (a): A saw-tooth profile of the LiF radiator used in the CLEO RICH detector. The special geometry solved the serious problem of the total internal reflection inside the radiator with high index of refraction $n = \sqrt{2}$. (b): Corresponding Cherenkov pattern. From [3.16].

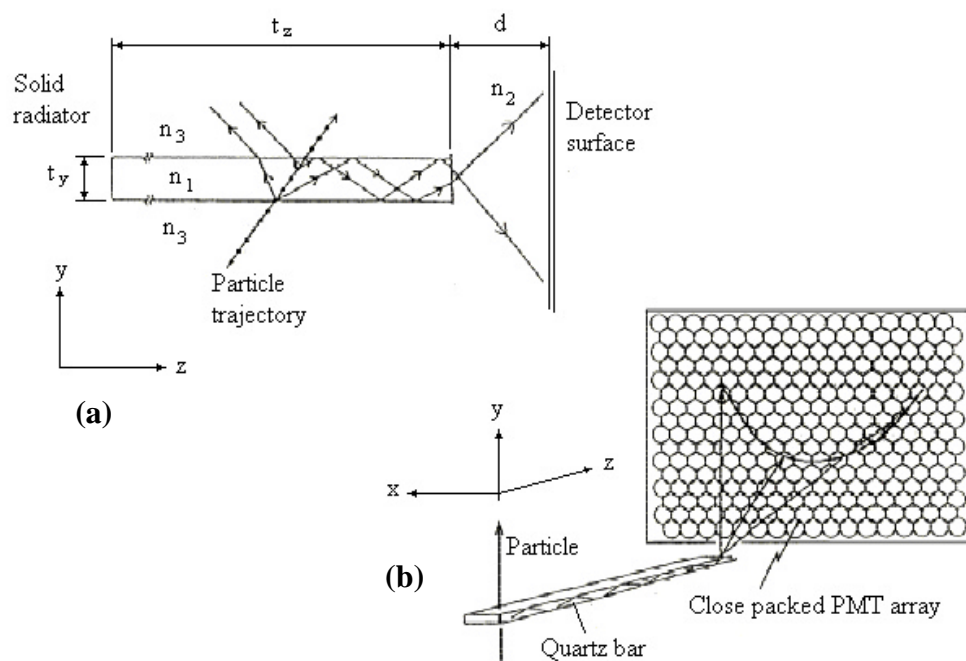**Fig. 3.20**: The DIRC detector of the BaBar experiment at SLAC takes advantage of the total internal reflection. (a): Principle of the transmission of Cherenkov light inside a quartz bar. (b): Formation of the proximity focussed Cherenkov image on the photodetector plane. From [3.23].
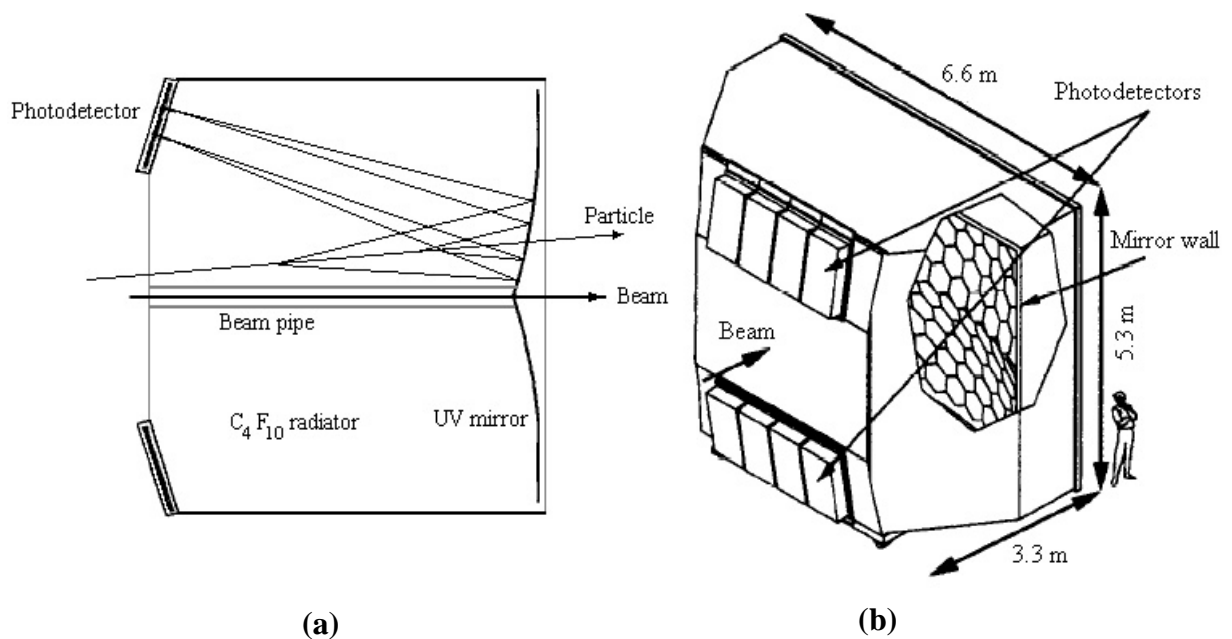
Fig. 3.21: (a): Schematic cross section of the COMPASS RICH 1 detector. (b): 3-D view of the detector vessel. From [3.26].

Fig. 3.22: Schematic view of the LHCb RICH 1 detector. Formation of Cherenkov rings with origin in the aerogel and gas is indicated.

Fig. 3.23: Schematic view of the LHCb RICH 2 detector. Apart from spherical mirrors, the optical system contains also planar mirrors to bring Cherenkov photons to the photodetectors and to make the vessel shorter.

3.4   The new generation of RICHes at CERN

LHCb RICH detectors

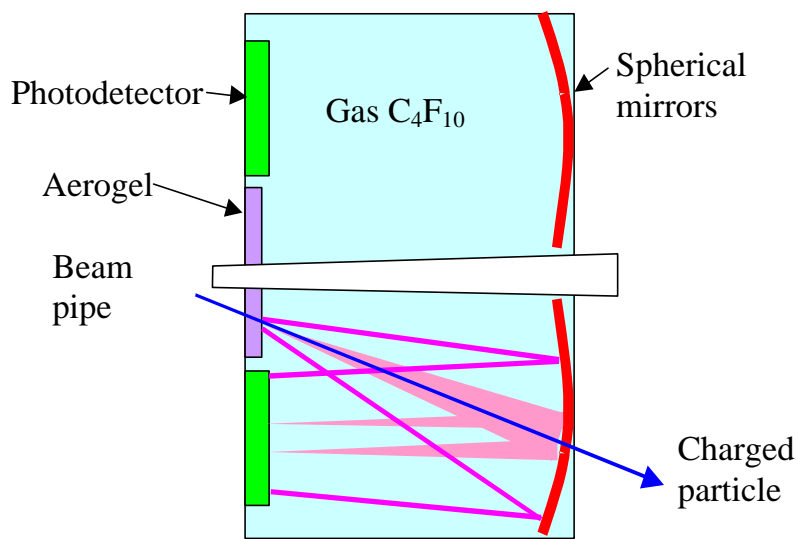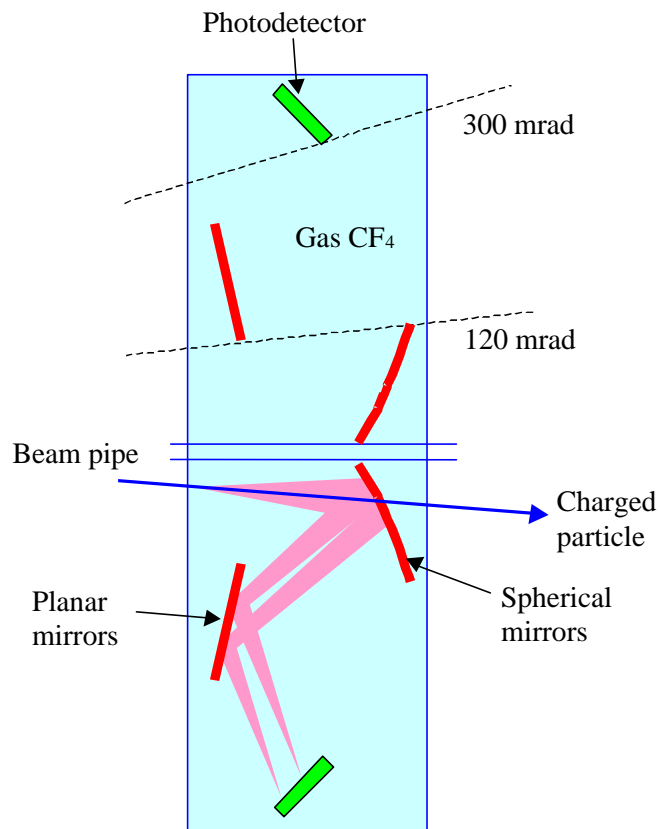The importance of the RICH system [3.24] for the measurement of CP asymmetry of $B_d \to \pi^+\pi^-$ decays can be seen in Fig. 3.24. Before positive particle identification is applied, the signal from $B_d \to \pi^+\pi^-$ is dwarfed by two-body backgrounds with the same topology: $B_d \to K^+\pi^-$, $B_d \to K^-\pi^+$ and $B_s \to K^+K^-$. Another example is extraction of $B_s \to D_s^{\pm}K^{\Upsilon}$ decays from overwhelming background from $B_s \to D_s^{\pm}\pi^{\Upsilon}$ decays, see Fig. 3.25.
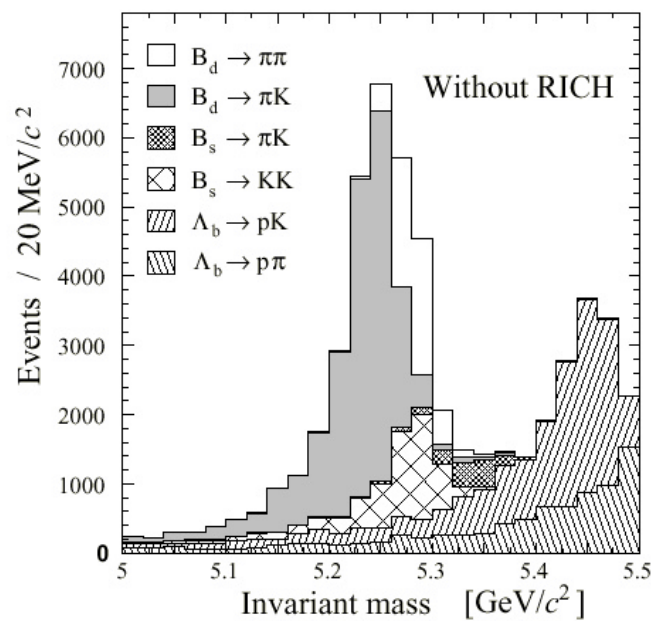

Fig. 3.24: Mass spectrum of $B_d \to \pi^+\pi^-$ candidates before any particle identification is applied. From [3.24].

In LHCb, charged particles over a wide momentum range 1-150 GeV/c will be identified, see Fig. 3.26, within an angular acceptance from 10 mrad to 300 mrad in the horizontal projection and to 250 mrad in the vertical projection. The lower momentum limit required for π/K separation is determined by the identification of tagging kaons (Fig. 3.27b), the upper limit by tracks from two-body B-decay channels (Fig. 3.27a). Efficiency of the positive identification of pions and kaons over the whole momentum range is shown in Fig. 3.28. To cover the whole momentum range, the system consists of two subdetectors, an upstream RICH 1 and a downstream RICH 2. RICH 1 contains a silica aerogel and a C_4F_{10} gas radiator. Silica aerogel, with relatively high refractive index $n = 1.03$, is suitable for the lowest momentum particles. The intermediate momentum region is covered by gaseous C_4F_{10}. RICH 2, with CF_4, is used to identify the highest momentum tracks.

In Fig. 3.29, the polar angle q is plotted as a function of momentum for all tracks in simulated $B_d \to \pi^+\pi^-$ events. There is a clear correlation between the polar angle
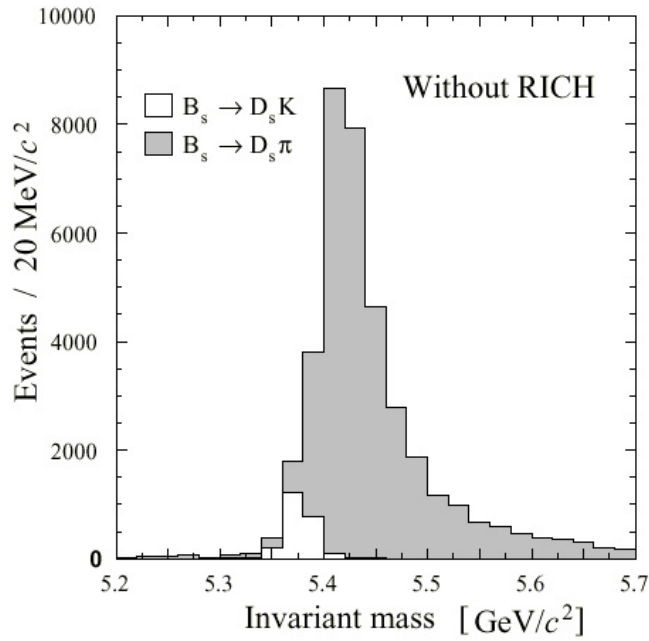
Fig. 3.25: Mass spectrum of $B_s \rightarrow D_s^{\pm} K^{\Upsilon}$ candidates before any particle identification is applied. From [3.24].
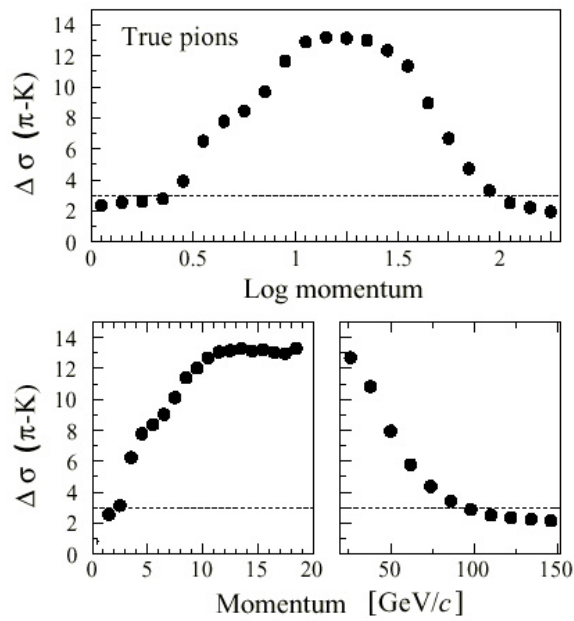
Fig. 3.26: Number of sigma separation between pion and kaon hypothesis versus momentum for true pions in triggered and accepted signal events. Top: logarithmic momentum scale, Bottom: linear momentum scales. From [3.24].
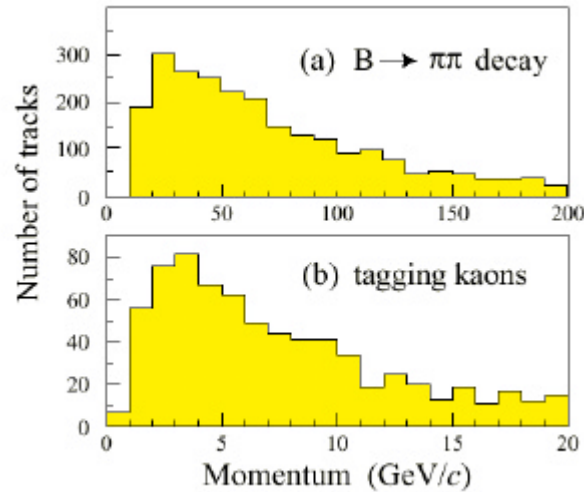
Fig. 3.27: Momentum distribution for (a) the highest momentum pion from $B_d \rightarrow \pi^+\pi^-$ decays, (b) tagging kaons. From [3.24].
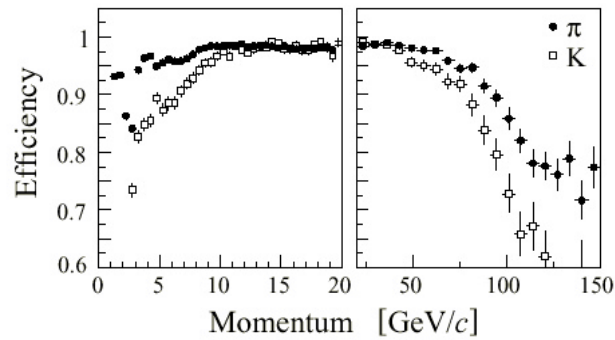
Fig. 3.28: Identification efficiency for pions and kaons versus momentum, for triggered and accepted signal events. From [3.24].
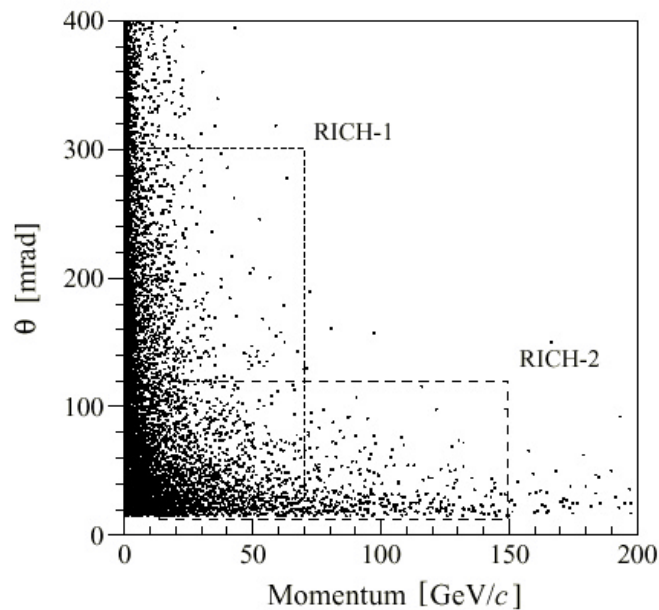
Fig. 3.29: Polar angle *q* versus momentum, for all tracks in simulated $B_d \rightarrow \pi^+\pi^-$ events. The regions of interest for RICH 1 and RICH 2 are indicated by the dashed lines. From [3.24].

and momentum of tracks. The dashed lines in the same figure indicate regions of interest for both RICH 1 and RICH 2.

The layout of RICH 1 is shown in Fig. 3.22. It has wide angular acceptance of 300 mrad (horizontal) $\times$ 250 mrad (vertical), therefore to reduce its physical size it is placed upstream of the spectrometer magnet. The aerogel radiator is 5 cm thick and the C_4F_{10} gas radiator is 85 cm long. The Cherenkov light is focused onto four photodetector planes by spherical mirrors with a curvature radius of 1700 mm hence focal length $f = 850$ mm. The total mirror surface is segmented into four quadrants each 900×750 mm^2. The axes of the mirror quadrants are tilted with respect to the beam axis by ± 286 mrad horizontally and ± 65 mrad vertically, to bring the image out of the spectrometer acceptance, so that the material of the photodetectors does not degrade the tracking.

RICH 2, schematically shown in Fig. 3.23, has a reduced angular acceptance of 120 mrad (horizontal) $\times$ 100 mrad (vertical). The CF_4 gas radiator has an approximate length of 170 cm. To make the RICH 2 system shorter, it has two sets of mirrors. The primary spherical mirrors with a curvature radius of 8000 mm ($f = 4000$ mm) are followed by a secondary flat mirrors. Two spherical mirrors have axes tilted by ± 450 mrad horizontally with respect to the beam axis. The flat mirror planes are tilted by ± 140 mrad with respect to the horizontal.

Photons, forming Cherenkov ring-images, are detected at photodetector planes. A total area of about 2.6 m^2 is required, with an effective detector granularity of about 2.5 mm $\times$ 2.5 mm. Photodetector planes are created as arrays of cylindrical phototubes. Hybrid photodiodes with pixel readout (Pixel HPD) have been selected by the LHCb collaboration as the baseline photodetector. It is necessary to detect single photons with the highest possible efficiency over the wavelength range of interest from 195 nm to 700 nm. A schematic drawing of the HPD is shown in Fig. 3.30. The photocathode converts incident photons to photoelectrons, which are focused by two intermediate electrodes on the silicon diode sensor. Each HPD has 1024 pixels of size 0.5 mm $\times$ 0.5 mm which, for an electrostatic demagnification factor of five, corresponds to 2.5 mm $\times$ 2.5 mm on the HPD photocathode.

Example of what should be detected in photodetector planes of RICH 1 and RICH 2 can be seen in Fig. 3.31. It is a simulated $B_d \rightarrow \pi^+\pi^-$ event. Points represent detected photons, superimposed circles then reconstructed Cherenkov ring-images. The Chererenkov rings are not perfect circles, but are roughly elliptical in shape, with a degree of distortion that depends on the direction of the track. In RICH 1 two types of rings can be seen, those with big diameter come from the aerogel and others, with small diameter, from the C_4F_{10} gas radiator. The expected number of detected photoelectrons from a track passing through a Cherenkov radiator is given by relations (3.4), (3.5) and (3.6):

$$N_{\text{pe}} = \left(\frac{\alpha}{\hbar c} \right) L \epsilon_A \eta \int QRT \sin^2 \theta_c \, dE_\gamma \,, \tag{3.12}$$
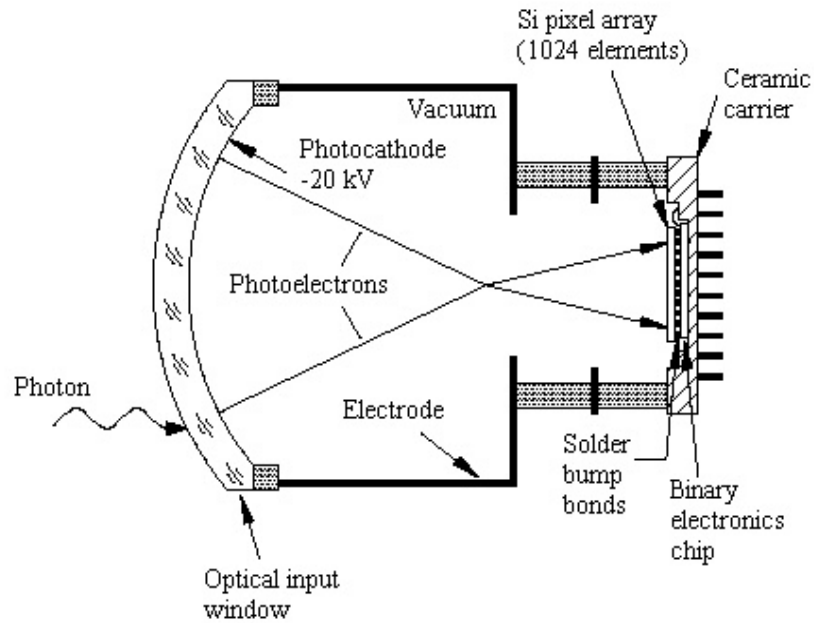
Fig. 3.30: Schematic view of the Pixel HPD, showing the principle of photon detection. From [3.24].
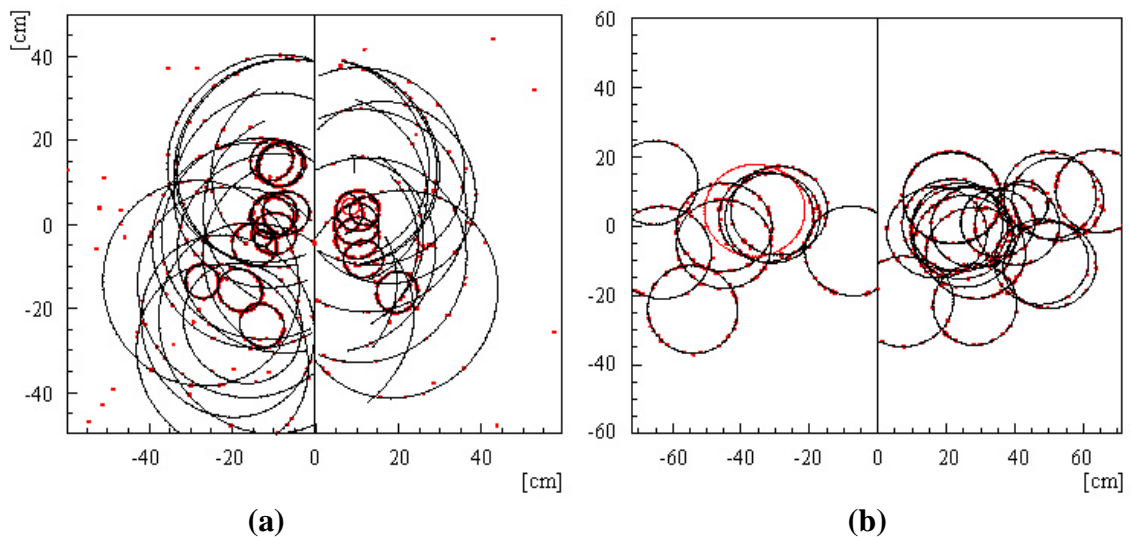
Fig. 3.31: (a) Event display of a simulated $B_d \rightarrow \pi^+\pi^-$ event, with the photodetector planes of RICH 1 drawn side by side, and the Cherenkov rings superimposed. (b) Event display of the same event for RICH 2. From [3.24].

where the first factor is a constant with value $370 \, \text{eV}^{-1}\text{cm}^{-1}$, L is a length of Cherenkov radiator, e_A is the coverage of the photodetector active area, $h = 0.9$ is the HPD single photoelectron detection efficiency, Q is the HPD quantum efficiency, R is the mirror reflectivity and T is the transmission of a 5 mm thick quartz plate which seals the Cherenkov gas volume in front of the HPD's.

   The particle identification performance is tied to the Cherenkov angle resolution. There are a number of contributions to the single photon resolution:

- Chromatic aberrations due to dispersion of refractive index over the bandwidth.
- Multiple scattering of the charged particle in the radiator and track bending due to magnetic fields.
- Readout accuracy, depending on granularity of photodetector and quality of interpolation.
- Optics errors: mirror quality and alignment, optical aberrations, approximation of curved focal surfaces by flat detectors.

Contribution of variable v_i to the Cherenkov angle resolution is in general given by:

$$\boldsymbol{s}_{\boldsymbol{q}}(v_i) = \left(\frac{\partial \boldsymbol{q}}{\partial v_i}\right)\boldsymbol{s}_{v_i} \tag{3.13}$$

Cherenkov angle error caused by energy bandwidth $\boldsymbol{DE}$ is:

$$\boldsymbol{s}_{\boldsymbol{q}}^{\text{chromatic}} = \left(\frac{\partial \boldsymbol{q}}{\partial n}\right)\left(\frac{dn}{dE}\right)\boldsymbol{s}_E \tag{3.14}$$

Factor dn/dE is the chromatic dispersion of radiator media, shown in Fig. 3.32, which causes a smearing of the Cherenkov angle. This is an aberration, which cannot be reduced for a chosen radiator. In the LHCb RICH detectors, the chromatic aberrations were reduced by the choice of longer wavelength bandwidth in visible and near UV region.

Multiple scattering (ms) and magnetic deflection (ma) in the radiator medium are momentum dependent sources of Cherenkov angle error given by $\boldsymbol{s}_{\boldsymbol{q}}^{\text{track}} = p_{\text{a}}/p$ with contributions:

$$p_{\text{ms}} = k_{\text{ms}}\sqrt{L/X_0} \quad \text{and} \quad p_{\text{ma}} = k_{\text{ma}}BL\sin\boldsymbol{q}_{\text{ma}} \tag{3.15}$$

with a resulting momentum $p_{\text{a}} = \sqrt{p_{\text{ms}}^2 + p_{\text{ma}}^2}$. k_{ma} and k_{ms} are constants, X_0 is the radiation length, B is the magnetic field strength, L is the radiator length and $\boldsymbol{q}_{\text{ma}}$ the particle angle relative to the magnetic field direction. For short solid and liquid radiators, the contribution of multiple scattering and magnetic deflection is very small, for longer gas radiators it increases. In comparison with the chromatic aberrations, these aberrations are usually negligible.

The finite granularity a of the photodetectors contributes to the Cherenkov angle resolution by:

$$\boldsymbol{s}_{\boldsymbol{q}}^{\text{pixel}} = \frac{a}{f\sqrt{12}}, \tag{3.16}$$

where f is a focal length of the focusing mirror.
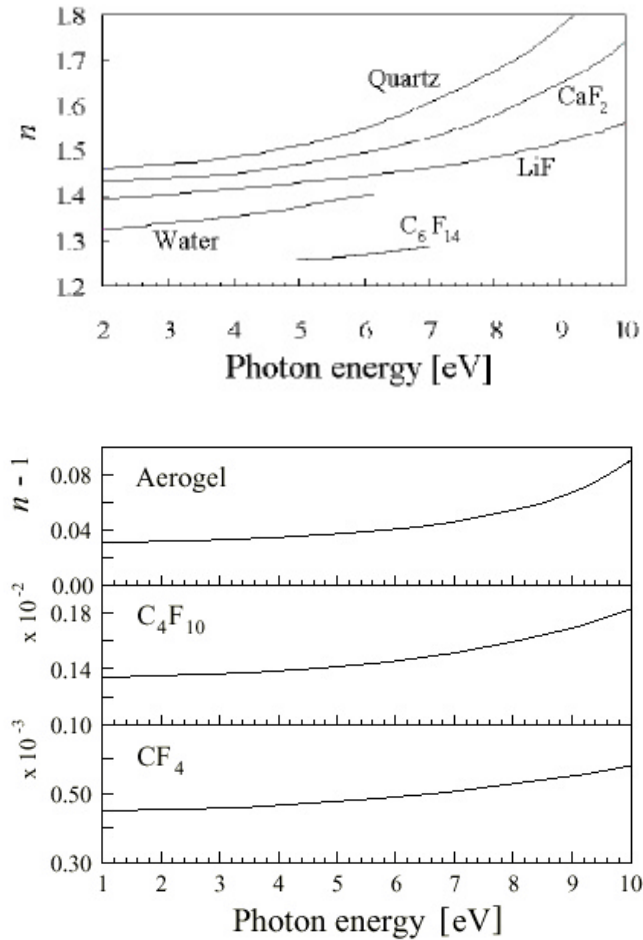
Fig. 3.32: Refractive index of different radiator media as a function of the photon energy. From [3.24].

The big tilting of the spherical mirror leads to not negligible optical aberrations like the spherical aberration, coma and astigmatism. Position of the image of a Cherenkov photon depends on its emission point on the track inside the radiator. Fig. 3.33 shows dependence of the total optical aberration in the xz-plane on the mirror tilt in RICH 2 for the maximum Cherenkov angle $q_{max} \cong 32$ mrad. The dependence was obtained by ray tracing. Mean value for the whole spectrum of Cherenkov angles is $s_q^{emission} = 0.31$ mrad.

Values of resolution on the reconstructed Cherenkov angle for all three radiators are shown in Table 3.2, together with other basic parameters. The following contributions are considered:

1. $s_q^{emission}$, emission point: in reconstruction, it is supposed that all photons are emitted at the mid-point of the track through the radiator. The spherical mirror is tilted so this approximation leads to error of the reconstructed angle q.
2. $s_q^{chromatic}$, chromatic: Cherenkov angle is dependent on the photon energy due to the chromatic dispersion of the radiators.
3. s_q^{pixel}, pixel: due to the finite granularity of the photodetector.
4. s_q^{track}, tracking: due to errors in the reconstructed track parameters.

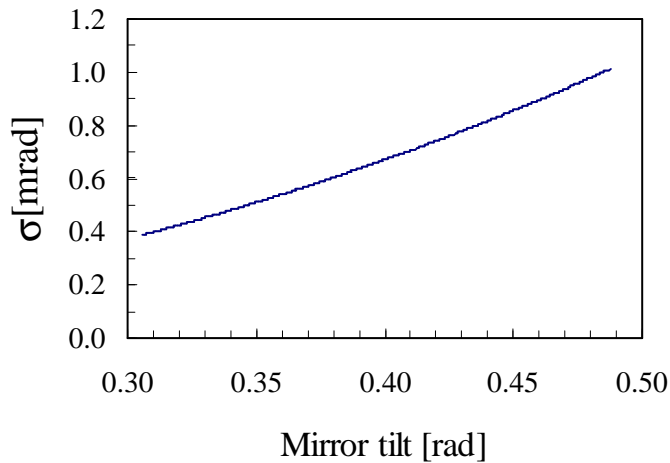**Fig. 3.33**: Total optical aberration in the xz-plane versus the mirror tilt in RICH 2 for maximum Cherenkov angle $q_{max} \cong 32$ mrad. The dependence was obtained by ray tracing.

If the precision of the focusing optics should not affect the total angular resolution s_q^{total} of the new RICH system it has to be at level of $s \sim 0.5$ mrad in RICH 1, and ~ 0.1 mrad in RICH 2 (see Sect. 4.1). The required precision of the RICH mirrors is then approximately one order of magnitude higher than in any previous RICH system at CERN.

At the same time, the fraction of the radiation length X_0 has to be kept as low as possible especially in upstream parts of the LHCb detector, see Sect. 2.3. Table 3.3 shows planned material budged for different components in both RICH detectors expressed in fractions of X_0.

COMPASS RICH detector

COMPASS[5] [3.25] is a fixed target experiment at CERN SPS[6]. Its physics program includes measurements of polarised deep inelastic scattering with the SPS polarised muon beam and polarised hydrogen and deuterium targets, hadron spectroscopy studies with charm production and search for exotic states in the hadronic spectra.

The RICH system [3.26] will separate pions from kaons and protons above three sigma level between 3 and 120 GeV/c. To achieve this, two RICH counters are needed. Their expected resolutions of π-K separation are shown in Fig. 3.34. At present, RICH 1 is being built.

---

[5] Common Muon and Proton Apparatus for Structure and Spectroscopy
[6] Super Proton Synchrotron.

Table 3.2: Basic parameters of LHCb RICH radiators determined from the simulation. The lower part lists the contributions to the resolution, the total resolution per photoelectron and the mean value of detected photoelectrons per ring image. From [3.24].

Radiator		CF_4	C_4F_{10}	Aerogel
L	[cm]	167	85	5
n		1.0005	1.0014	1.03
q_{max}	[mrad]	32	53	242
$p_{th}(\pi)$	[GeV]	4.4	2.6	0.6
$p_{th}(K)$	[GeV]	15.6	9.3	2.0
$s_q^{emission}$	[mrad]	0.31	0.74	0.60
$s_q^{chromatic}$	[mrad]	0.42	0.81	1.61
s_q^{pixel}	[mrad]	0.18	0.83	0.78
s_q^{track}	[mrad]	0.20	0.42	0.26
s_q^{total}	[mrad]	0.58	1.45	2.00
N_{pe}		18.4	32.7	6.6

Table 3.3: Contributions (expressed in fractions of X_0) to the material budget inside the LHCb acceptance. From [3.24].

Item	RICH 1	RICH 2
Entrance window	0.001	0.014
Aerogel	0.033	-
Gas radiator	0.024	0.017
Mirror	0.046	0.046
Mirror support	0.030	0.033
Exit window	0.006	0.014
Total (X_0)	0.140	0.124

A scheme of RICH 1 is shown in Fig. 3.21. Within an angular acceptance of ± 250 mrad in horizontal projection and ± 200 mrad in vertical projection, it will provide hadron identification up to 60 GeV/c. C_4F_{10} radiator is 3 m long to produce enough photons per ring in the region of interest, which is between 160 and 200 nm.
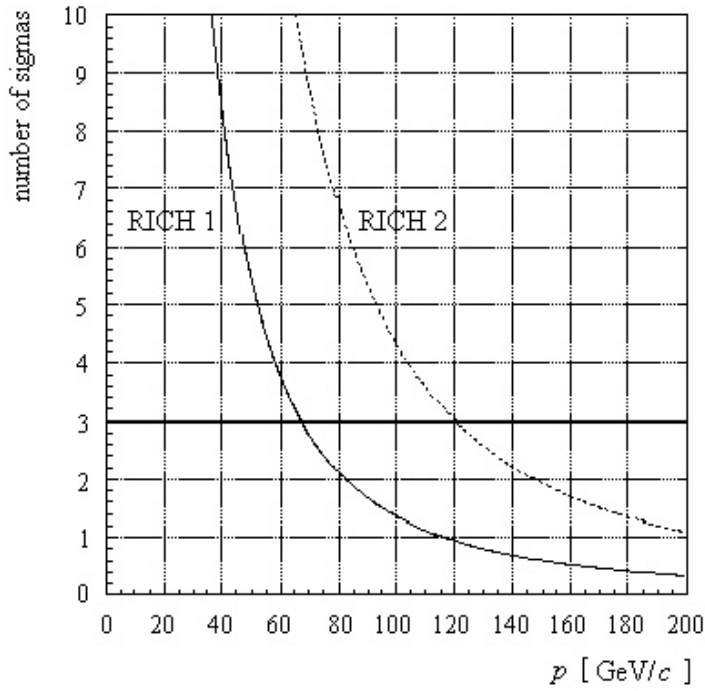
Fig. 3.34: Expected resolution for π/K separation in number of sigmas versus momentum. From [3.25].

The threshold momenta for emission of Cherenkov photons are $p_{th} = 2.5$ GeV/c for pions, $p_{th} = 8.9$ GeV/c for kaons and $p_{th} = 17.0$ GeV/c for protons. The optical system consists of two UV reflecting spherical mirrors with the radius of curvature $R = 6600$ mm, which focus the Cherenkov light on two photodetector planes. The two mirrors are segmented in a total number of 116 elements (34 hexagonal and 24 pentagonal each), covering a total area large than 20 m². The photodetectors consist of MWPC's equipped with CsI photocathodes and quartz window with total active surface of 5.3 m². With pixel size of 8×8 mm² it features about 80000 channels.

The downstream RICH 2 will be built in the second phase of the experiment construction. The gas mixture of C_2F_6 and Ne used for the radiator will cover momentum range from 30 GeV/c up to 120 GeV/c with angular acceptance of 56 mrad in vertical projection and 112 mrad in horizontal projection. The optical set up of RICH 2 is similar to RICH 1. Mirrors will have a radius of curvature $R = 16$ m.

Basic parameters of both RICH detectors are given in Table 3.4. Required precision of the opto-mechanical system is at level $\sigma \sim 0.17$ mrad for RICH 1 and $\sigma \sim 0.1$ mrad for RICH 2.

Table 3.4: Basic parameters of COMPASS RICH radiators determined from a simulation. The lower part shows the total resolution of per photoelectron and per ring, and the mean value of detected photoelectrons per ring image. From [3.25].

Radiator		C_4F_{10}	$C_2F_6 + Ne$
L	[cm]	300	800
n		1.0015	1.0005
q_{max}	[mrad]	55	32
$p_{th}(\pi)$	[GeV]	2.5	4.4
$p_{th}(K)$	[GeV]	8.9	15.5
$p_{th}(p)$	[GeV]	17.0	29.5
$s_q^{p.e.}$	[mrad]	0.07	0.03
s_q^{ring}	[mrad]	0.16	0.08
N_{pe}		34	23

.

4   Characterisation of RICH opto-mechanical components

The high requirements on precision of the new generation of RICH systems have become a challenge for physicists and engineers working on their preparation. On the base of given requirements, parameters of opto-mechanical components have to be determined, taking in account technological possibilities of industry. An interaction with industry has to be established and collaboration on development of prototypes has to be started. In order to evaluate prototypes and to provide a feedback to industry, an optical laboratory has to be established and relevant measurement set ups developed and installed. To ensure the required resolution of the Cherenkov angle measurement, it is very important to test quality and parameters of all components forming the new RICH opto-mechanical systems.

4.1   Requirements and parameters of LHCb RICH 2 opto-mechanical system

In the following, we will focus mainly on an analysis of the LHCb RICH 2 opto-mechanical system. This system will become the most precise existing RICH system. The starting point for the determination of mirrors and mirror mounts parameters is given by two basic requirements: high resolution of the Cherenkov angle reconstruction and low fraction of radiation length presented by the RICH system. These requirements being in principle conflicting, it becomes necessary to find a compromise.

Precision of the RICH 2 opto-mechanical components

Resulting value of the total single photon resolution $s_q^{\text{total}} \leq 0.6$ mrad [3.24] is given by:

$$s_q^{\text{total}} = \sqrt{\sum_i s_i^{\,2}} \, , \qquad\qquad (4.1)$$

where s_i are contributions summarised in Table 3.2. It must not be degraded by precision s_{oms} of the RICH opto-mechanical system, which therefore has to be $s_{\text{oms}} \leq 0.1$ mrad. The opto-mechanical system of RICH 2 consists of four parts: spherical and planar mirrors, both fixed by means of adjustable mirror mounts on supporting panels. For our analysis, we regard the supporting panels as perfectly rigid

and so they do not contribute to the errors of the system. As the first approximation, we suppose that contributions of four considered parts are equal and independent:

$$s_{part} = \sqrt{\frac{s_{oms}^2}{4}} = \frac{s_{oms}}{2} = 0.05 \ \text{mrad} \qquad (4.2)$$

Intrinsic precision of each optical or mechanical component has half value because reflection doubles any angular deviation:

$$s_{comp} = \frac{s_{part}}{2} \cong 0.03 \ \text{mrad} \qquad (4.3)$$

The assumption of equal contributions to the precision of the opto-mechanical system would be correct if both spherical and planar mirrors would be fabricated at equal grinding and polishing precision, mirror mounts would be of the same precision, and distances of all components from the photodetector plane would be equal. The condition of equal precision of the spherical and planar mirrors and the mounts is realisable. But the second condition cannot be fulfilled; the planar mirrors are placed roughly at half distance from the photodetectors than the spherical ones. Their contribution to the photon shift at the photodetector plane is therefore two times smaller than in the case of spherical mirrors, and the assumption is safe.

Fractions of the radiation length

Table 3.3 shows maximum desired contributions of individual components to the material budget in both RICH detectors, expressed in units of the radiation length.

Table 4.1: Basic properties of chosen materials convenient for manufacturing of lightweight mirrors. *a* is a coefficient of thermal expansion.

Material	X_0 [cm]	E [10^4 MPa]	a [10^{-6}/°C]
Pyrex glass	12.7	6.17	3.2
Beryllium	35.3	28.9	11.3
Aluminium	8.9	6.9	23.9
Plexiglas	34.4	0.33	70

Values of the radiation length for chosen materials are presented for illustration in Table 4.1. The requirement for maximum transparency of RICH systems for traversing particles means not only to use minimum amount of material, but also to avoid its local concentration. The RICH system is designed with the intent to spread the material uniformly in the *xy*-plane, which is perpendicular to the lateral axis *z* of the detector.

4.2   Mirrors

Spherical mirrors in the RICH detectors focus Cherenkov photons into the ring-images, as briefly introduced in Sect. 3.1 and 3.3. This enables to increase the measurement resolution and to reduce a size of the area covered by photodetectors. Tilted mirrors allow installing the photodetectors outside of the detector angular acceptance. In order to make the vessel of RICH 2 shorter, two flat mirror planes are used.

4.2.1   Given requirements and parameters

To cover efficiently a certain surface with an array of mirrors, we need to establish a relation between their physical qualities (material, shape, size, thickness and weight), their optical qualities (geometrical precision and reflectivity) and the characteristics of the formed array (number of mirrors, complexity, overall weight and fraction of radiation length) and cost.

The number of mirrors covering the required surface has to be kept as small as possible to reduce complexity, optical tests and material budget. Minimum number of mirrors covering given reflective surface is determined by their maximum acceptable size, which is related to required thickness and precision. Thickness of the mirrors for the LHCb RICH detectors should not exceed 4 to 5 % of the radiation length. Table 4.1 lists materials applicable for manufacturing of mirror substrates with low fraction of radiation length. The material and the design must ensure at the same time a high precision of the reflective surface. This requirement represents a need of high rigidity of the mirror substrate structure, its small thermal dilatations, and good long-term stability. The rigidity *K* of a thin mirror substrate is roughly given by:

$$K \propto \frac{Et^3}{d^2},\tag{4.4}$$

where *E* is Young's Modulus of the material, *t* is mirror thickness, and *d* is its diameter. Fig. 4.1 shows a relation between *E* and X_0 for chosen materials.
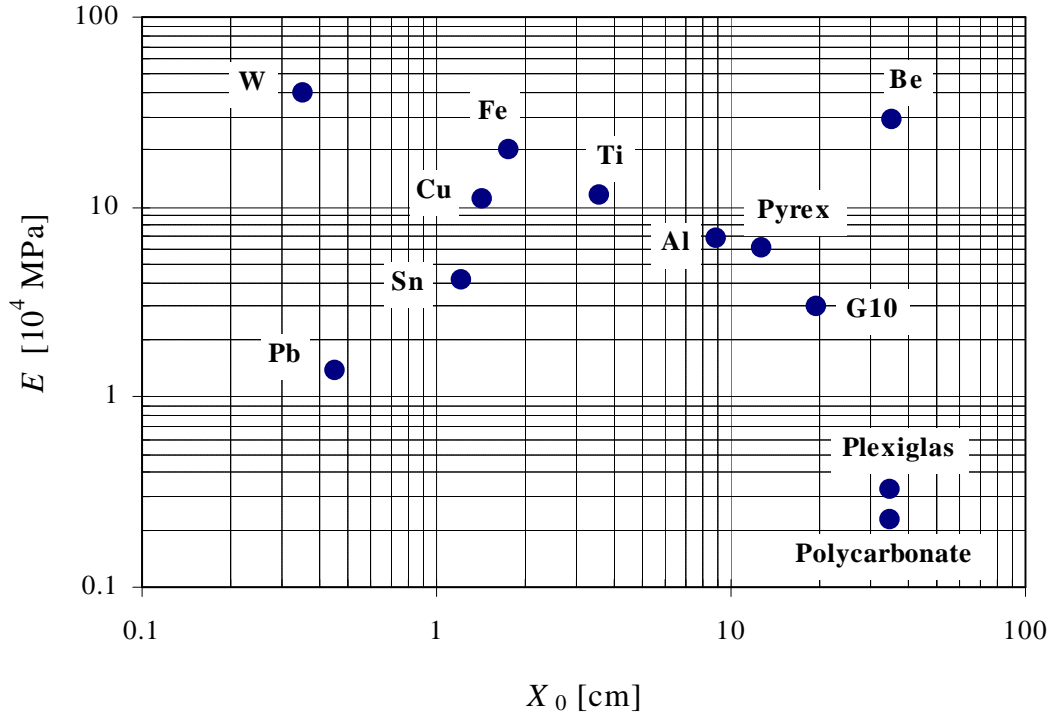
Fig. 4.1: Relation between Young's Modulus of Elasticity E and radiation length X_0 for chosen materials. Beryllium features the best combination of these two properties important for lightweight mirrors.

A very important parameter of the RICH mirrors is their high reflectivity. The reflectivity should be higher than 85 % for the whole region of interest and if possible close to 90 %. The reflective surface of RICH mirrors is usually made as a thin metallic coating, vacuum evaporated on the substrate and protected by a dielectric layer. Fig. 4.2 demonstrates a few coatings with high reflectivity in the wavelength region 200 – 500 nm of the LHCb RICH system. The region of interest is given by the photodetector choice.

The active surface of the mirror substrate is polished to a high degree of smoothness. To minimise a scattering of the reflected light, it is important to achieve a smoothness of at least $\lambda/100$. For the LHCb mirrors this means 2 nm rms.

Concerning the radius of curvature R, its standard deviation s_R should not exceed 1.9 % of R:

$$s_R = \frac{\sqrt{12}}{2.36} \cdot \frac{s_d}{r_c} \cdot R = 1.9\,\% \ R, \qquad (4.5)$$

where r_c is a maximum base radius of the Cherenkov cones on the mirrors and $s_d = 0.72$ mm is a photodetector resolution. As the gas thickness is relatively short

(~1.7 m) and $q_{max} \cong 32$ mrad, then $r_c = 1.7 \cdot q_{max} \cong 55$ mm. For RICH 2 s_R corresponds to ~ 150 mm.
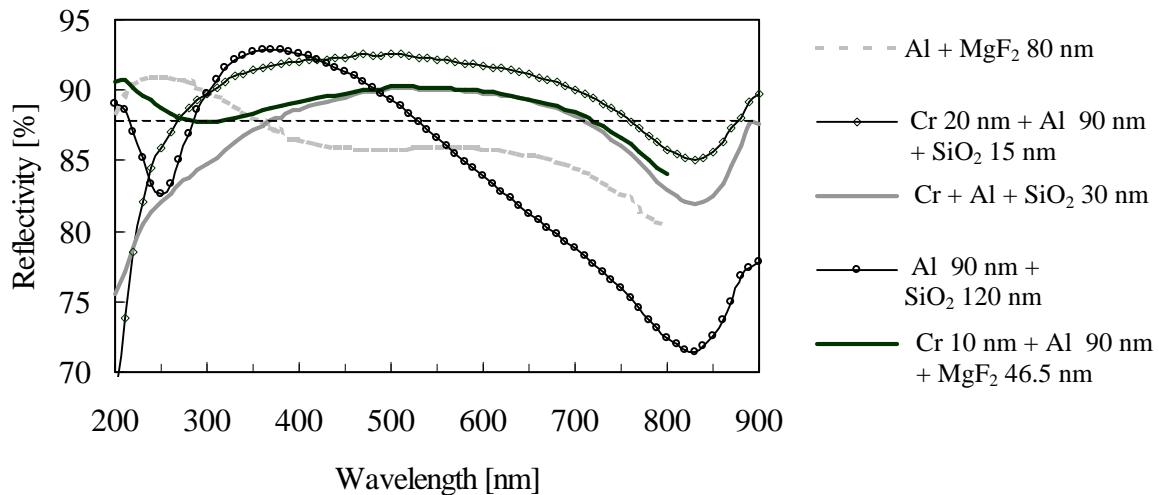

Fig. 4.2: Spectral reflectivity of several examples of coatings and their composition. Courtesy to A. Braem.

Mirrors will be installed in a vessel filled by a fluorocarbon gas radiator. For a high efficiency of the photon detection, a high purity of the gas is needed [4.1]. Mirror substrates have to ensure no or very limited level of outgassing. Some materials are excluded because of this particular reason.
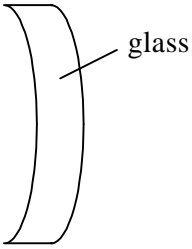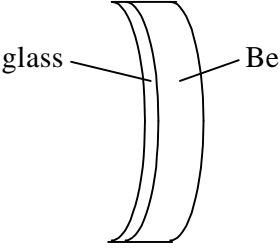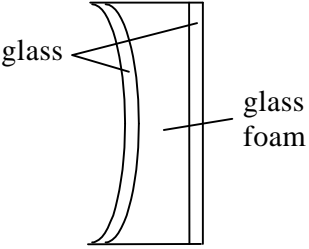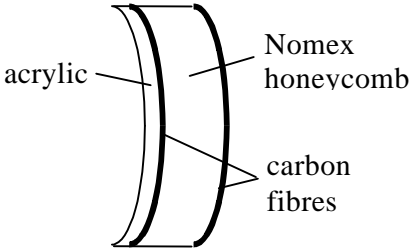
4.2.2 Possible designs, materials and technologies

In the framework of preparation of the LHCb system, we have contacted several mirror manufactures and discussed the mirror requirements and technological possibilities. According to analysis of convenient materials and of manufacturing technologies [4.2], following possibilities, summarised in Table 4.2, are available:

1) Simple glass substrate
   Technology of relatively thick mirror substrates made of glass at very high precision is well verified in the field of astronomical mirrors. The requirement for precision of the RICH mirrors is lower than in the case of astronomical mirrors. Thickness of 6.4 mm, corresponding to 5 % of X_0 is relatively small. Maximum mirror diameter for which the substrate would be still stable enough is therefore limited. Advantages of glass substrates are: no gas pollution, high radiation hardness and relatively well-known technology. Their disadvantages are: fragility, high weight, and the creep effect.

Table 4.2: Structures of lightweight mirror designs.

Simple glass mirror	Beryllium technique mirror
glass	glass — Be
6.4 mm $\propto$ 5 % X_0	6 mm $\propto$ 2.2 % X_0
Glass foam sandwich	Composite mirror
glass — glass foam	acrylic — Nomex honeycomb — carbon fibres
44 mm $\propto$ 6 % X_0	10 mm $\propto$ 1 % X_0

2) Glass foam sandwich

The sandwich consists of two thin layers of glass and thicker layer of glass foam. The three layers are unified under high temperature and pressure. The thermal cycle has to be precisely tuned. The structure with two 2-mm glass layers and 40 mm of glass foam corresponds to ~ 6 % of X_0. Since the material is in principle the same as in case 1), also properties are similar. The structure is more rigid but the technology is more difficult and time-consuming.

3) Beryllium-technique mirrors

Beryllium substrate can be polished but the smoothness is not good enough for RICH applications. This handicap can be overcome by Beryllium-glass technique. A thin layer of glass is melted and unified with grinded Beryllium base. The glass surface is then polished. The glass must have the same coefficient of thermal expansion as Beryllium. Beryllium is convenient for applications where fraction of X_0 should be significantly lower than 5 % of X_0 which is represented by thickness of 17.7 mm. High rigidity of resulting mirrors is paid by rather complicated technology and high cost. The handling of Beryllium demands a special care.

4) Plastic composite mirrors

This technology is not as well mastered in practical applications as previous examples; nevertheless, knowledge and experience are rapidly increasing in this field. The prototype we measured was manufactured by moulding 2-mm layer of Acrylic and putting reinforcing structure of two thin layers of carbon fibres, 8 mm of Nomex honeycomb and adhesives. This structure was light and corresponded to about 1 % of X_0. Its outgassing, radiation hardness and mechanical stability should be properly verified.

The most convenient shape of mirror segments creating a spherical matrix is the hexagonal shape. This shape is also relatively good for the polishing technology because it is close to the circular shape. If some of matrix edges have to form a straight line, pentagonal shape segments can fulfil this requirement. The manufacture is then more difficult because of 90° corners.

All the following discussion is focussed mainly on the spherical mirrors. However, most of the considerations are valid also for the planar mirrors. They will be most probably of hexagonal shape too and of the same thickness as the spherical mirrors. With planar mirrors, a complication arises from the fact that they do not have a finite focal plane and therefore both the definition and the measurement of the reflective surface precision have to be redefined to some extent. This point will be addressed in Sect. 4.2.5.2.

4.2.3   Parameters to determine

Number of mirror segments, their size and thickness

The number of mirrors (N_m) covering given surface is determined by their size. We will characterise it by a diameter r_m of circumcircle. The lower limit for N_m will be set by [4.3]:

- Their maximum acceptable thickness t_m, which has to increase with their radius r_m in order to retain their optical properties. These are essentially given by the radius of curvature $R = 8$ m and the average angular precision, set to $s_J = s_{comp} = 0.03$ mrad, to not exceed the required total single photon resolution (see Sect. 4.1).

- The mirror weight, which has to be acceptable for the adjustable mirror mount. This has to keep fraction $X_{0\ mount}$ of the radiation length low (~3 % of X_0) and similar to the support wall (3.3 % of X_0) in which it is inserted [4.4]. Long term stability [4.5] and mount alignment precision [4.6] were demonstrated for a weight of ~2 kg, which sets the maximum acceptable mirror radius r_m to 230 mm for a thickness t_m of 6 mm (see Sect. 4.3.7.2). Future measurements should demonstrate the same behaviour for heavier mirrors corresponding to larger sizes.

Another important parameter to take in account is given by the ratio between the maximum base radius r_c of the Cherenkov cones on the mirrors and the mirror radius r_m:

$$p_c = (r_m - r_c)^2 / r_m^2 \,, \tag{4.6}$$

where p_c gives the probability of having a ring imaged by a single mirror. The dependence $p_c(r_m)$ is displayed in Fig. 4.3. For example, for $r_m = 200$ mm, $p_c = 53$ %. To have most of the rings imaged each by single mirror, provides us with an easier pattern recognition and correction in case of mirror misalignments.
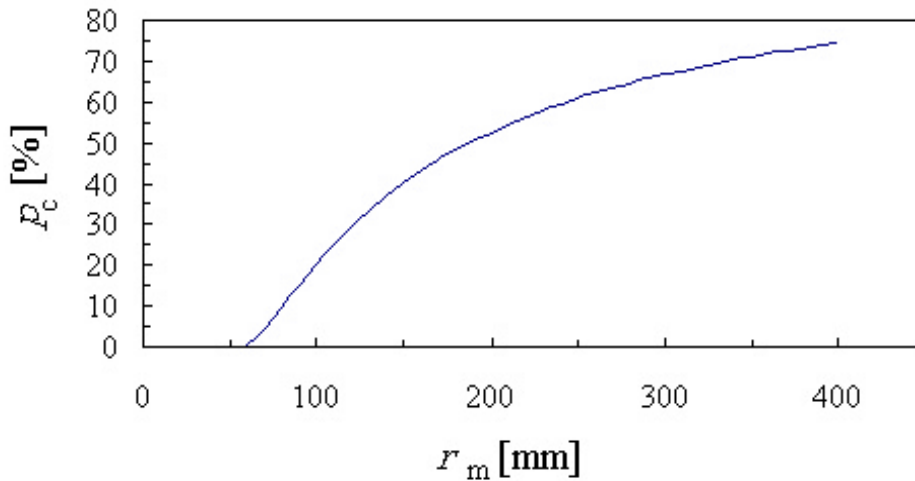
Fig. 4.3: Probability $p_c(r_m)$ of having a Cherenkov ring imaged by a single mirror for circular and hexagonal mirrors. r_m is the radius of mirror circumcircle.

Mirror substrates parameters depend very strongly on the manufacture technology. The precision of the reflective surface is often very sensitive to tiny changes of manufacturing and environmental conditions. Although general relations between dependent parameters are valid, factual values will differ for different manufacturers. Then the only way, how to precisely characterise and compare different mirror prototypes, is to measure them. These measurements give a feedback to mirror manufactures that is essential for improvement and optimisation of mirror parameters.

The parameters to measure is the radius of curvature R, the geometrical precision of the reflective surface given by the quantity $\boldsymbol{s_J}$ ($\boldsymbol{s_J} = \boldsymbol{s}_{comp}$), the reflectivity r_l and the roughness R_a. For particular cases the measurement of the outgassing would be also useful. Apart from instant measurements, long-term tests should be performed as well.

4.2.4   Analysis of possible measurement methods

In this section, we will concentrate on measurement of the radius of curvature and of the geometrical precision of the mirror reflective surface. As shown in Sect. 4.1 and 4.2.1, the tolerance of mirror geometry is $\boldsymbol{s_J} \leq 0.03$ mrad and for radius of curvature it is $\boldsymbol{s_R} \leq 150$ mm. To measure reliably these quantities, we need approximately a resolution of $\boldsymbol{Ds_J} = 0.005$ mrad and $\boldsymbol{Ds_R} = 10$ mm. The measurement set-ups should be simple in application and interpretation. To ensure reproducibility and efficiency of measurements for high numbers of mirrors we decided to automate the measurement procedure as much as possible.

4.2.4.1 Interferometric measurement methods

Interferometers provide high-resolution measurements with a precision of a fraction of the light wavelength. In the case of a general type of interferometer, like Newton, Fizeau, Twyman-Green or Mach-Zehnder, the two interfering beams follow widely separated paths [4.7]. The high precision is paid by a high sensitivity to the mechanical vibrations, the air turbulence and temperature changes. Another disadvantage is necessity of a very precise reference plane or spherical surface with the same aperture as the measured sample. Both these factors are particularly severe in case of the RICH mirrors with large apertures. In this case, also the counting of fringes is not a very efficient method. Because of these drawbacks, we decided not to use the interferometric methods for our measurements.

4.2.4.2 Spot size measurement

As follows from next two formulas, a spherical mirror images an object, placed at its centre of curvature, into an image at the same position and size, Fig. 4.4:

$$\frac{2}{R} = \frac{1}{s} + \frac{1}{s'} \tag{4.7}$$

$$M = -\frac{s'}{s} \tag{4.8}$$

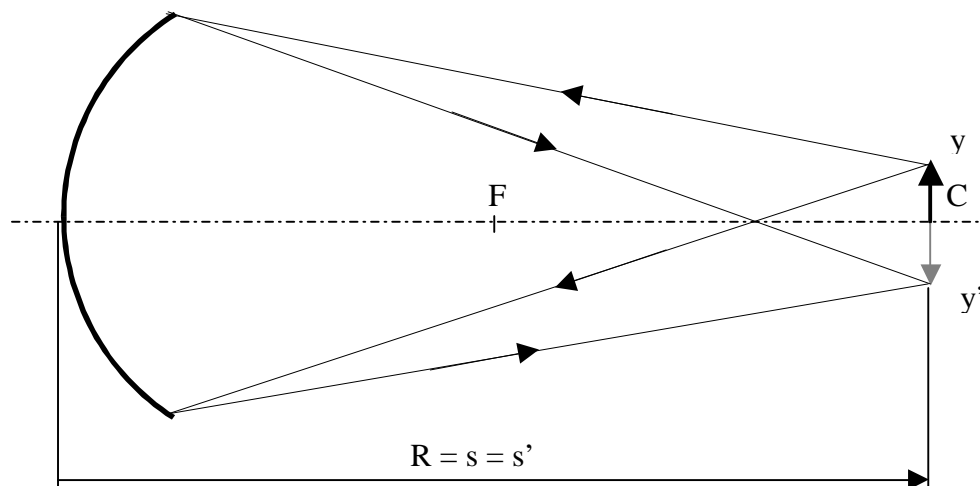where s (s') is a distance mirror – object (mirror – image) and M is the image

Fig. 4.4: Optical imaging by the spherical mirror. The object with size y placed at the centre of curvature is imaged into the image with size $y' = -y$ placed at the centre of curvature.

magnification. This property of the spherical mirror can be used with advantage for the determination of the mirror reflective surface quality and of the mirror radius of curvature R. In terms of geometrical optics, the ideal point source should be imaged by a perfect spherical mirror into the ideal point image. In reality, because the mirror has a certain limited aperture, light intensity distribution of the point source image is described by a Fresnel diffraction integral [4.8]. The spherical mirror can be then represented by an optical system made of a lens and an aperture with a shape corresponding to the mirror, see Fig. 4.5.
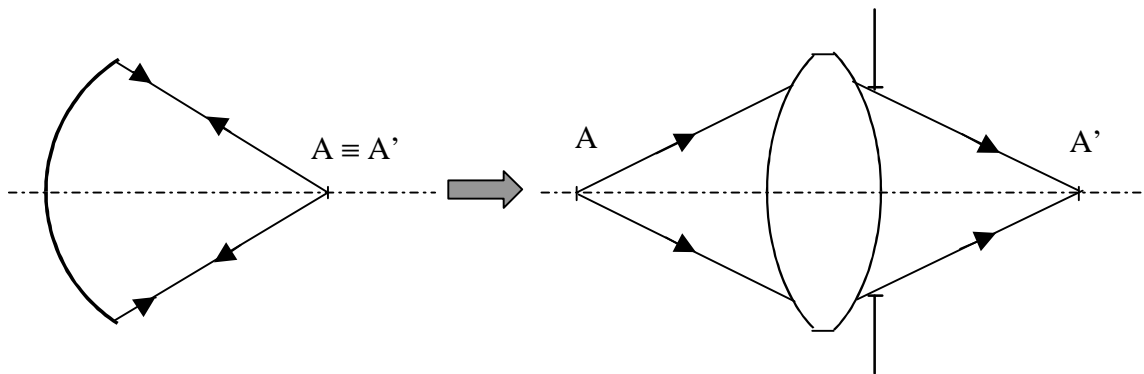

Fig. 4.5: Optical representation of the spherical mirror by an optical system consisting of a lens and a aperture with a shape corresponding to the shape of the mirror.

If the mirror had a perfect spherical surface, the spot on the focal plane would have dimensions given by the diffraction limit. For a circular mirror with diameter d, the diffraction limited spot diameter at the 3rd maximum, corresponding to 95.3 % of focused light, would be:

$$D_{diff} = 2R\tan a , \qquad (4.9)$$

$$\text{where } \sin a = \frac{l x}{p d} \qquad (4.10)$$

For the wavelength $l = 641$ nm, $x = 3.7 \cdot p$ (3rd maximum), $d = 0.45$ m and $R = 8$ m, the diffraction limited spot has diameter $D_{diff} = 85$ μm. In practice, every mirror has some geometrical imperfections of the reflective surface. Fig. 4.6 shows a spot from a high precision glass mirror with diameter $d = 400$ mm, $R = 7.8$ m and thickness 50 mm. The size of the spot, corresponding to 95 % of focused light, had diameter $D = 230$ μm. As explained in Sect. 4.2.1, thin and large RICH mirrors cannot achieve such a precision. In Fig. 4.7 we can see an image of the point source coming from a circular prototype of the LHCb RICH 2 mirror with diameter $d = 400$ mm, $R = 7.8$ m and thickness t = 7.5 mm. The difference is obvious. The latter spot is not only larger (95 % of light at $D = 3.4$ mm) but it also features irregularities on the borders. Determination of the reflective surface quality that would take in account the spot size and shape and that would allow comparison of quality for mirrors with different
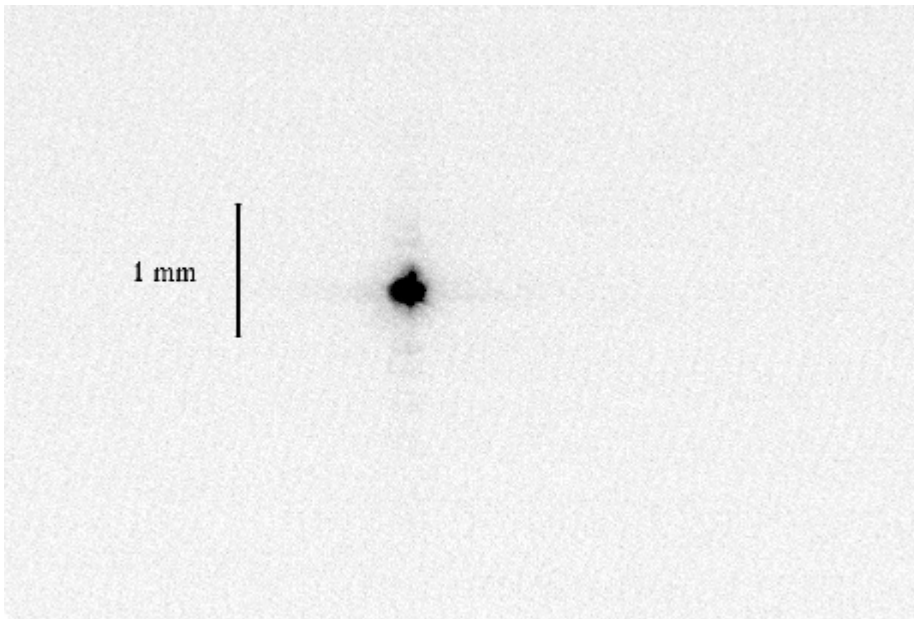
Fig. 4.6: Spot image from a high precision glass mirror with diameter $d = 400$ mm, radius of curvature $R = 7800$ mm and thickness $t = 50$ mm. 95 % of the reflected light was focussed inside a circle with diameter $D = 0.23$ mm.

Fig. 4.7: Spot image from the circular prototype of the LHCb RICH 2 mirror with $d = 400$ mm, $R = 7800$ mm and $t = 7.5$ mm. 95 % of the reflected light was focussed inside a circle with diameter $D = 3.4$ mm.

spot shapes is essential. Average quality can be quantified by a diameter of the smallest circle, inside which certain percentage of light is integrated.

The radius of curvature of the reflective surface can be measured as a distance between the vertex of the mirror and the point source placed at the centre of

curvature. This position is found when $s = s'$. From equation (4.7), then $s = s' = R$. The spot size of the point source image has to be measured at the R plane. Then both measurements of R and of the average geometrical quality s_J would be taken by performing one positioning operation. The procedure for the centre of curvature finding is illustrated in Fig. 4.8.

CCD image acquisition and following digital image processing can make this measurement very flexible and effective. Resolution of CCD's enables a high measurement precision.
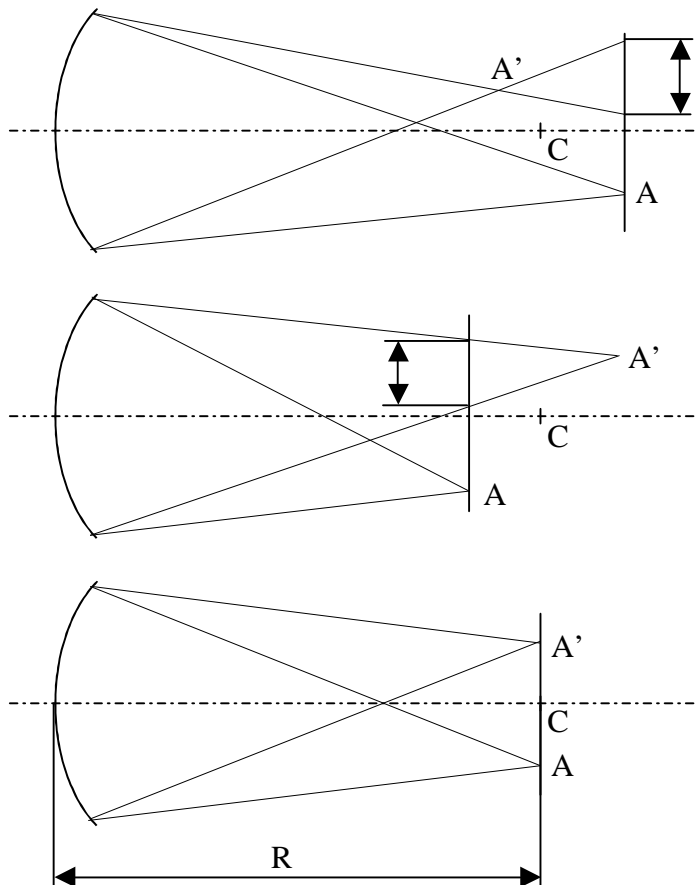
Fig. 4.8: Procedure for the centre of curvature finding. The centre of curvature can be found by moving the point source along the optical axis of the mirror and looking for the smallest size of the spot at the plane of the point source.

4.2.4.3 Shack-Hartmann sensor

The Shack-Hartmann (SH) wavefront sensor enables to reconstruct the topography of the mirror reflective surface. Apart from the evaluation of the reflective surface geometrical precision, it can give information about location of mirror deformations and deviations from an ideal spherical surface. The optical test technique known as the Hartmann test [4.9] was originally developed for the characterisation of large

astronomical telescope optics. Nowadays, up-dated and modified Shack Hartmann wavefront sensors [4.10] are applied not only in the field of sophisticated astrophysics instruments (active and adaptive optics) but have also started in other fields (for example metrology, laser ophtalmo-surgery).

Fig. 4.9: Interaction of the perfect spherical wavefront with an imperfect spherical mirror. The shape of the distorted wavefront corresponds to the shape of the reflective surface. Wavefront distortion $W = 2h$, where h is height above or below ideal mirror surface.
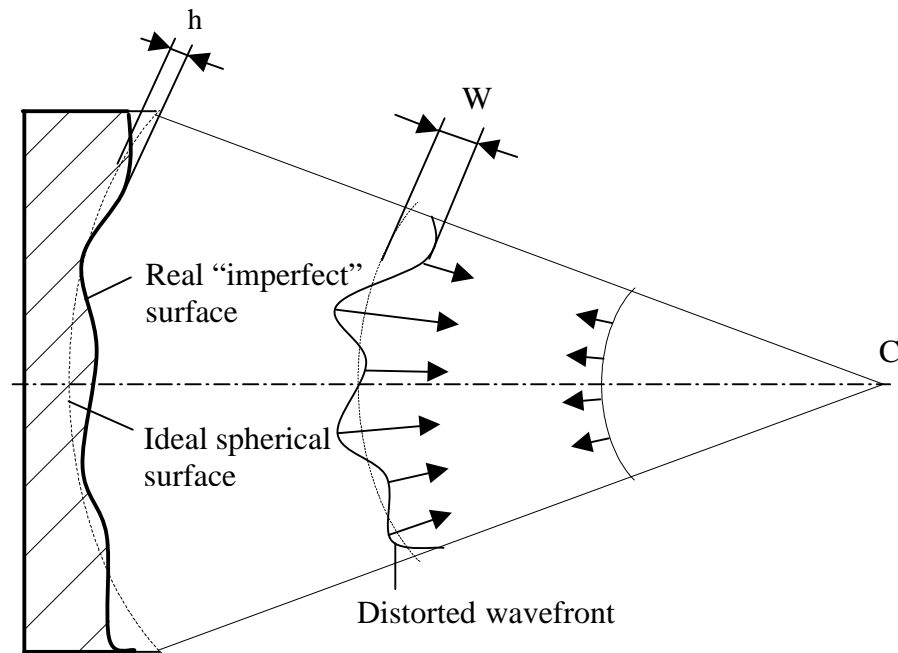
The principle of the SH sensor is as follows. The original divergent perfectly spherical wavefront, produced by the point source in the centre of curvature of the mirror, propagates towards the mirror. After reflection on its perfect spherical reflective surface, convergent perfectly spherical wavefront focuses at the centre of curvature. In a real world, the mirror surface cannot be perfect. Then the incidencing wavefront reflects on an imperfect reflective surface and its ideally spherical shape is distorted, see Fig. 4.9. A function $W(x,y)$ is used to describe the distorted wavefront [4.11]. It measures the optical path difference between the reference spherical surface and the distorted wavefront along the radius of the reference sphere. The shape of the distorted wavefront corresponds to the shape of the imperfect reflective surface. The relation is given by $W = 2h$, where h is a height of the real reflective surface above or below the ideal surface. In terms of the interferometric measurement methods, the number of wavelengths would be $N = h/\textbf{\textit{l}}$. The transverse ray aberration (Fig. 4.10) can be obtained by differentiation of the function $W(x,y)$:

$$\textbf{\textit{e}}_x(x, y) = -R \cdot \frac{\partial W(x, y)}{\partial x} \tag{4.11}$$

$$e_y(x,y) = -R \cdot \frac{\partial W(x,y)}{\partial y} , \qquad (4.12)$$

where e_x and e_y are transverse ray aberrations in x and y directions respectively. Ray bundle crossing near the focal point can be recorded as the spot enlargement at mirror focus, see Sect. 4.2.4.2.
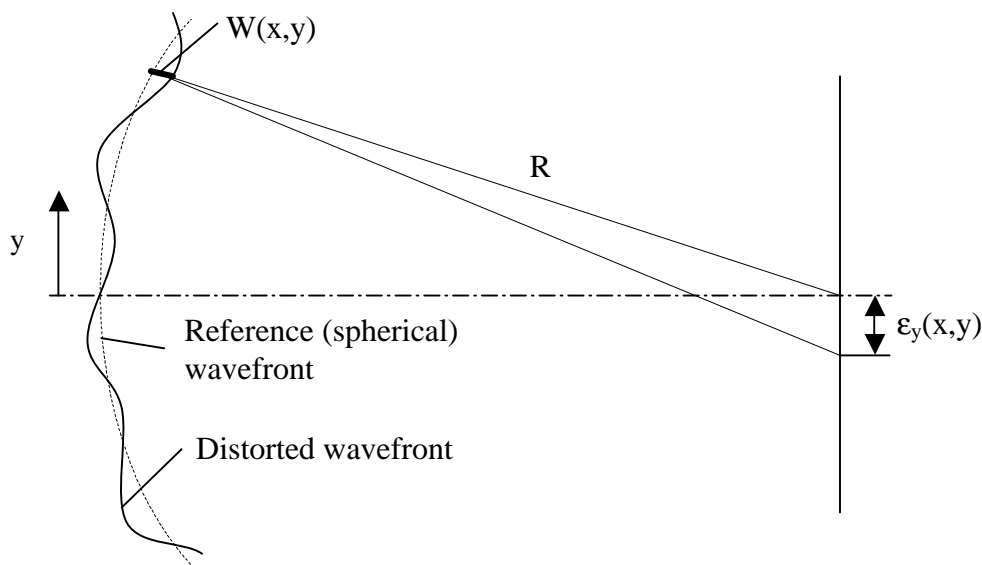
Fig. 4.10: Relation between the wavefront distortion $W(x,y)$, and ray aberration $e(x,y)$.

A wavefront sensor is an instrument, which measures the function $W(x,y)$. The main parts of the SH sensor are a microlens array and a CCD. The principle of the sensor is demonstrated in Fig. 4.11. The collimating lens transforms the aberrated spherical wavefront into a plane wavefront. The microlens array is placed at the location of the demagnified image of the mirror. The array is superimposed on the mirror image and cuts the wavefront, see Fig. 4.12. Each microlens forms a spot from the light falling on the corresponding part of the image. The local slope $q(x,y)$ of the impinging wavefront is converted into a displacement $d(x,y)$ of the corresponding focal spot. The spot displacement is directly proportional to the average slope of the local wavefront distortion:

$$d(x,y) = q(x,y)f , \qquad (4.13)$$

where f is a focal length of the microlens array. Components q_x, q_y can be expressed as:

$$q_x = \frac{\partial W}{\partial x} \text{ and } q_y = \frac{\partial W}{\partial y} \qquad (4.14a,b)$$
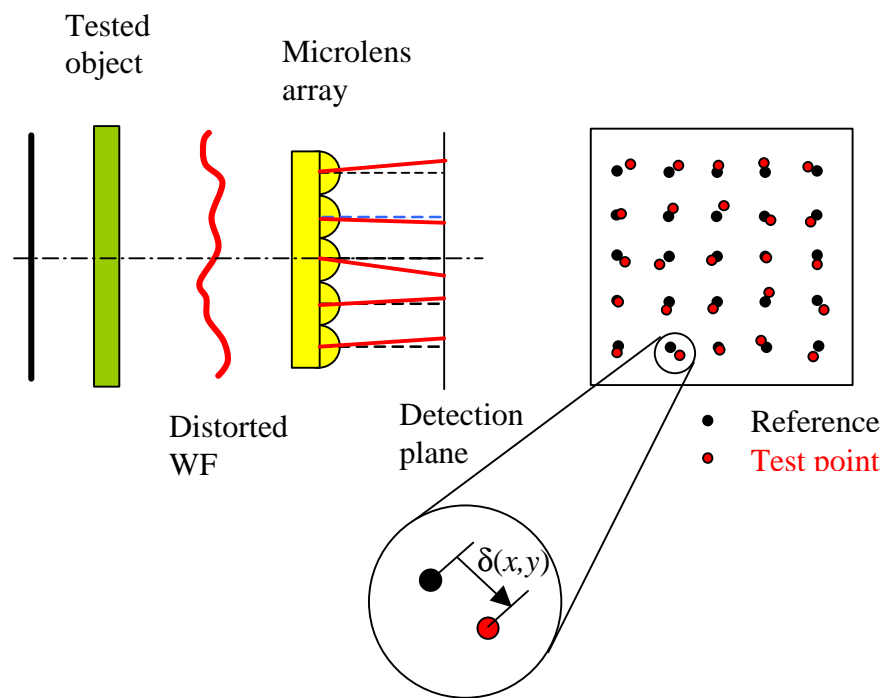
Fig. 4.11: Principle of the Shack-Hartmann wavefront sensor.
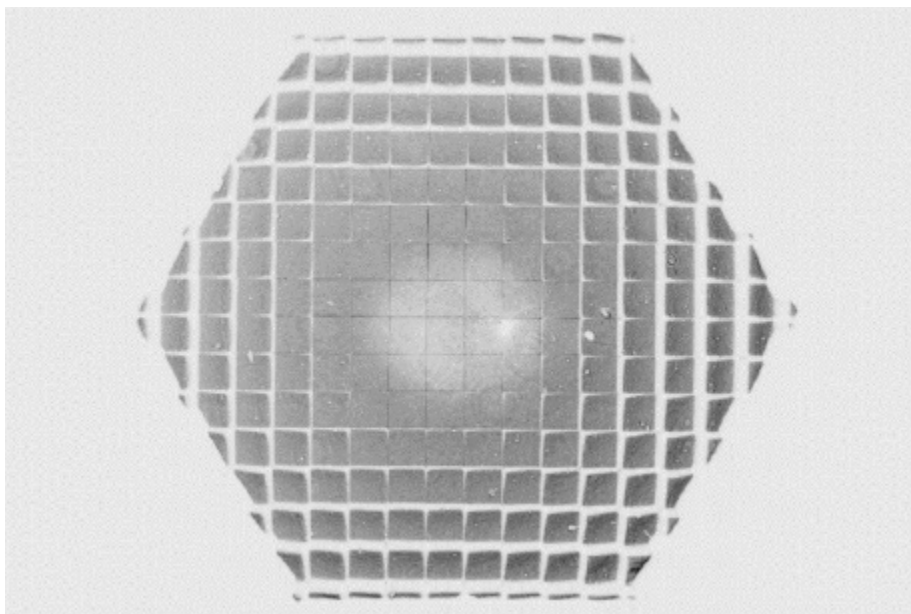
Fig. 4.12: Demagnified image of the hexagonal mirror pupil superimposed by the microlens array.

The positions of focal spots are detected by the CCD and their displacements from reference positions are measured. The wavefront phase may be derived from obtained data by performing, for example, the least squares fit of the measured local slopes to a basis of function chosen to represent the surface [4.12]. The SH sensor performs a geometric measurement and is therefore free of some constraints of

interferometry. In comparison with interferometers, this compact and robust instrument is insensitive to mechanical vibrations and allows wavefront measurement without reference sample and necessity of coherent light sources. Further advantages are a high flexibility and possibility of achieving a high measurement precision, comparable even with interferometric measurements, as shown in [4.13].

4.2.4.4 Ronchi method

The Ronchi test carries a name of its inventor who invented it in 1923 [4.14] to test optical surfaces. The principle is quite simple, see Fig. 4.13. A point source is placed approximately at the centre of curvature of the mirror to be studied, at distance s from the mirror. The reflected light forms an image at a distance s' from the mirror, given by relation (4.7). A ruled grating, called the Ronchi ruling, is placed in the path of the reflected light at the vicinity of focus at a distance l from the mirror. This grating has opaque and clear lines of equal widths with pitch P. The light, passing the grating, produces combination fringes with a shape dependent on aberrations of the mirror. If
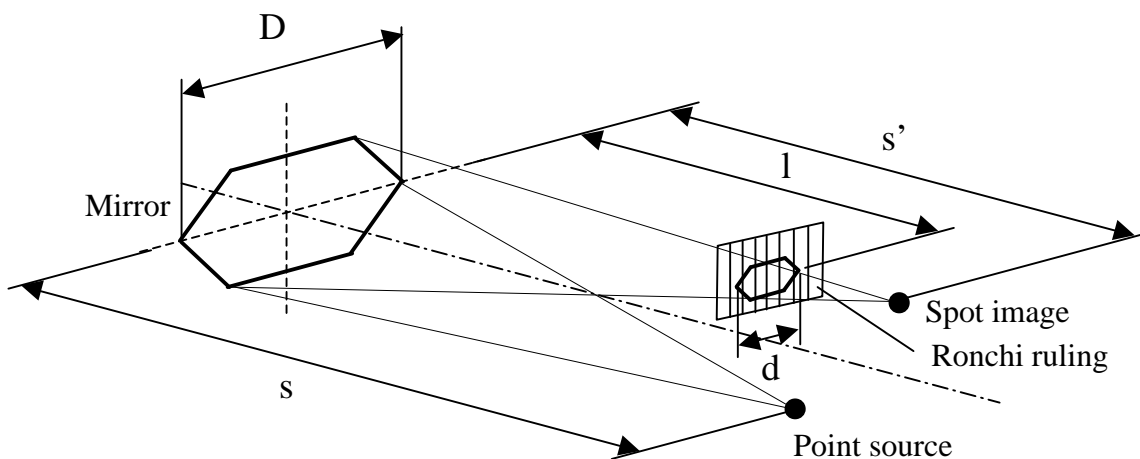
Fig. 4.13: The principle of the Ronchi method.

the mirror had ideally spherical shape, the combination fringes would appear straight. Deviations from spherical surface cause deformations of fringes, but measurement is only sensitive to changes of the radius of curvature perpendicular to the grating direction. In general, to get a complete picture of a given mirror, several different orientations should be measured. The combination fringes can be detected by a CCD camera or observed directly by eye. The method is widely used for a qualitative evaluation of aberrations of optical systems. However, possibilities of quantitative measurements were also studied [4.15, 4.16]. Figs 4.14 and 4.15 compare Ronchi patterns obtained from precise etalon mirror and from a thin prototype of the LHCb RICH 2 mirror. A ronchigram from the high precision etalon mirror does not show any deviations from spherical shape. The measurement resolution can be increased by

using a finer Ronchi ruling. The less precise thin mirror features, on the other hand, a ronchigram with well visible deformations of the spherical surface. The ronchigram was detected for two mutually perpendicular orientations of the Ronchi ruling.
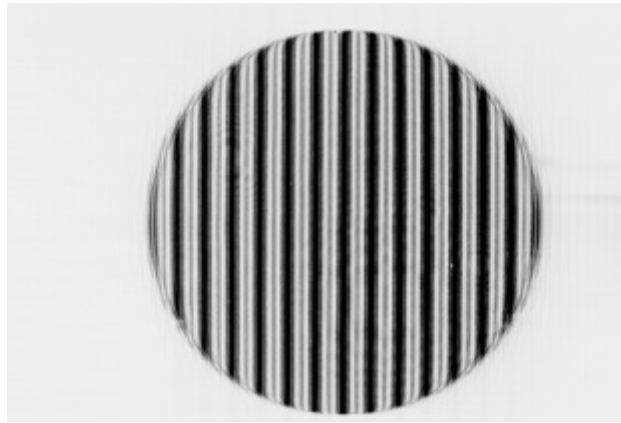
Fig. 4.14: Ronchigram from the high precision glass mirror (thickness 50 mm, diameter 400 mm, 95 % of reflected light focussed inside a circle with $D = 0.23$ mm). The lines are straight, which indicates that deviations from ideal spherical shape are smaller than resolution of the used Ronchi ruling (1/mm).

Fig. 4.15: Ronchigrams from the thin prototype of the LHCb RICH 2 mirror (thickness 4.5 mm, diagonal 502 mm, 95 % of reflected light focussed inside $D = 1.66$ mm). Deformed lines with varying thickness indicate distortions of the spherical shape.

The Ronchi test can be described either by a simple geometric optical theory or by physical optics. The latter one interprets combining fringes as result of diffraction. Patterns obtained with gratings with higher frequency of ruling demand description by the diffraction theory. To obtain good results, the pitch P of the grating should be chosen such that no more than two diffraction orders will overlap, see Fig. 4.16. The appropriate pitch is given by the wavelength l of the used light and by the numerical aperture $N.A. = \sin q$ of the measured mirror. Angular deviation q_n of the n-th diffraction order from surface normal is:

$$\sin q_n = \frac{nl}{P} \tag{4.15}$$

To separate $+1^{st}$ and -1st order, the condition $q \pounds q_n$ has to be fulfilled. Then:

$$P \leq \frac{nl}{N.A.} \tag{4.16}$$
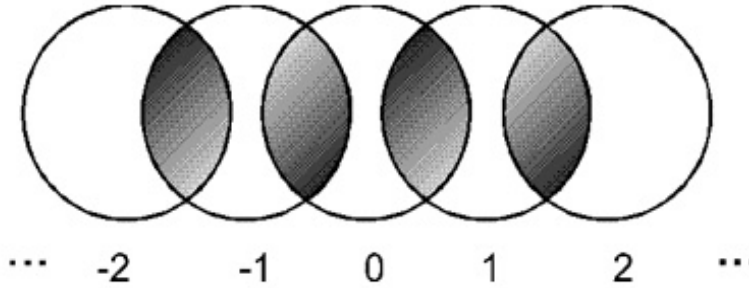
Fig. 4.16: Picture showing several diffracted orders in the far field of the grating. When the pitch of the grating is chosen properly, each diffracted order will overlap only with its nearest neighbors. From [4.17].

For the LHCb RICH 2 spherical mirror with $N.A. \cong 0.03$ and the point source with $l = 640\,nm$ we get $P \leq 20\,\mu m$. The grating should have at least $50\,lines/mm$. Computed diffraction patterns corresponding to the basic primary aberrations of a lens are shown in Fig. 4.17 [4.17].

For coarse gratings, the geometrical theory can be applied. If the grating is placed exactly at the image point, either a uniformly bright or a uniformly dark picture of the mirror is seen. As the grating is moved away from the image point, combination fringes with increasing frequency appear. With the nomenclature in Fig. 4.13 following relations can be seen:

$$\frac{d}{s'-l} = \frac{D}{s'} \tag{4.17}$$

$$N_{cf} = d/P,$$ (4.18)

where D is a diameter of the mirror, d is a diameter of the beam on grating and N_{cf} is a number of combination fringes observed across the image of the mirror. From relations (4.17), (4.18) and (4.7) we obtain value of the radius of curvature of measured mirror:

$$R = \frac{2sDl}{s(D - PN_{cf}) + Dl}$$ (4.19)

For a mirror with variation in the radius of curvature the local radius of curvature R_{loc} can be measured by measuring local pitch of fringes P_{loc} and by putting $N_{cf} = 1$ and $D = P_{loc}$:

$$R_{loc} = \frac{2sP_{loc}l}{s(P_{loc} - P) + P_{loc}l}$$ (4.20)

Measurement of the radius of curvature of a RICH mirror by the Ronchi method is demonstrated in [4.18]. The quantitative measurement is rather complicated. We decided not to incorporate this method in our measurement set-up.
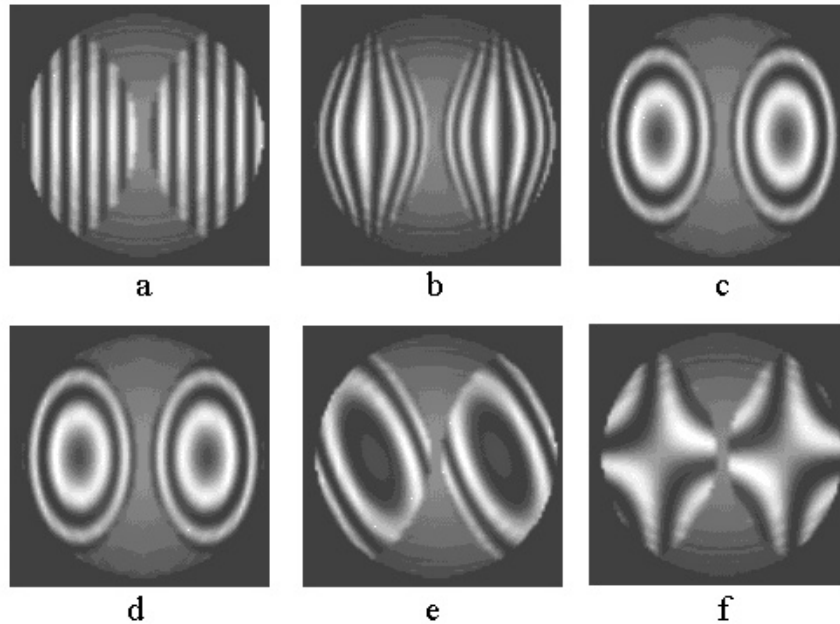

Fig. 4.17: The computed Ronchi patterns corresponding to different types of primary (Seidel) aberrations of the lens: (a) defocus, (b) spherical, (c) astigmatism oriented at 45°, (d) coma at 0°, (e) coma at 45°, (f) coma at 90°. Astigmatism (c) and coma (d) give the same pattern. From [4.17].

4.2.4.5 Other methods

A number of other measurement methods exists. The most famous is the Foucault method, known as the knife-edge method, and its modifications. They are described in detail in [4.7]. The principle is based on blocking out a part of light diffracted by reflection on the measured mirror. A shadow pattern appears over otherwise uniformly illuminated surface of the mirror. The shape of this pattern is related to the wavefront aberrations. These methods are more convenient for a qualitative evaluation of the mirror surface than for quantitative measurements. Despite their simplicity of operation, methods of Foucault type did not meet our requirements for quantitative measurement with easily comparable results and possibility of automation of the measurement procedure.

4.2.5   Measurements in the optical laboratory

To measure the parameters of RICH opto-mechanical components, we established in the TA2 group an optical laboratory. In order to complete precise and in some cases long-term optical measurements, the laboratory had to fulfil strict criteria. Essentially, it is placed underground, without windows. The dark room is necessary for optical measurements. Stable temperature and humidity are required for long-term measurements. The laboratory is equipped with air circulation with dust filters and classified as the 3b-class laser workplace.

4.2.5.1 Bench for measurement of average geometrical quality and radius of curvature

On the base of the analysis of measurement methods made in Sect. 4.2.4, we chose the spot size measurement as the most convenient for our purpose. As shown in Sect. 4.2.4.2, we can obtain both values of mirror precision and of the radius of curvature by performing a single adjusting and positioning operation. Another advantage is the possibility of automation of the measurement procedure and of the data processing. For topographic measurements, we decided to develop the modified Shack-Hartmann sensor, which will be treated in Sect. 4.2.5.3.

Measurement method and set up

The set up (Fig. 4.18) measures the rms variation from the ideal mirror spherical surface by imaging a point source via the sample mirror and by analysing the size and shape of the resulting focal spot. A diode laser beam at 641 nm (a) is injected into a mono-mode optical fibre (b). The output of the fibre creates the point-like source and illuminates the mirror (d). Reflected light is focused and detected by a CCD camera (e) placed in the focus. For a given distance s the focus is found at a position s' where the spot is the smallest. The average radius of curvature can be then obtained from equation (4.7). To make the measurement procedure easy we installed the point source and the CCD camera on the sliding table (f) allowing movement along the
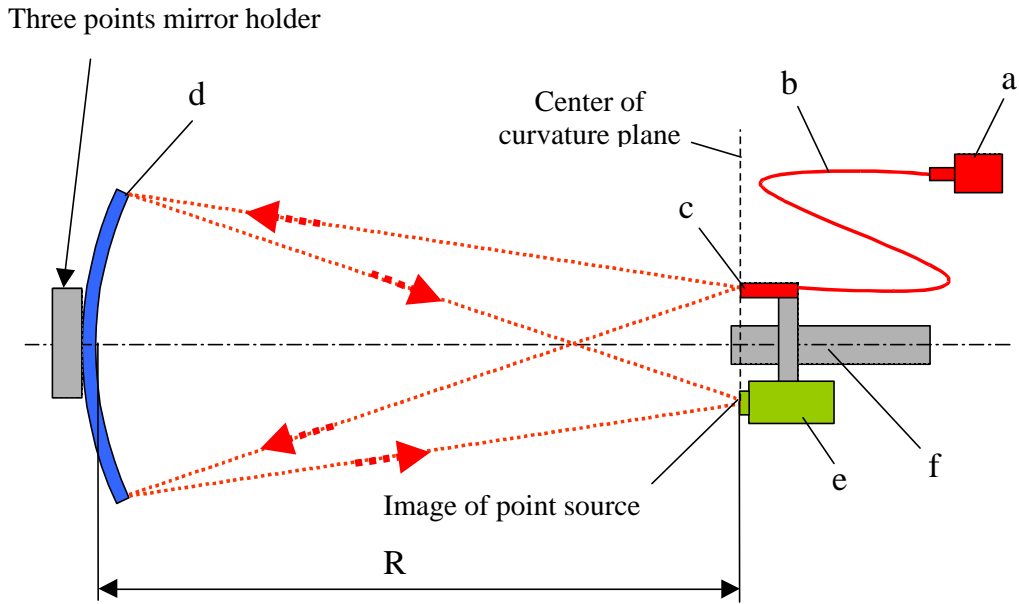
Three points mirror holder

Fig. 4.18: Scheme of the set up for *R* and spot size measurement.

optical axis of the mirror. The active area of the CCD and the point source are in the same plane orthogonal to the optical axis of the mirror. Then, after finding the focus, $s = s' = R$ and the point source is imaged with magnification $M = 1$. In this position, the spot image is spherical aberration free and the average geometrical precision of the mirror can be determined by measurement of the spot size.

The point source is created by the optical fibre with diameter 8 μm. The diode laser (Melles Griot model 56DOL647) injects a laser beam with intensity controlled by the diode laser driver (Melles Griot model 06DLD203). Fig. 4.19 shows the optical power output P_{ps} vs. forward current I_F characteristics as it was measured at the output of the fibre. We measured also the polar characteristics of the point source, see Fig. 4.20. The numerical aperture *N.A.* is an important parameter of the point source. For correct measurement of the spot size, the numerical aperture of the point source $N.A._{ps}$ has to correspond to f-number *f/#* of the measured mirror:

$$N.A._{ps} \geq \frac{1}{2 \cdot f \, /\#} \, , \tag{4.21}$$

where $f/\# = f \, /d$, *f* is a focal length and *d* is a diameter of the mirror. Intensity of the light at the edge of the mirror should not be lover than 50 % of the maximum intensity. Table 4.3 lists values of *f/#* and *N.A.* for the LHCb and COMPASS RICH mirrors. The value $N.A._{ps} = 0.17$ of the fibre (50 % at $N.A. \cong 0.05$) is sufficient for the LHCb RICH 2 and COMPASS RICH 1 mirrors but not for the LHCb RICH 1 mirrors. To increase $N.A._{ps}$, we installed a microscope objective 25/0.65 at the point source. Fig. 4.20 demonstrates the obtained improvement. This change caused a displacement of the point source expressed by $s' - s = 50$ mm. Then, when the smallest spot is found, $R = (s + s') \, / \, 2$ and the magnification *M* of the spot image,

given by (4.8), is bigger than 1. The correct value of the spot size is obtained by multiplication by $1/M$.
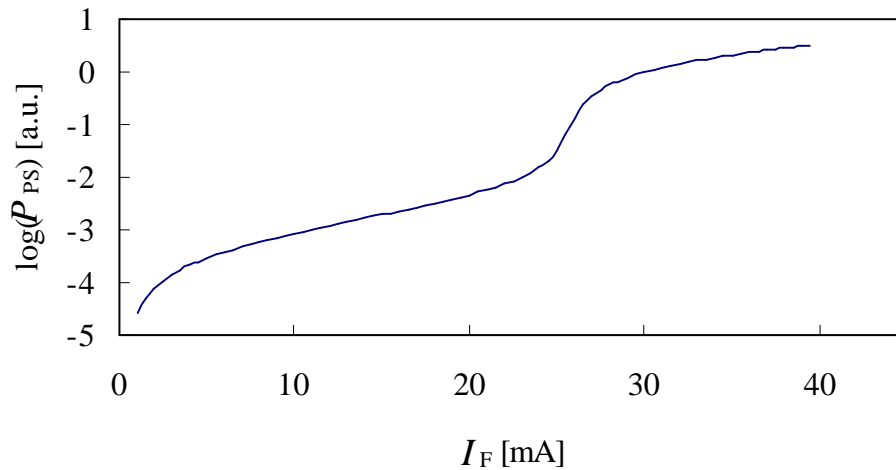

Fig. 4.19: Characteristics $P_{ps}(I_F)$. Top: linear scale. Bottom: the output power P_{ps} in logaritmic units.
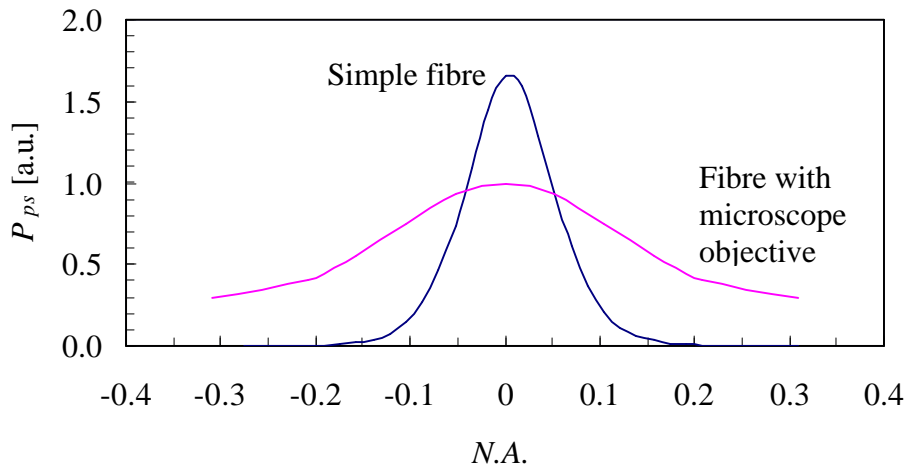

Fig. 4.20: Polar characteristics of the point source. The simple fibre had too low *N.A.* for large mirrors with short radius of curvature. An improvement was achieved by means of a microscope objective.

To quantify the spot size, we define a quantity D_0 as the diameter of the smallest circle, which contains 95 % of the total light distributed in the R plane for a certain mirror. The smallest circle is centred at the centre of gravity of the spot. We also define a quantity $s_s = D_0 / 4$, which would represent the rms value of the distribution, if this had Gaussian shape. It can be demonstrated that:

$$s_J = \frac{\sqrt{s_s^2 - s_p^2}}{2R} \approx \frac{s_s}{2R} = \frac{D_0}{8R} , \tag{4.22}$$

where the factor 2 in the denominator takes in account a mirror reflection, s_J is the rms value of the radius of curvature values taken over the mirror surface and expressed in radians and $s_{s,p}$, the rms values for the spot size and the source size, respectively. The quantity s_J allows a comparison of precision for mirrors with diverse R.

The intensity distribution of the spot is detected by 16-bit CCD camera (DTA model HR400E equipped with KODAK sensor model KAF-400E CCD). This slow-scan digital CCD cooled camera is designed for applications where the maximum performance and the high dynamic range are required. The CCD fulfils well the requirement for precise measurement of the spot size where the operating speed is not critical but the high dynamic range has big importance. The pixel size of 9×9 μm^2 is small in comparison with the spot size, therefore ensures a high spatial resolution. Fig. 4.21 illustrates the spectral response of the CCD sensor, which fits well the wavelength of the used diode laser beam. A standard 8-bit CCD camera is not sufficient for correct spot size measurement. However, we developed a sophisticated procedure that enables in case of necessity the measurement with 8-bit CCD. The description will be given later in this section.

Table 4.3: Values of diameter d, focal length f, f-number $f / \#$ and numerical aperture $N.A.$ for the RICH mirrors.

Mirror	d [mm]	f [mm]	$f / \#$	$N.A.$
LHCb RICH 2	502	8000	15.9	0.03
LHCb RICH 1	586	1700	2.9	0.17
COMPASS RICH 1	520	6600	13.1	0.04

The CCD sensor converts the incident illumination into a proportional quantity $I_r(x_i, y_j)$ of electrical charge for a pixel at the position (x_i, y_j) on the CCD mosaic. After subtraction of a background and dark signal we get a signal $I(x_i, y_j)$. Co-ordinates (x_c, y_c) of the centre of gravity are in general given by formulas:
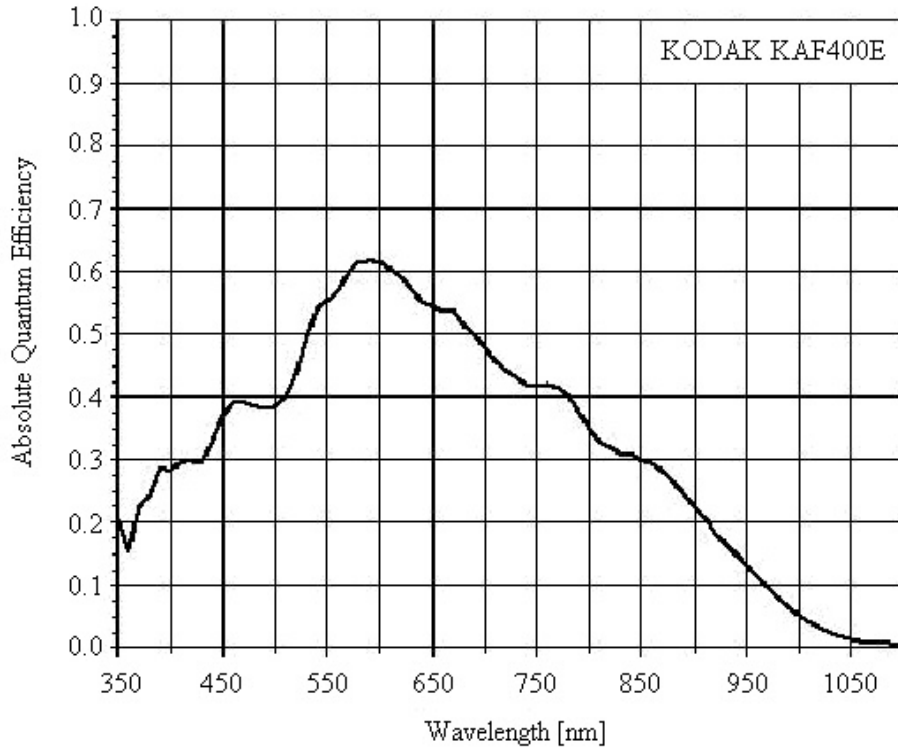
Fig. 4.21: Spectral response of KODAK sensor KAF-400E. From DTA catalogue.

$$x_c = \frac{\int_W x \cdot I(x, y) dW}{\int_W I(x, y) dW} , \quad y_c = \frac{\int_W y \cdot I(x, y) dW}{\int_W I(x, y) dW} \tag{4.23a,b}$$

In the case of CCD array with finite pixel size, pixel signal and dead space between pixels, we can use formulas:

$$x_c = \frac{\sum_{i,j}^{M,N} \left(x_i \cdot I(x_i, y_j) \right)}{\sum_{i,j}^{M,N} I(x_i, y_j)} , \quad j_c = \frac{\sum_{i,j}^{M,N} \left(y_j \cdot I(x_i, y_j) \right)}{\sum_{i,j}^{M,N} I(x_i, y_j)} , \tag{4.24a,b}$$

where an area W is created by $M \times N$ pixels. A Visual Basic program, developed for the measurement of intensity percentage focused inside a circle with the centre at (i_c, j_c), integrates detected intensities over the area W at varied diameter D of the circle, see Fig. 4.22:

$$S_D = \int_\Omega I(x, y) \, d\Omega \quad \text{or} \quad S_D = \sum_{i,j}^{M,N} I(x_i, y_j), \tag{4.25a,b}$$
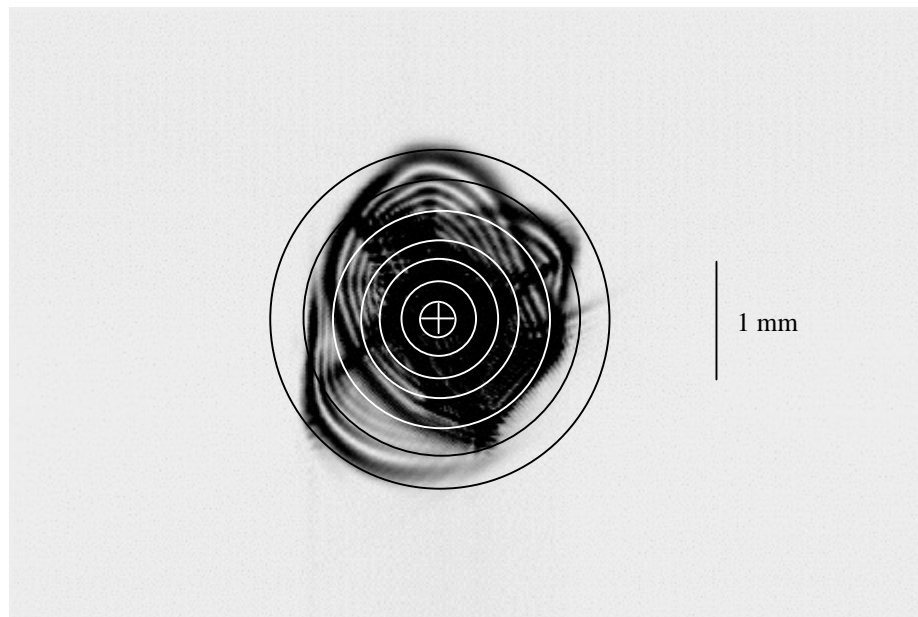
Fig. 4.22: Principle of measurement of the characteristics $S_D(D)$.

where S_D is an amount of light focused inside a circle with diameter D. The percentage P_D is obtained after normalisation by the total light S_{tot} integrated on the whole CCD sensor area:

$$P_D = S_D / S_{tot} \tag{4.26}$$

An example of resulting characteristics $P_D(D)$ is shown in Fig. 4.23. The parameter D_0 is then determined as a diameter D at $P_D = 95\ \%$ of integrated light.
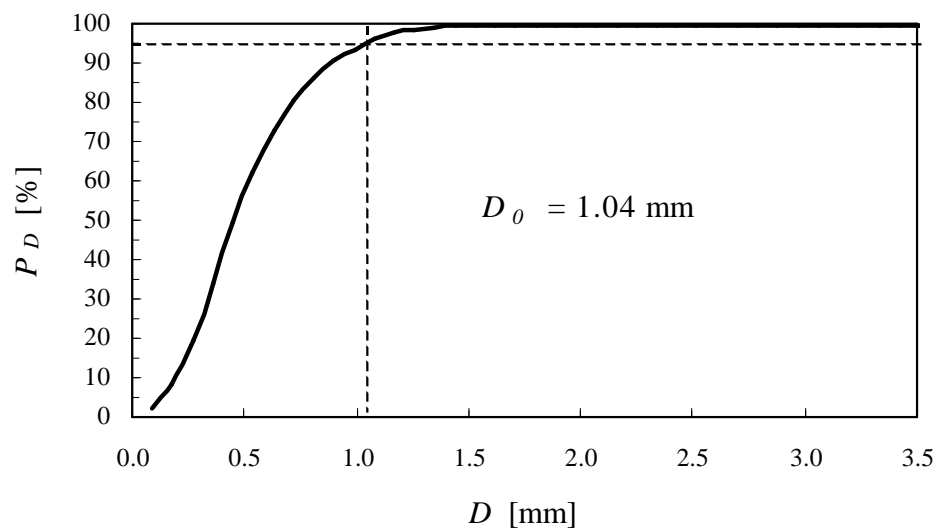
Fig. 4.23: Example of characteristics $P_D(D)$.

Since we use a fine sampling of $DD \sim 10$ pixels and the characteristics are nearly linear between sampling points, we can use linear interpolation to obtain the value of D_0. For a correct measurement, the whole spot image has to be inside the CCD active area. This condition limits the measurement. For mirrors with bigger spot size, the spot image can be demagnified by means of a proper objective.

The Fraunhofer diffraction theory describes the intensity distribution for an ideal circular mirror by the Airy function:

$$I(\boldsymbol{q}) = I(0)\left[\frac{2J_1(kr\sin\boldsymbol{q})}{kr\sin\boldsymbol{q}}\right]^2, \qquad (4.27)$$

where $\boldsymbol{q}$ is an angular distance from the centre of the spot given by $\sin\boldsymbol{q} = q/R$, see Fig. 4.24, $I(0)$ is an intensity amplitude in the centre of the spot, $k = 2\boldsymbol{p}/\boldsymbol{l}$, r is a radius of the mirror circular aperture and J_1 is the Bessel function of the first order:

$$J_1(u) = \frac{i^{-1}}{2\boldsymbol{p}}\int_0^{2\boldsymbol{p}} e^{i(v+u\cos v)}dv \qquad (4.28)$$
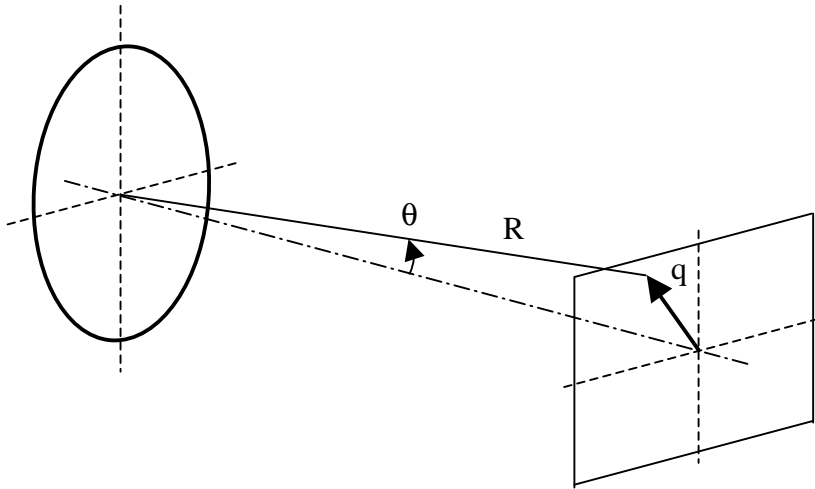
Fig. 4.24: Relation between $\boldsymbol{q}$, R and q important for expression of Airy function.

Fig. 4.25 represents the Airy pattern. Since the central peak contains 83.8 % of the light intensity, we can, for an approximate analytical determination of $P_D(D)$, neglect maxima of higher orders and replace the Airy pattern by the Gaussian function:

$$P(x) = \frac{1}{\boldsymbol{s}\sqrt{2\boldsymbol{p}}}\exp\left(-\frac{(x-\boldsymbol{m})^2}{2\boldsymbol{s}^2}\right), \qquad (4.29)$$
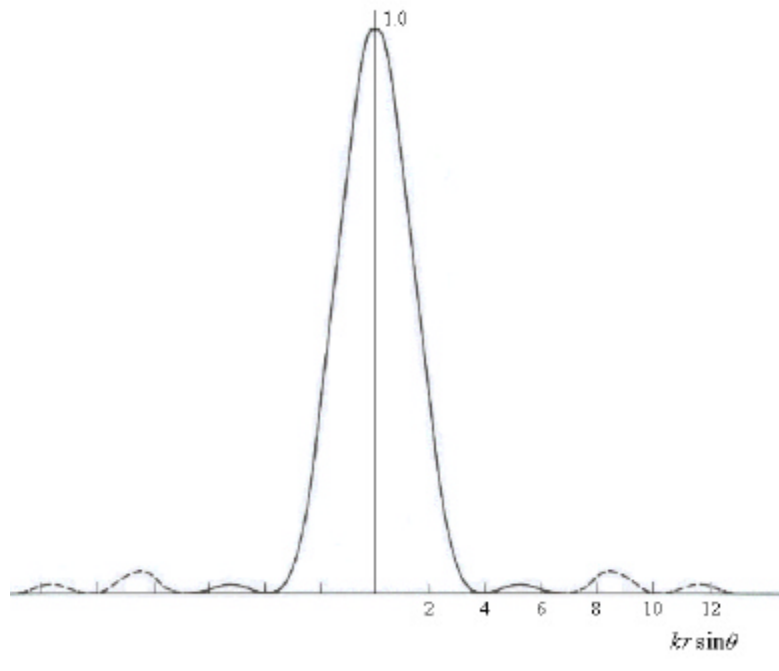
Fig. 4.25: The Airy pattern, the aberration free image of a monochromatic point source formed by a system with a circular aperture. The second and third rings are plotted at 10 times the actual ordinate.

where $P(x)$ is the density, $\boldsymbol{m}$ is the mean and $\boldsymbol{s}^2$ is the variance of the distribution. We get function $S_D(x)$ by integration of the volume inside 3D Gaussian peak:

$$S_D(x) = \frac{2\boldsymbol{p}}{\boldsymbol{s}\sqrt{2\boldsymbol{p}}} \int_0^x x e^{-\frac{x^2}{2\boldsymbol{s}^2}} dx = \frac{\boldsymbol{s}\sqrt{\boldsymbol{p}}}{\sqrt{2}} \left(1 - e^{-\frac{x^2}{2\boldsymbol{s}^2}} \right) \tag{4.30}$$

In the formula, we consider $\boldsymbol{m} = 0$. The function $P_D(D)$, where $D = 2x$, and using (4.26), is given by:

$$P_D(D) = 1 - e^{-\frac{D^2}{8\boldsymbol{s}^2}} \tag{4.31}$$

S_{tot} is obtained as $\lim_{x \to \infty} S_D(x) = \dfrac{\boldsymbol{s}\sqrt{\boldsymbol{p}}}{\sqrt{2}}$. Fig. 4.26 compares one of the measured $P_D(D)$ distributions with the one determined analytically. They are similar and present only small deviations.

To take full advantage of the high dynamic range of the 16-bit CCD camera, it is necessary to adjust the value of the intensity amplitude $I(0)$. It depends on output power $P_{\text{ps}}$ of the point source given by the forward current I_F, *N.A.* of the point source, *f/#* of the measured mirror, spectral reflectivity and geometrical quality of the mirror surface, exposure time t of the CCD camera and its temperature T and other, less important parameters. The maximum signal I_{max} should reach at least 2/3 of the dynamic range. At the same time, no pixel should be saturated. Usually we use a fixed exposure time t and CCD temperature T and we adjust the forward current I_F according to the relevant mirror parameters. For example, for COMPASS RICH 1
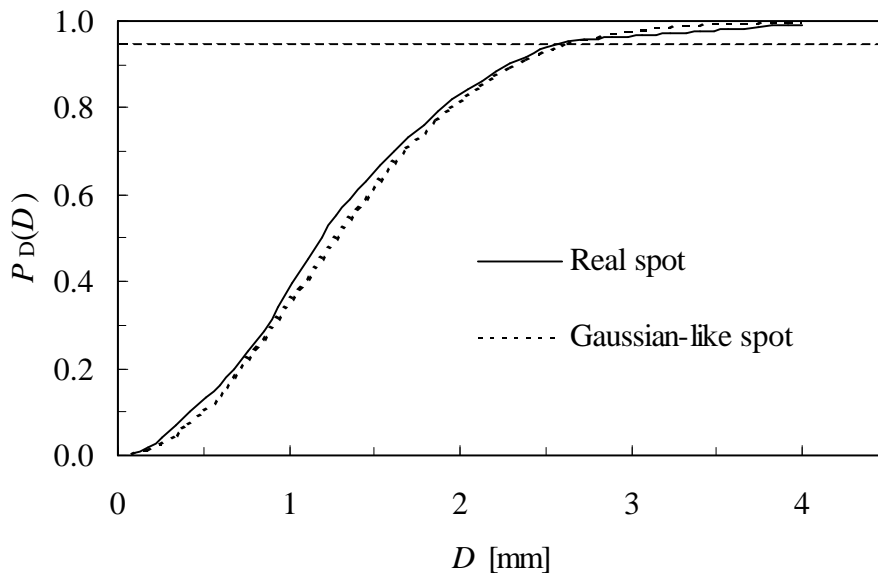
Fig. 4.26: Comparison of characteristics $P_D(D)$ for a real measured spot and for an analytically determined Gaussian-like spot ($\sigma_s = 0.54$ mm).

mirror substrates without coating we use following values: $t = 0.01$ s, $T = 10$ °C, $I_F = 20$ mA. Corresponding power output of the point source is 5.02×10^{-7} W. Reflectivity r of the polished glass substrate for perpendicularly incident light is:

$$r = \left(\frac{n-1}{n+1}\right)^2 \cong 0.04, \tag{4.32}$$

where $n \cong 1.5$ is approximate value of refractive index for glass. For the same mirrors with reflective coating, the reflectivity is about 20 times higher. We have to reduce power output of the point source to approximately 2.5×10^{-8} W, therefore according to the diode laser characteristics in Fig. 4.19, we use $I_F = 4$ mA.

Position determination of the smallest spot and of the corresponding centre of curvature by a subjective decision is difficult and not precise. Fig. 4.27 demonstrates this fact at a sequence of spot images taken at varied positions around the centre of curvature. Therefore, an objective quantitative method has to be used. After the first experience with the set up, we decided to take images of the spot in a range of 40 mm with the step of 1 mm. The centre of this range is placed at the roughly determined position of the smallest spot. The spot image can be observed on a monitor that displays the output of ½ inch 8-bit CCD camera equipped with a 75-mm objective, see Fig. 4.28. Installation of the 50-mm separator provides resulting magnification of $25 \times$ on the monitor and makes the decision easier. $P_D(D)$ is calculated for each image. Fig. 4.29 shows a graph with values of D for $P_D = 95$ % versus distance from mirror. The value of R is defined as the distance from mirror for the minimum D, that is D_0.

The mirror is installed in an adjustable three-point holder shown in Fig. 4.30. Fast and precise adjustment around two independent axes is made on the base of the spot image displayed on the monitor, as described above, and the hair cross. A fine

1 mm

Range of
40 mm

C
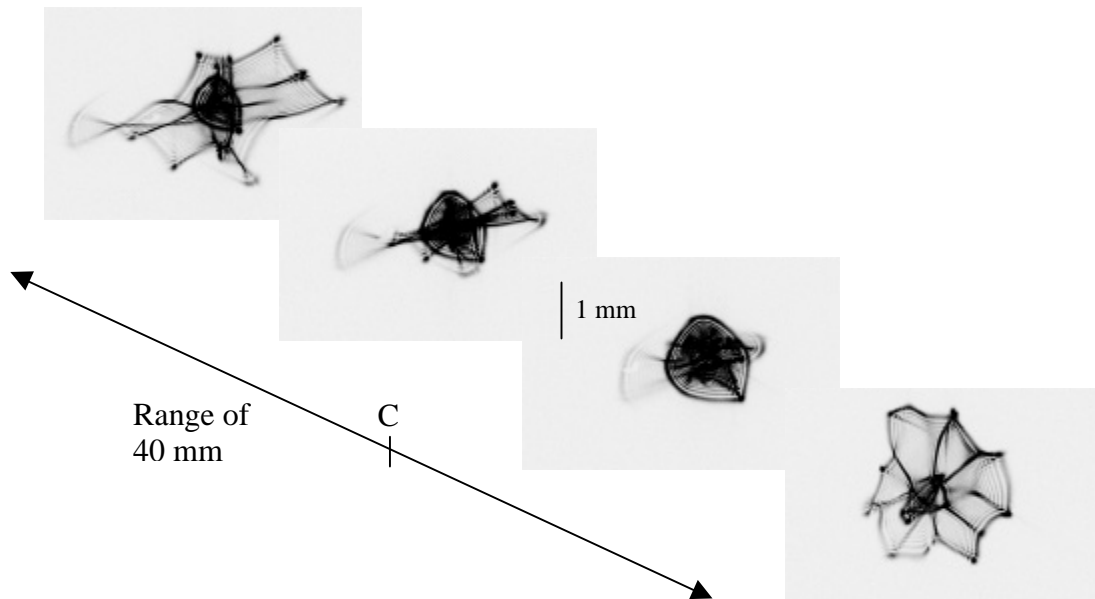
Fig. 4.27: Series of spot images around the centre of curvature.

adjustment of the spot position is made by positioning the point source by means of a x-y micrometric stage.

The maximum value of the radius of curvature that can be measured in the TA2 optical laboratory is 10 m. Mirrors with longer radius of curvature could be measured either in a longer dark room or with a modified set up, as demonstrated in Fig. 4.31. The modification is based in an incorporation of a high quality planar mirror which can double the measurement range.

8-bit CCD

16-bit CCD

Point source

75-mm
objective

50-mm
separator

Stepping
motor

Sliding table
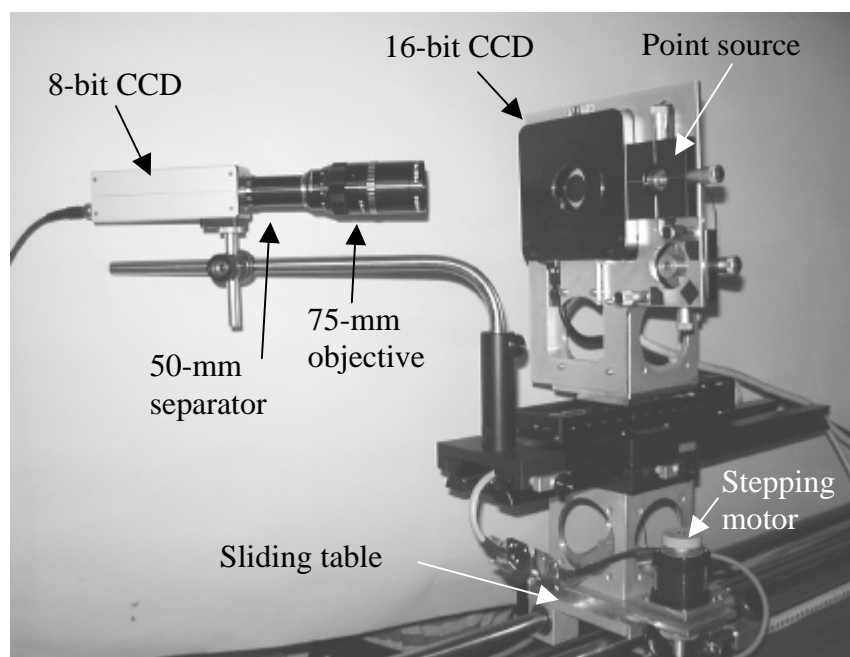
Fig. 4.28: Set up for spot size measurement. The 8-bit CCD serves for preliminary adjustment of the spot position. The final measurement is performed by the 16-bit CCD.
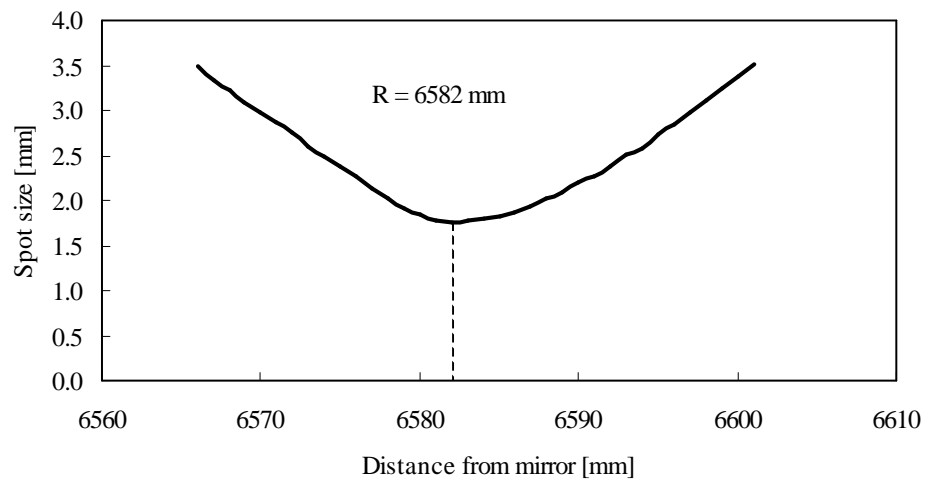
Fig. 4.29: Determination of the radius of curvature *R* for measured mirror.
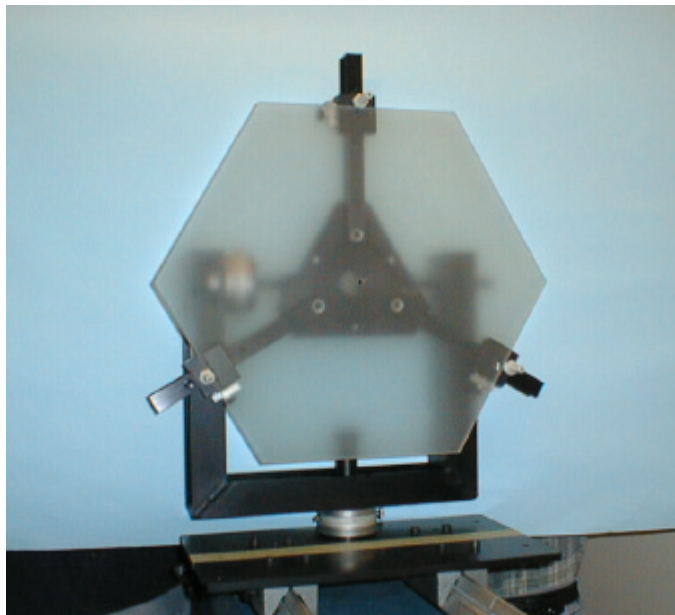
Fig. 4.30: The adjustable three-point mirror holder.
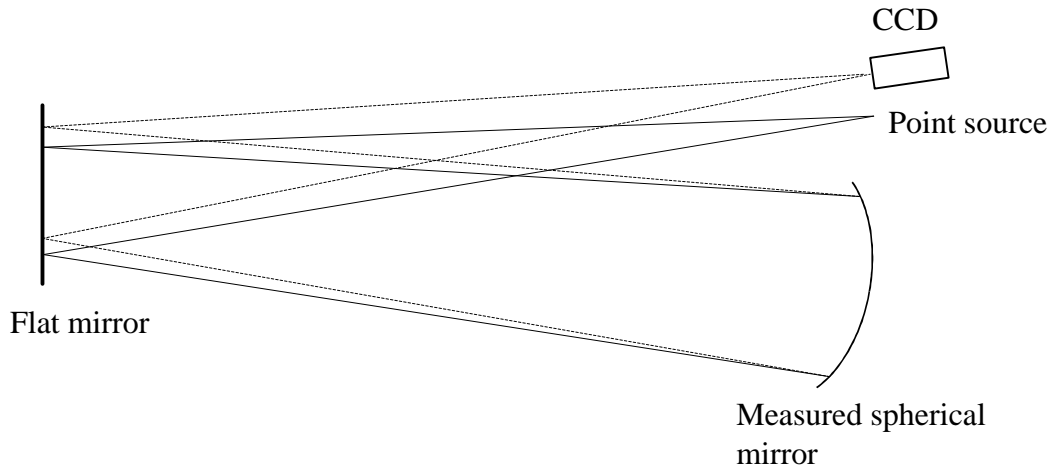
Fig. 4.31: Extension of the set up for measurement of long radius mirrors.

Precision and reproducibility of the measurement

Due to the small pixel size and to the high dynamic range of the 16-bit CCD, the resolution of the measurement is high, theoretically it is equal to the pixel size. In reality, it depends on ratio signal/noise.

Therefore, it is important to maximise this ratio. The measurement has to be performed in a dark room, without parasitic light. This can be produced by emitting diode indicators, computer screens and similar devices, which are present in the optical laboratory. As mentioned before, the maximum signal $I_{r\,Max}$ should reach a value over 2/3 of the dynamic range. Important is also correct subtraction of the dark current caused mainly by thermal charges. The camera is equipped with Peltier cooling, but for the set temperature 10 °C, the dark current is not negligible.

In general, the precision $\boldsymbol{s}_{Do}$ of the spot size measurement is given by:

$$\boldsymbol{s}_{Do}^{2} = \left(\frac{\boldsymbol{s}_G}{\sqrt{n}} \right)^2 + \left(\frac{\boldsymbol{D}x}{\sqrt{n}} \right)^2 + \left(\frac{\boldsymbol{s}_n}{N} \right)^2, \qquad (4.33)$$

where σ_G is a rms value of the spot intensity distribution (supposing that the distribution is Gaussian), n is a number of irradiated pixels, $\boldsymbol{D}x$ is a pixel size, $\boldsymbol{s}_n$ is a rms value of noise, and N is a dynamic range of the CCD. Our estimation of the measurement precision is $\boldsymbol{s}_{Do} \cong 0.02$ mm.

Precision of the radius of curvature measurement depends on the precision of the measured distance between the mirror vertex and the point source/CCD and on the precision of the mirror positioning on the holder. Estimated rms value is $\boldsymbol{s}_R \cong 1$ mm.

We have studied the reproducibility of the spot size measurement, which is given by the measurement precision, by the influence of the installation of the mirror on the holder and by the influence of the holder itself. We measured one of the COMPASS mirrors repetitively without any change, then at the same position but for each

measurement installed newly on the holder, and at the end, at varied positions on the holder, see Fig. 4.32. Results are summarised in Table 4.4.

Fluctuation of the radius of curvature was consistent with the estimated precision. The measurement of the parameter D_0 was weakly but not negligibly affected by the holder influence. The measurement fluctuation was $s_{D_o} = 0.06$ mm.
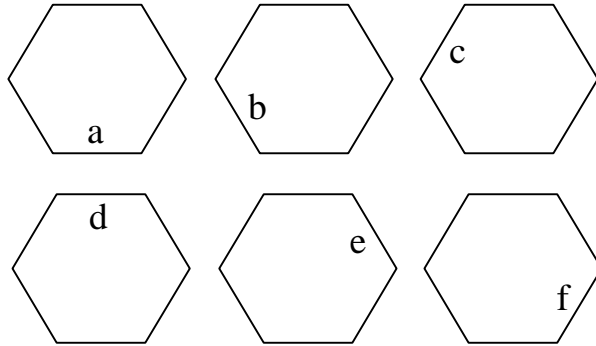
Fig. 4.32: Varied positions of the hexagonal mirror on the three-point holder.

Table 4.4: Reproducibility of the measurement of D_0 and of R measurement. Results A were obtained for repeated measurement without any change, results B for repeated measurement with the mirror always newly installed on the holder and results C for varied position of the mirror on the holder.

	D_0 [mm]	R [mm]	rms of D_0 [mm]	rms of R [mm]
A	1.07 1.05 1.05 1.05 1.07	6606 6606 6606 6606 6607	0.01	0.45
B	1.07 1.02 1.03 1.02 1.02	6607 6606 6605 6606 6606	0.02	0.71
C	1.02 1.16 1.06 1.17 1.15 1.14	6606 6607 6607 6608 6607 6606	0.06	0.75

START

Preliminary position of the smallest spot. (manual)

Calibration of the switches position and setting of the initial position.

CCD triggering and saving of the spot image.

New position of the CCD and the point source.

The last image?

No

Yes

Setting of the initial position.
Analysis of spot images.

Presentation of obtained results.

END

Fig. 4.33: Automatic procedure for the spot size measurement presented in form of a diagram. The whole procedure took 33 minutes.

Automation of the set up

This set up is foreseen for the characterisation of hundreds of mirrors. Therefore, we automated the set up as much as possible.

The measurement process is controlled by an executable LabVIEW program. The program triggers the CCD and controls the movements of the stepping motor. The triggering TTL signal is sent to the CCD User Port via NI-DAQ PCI-1200 card (National Instrument). The translation stage VT-80 150-2SM is driven by SMC pc Microstep Controller (both Micos). The whole procedure is described in the diagram in Fig. 4.33. The range of 40 mm with 1-mm step is chosen for the smallest spot finding process. The CCD registers the spot image every 12 seconds. The whole image registration process lasts 8 minutes.

The executable LabVIEW program then launches the Visual Basic program, which processes the image data. Though we use a powerful computer and fast program code, the amount of processed data demands 25 minutes of computer time. At the end, results are saved in form of text files on the hard disk and presented in graphs on the virtual instrument graphical interface, see Fig. 4.34.

Fig. 4.34: Graphical interface of the LabVIEW program, which controls the set up for spot size measurement. The virtual instrument contains controls, indicators of status of the measurement process and presentation of results.

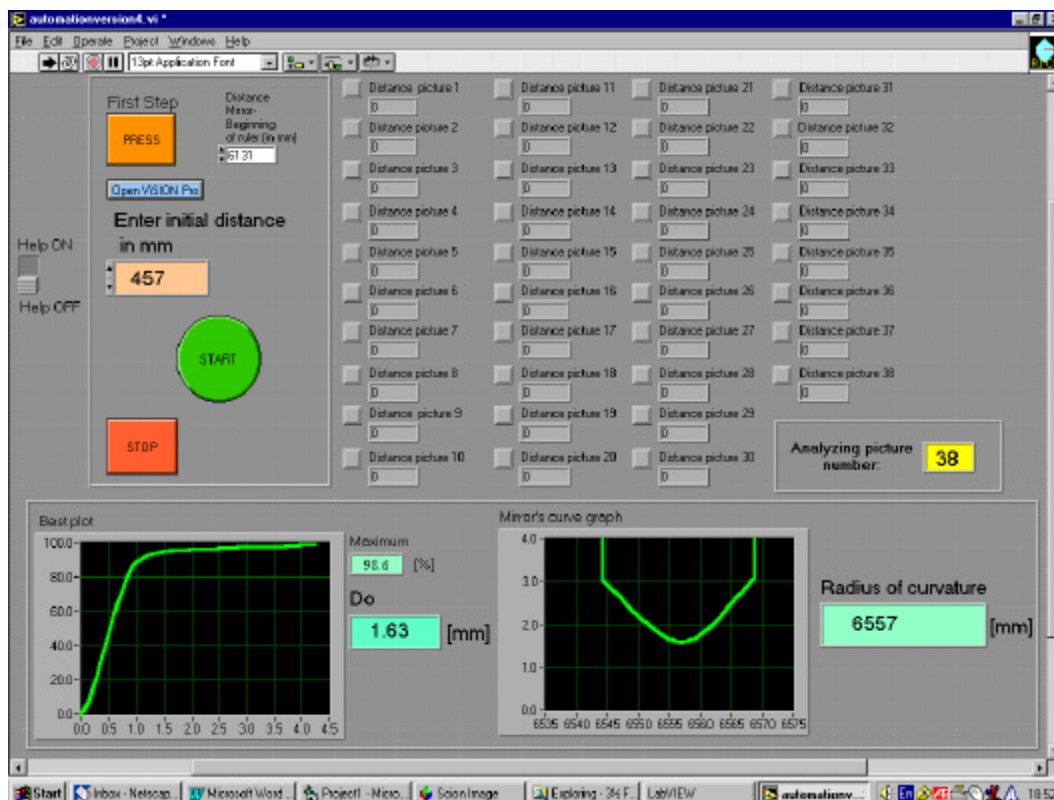## Version of the set up with 8-bit CCD camera

In case the 16-bit CCD camera is not available, a standard 8-bit CCD can be used. The handicap of low dynamic range can be partially compensated by well-considered image capturing and processing. Of course, the reached precision can never be as high as in the case of the 16-bit device.
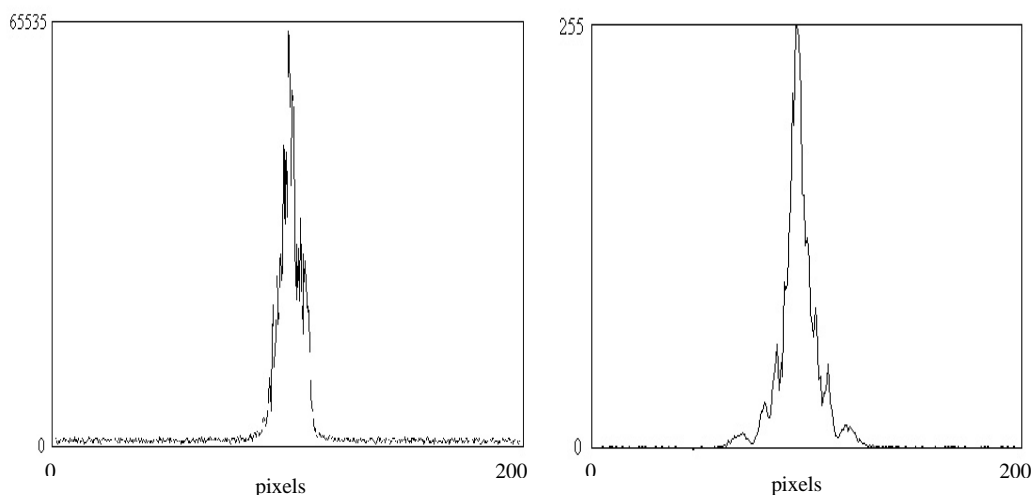

Fig. 4.35: The dynamic range for a 16-bit (left) and an 8-bit (right) CCD camera. The 8-bit CCD does not register lower intensities. Each unit increment of pixel value in the 8-bit image can be expressed by 256 values in the 16-bit image.

Fig. 4.35 illustrates a spot profile detected by 16-bit and 8-bit CCD. Low intensities with value up to 256 for 16-bit CCD have for 8-bit CCD value 0. It means that they are not detected. The contribution of low intensities to the intensity integral is significant. Its significance increases with decreasing mirror quality. If we want to detect spot regions with low intensities, it is necessary to increase the intensity of the point source by increasing I_F. Then, higher intensities will cause saturation of corresponding pixels, see Fig. 4.36. To solve this problem we decided to 'scan' the range of spot intensities by several images taken at varied intensities of the point source, as illustrated in Fig. 4.37. Three images with 8-bit range provide satisfying results. Determination of convenient values of the point source intensities is very important for the successful measurement. For COMPASS RICH 1 mirror substrates without coating, we obtained good results with three images at $I_F = 14.0$ mA (image A), 24.5 mA (image B) and 26.0 mA (image C). An example of spot images is demonstrated in Fig. 4.38 together with an image of the same spot taken by the 16-bit CCD. A program, written in Scion Image macro language, processes first the image A. The procedure is the same as for 16-bit image: the background is subtracted, the centre of gravity is found and intensity $I(i,j)$ inside increasing diameter D is integrated. Obtained values S_D have to be multiplied by a weight constant W_i, $i = $ A, B, C, according to applied output power P_{ps} of the point source. After the relative increment dS_D is smaller than a given limit dS_{lim}, the criterion for passing to the next image is fulfilled:

$$dS_D = \frac{4\Delta S_D}{S_D \cdot p\Delta D(\Delta D + 2D)} \leq dS_{\text{lim}}, \tag{4.34}$$

where $\boldsymbol{D}S_D = S_D - S_{D\text{-}\boldsymbol{DD}}$. The biggest diameter D processed in the image is D_{max}. Images B and C are processed in the same way, but the position of the centre of gravity is transferred from the image A and a circle with diameter D_{max} from previous image is subtracted from the following one. The weight constant is $W_C = 1$. Results obtained by both set up versions from the same spot, shown in Fig. 4.38, are compared in Fig. 4.39. The measurement of D_0 made by 8-bit CCD differed of a 3 % from the value obtained from 16-bit CCD, which was 0.05 mm smaller.
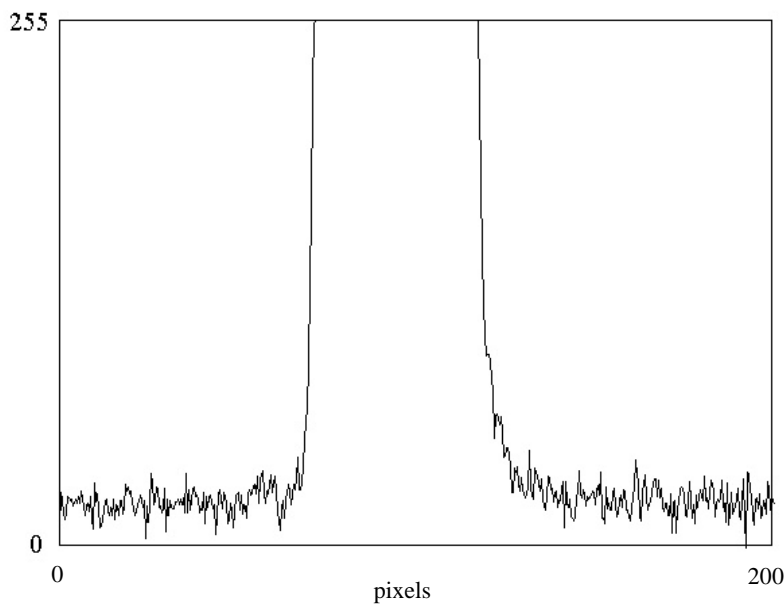
Fig. 4.36: Problem of an 8-bit CCD camera: if lower intensities are detected, pixels exposed to higher intensities are saturated.
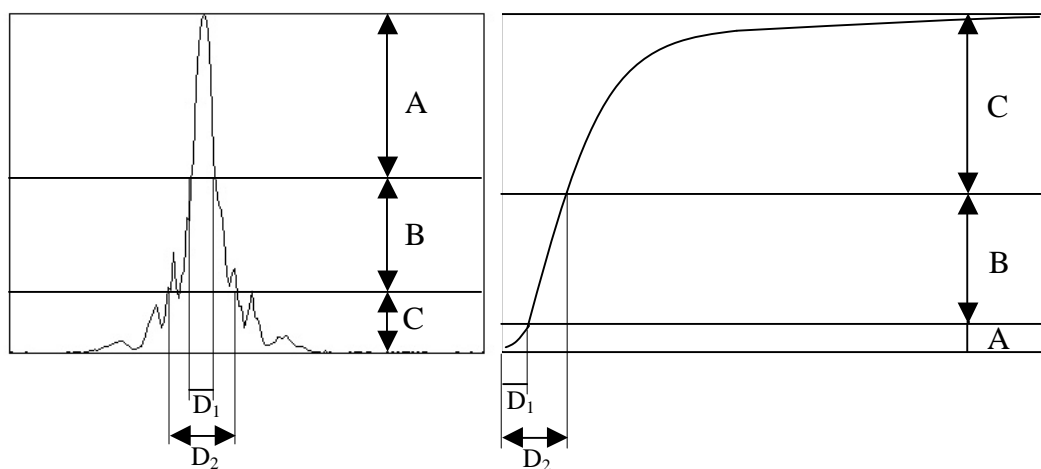
Fig. 4.37: 'Scanning' of the spot intensities by three 8-bit images (A, B, C) at different intensities (left). Corresponding characteristics $P_D(D)$ (right).
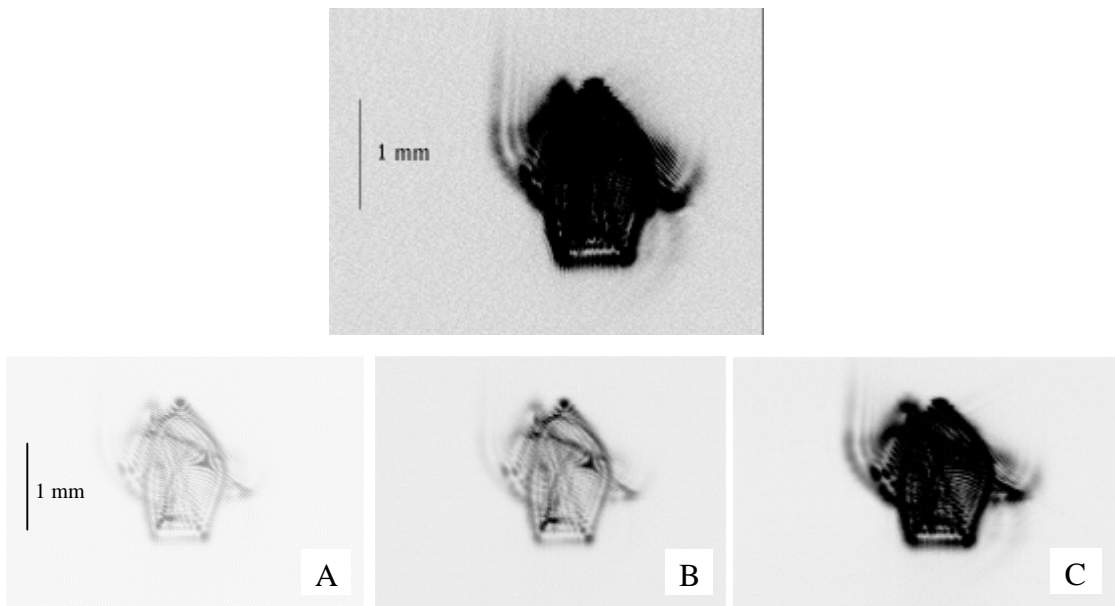
Fig. 4.38: Top: Spot image from 16-bit CCD. Bottom:Three spot images from 8-bit CCD at different intensities. A: I_F = 14.0 mA, B: I_F = 24.5 mA, C: I_F = 26.0 mA
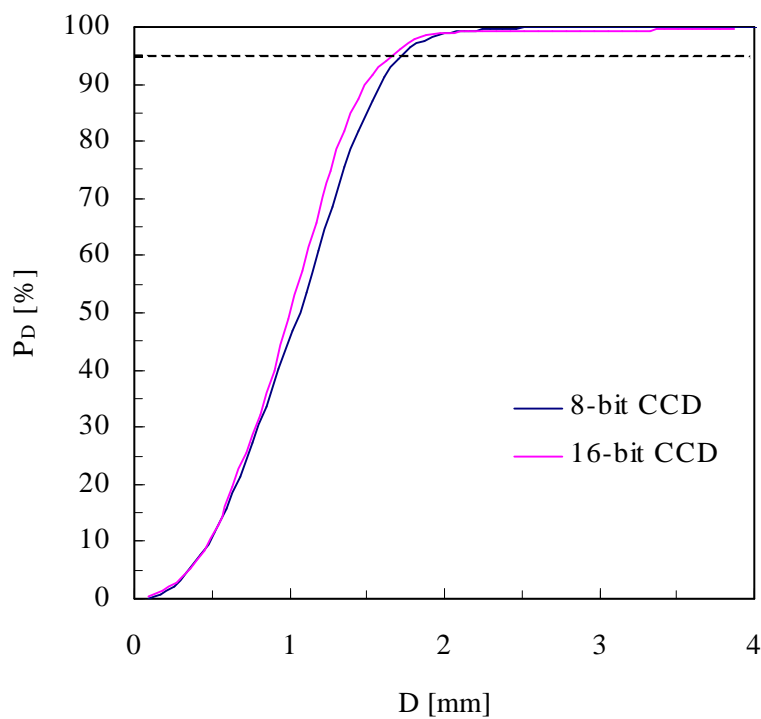
Fig. 4.39: Comparison of results from the LHCb RICH-2 prototype obtained by:
         8-bit CCD D_0 = 1.72 ± 0.17 mm
        16-bit CCD D_0 = 1.67 ± 0.02 mm

4.2.5.2 Modification of the set up for planar mirrors

Two planar mirrors with size 1754×2193 mm^2 each make the detector vessel shorter and reflect the Cherenkov photons towards two photodetector planes. The mirrors will be created as mosaics of smaller hexagonal or square elements. They will be fixed on the same type of supporting panels by means of the same type of adjustable mounts, as in the case of spherical mirrors. The required precision is also the same, see Sect. 4.1. The thickness should be the same to ensure the uniformity of the fraction of radiation length over the whole range of the detector angular acceptance.

Since planar mirrors do not have a finite focal plane the measurement set up has to be modified. In principle, four arrangements are possible, see Fig. 4.40. All possibilities require a high quality spherical mirror that will focus the light but will not contribute significantly to the wavefront distortion. For this purpose we have a high precision glass reference mirror with $D_{0ref} = 0.2$ mm and $R_{ref} = 7.8$ m, see Fig. 4.6. The first arrangement (Fig. 4.40a) works in autocollimating mode. Let us denote l_1 the distance point source – planar mirror, and l_2 the distance planar mirror – reference mirror. The reference mirror is placed at distance $R_{ref}/2$ from the point source. Collimated beam is declined and, after reflection on the measured planar mirror, again focused on the CCD camera. The planar mirror is not completely orthogonal to the beam, which separates the point source and the spot in order to make a space for the CCD. In the second variant (Fig. 4.40b), the point source illuminates first the planar mirror. Declined diverging beam is focused by the reference mirror back to the CCD via the planar mirror. Another possibility is not to use the same path for back-reflected beam but to decline it twice. The CCD and the point source are then placed on opposite sides of the bench. The beam can be reflected first by the reference mirror (Fig. 4.40c) or by the planar mirror (Fig. 4.40d).

An advantage of the variant b is the fact that coma and astigmatism are due to smaller tilt of the spherical mirror reduced to minimum, which is not the case for other three solutions. The beam is reflected on the measured mirror twice and this makes the measurement more sensitive. For all variants, a small contribution of the reference mirror to the spot size has to be considered. The contribution is approximately equal for variants b, c, d where the value of D_{0ref} should be subtracted from the measured D_0. In the case a, the subtracted value increases to $D_{0ref} \cdot (2 \cdot l_2 + R_{ref})/R_{ref}$ because of double reflection on the reference mirror. To get an absolute value, also the optical path length between the measured mirror and the CCD has to be taken in account. Then the result for variant b has to be multiplied by coefficient $k_{abs} = 0.5$ because of double reflection on the measured mirror. Values of the coefficient k_{abs} for all variants are given in Fig. 4.40.

In order to obtain adequate results, it is necessary to reduce the angles of the mirror tilts between the point source and the CCD. Big angles cause not acceptable astigmatism, which affects the measured results. The problem is illustrated in Fig. 4.41. A typical behaviour of the spot, aberrated with astigmatism, is shown in Fig. 4.42.

a)

CCD

Point source

Reference mirror
(spherical)

Plane mirror

$$k_{ref} = \frac{2 \cdot l_2 + R_{ref}}{R_{ref}}$$

$$k_{abs} = \frac{R_{ref}}{l_2 + \dfrac{R_{ref}}{2}}$$

b)

$$k_{ref} = 1$$

$$k_{abs} = \frac{1}{2}$$

c)

$$k_{ref} = 1$$

$$k_{abs} = \frac{R_{ref}}{R_{ref} + l_2}$$

d)

$$k_{ref} = 1$$

$$k_{abs} = \frac{R_{ref}}{R_{ref} - l_2}$$
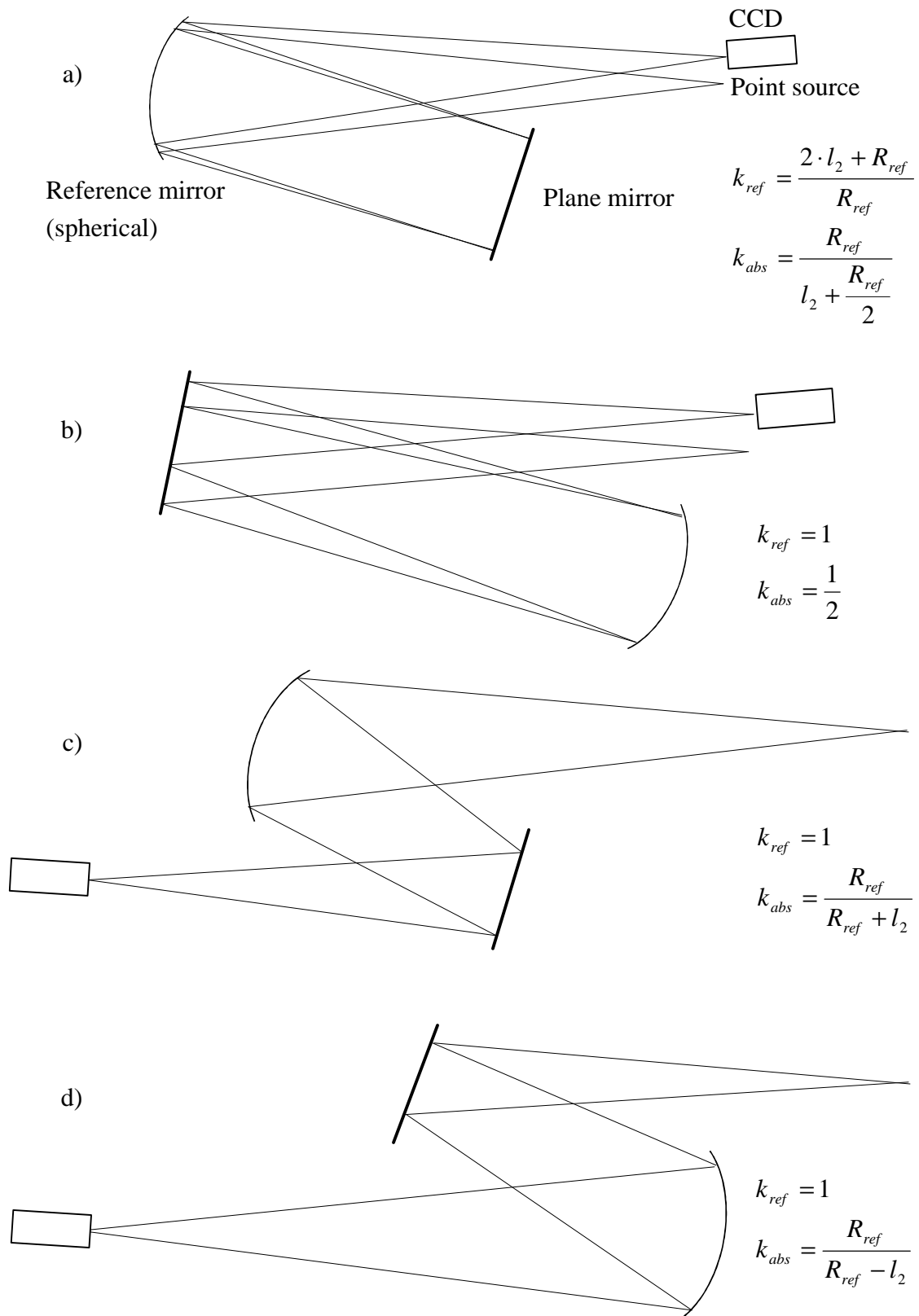
Fig. 4.40: Four different arrangements of the set up for spot size measurement for plane mirrors. The spot size parameter D_0 is given by: $D_0 = k_{abs} \cdot (D_0' - k_{ref} \cdot D_{0ref})$, where k_{abs} and k_{ref} are coefficients given in the figure, D_0' is a spot size parameter measured by the CCD and D_{0ref} is a spot size parameter of the reference mirror.
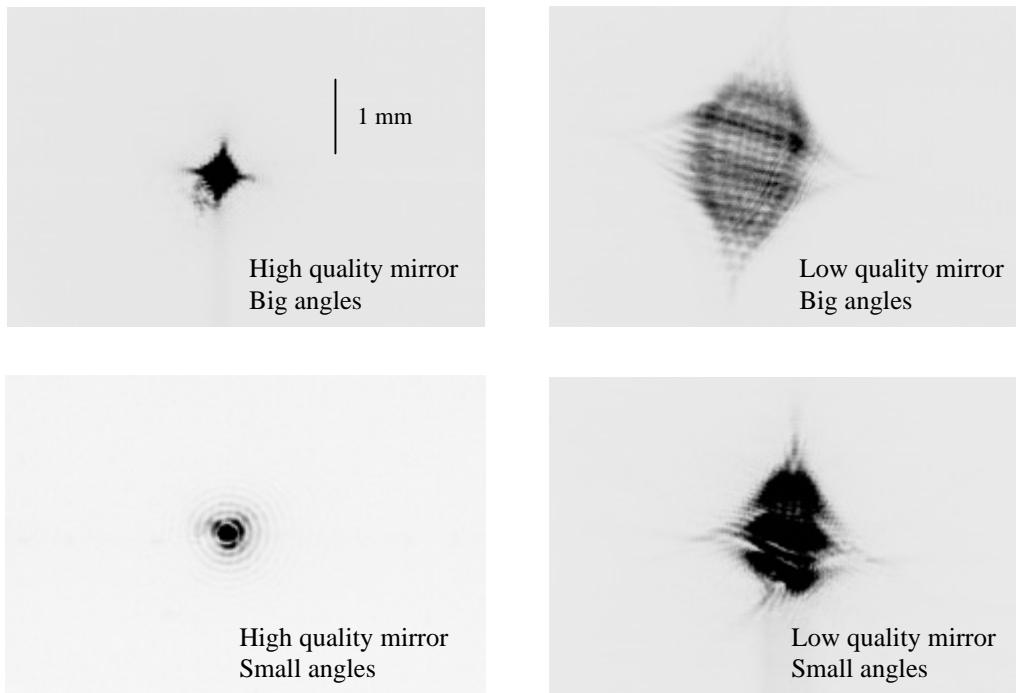
Fig. 4.41: Dependence of degree of astigmatism on tilt angles of mirrors. Top pictures show spots obtained with set up with large angles, bottom pictures then spots from set up with minimized angles. Left images are from high quality plane mirror, right ones from lower quality plane mirror.
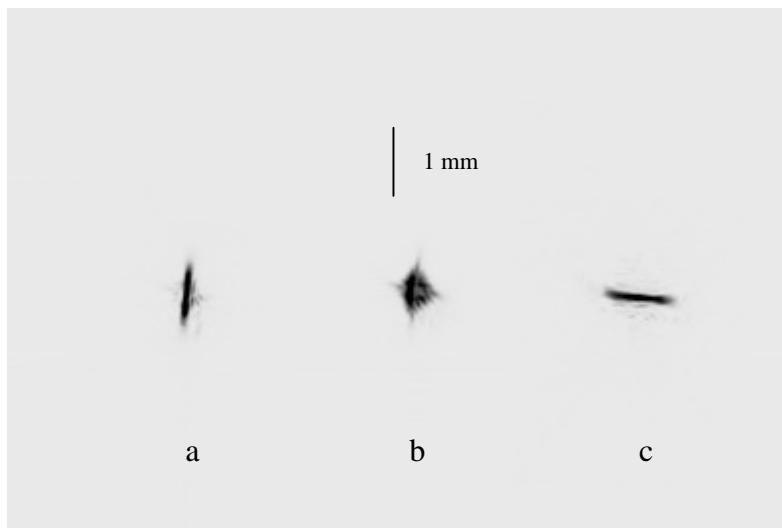
Fig. 4.42: Shape of the spot aberrated by astigmatism. Detection plane was: (a) in front of focus, (b) at focus, (c) behind focus.

4.2.5.3 Bench for topographic measurement of reflective surfaces

Information about mirror substrates obtained by the previously described set up for the spot size measurement is limited. Apart from the values of R and D_0, respectively s_J, and the shape of the spot image, we have no indication concerning the geometry of the substrate surface. In other words, we know how good or bad the geometrical precision is but we do not know why. That is why we decided to incorporate into the optical laboratory the Shack-Hartmann method, which was briefly introduced and analysed in Sect. 4.2.4.3.

Measurement method and set up

The Shack-Hartmann (SH) method is especially convenient for measurements of large mirrors and mirrors with long focal lengths, where an interferometric measurement usually fails. The failure is caused by turbulent or rapidly changing medium between the mirror under test and the interferometer. Rapid vibrations of the measured mirror can also be problematic. The SH sensor can be very useful in case of large mirrors with small deviations in slope of the reflecting surface. Widely used Foucault test is insensitive to small slope deviations although they can make big departures from an ideal shape over large apertures. On the other hand, the SH method presumes that changes of the wavefront phase between discreet sampling points are rather gradual than abrupt [4.7]. This assumption is quite save, because from its nature the geometry of properly polished glass surfaces is usually smooth.

A scheme of the SH sensor is presented in Fig. 4.43. The set up was incorporated into that for average geometrical quality measurement (Sect. 4.2.5.1). A point-like source (a) placed at the centre of curvature plane of the tested mirror illuminates the mirror (b). Reflected light passes the focus (c) and then it is collimated by an objective (d). A microlens array (e) is placed at the location of the demagnified mirror image projected by the objective. A system of sampling Hartmann spots (f) is formed at focal plane of the microlens array. A CCD (g) detects demagnified image of these spots via a relay lens (h). Positions of these spots are compared with system of reference Hartmann spots, which is obtained by introducing a wavefront without distortions. To achieve this, we place the point source at the position of the mirror focus, facing the CCD as illustrated in Fig. 4.43b. To our knowledge and according to a publication recherche we made, such an arrangement for creating the reference wavefront has never been used before. The advantage is that an influence of all the optical components of the sensor is compensated. In a classical arrangement (see Fig. 4.44), a beam splitter is used to bring the reference wavefront to the microlens array. Any distortion of the reference wavefront caused by the beam splitter cannot be compensated.

We have calculated the parameters of the set up, replacing the spherical mirror by a lens with the same value of focal length, see Fig. 4.45. Values of some of parameters are fixed: the diameter of measured mirrors will not be much bigger than 500 mm. The radius of curvature is $R = 8$ m for the LHCb RICH 2 mirrors. The size
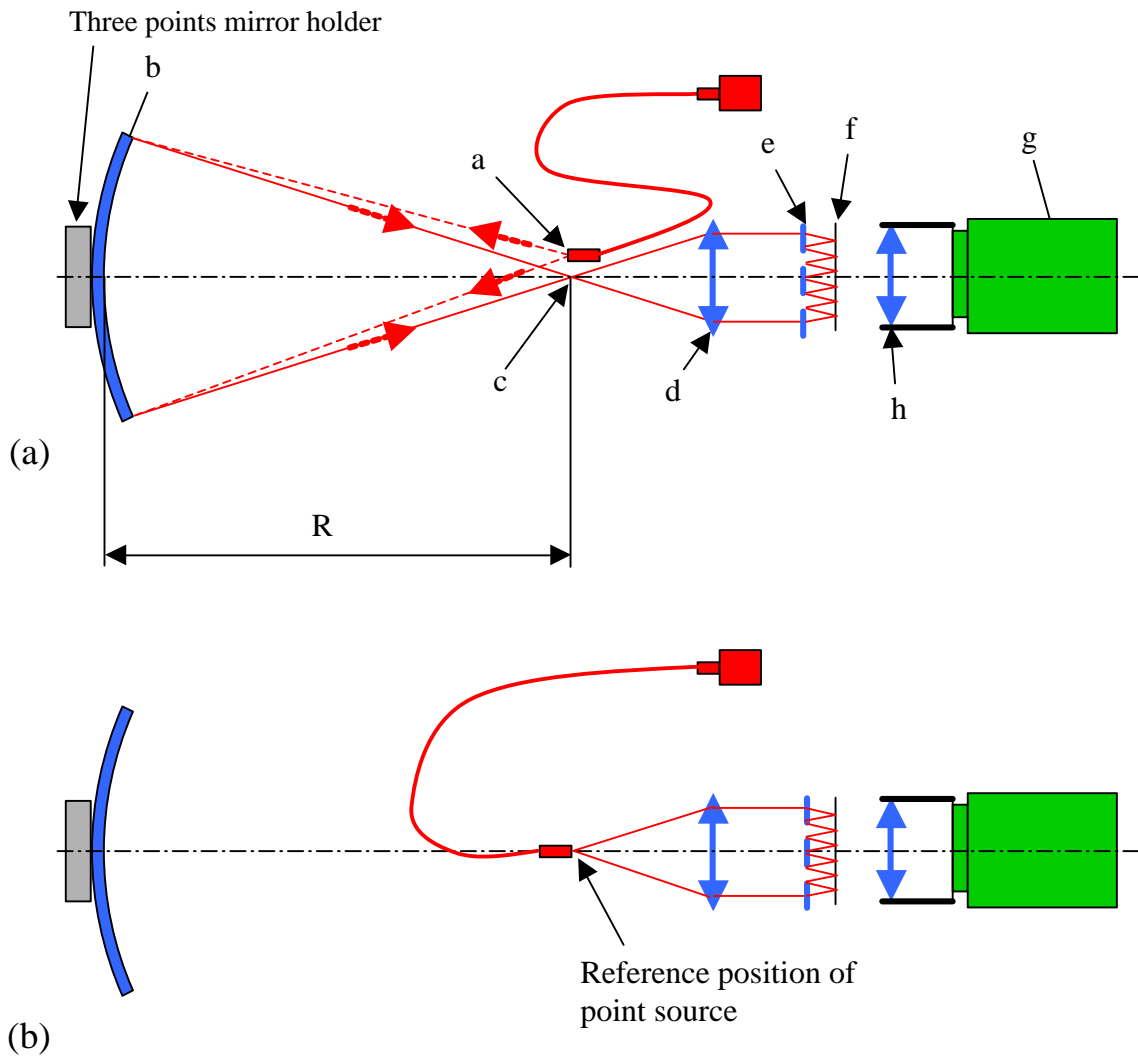
Fig. 4.43: Scheme of the SH sensor. (a) Standard arrangement for detection of sampling Hartmann spots. (b) Innovative arrangement for detection of reference Hartmann spots. The point source is moved to the previous position of the spot image and turned 180 °.

of the microlens array[7] is 18×18 mm^2 and the CCD active area has dimensions 6.9×4.6 mm^2. Values obtained from calculation are: the focal length of objective (d) $f' = 260$ mm, the distance p' between the objective and the microlens array $p' = 268.5$ mm. The diameter of the mirror image d' projected on the microlens array would be $d' = 16.25$ mm for the mirror with diameter $d = 500$ mm. The distance between microlens array and the Hartmann spots is equal to a chosen focal length of the microlens array. The relay lens (Melles Griot model 59 LGF 410, 59 LGC 525) mounted directly on the CCD head has magnification $M = 0.25$.

The range and resolution of the wavefront slope measurement depend mainly on the parameters of the microlens array. A maximum measurable wavefront slope a_{max} is given by (Fig. 4.46a):

---
[7] Sampler from AOA, Inc.

$$\boldsymbol{a}_{\max} = D/2f \ , \tag{4.35}$$

where D is a pitch of microlenses and f is their focal length. The resolution on the slope determination $\boldsymbol{s_a}$ is given by (Fig. 4.46b):

$$\boldsymbol{s}_a = \boldsymbol{s}_{\mathrm{m}}/2f \ , \tag{4.36}$$

where $\boldsymbol{s}_{\mathrm{m}}$ is a resolution of the spot positions finding algorithm. $\boldsymbol{s}_{\mathrm{m}}$ can be evaluated by relation (4.59) in Sect. 4.3.4. A deeper analysis, which takes in account photon noise and read-out noise, is given in [4.19]. Values of the range and resolution for different values of D and f are listed in Table 4.5. Values of D and f have to be carefully selected for specific mirrors. It is not only question of the slope measurement range and resolution. In case of large local curvature of the wavefront, corresponding Hartmann spots will feature large coma, which affects measurement of their positions. The problem can be solved by decreasing of parameter D, which will reduce the aberration. Another problem can be caused by insufficient light level of the spots. By increasing D twice, the light level per spot will increase four times.
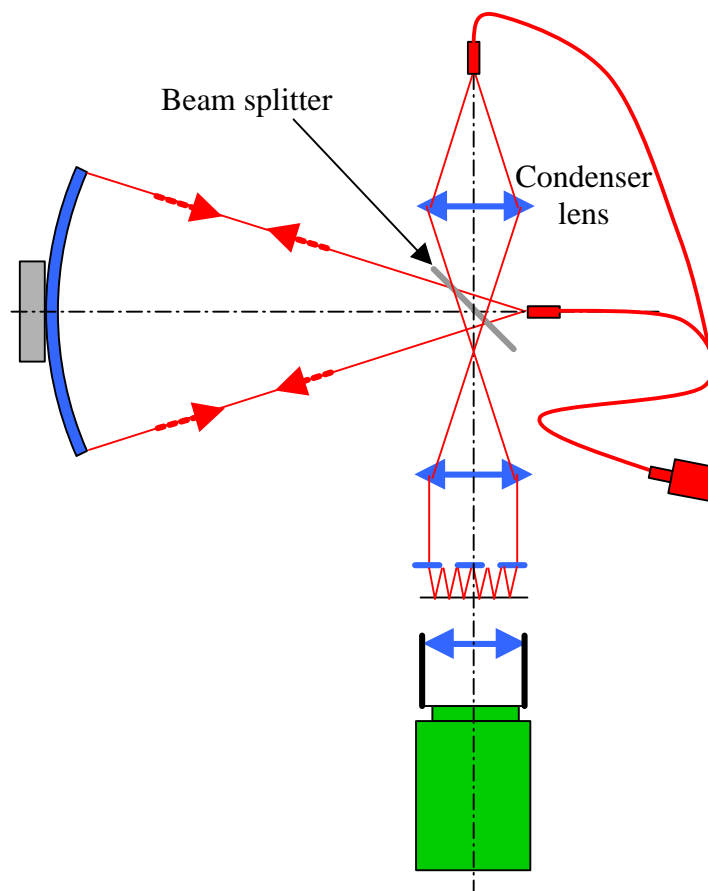
Fig. 4.44: Classical arrangement of Shack-Hartmann sensor. The point source is placed in the center of curvature and the reflected wavefront is declined by a beam splitter. The influence of the beam splitter and of the condenser lens cannot be compensated.
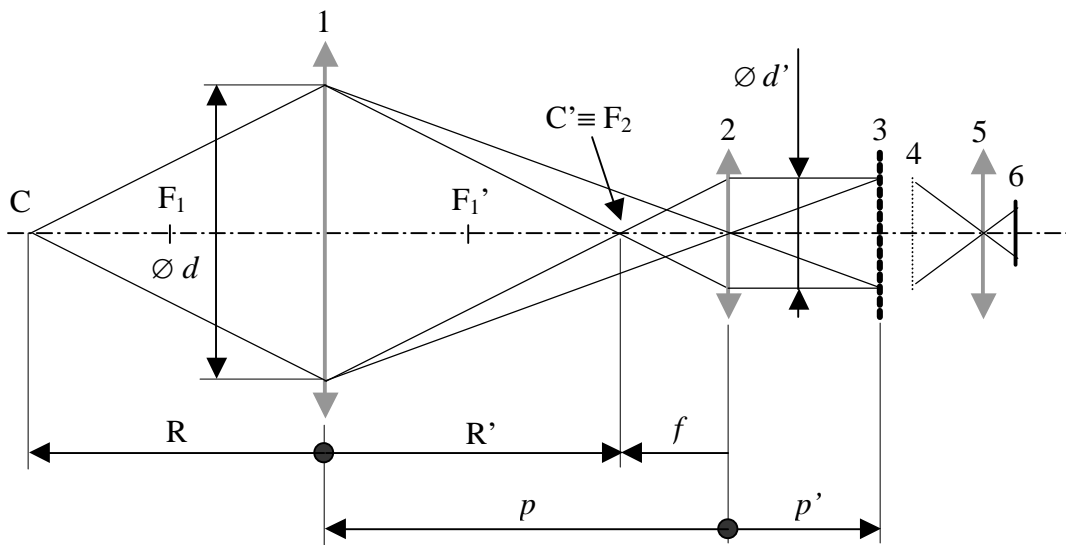
Fig. 4.45: Scheme for calculation of parameters of the set up. The measured mirror with diameter D is replaced by a lens (1). The point source, placed in C, is imaged in C, which coincides with F_2 of the objective (2). The microlens array (3) is placed in the plane of the demagnified image of the lens (1). Hartmann spots (4) are demagnified by the relay lens (5) on the active area of the CCD (6).
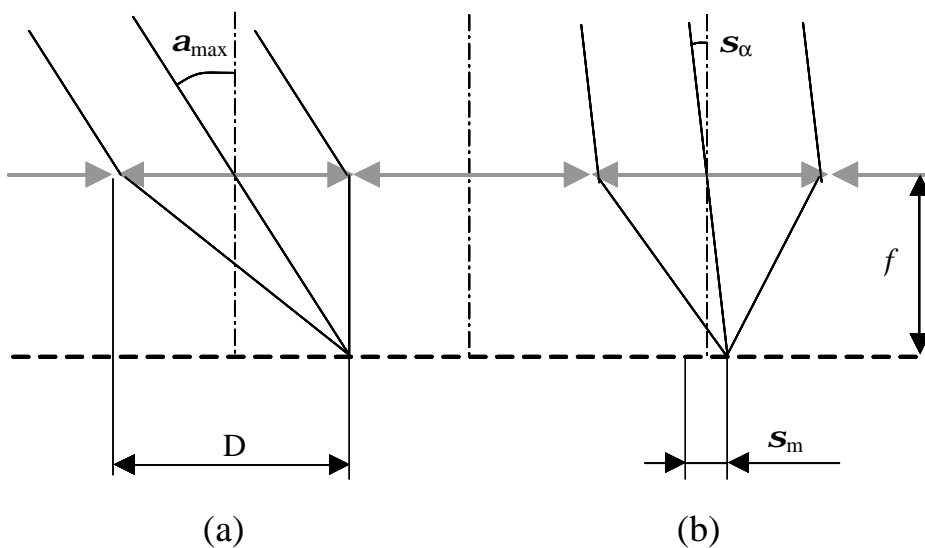
Fig. 4.46: (a) The maximum measurable wavefront slope a_{max} depends on the microlens pitch D and focal length f. (b) The resolution of the slope determination s_a is given by the resolution of the spot positions finding algorithm s_m and focal length of the microlens array.

Table 4.5: Parameters of microlens arrays from AOA sampler: position on the sampler, pitch D, focal length f, number of microlenses N. Given is also maximum measurable wavefront slope a_{max} and resolution of the slope measurement s_α All arrays have size 18×18 mm^2 and square microlenses.

Microlens array		D [mm]	f [mm]	a_{max} [mrad]	$s_\alpha{}^*$ [mrad]	N
Row	Column					
1	A	1.00	29.3	17.1	0.06	18
	B		20.5	24.4	0.08	
	C		16.5	30.3	0.10	
	D		12.7	39.4	0.13	
	E		10.0	50.0	0.17	
2	A	0.75	20.1	18.7	0.08	24
	B		13.0	28.8	0.13	
	C		7.5	50.0	0.22	
	D		6.0	62.5	0.28	
	E		4.0	93.8	0.42	
3	A	0.50	16.5	15.2	0.10	36
	B		10.4	24.0	0.16	
	C		5.0	50.0	0.33	
	D		2.5	100.0	0.66	
	E		1.2	208.3	1.39	
4	A	0.40	10.7	18.7	0.16	45
	B		5.2	38.5	0.32	
	C		3.0	66.7	0.56	
	D		2.0	100.0	0.83	
	E		1.0	200.0	1.67	
5	A	0.20	7.9	12.7	0.21	90
	B		5.0	20.0	0.33	
	C		2.0	50.0	0.83	
	D		1.0	100.0	1.67	
	E		0.5	200.0	3.33	

* Resolution given for 8-bit CCD.

Alignment of the sensor

A precise alignment of the optical components of the SH sensor is, together with their high quality, critical to the successful estimation of the wavefront topography. The co-ordinate system is displayed in Fig. 4.47. Before an actual wavefront measurement can be started, the position of the centre of curvature is determined by means of the set up for average geometrical quality measurement as described in Sect. 4.2.5.1. The
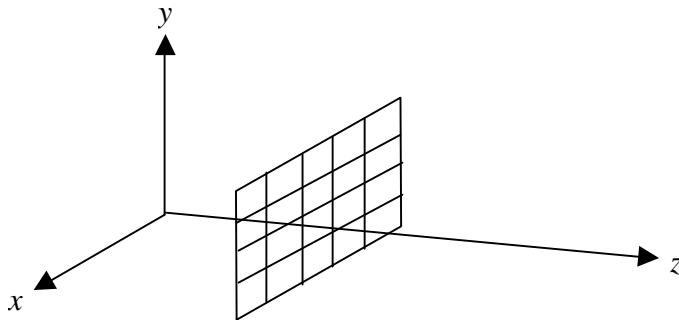
Fig. 4.47: Co-ordinate system used for set up alignment.
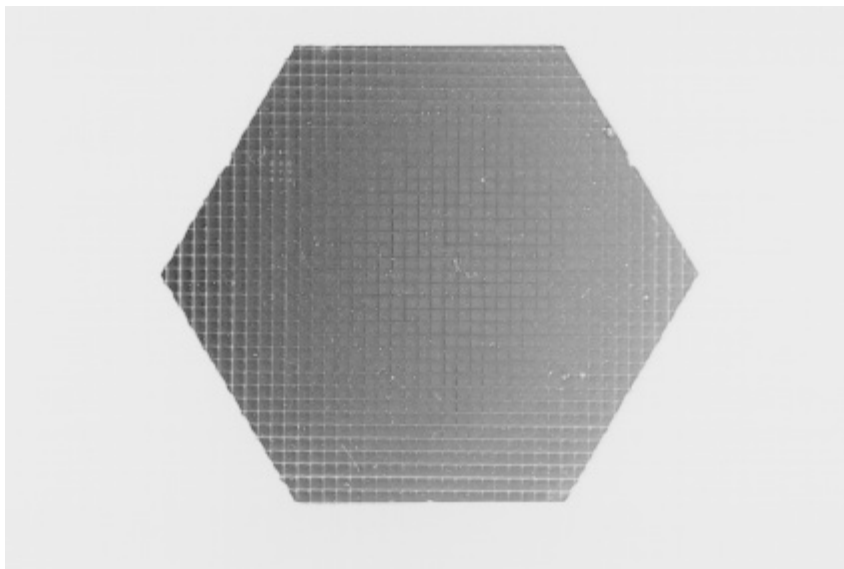
Fig. 4.48: An image of the microlens array with pitch $D = 400$ μm superimposed over a demagnified image of the measured mirror. Both images are well focused which means that microlens array is placed in the correct position.

spot image of the point source is carefully centred on the active area of an auxiliary CCD. The CCD is moved out of the beam. The collimating objective is installed and its position is adjusted along axis z, so that the beam is well collimated. The adjustment is performed by means of the main CCD equipped with the relay lens. If this adjustment is not exact, a defocus is introduced. The precise position of the mirror image is found by moving the CCD along axis z. The microlens array is

installed roughly at the position of the mirror image. A system of three micrometric sliding and of two rotating stages allows a fine adjustment in the all five co-ordinates. The array is centred in the plane *xy* relatively to the mirror image and adjusted along axis *z* to be seen sharply by the CCD (Fig. 4.48). Then the CCD is moved backwards and the position of the Hartmann spots is focused (Fig. 4.49a). The intensity of the point source can be adjusted and the image of the sampling spots is saved.

To obtain the reference spots, the point source is placed at the position shown in Fig. 4.43b. The mechanics of the point source support was designed in such a way that the new position of the point source coincides with the previous position of the centre of the auxiliary CCD. Then the position of the point source and of the spot image are identical. The positions of the collimating objective, the microlens array and the main CCD, adjusted for the sampling beam, must not be changed. Finally, the image of the Hartmann reference spots (Fig. 4.49b) at a convenient light intensity is saved. Misalignment effects of the Shack-Hartmann sensor are analysed in [4.20].

a)   b)
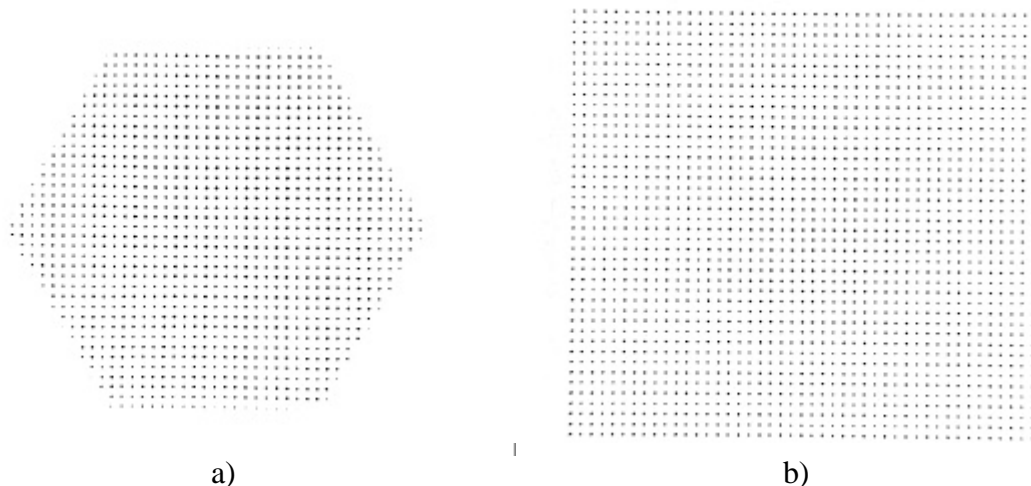
Fig. 4.49: Detected Hartmann spots. (a): sampling spots. (b): reference spots.

Data processing

We developed a program for the SH data processing. It is written in a PASCAL-like Scion Image macro language. A user first opens sampling and reference images. Then values of the pixel size of the used CCD camera and of a pitch *D* and a focal length *f* of the chosen microlens array have to be input. The program proposes a network of subapertures corresponding to the microlens array. The user corrects eventual misalignment of the network positioning to have each single Hartmann spot inside one subaperture (Fig. 4.50). The same network is applied for both images. After a visual check that spots are more or less centred in subapertures, the user is asked to select a system of relevant subapertures for processing. The selection is performed on the sampling image (Fig. 4.51). After this, all input parameters are
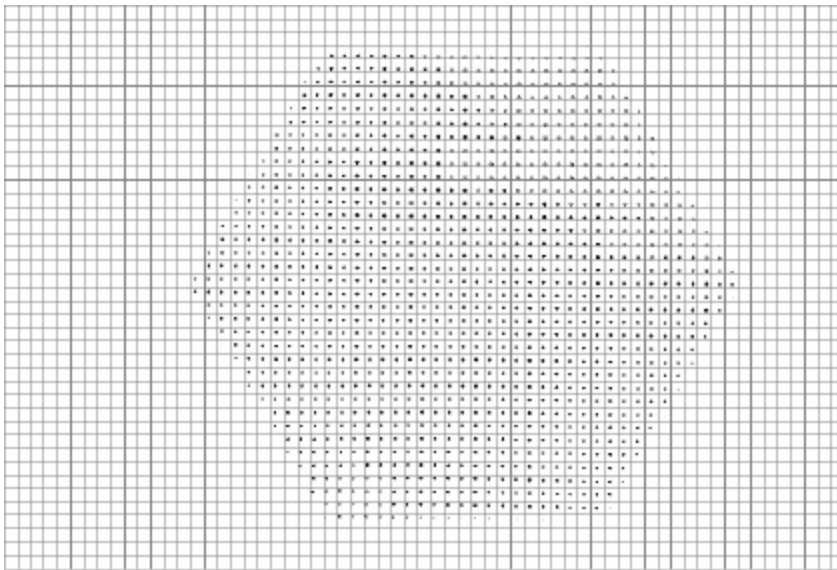
Fig. 4.50: Network of subapertures with each sampling spot inside a single subaperture.
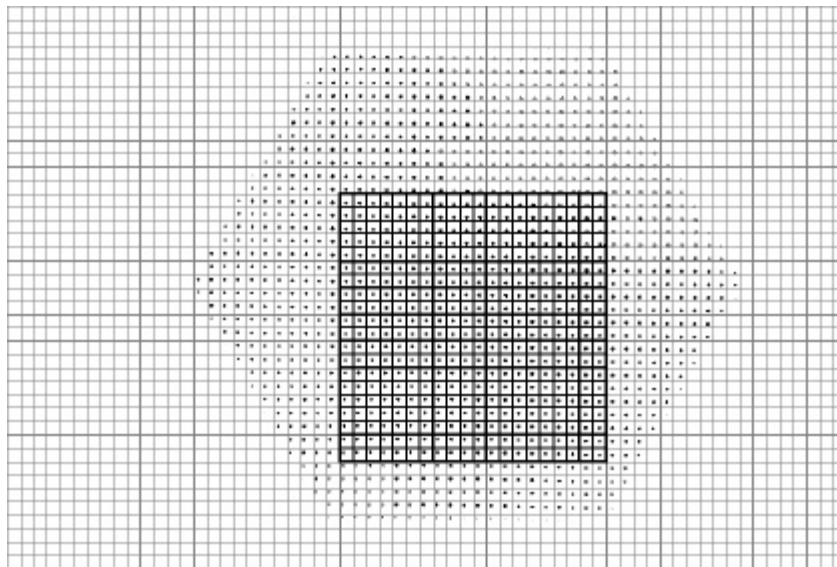
Fig. 4.51: Selected subapertures for data processing.

known and program starts a processing procedure. Centres of gravity of both sampling and reference spots are found for each selected subaperture, and their relative distances $d(x,y)$ are calculated. The procedure for the centre of gravity finding was described in Sect. 4.2.5.1. Results are written in a table and displayed in a graphical window (Fig. 4.52).
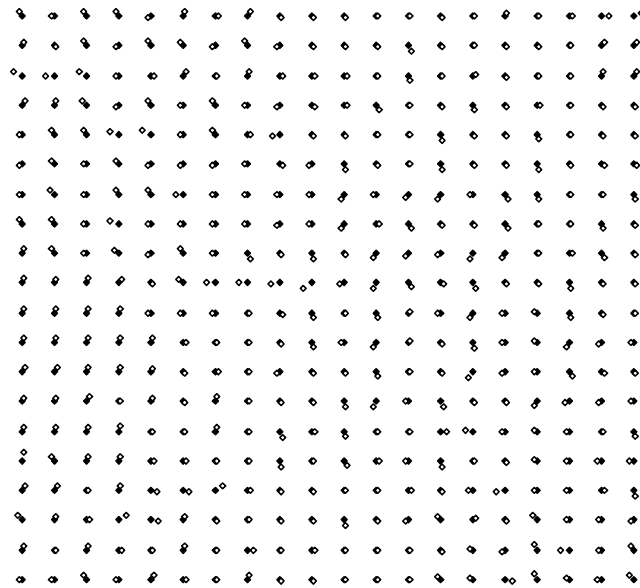
Fig. 4.52: Graphical interpretation of result of the data processing. Oriented vectors indicate direction and value of local slopes in sampling points.

Data analysis - reconstruction of wavefront topography

As a result of the measurement with the SH sensor, we obtain values of the local slopes $q(x,y)$ of the wavefront in discrete sampling points, see Fig. 4.53. From these data, topography of the wavefront can be reconstructed and consequently topography of the mirror surface estimated. Before starting the reconstruction, a contingent
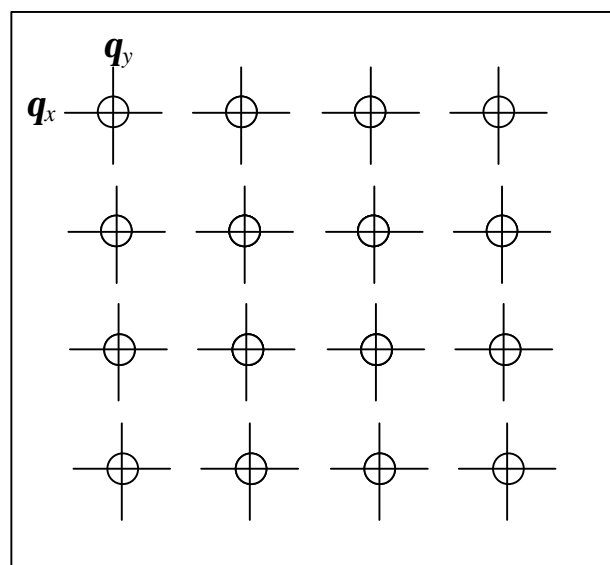
Fig. 4.53: Discrete sampling points with indicated orientation of associated measured local slope components.

wavefront tilt should be removed from the data, because it had been introduced by misalignment and not by the mirror itself. The tilt can be excluded by subtraction of the mean $\overline{\boldsymbol{q}}$ of the slope values from local slope components:

$$\boldsymbol{q}_{xc}(x, y) = \boldsymbol{q}_x(x, y) - \overline{\boldsymbol{q}}_x \qquad (4.37a)$$

$$\boldsymbol{q}_{yc}(x, y) = \boldsymbol{q}_y(x, y) - \overline{\boldsymbol{q}}_y \ , \qquad (4.37b)$$

where $\boldsymbol{q}_{xc}$, $\boldsymbol{q}_{yc}$ are corrected values. Another possibility is to use the least squares method.

Fig. 4.54 illustrates the problem of the wavefront phase reconstruction from local slope data. The main assumption is made that the wavefront is continuous. To reconstruct the whole wavefront, the problem has to be extended to two dimensions. Example of a reconstructed two-dimensional wavefront is shown in Fig. 4.55.
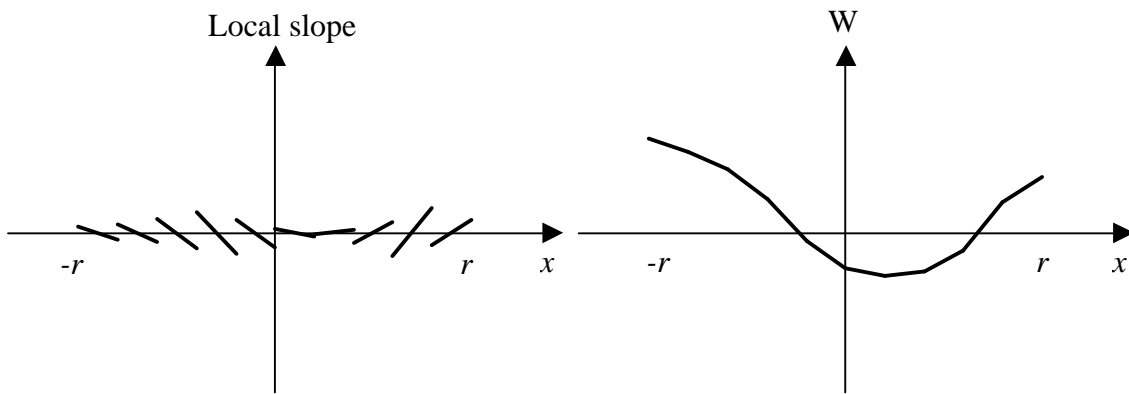
Fig. 4.54: Principle of reconstruction of wavefront profile from local slope data over mirror aperture with radius *r*.

Two basic approaches to the reconstruction are possible: a zonal approach and a modal approach. In the zonal approach, we approximate the wavefront as composed of tilted flat planes (Fig. 4.55). Each sampling point is located in the centre of one flat plane with tilt corresponding to the measured local slope. From relations (4.13, 4.14a,b) we get:

$$W = \frac{1}{f} \int_0^x \boldsymbol{dx}(x, y)dx \qquad (4.38a)$$

$$\text{and } W = \frac{1}{f} \int_0^y \boldsymbol{dy}(x, y)dy \qquad (4.38b)$$
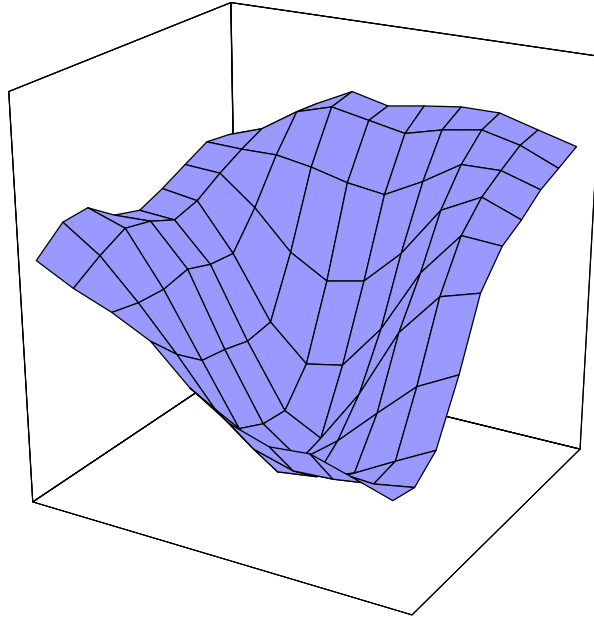
Fig. 4.55: Example of 2-D reconstructed wavefront.

Because of the discrete sampling of the wavefront, we can compute the integrals by use of the following formulas [4.7]:

$$W_N = \frac{1}{f} \sum_{n=2}^{N} \left(\frac{dx_{n-1} + dx_n}{2} \right) \cdot D \qquad (4.39a)$$

$$W_M = \frac{1}{f} \sum_{m=2}^{M} \left(\frac{dy_{m-1} + dy_m}{2} \right) \cdot D \qquad (4.39b)$$

Values of function $W(x,y)$ are computed in $N \times M$ sampling points with relation to the reference point $N = 1$ and $M = 1$. Alternatively, quantities W_N, W_M can be obtained from:

$$W_N = \frac{2}{f} \left(\frac{dx_1}{2} + \sum_{n=2}^{N-1} dx_n + \frac{dx_N}{2} \right) \cdot D \qquad (4.40a)$$

$$W_M = \frac{2}{f} \left(\frac{dy_1}{2} + \sum_{m=2}^{M-1} dy_m + \frac{dy_M}{2} \right) \cdot D \qquad (4.40b)$$

Instead of flat planes two-dimensional cubic spline functions [4.21] can be used to interpolate surface between sampling points.

In the modal approach, the wavefront is reconstructed by a polynomial fit. This agrees better with wavefront continuity. Zernike polynomials and Karhunen-Loeve

functions have become very popular in the field of astronomical telescopes [4.12]. In general, two-dimensional polynomial of k-th degree can be used for wavefront representation [4.7]:

$$W(x, y) = \sum_{i=0}^{k} \sum_{j=0}^{i} B_{ij} x^j y^{i-j} \tag{4.41}$$

The partial derivatives of $W(x,y)$ with respect to x and y are:

$$\frac{\partial W}{\partial x} = \sum_{i=0}^{k-1} \sum_{j=0}^{i} (j+1) B_{i+1,j+1} x^j y^{i-j} \tag{4.42a}$$

$$\frac{\partial W}{\partial y} = \sum_{i=0}^{k-1} \sum_{j=0}^{i} (i-j+1) B_{i+1,j} x^i y^{i-j} \tag{4.42b}$$

To get values of coefficients B_{ij}, the values of local slope measurement are fitted to two-dimensional polynomial of $(k$-1)-th degree by means of a least squares procedure:

$$\frac{\partial W}{\partial x} = \sum_{i=0}^{k-1} \sum_{j=0}^{i} C_{ij} x^i y^{i-j} \tag{4.43a}$$

$$\frac{\partial W}{\partial y} = \sum_{i=0}^{k-1} \sum_{j=0}^{i} D_{ij} x^j y^{i-j} \tag{4.43b}$$

Then coefficients B_{ij} are given by:

$$B_{i0} = \frac{D_{i-1,0}}{i} \qquad \text{for} \quad i = 1,2,3,\ldots,k \tag{4.44a}$$

$$B_{ii} = \frac{C_{i-1,i-1}}{i} \qquad \text{for} \quad i = 1,2,3,\ldots,k \tag{4.44b}$$

$$B_{ij} = \frac{1}{2} \left(\frac{C_{i-1,j-1}}{j} + \frac{D_{i-1,j-1}}{i-j} \right) \quad \text{for} \quad i \neq j \text{ and } \begin{cases} i = 2,3,\ldots,k \\ j = 1,2,3,\ldots,(i-1) \end{cases} \tag{4.44c}$$

After all coefficients B_{ij} have been found, the function $W(x,y)$ can be determined from relation (4.41).

The modal approach is in general better than the described zonal solution because cumulative errors due to numerical integration are removed. On the other hand, the polynomial fitting can introduce errors due to low or high order of polynomial fit. The effect shows up by smoothing up relevant sharp features or by forming non-existing oscillations respectively. Another source of errors is a noise in

the slope measurement data. Random noise can be reduced by taking several measurements and using mean values.

To remove numerical integration errors from the zonal reconstruction problem, least square method can be implemented. In the following, we consider a grid of $N \times N$ sampling points. The wavefront phase between sampling points in the x direction can be represented by the polynomial:

$$W = c_0 + c_1 x + c_2 x^2 \tag{4.45}$$

Then the slope in co-ordinate x is:

$$\boldsymbol{q}_x = c_1 + 2c_2 x \tag{4.46}$$

Equivalent relations are valid for y direction. We formulate relation between slopes and phases as a matrix equation:

$$\mathbf{MS} = \mathbf{AW}, \tag{4.47}$$

where $\mathbf{S}$ is a vector containing all $2N^2$ slope measurements, $\mathbf{W}$ is a vector of length N^2 containing all unknown phase values, $\mathbf{M}$ is a sparse matrix of size $2N^2 \times 2N(N\text{-}1)$ that performs the adjacent slope averaging and $\mathbf{A}$ is a sparse rectangular matrix of size $N^2 \times 2N(N\text{-}1)$. To determine local values W_{ij} from measured slopes $\boldsymbol{q}_x$ and $\boldsymbol{q}_y$ by the least squares method, corresponding normal matrix equation has to be solved:

$$\left(\mathbf{A}^{\mathrm{T}}\mathbf{A}\right)\mathbf{W} = \mathbf{A}^{\mathrm{T}}\mathbf{MS} \tag{4.48}$$

The solution can be found with matrix iterative methods like Jacobi or Gauss-Seidel method. The latter generally converges faster, approximately in N^2 iterations.

A system of equations defined by the matrix equation (4.48) was built with help of the Mathematica software. We prepared a Visual Basic program for iterative wavefront estimation based on the above-described zonal approach.

Evaluation of the reconstruction program and first results

The reconstruction algorithm should provide a quick convergence with the smallest possible error of the reconstructed wavefront. To verify these properties, we applied the recursive algorithm on a simulated wavefront containing astigmatism of the form:

$$W(x, y) = 2.3717(x^2 - y^2)/a^2 + 6xy/a^2 \tag{4.49}$$

over a square aperture of area $4a^2$. For $a = 1$ and a sampling $N = 4$, the wavefront phase is (see Fig. 4.56a):

$$W = \begin{pmatrix} 6.000 & -0.108 & -4.108 & -6.000 \\ 4.108 & 0.667 & -0.667 & 0.108 \\ 0.108 & -0.667 & 0.667 & 4.108 \\ -6.000 & -4.108 & -0.108 & 6.000 \end{pmatrix}$$
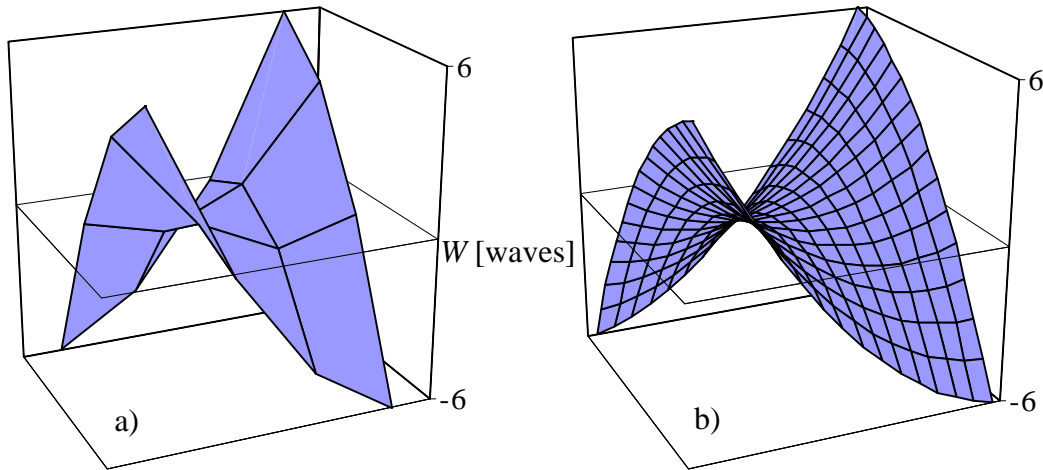
Fig. 4.56: Simulated wavefront containing astigmatism: $W(x,y) = 2.3717(x^2 - y^2)/a^2 + 6xy/a^2$. Over square aperture of area $4a^2$, where $a = 1$, the phase ranged ± 6 waves. Sampling density $N = 4$ (a) and $N = 16$ (b) are compared.

The same wavefront for a sampling $N = 8$:

$$W = \begin{pmatrix} 6.000 & 3.124 & 0.635 & -1.466 & -3.180 & -4.508 & -5.447 & -6.000 \\ 5.447 & 3.061 & 1.062 & -0.549 & -1.774 & -2.611 & -3.061 & -3.124 \\ 4.508 & 2.611 & 1.102 & -0.020 & -0.755 & -1.102 & -1.062 & -0.635 \\ 3.180 & 1.774 & 0.755 & 0.122 & -0.122 & 0.020 & 0.549 & 1.466 \\ 1.466 & 0.549 & 0.020 & -0.122 & 0.122 & 0.755 & 1.774 & 3.180 \\ -0.635 & -1.062 & -1.102 & -0.755 & -0.020 & 1.102 & 2.611 & 4.508 \\ -3.124 & -3.061 & -2.611 & -1.774 & -0.549 & 1.062 & 3.061 & 5.447 \\ -6.000 & -5.447 & -4.508 & -3.180 & -1.466 & 0.635 & 3.124 & 6.000 \end{pmatrix}$$

The slope measurements were generated from the analytical derivatives of a simulated wavefront. The reconstructed wavefront was compared with the simulated one and an rms error of the wavefront reconstruction was calculated.

The results are summarised in Table 4.6. The algorithm based on the Gauss-Seidel method converged in approximately $2N^2$ iterations and left zero residual error. We proved that the reconstruction algorithm is precise and converges quickly.

Table 4.6: rms wavefront reconstruction error as a function of number of iterations and of number of sampling points N.

Number of iterations	rms error [waves]	N
4	0.45734	
8	0.45729	4
16	0.00040	
32	3.81×10^{-8}	
64	0	
128	0	
256	0	
512	0	
1024	0	
4	0.873904	
8	0.690392	8
16	0.391860	
32	0.028612	
64	7.96×10^{-5}	
128	6.12×10^{-10}	
256	0	
512	0	
1024	0	
4	1.321239	
8	0.779426	16
16	0.623297	
32	0.342339	
64	0.052533	
128	0.000548	
256	5.91×10^{-8}	
512	2.46×10^{-15}	
1024	0	

We installed the experimental set up (see Fig. 4.57) on the optical bench and aligned the sensor, following the procedure described above. To verify that the sensor measures correctly a wavefront phase, we performed the following procedure. We measured a wavefront from a thin glass prototype of the LHCb RICH 2 mirror. Parameters of the hexagonal mirror were: $R = 8$ m, diagonal 502 mm, thickness 4.5 mm. The mirror image and the focused microlens array are displayed in Fig. 4.48. We used a microlens array with pitch $D = 400$ μm and focal length $f = 10.7$ mm (item A4 in Table 4.5). We tried to reconstruct the mirror reflecting surface over a square aperture 240×240 mm^2 (Fig. 4.58a), which represented $N = 20$. The detected sampling and reference spots are shown in Fig. 4.49. To reduce a random noise, the
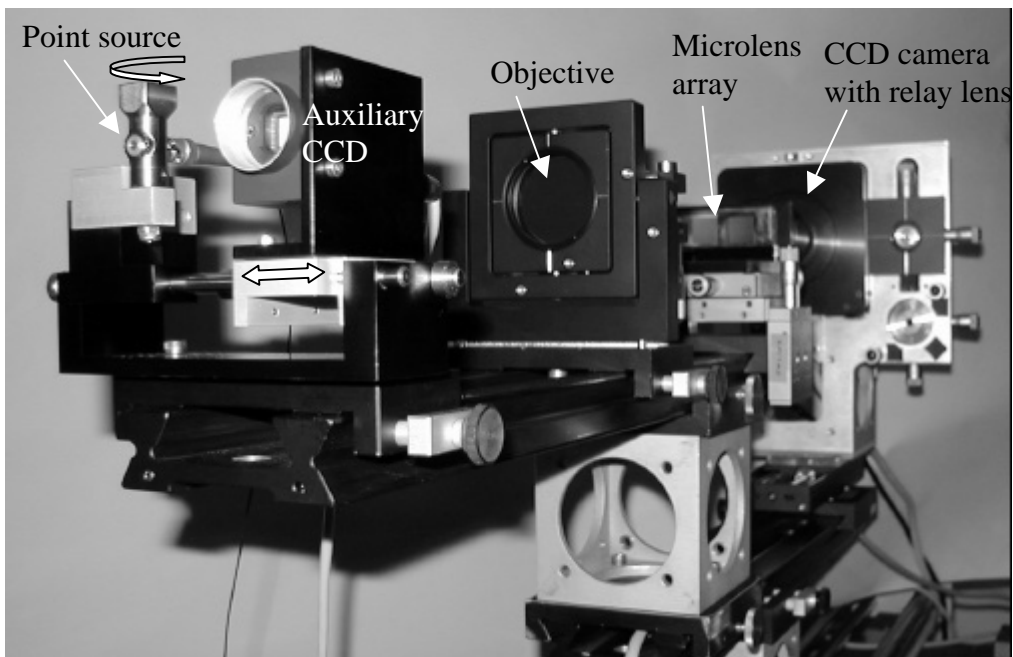
Fig. 4.57:Shack-Hartmann sensor. The point source can be turned 180 ° to the reference position. Then the auxiliary CCD, used for spot image centering, moves out of the beam.

CCD integrated 10 images over period of 5 seconds. Then we changed the position of the mirror on the three-point holder, rotating it 180 ° around its optical axis, see Fig. 4.58b. We measured again the wavefront of the 'upside down' mirror and reconstructed the mirror reflecting surface over the same aperture. Knowing that the influence of the three-point holder on the mirror reflecting surface geometry was small (see Sect. 4.2.5.1), we should get a similar but rotated topography.
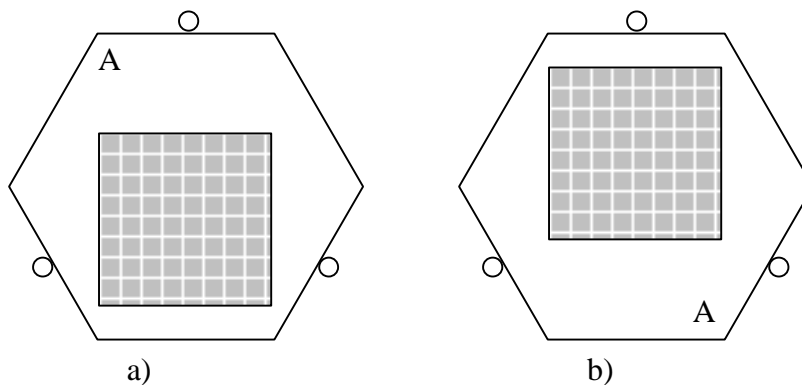
Fig. 4.58: Measurement of a hexagonal glass mirror prototype in (a) first position, (b) second position, rotated 180 °. The indicated measured square aperture corresponds to the same part of the mirror surface.

The obtained result is presented in Fig. 4.59. After rotating the second chart 180 °, the results evidently represent the same topography. Small differences inside 2 % of the corresponding values can be caused by a weak influence of the mirror holder. Considering that we used only a cheap microlens array sampler with lower
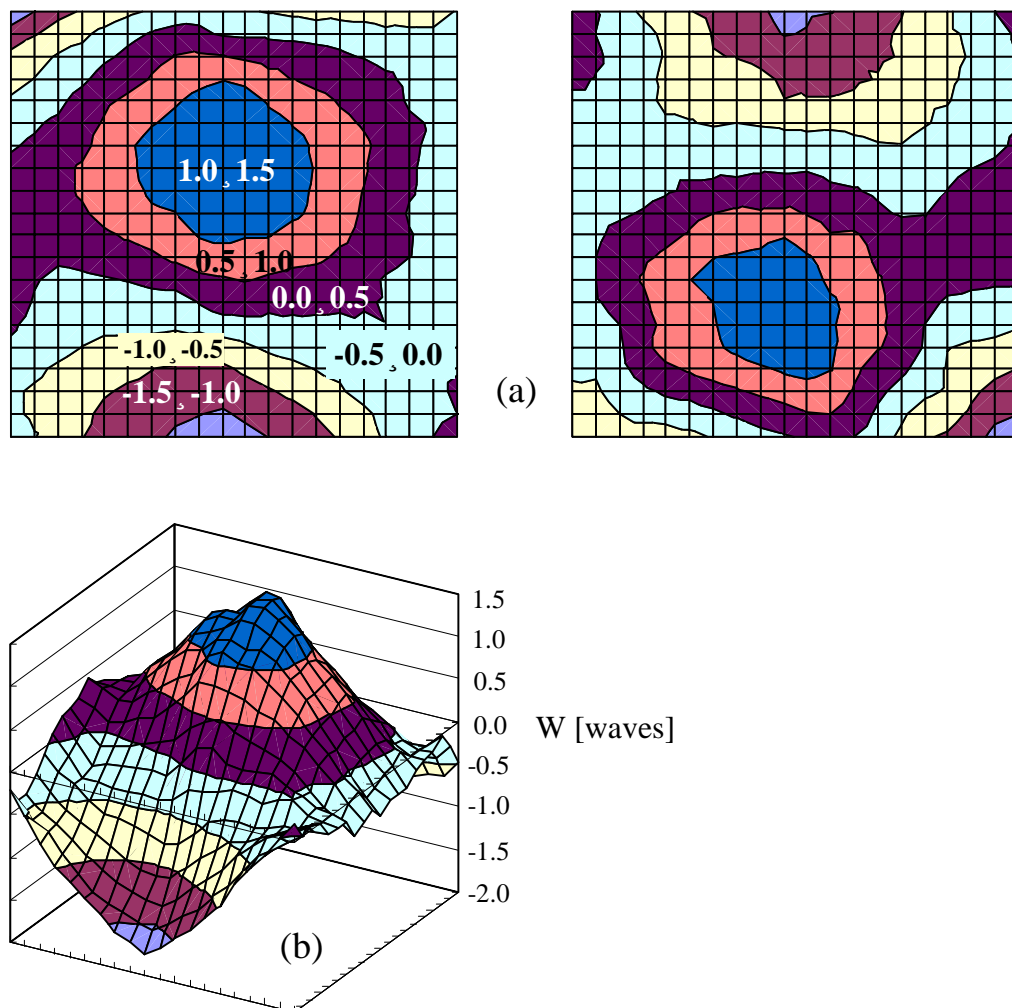
Fig. 4.59: Results of measurement of a hexagonal glass mirror prototype. (a): Identical square area of the mirror surface was measured and reconstructed in two mirror positions. The second position (right) was set up by rotating the mirror 180 ° around its optical axis. (b): Reconstructed mirror surface shown in 3-D plot.

quality and that the measurement conditions were not optimised, we demonstrated that the measurement method and device were functional and successfully working. To calibrate the sensor and to determine its resolution, precision and reproducibility, we will need a comparative measurement performed on a precise and well calibrated interferometer. We aim to continue in the development of the sensor and to prepare a fully operational device. The sensor could then contribute to a better understanding of the processes that cause mirror deformations, and to the finding of boundaries in size and thickness for large and light mirrors. It could be used to study their long-term stability, to find optimal geometry of an interface between the mirror and the mirror adjustable mount, and to detect eventual technological problems in the mirror production.

4.2.6   Tested substrates and experimental results

We have tested over forty RICH mirror prototypes for both the LHCb and COMPASS RICH detectors. Based on the obtained results, a feedback to the mirror manufacturers was provided. The first prototypes were mostly not satisfying, but the later ones were good and they can give us an idea of the achievable parameters. We also tested and qualified all 126 final COMPASS RICH 1 substrates. This was a significant sample of mirror production, on which we have obtained new experience.

4.2.6.1 Mirror prototypes

Measurement with the 8-bit set up

Results on the average geometrical quality together with basic mirror parameters are presented in Table 4.7. All these results were obtained by means of the set up equipped with the 8-bit CCD camera. The set up with the 16-bit CCD camera was under development. Mirrors had circular or hexagonal shape with circumference diameter from 300 to 600 mm and thickness from 6 to 50 mm. They were of simple-glass type made of Pyrex or Simax glass, apart from OMEGA mirrors [4.24], which consisted of a glass-sandwiched glass foam with total thickness of 50 mm. Radius of curvature varied from 6.6 to 10.0 m. Some of the mirror substrates were not coated. This does not affect the measurement of the geometrical quality of the substrate.

The LHCb RICH 2 requirement of $s_J = 0.03$ mrad on the mirror average geometrical quality would be fulfilled by the COMPASS prototype No. 5[8]. The thickness of this prototype was 7.5 mm, which is more than is allowed for LHCb mirrors. We obtained more significant data from the measurement of the first ten preliminary COMPASS mirrors[8] [4.23]. Hexagonal substrates with diagonal 520 mm had thickness of 7 mm and R = 6.6 m. Results on measurements of the average geometrical quality are shown in Fig. 4.60, together with results on the radius of curvature in Table 4.8. From these results we can approximately see what dispersion of values for R and for s_J we could expect in the production. The fluctuation of R was $s_R = 25$ mm, four sigmas representing 1.5 % of the R nominal value. The fluctuation of the average geometrical quality was $s_J = 0.045$ mrad. The spot images, corresponding to mirror No. 9 and mirror No. 2 are shown in Figs 4.61a and 4.61b, respectively. Evidently different characters of these two spot images correspond to different trends in the $P_D(D)$ curves. Mirror No. 4 (Fig. 4.62) had to be rejected because the parameter $D_0 = 4.02$ mm was outside the requirement. The analysis of the ten measured substrates resulted in an improvement of the manufacturing technology. Therefore, the COMPASS mirror No. 0 (Fig. 4.63), which replaced No. 4, had better quality. This mirror would be inside the LHCb RICH 2 requirement for precision and for the thickness of 6 mm.

---

[8] Developed and manufactured by IMMA Turnov, CZ.

Table 4.7: Parameters of measured mirror prototypes and mirrors.

Mirror	Shape	Coating	Diameter [mm]	Thick. [mm]	R^* [m]	D_0 [mm]	σ_ϑ [mrad]
COMPASS proto 1	Hex.	No	520	7	6.0	1.95	0.040
COMPASS proto 2	Circ.	No	600	8	6.6	2.55	0.048
COMPASS proto 3	Circ.	No	600	8	6.6	-	-
COMPASS proto 4	Hex.	No	540	8	6.6	2.12	0.040
COMPASS proto 5	Hex.	No	540	7.5	6.6	1.44	0.027
COMPASS 1	Hex.	No	520	7	6.6	2.22	0.042
COMPASS 2	Hex.	No	520	7	6.6	2.91	0.055
COMPASS 3	Hex.	No	520	7	6.6	2.39	0.045
COMPASS 4	Hex.	No	520	7	6.6	4.02	0.076
COMPASS 5	Hex.	No	520	7	6.6	1.79	0.034
COMPASS 6	Hex.	No	520	7	6.6	2.56	0.048
COMPASS 7	Hex.	No	520	7	6.6	2.65	0.050
COMPASS 8	Hex.	No	520	7	6.6	2.82	0.053
COMPASS 9	Hex.	No	520	7	6.6	1.71	0.032
COMPASS 10	Hex.	No	520	7	6.6	2.31	0.044
COMPASS 0	Hex.	No	520	6	6.6	1.39	0.026
LHCb proto 1	Circ.	No	340	8.5	7.8	2.46	0.039
LHCb proto 2	Circ.	No	400	7.5	7.8	3.40	0.054
LHCb proto 3	Circ.	Yes	340	7	7.8	-	-
LHCb proto 4	Circ.	No	400	10	7.8	1.95	0.031
LHCb proto 5	Circ.	Yes	300	25	7.8	0.93	0.015
Best OMEGA	Hex.	Yes	430	50**	10.0	1.53	0.019

*   Nominal values

** OMEGA mirrors are sandwich type with glass-foam

Table 4.8: Results of radius of curvature R and of diameter D_0 measurements for COMPASS mirrors.

Mirror	R [mm]	D_0 [mm]	σ_ϑ [mrad]
COMPASS 1	6620	2.22	0.042
COMPASS 2	6639	2.91	0.055
COMPASS 3	6654	2.39	0.045
COMPASS 4	6607	4.02*	0.076*
COMPASS 5	6653	1.79	0.034
COMPASS 6	6660	2.56	0.048
COMPASS 7	6605	2.65	0.050
COMPASS 8	6632	2.82	0.053
COMPASS 9	6637	1.71	0.032
COMPASS 10	6583	2.31	0.044
Average	6629	2.37	0.045
rms	25	0.42	0.008

*This value was not considered in the average and rms calculations.

Table 4.9: Results of radius of curvature R and of diameter D_0 measurements for COMPASS mirror No. 0, placed each time on the mirror holder varying its edge position.

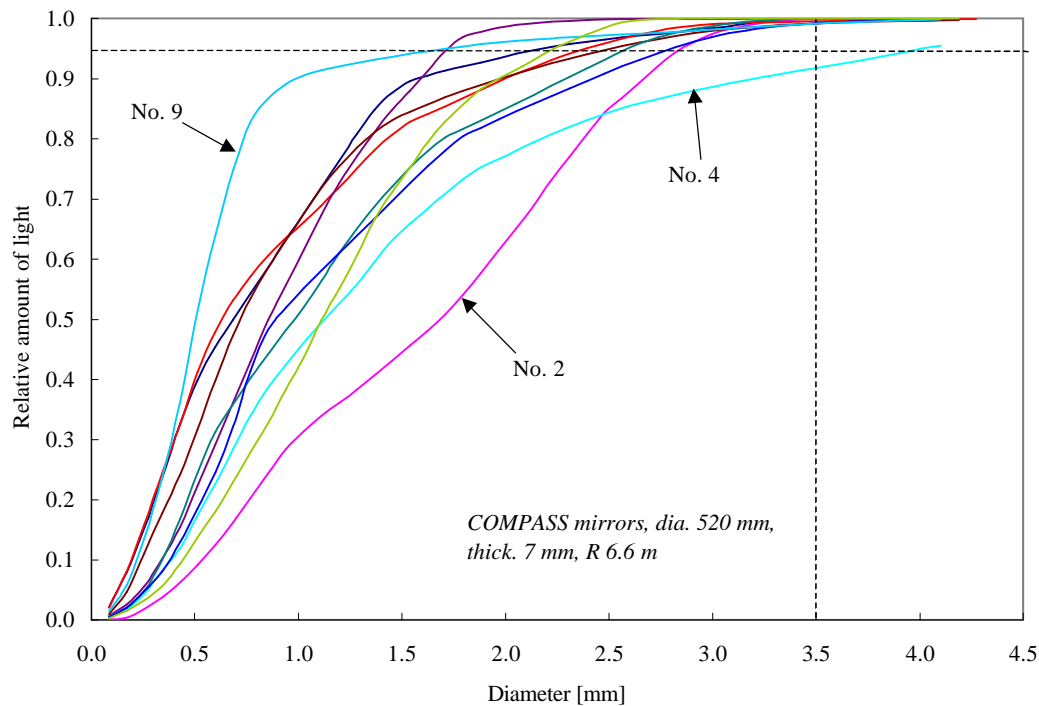| Position	R [mm]	D_0 [mm]	σ_ϑ [mrad]
a	6642	1.45	0.027
b	6645	1.20	0.023
c	6644	1.54	0.029
d	6644	1.62	0.031
e	6647	1.28	0.024
f	6647	1.20	0.023
a(2)	6642	1.45	0.027
Average	6644.43	1.39	0.026
rms	2.07	0.17	0.003

Fig. 4.60: Results from the preliminary first ten COMPASS RICH 1 mirrors. Mirror No. 4 was not accepted because $D_0 = 4.02 > 3.5$ mm. Mirrors No. 9 and No. 2 deviated from in other case quite uniform production.
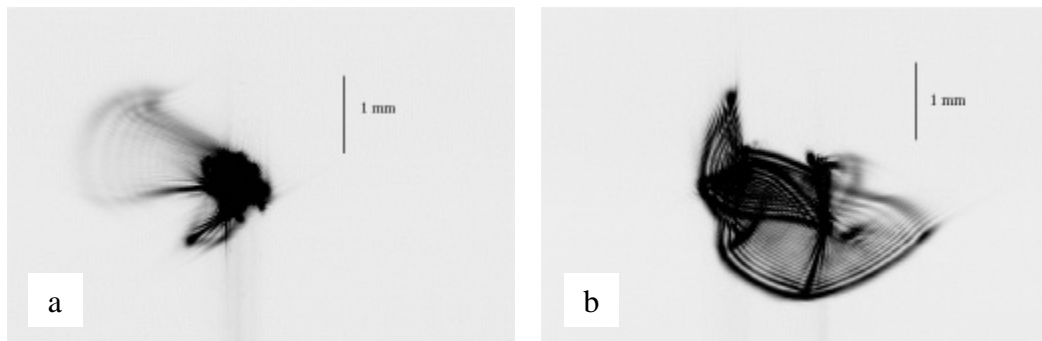

Fig. 4.61: Spot images from the COMPASS mirrors No. 9 (a) and No. 2 (b).

We tested precision of the measurement method and possible influence of the mirror holder. We used the same procedure as in the case of 16-bit set up (see Sect. 4.2.5.1). Fig. 4.64 demonstrates the procedure for determination of R. The value of R was found at different percentages of light focused in the smallest possible circle. It came out that the procedure was independent on chosen percentage. The influence of the three-point mirror holder was studied by varying position of the mirror as shown in Fig. 4.32. Corresponding results are displayed in Table 4.9 and in Fig. 4.65. For thickness of 6 mm we can see a weak influence of the mirror holder on the measurement result. Including measurement uncertainty, the rms fluctuation has value 2.1 mm for R and 0.003 mrad for s_J. A definite assessment of s_J can be only given when this is measured on the final mount. The measurement performed with

16-bit CCD (see Table 4.4) had smaller fluctuation, which is given partially by the more precise and objective measurement, and partially by a higher stability of the mirror with thickness of 7 mm.
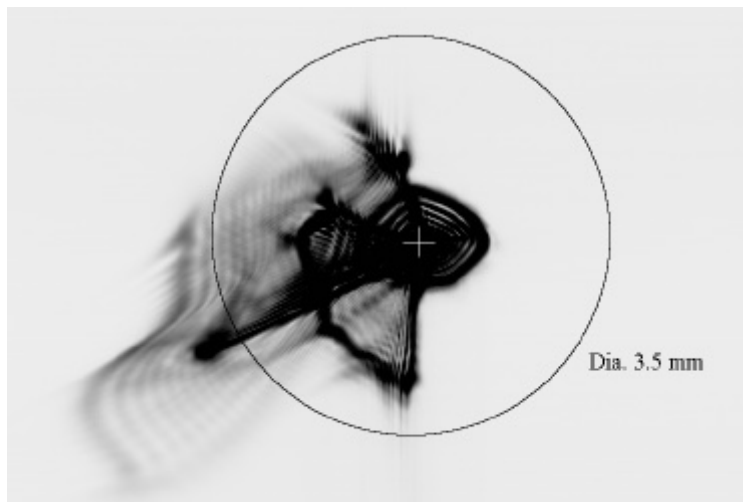

Fig. 4.62: Spot image of the COMPASS mirror No. 4. The image is overexposed to show low intensity regions.
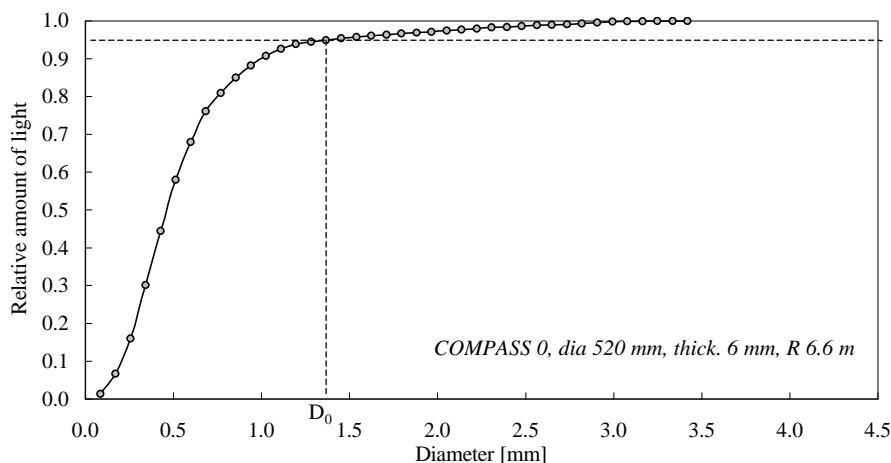

Fig. 4.63: Result from the COMPASS mirror No. 0 after improvement of the manufacture technology. Apart from better precision, the substrate was 1 mm thinner than in the case of previous ten mirrors.

We measured also prototypes of LHCb RICH 2 mirrors with radius of curvature 7.8 m (Table 4.7). All of them were circular. Prototype No. 4[9] with diameter 400 mm fulfilled the criteria for the average geometrical quality, but its thickness was 10 mm. Prototype No. 5[10] with diameter 300 mm and thickness 25 mm had average geometrical quality $s_J = 0.015$ mrad. With increasing mirror diameter and decreasing

---

[9] Developed and manufactured by IMMA Turnov, CZ.
[10] Developed and manufactured by Optical Works Ltd, UK.

mirror thickness, the geometrical quality of glass mirrors decreases rapidly. The main reason is a decreasing rigidity of the substrate, which changes with the third power of thickness, see formula (4.4).
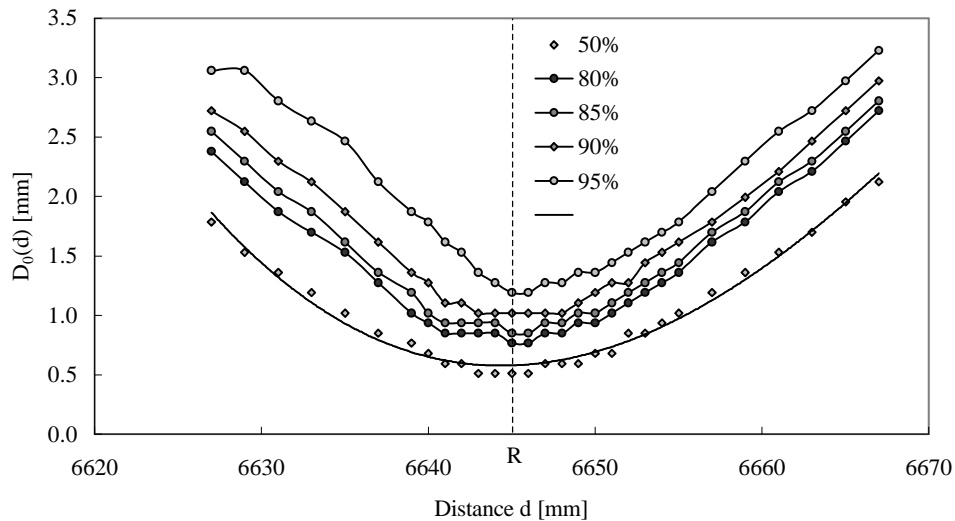
Fig. 4.64: Spot size vs. distance d for COMPASS mirror No. 0. It shows the procedure for the center of curvature finding and that the minimum spot size stays the same for different circles containing different fractions of light. For the 50% curve, a hyperbolic curve is shown, which fits well the data. This would not be the case for the 95% curve, showing that the spot is not Gaussian.

Fig. 4.65: Spot shape variation for mirror positions indicated in Fig. 4.32. The spot orientation corresponds to the orientation of the mirror on the holder, but also the spot shape changes. This proves small but not negligible influence of the holder on the spot size and shape.

Before we received the first prototypes of LHCb and COMPASS RICH mirrors, twelve former OMEGA mirrors[11] had been measured. Results are shown in Fig. 4.66. The best of them had average geometrical quality $s_J = 0.02$ mrad ($D_0 = 1.5$ mm). Three of them had more than 90 % of reflected light inside a diameter $D = 1.6$ mm. By means of optical interference and an objective, we could observe on most OMEGA mirrors deformations of the reflecting surface, see Fig. 4.67. We found correlation between the position of the deformations and the positions of the mounting points at the rear side of the mirrors.
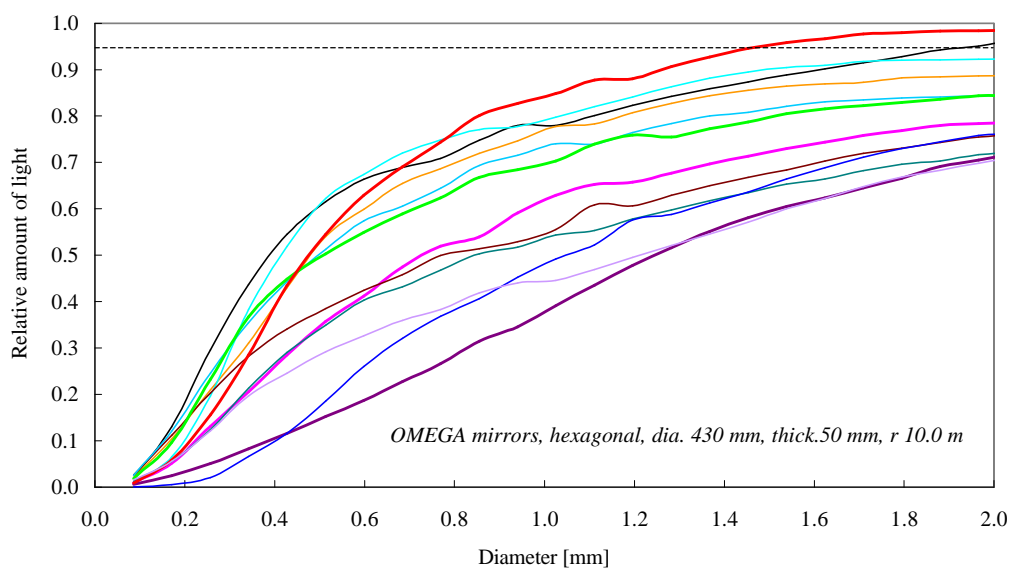

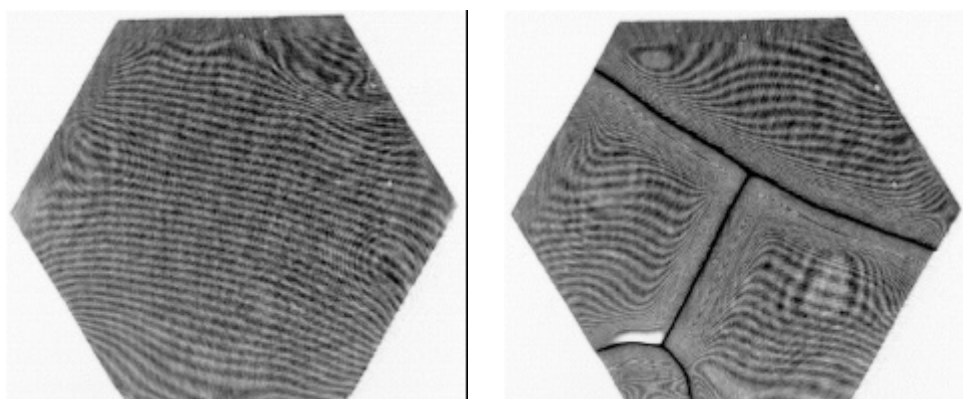**Fig. 4.66**: Light fraction inside a circle at different diameters. Results from twelve OMEGA mirrors.

Fig. 4.67: Images of OMEGA mirrors. Left: mirror No. 10 without any big fault. Right: mirror No. 5 with deformations, which correspond to position of mounts on backside.

---

[11] Developed and manufactured at CERN.

Measurement with the 16-bit set up

All the following prototypes were measured by the new set up with the 16-bit CCD. Results are summarised in Table 4.10. We tested the first five prototypes of the LHCb RICH 1 mirrors. Two full size (450×375 mm^2) rectangular substrates[12], made of Simax glass, had the required thickness of 5 mm. Radius of curvature was 2 m instead of the required 1.7 m because of available tooling. Resulting $P_D(D)$ curves are in Fig. 4.68. Both prototypes are well inside the requirement of $\mathbf{s}_J = 0.15$ mrad ($D_0 = 2$ mm) for the RICH 1 detector.

Table 4.10: Parameters of measured mirror prototypes.

Mirror	Shape	Coating	Dimens. [mm]	Thick. [mm]	R^* [m]	D_0 [mm]	σ_ϑ [mrad]
Beryllium proto 1	Circ.	No	$\varnothing$ 280	$6 \div 26$	8.0	0.85	0.013
Beryllium proto 2	Rect.	No	375×300	6	1.7	0.41	0.03
Composite proto honeycomb 1	Rect.	Yes	460×350	10	0.9	~ 4	~ 0.6
Composite proto honeycomb 2	Rect.	No	460×380	13	1.7	~ 4	~ 0.3
Composite proto foam 1	Hex.	No	$\varnothing$ 400	12	2.0	-	-
Composite proto foam 2	Rect.	No	450×375	12	2.0	3.26	0.2
LHCb RICH 1 proto glass 1	Rect.	No	450×375	5	2.0	1.51	0.09
LHCb RICH 1 proto glass 2	Rect.	No	450×375	5	2.0	1.27	0.08
COMPASS RICH 1 proto	Hex.	No	$\varnothing$ 520	4	6.6	1.77	0.033
LHCb RICH 1 proto	Hex.	No	$\varnothing$ 502	4.5	8.0	1.66	0.026

*   Nominal values

   Since the fraction of the radiation length is critical for LHCb RICH 1 detector, lighter types of mirrors are under development. We tested first composite prototypes from two different manufacturers. The first prototype[13] consisted of an acrylic layer (Perspex) supported by Nomex honeycomb and two layers of carbon fibres, corresponding to ~ 1 % of X_0. Rectangular substrate with dimensions 460×350 mm^2 and thickness 10 mm had $R = 90$ cm. Its weight was only ~ 400 g. The value of D_0 was only estimated, as not all reflected light was collected by the CCD. Its value was ~ 4 mm. The second prototype[12] was made of 1.5-mm thin glass layer supported by 10-mm carbon foam structure and covered by a layer of carbon fibres. The prototype

---

[12] Developed and manufactured by IMMA Turnov, CZ.
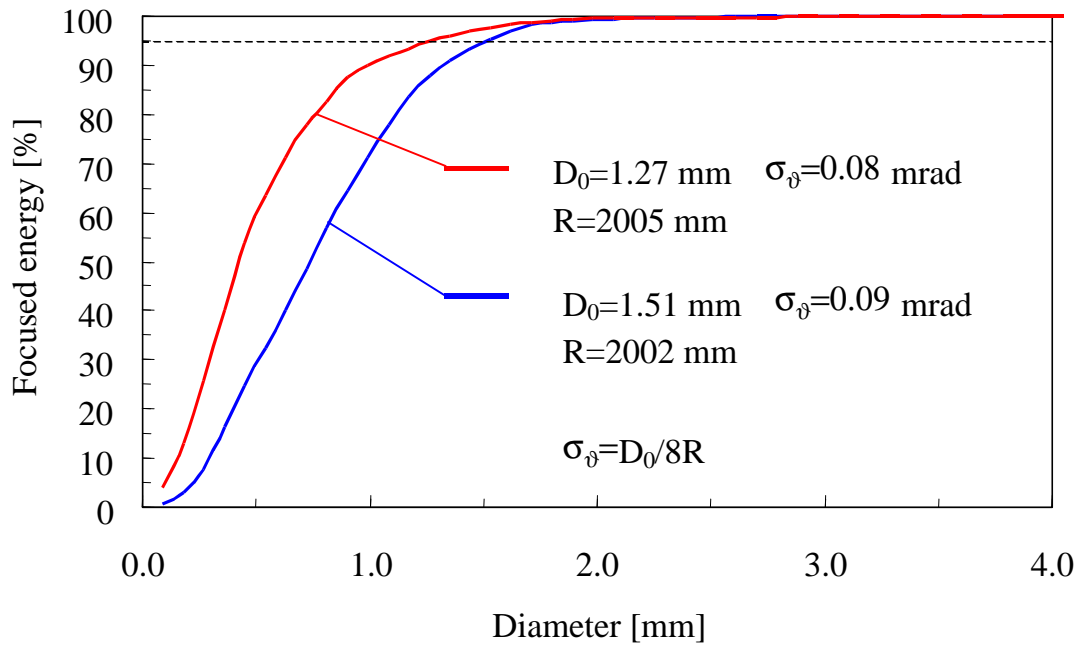[13] Developed and produced by INFN Sanita Roma, IT.

Fig. 4.68: Results from two full size (450×375 mm^2) rectangular glass prototypes of LHCb RICH 1 mirror. Thickness is 5 mm, corresponding to 3.9 5 of X_0. These prototypes fulfil the RICH 1 requirement of $s_J \leq 0.15$ mrad.

was hexagonal with diameter 400 mm. A corresponding spot and result is in Fig. 4.69. Reflected light was diffused over a big area around the spot. We provided feedback to manufacturers and received new, improved prototypes. They manifest progress in technology but until now, the desired quality was not achieved. As an example, a rectangular carbon foam prototype with dimensions 450×375 mm^2 was tested. The image spot is shown in Fig. 4.70a. Neither in this case, all the reflected light was focused on the CCD active area, but the error was negligible. We measured $D_0 = 3.26$ mm, which is still outside the requirement. We demonstrated the importance of a proper numerical aperture of the point source on this prototype. The same measurement without the microscope objective gave an incorrect result $D_0 = 2.88$ mm, see Fig. 4.70b. The development of composite mirror technologies is going on.

The first Beryllium-technique substrate[14] had a circular shape made of 5 mm of Beryllium plus 1 mm of glass and reinforced with structure of supporting 20-mm Beryllium ribs, see Fig. 4.71. It had diameter 280 mm and $R = 8$ m. The substrate represented in average 3.3 % of X_0, 2.2 % between ribs and 7.9 % at the ribs. The rigid structure provided $s_J = 0.01$ mrad as presented in Fig. 4.72. After this successful verification of the technology, a second prototype[14] was made, this time close to the LHCb RICH 1 specification. The prototype was rectangular, with dimensions 375×300 mm^2, $R = 1.7$ m, see Fig. 4.73. Thickness was 6 mm of Beryllium plus 0.3 mm of glass with no ribs, which represents only 2 % of X_0. The prototype with $s_J = 0.03$ mrad (Fig. 4.74) provided three times better quality than was required.

---

[14] Developed and manufactured by IHEP Protvino, Just Optic, Ltd. St. Petersburg and association Kompozit Korolev (all RU).
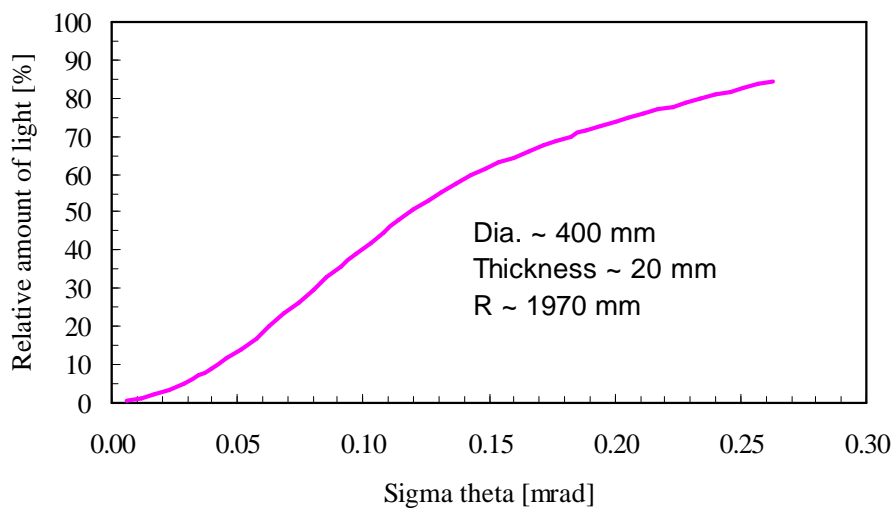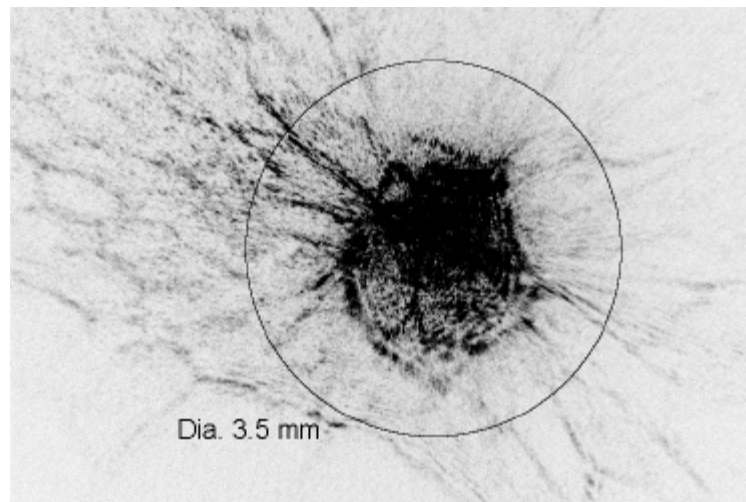
Fig. 4.69: Spot from the carbon foam hexagonal prototype of the LHCb RICH 1 mirror. A big diffusion of light mean that the angular precision was poor.

Based on the experience gained with production of 126 final COMPASS RICH 1 mirrors (see next section), two very thin glass mirror prototypes[15] were manufactured. Dimensions of the first substrate corresponded to the COMPASS RICH 1 mirror. This substrate with thickness 4.0 mm (3 % of X_0) reached $D_0 = 1.77$ mm ($s_J = 0.033$ mrad). The second prototype with geometry of the LHCb RICH 2 mirror had thickness 4.5 mm (3.5 % of X_0) and we measured $D_0 = 1.66$ mm ($s_J = 0.026$ mrad). Results for both prototypes are displayed in Fig. 4.75.

---

[15] Developed and manufactured by IMMA Turnov, CZ.
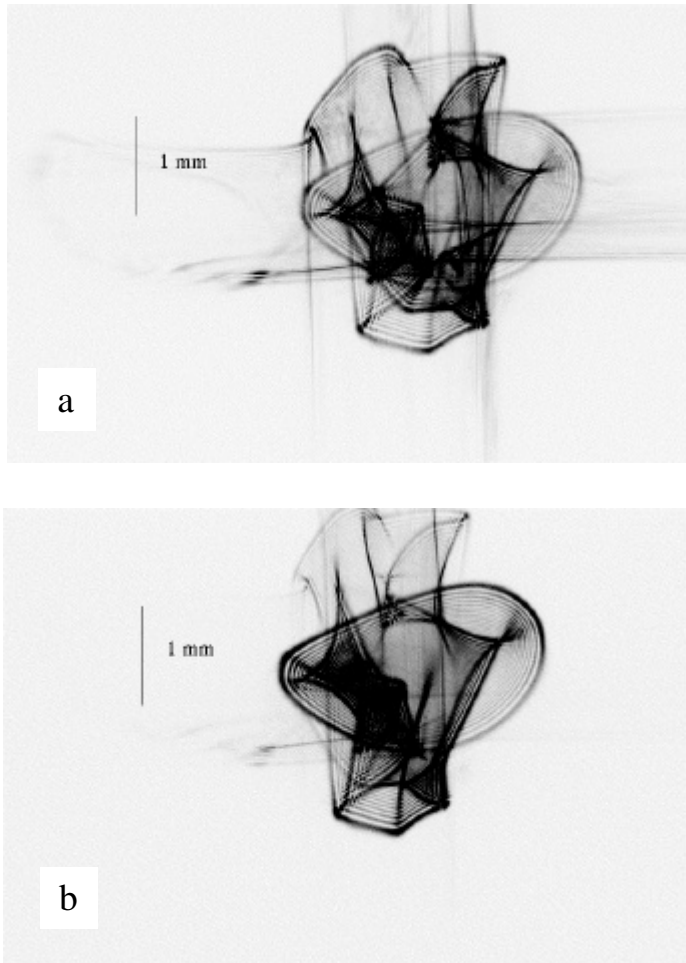
Fig. 4.70: The spot from the same composite prototype was illuminated by: (a) the point source with the microscope objective ($N.A._{ps} = 0.03$), (b) the point source with too low value of the numerical aperture ($N.A._{ps} = 0.017$).

Fig. 4.71: The first Beryllium prototype. Left: back side with a structure of reinforcing ribs. Right: front side with a polished glass layer.
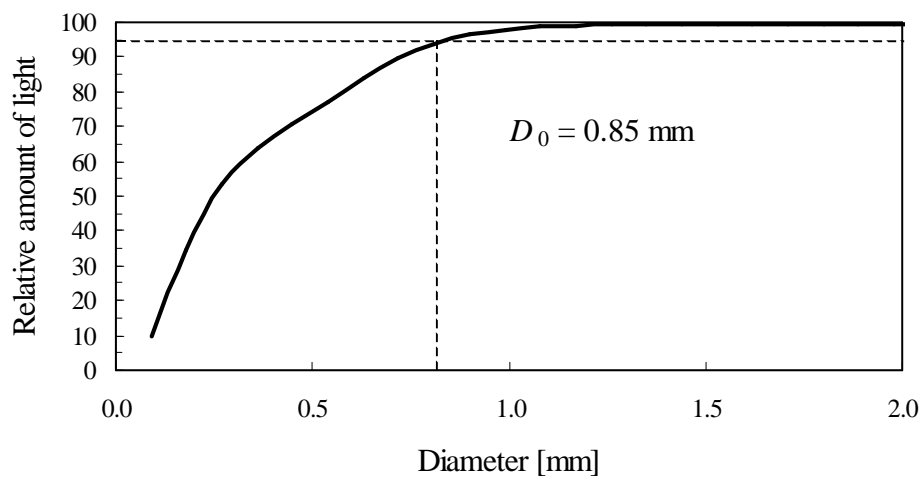
Fig. 4.72: Result from the first Beryllium prototype. Thanks to the very rigid structure, the precision of this mirror is very high: $s_J = 0.01$ mrad.
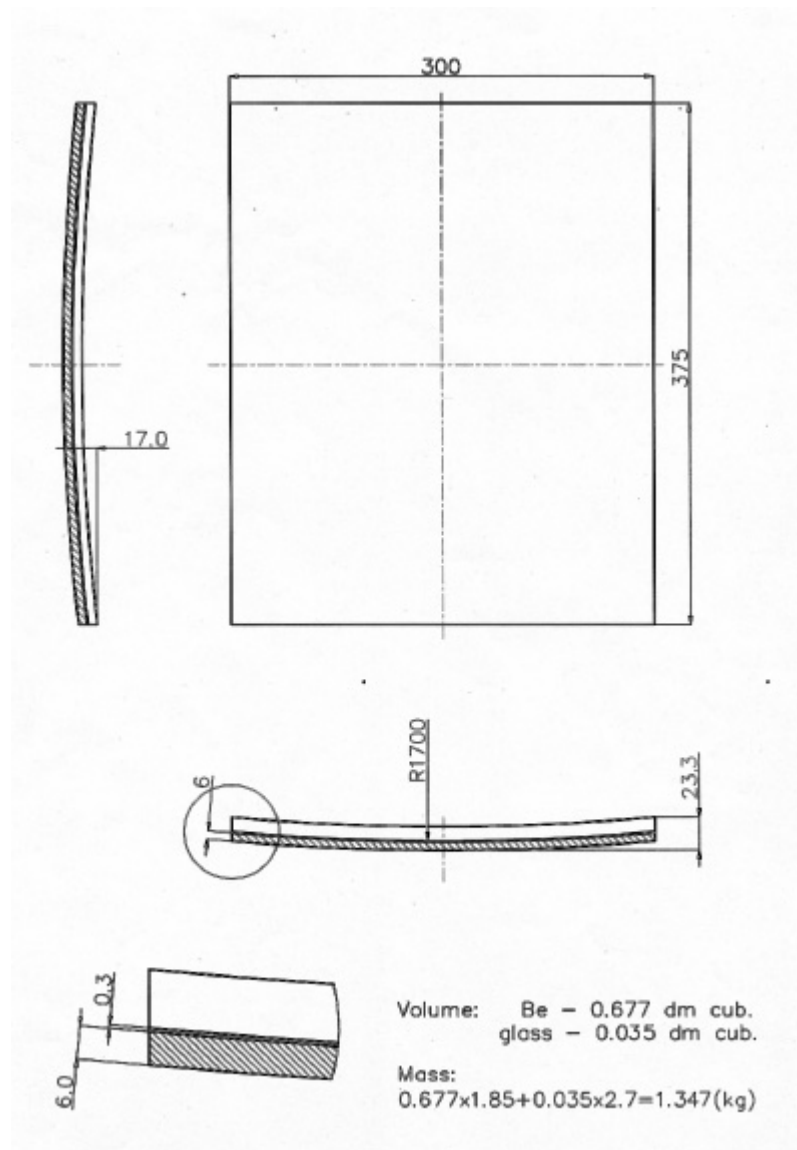
Fig. 4.73: Drawing of the second Beryllium prototype.
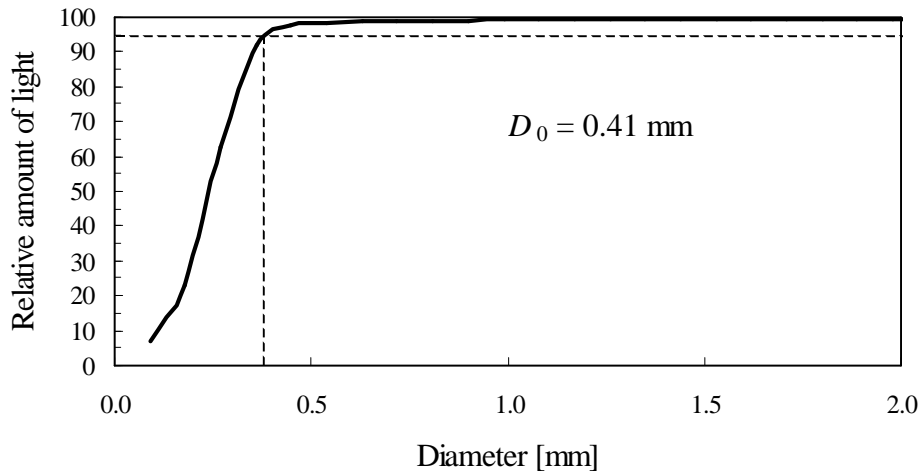
Fig. 4.74: The second Beryllium prototype features $s_J = 0.03$ mrad, which is three times better than the requirement for LHCb RICH 1.
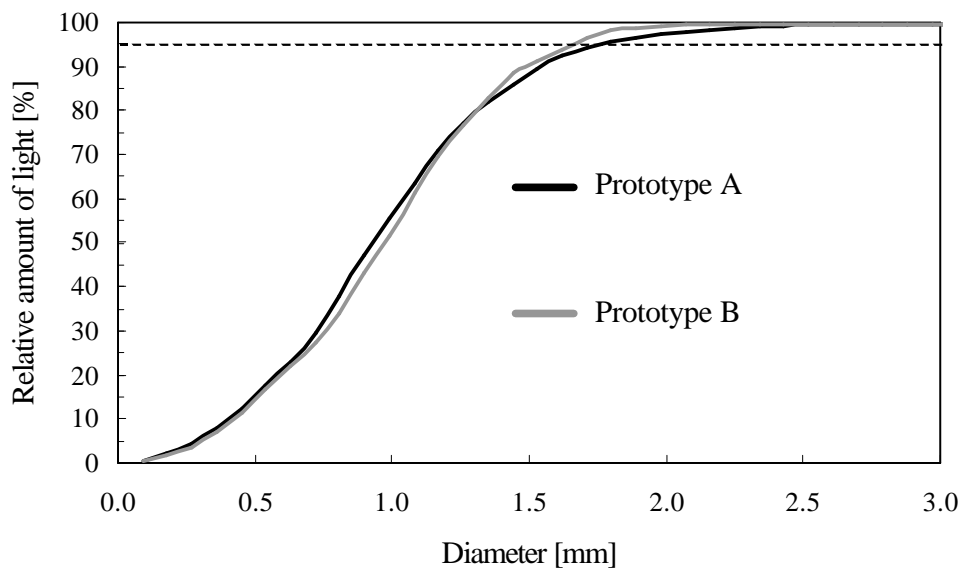
Fig. 4.75: Results from two thin glass prototypes. Prototype A: COMPASS RICH 1 geometry (diameter 520 mm, R = 6.6 m). Thickness 4 mm, $D_0 = 1.77$ mm ($s_J = 0.033$ mrad). Prototype B: LHCB RICH 2 geometry (diameter 502 mm, R = 8.0 m). Thickness 4.5 mm, $D_0 = 1.66$ mm ($s_J = 0.026$ mrad).

4.2.6.2 COMPASS RICH 1 substrates

Final COMPASS RICH 1 substrates[16] had two basic shapes: hexagonal and pentagonal. The hexagonal substrates had the same geometry as the first preliminary pieces described in the previous section. The pentagonal mirrors were of six sizes.

---

[16] Developed and manufactured by IMMA Turnov, CZ.

The substrates were made of Simax glass and represented 5.5 % of X_0. The requirements were $D_0 \leq 3.5$ mm ($s_J \leq 0.07$ mrad) and $R = (6600 \pm 60)$ mm. The substrates were being delivered in six batches, one per month. The first four batches contained exclusively hexagonal substrates (78 pieces), the last two pentagonal ones (48 pieces). Each substrate was controlled on dimensions and then measured by our automatic set up on D_0 and R [4.24]. Average value of $R \pm$ standard deviation was (6605.5 ± 23.0) mm and (6601.8 ± 20.1) mm for hexagonal and pentagonal substrates respectively. In case of D_0, it was (1.67 ± 0.51) mm and (1.74 ± 0.38) mm respectively. Fig. 4.76 demonstrates the average characteristics $P_D(D)$ with confidence interval at one sigma, showing the quality spread. Distributions of values of D_0 and R for hexagonal and pentagonal substrates are presented in Fig. 4.77. A trend of the production quality as a function of month of manufacture (Fig. 4.78) shows that with an increasing experience the quality was improving, asymptotically approaching probably a limiting value of $D_0 \sim 1$ mm for the hexagonal substrates. The trend confirms that manufacture of the pentagonal substrates is more difficult.
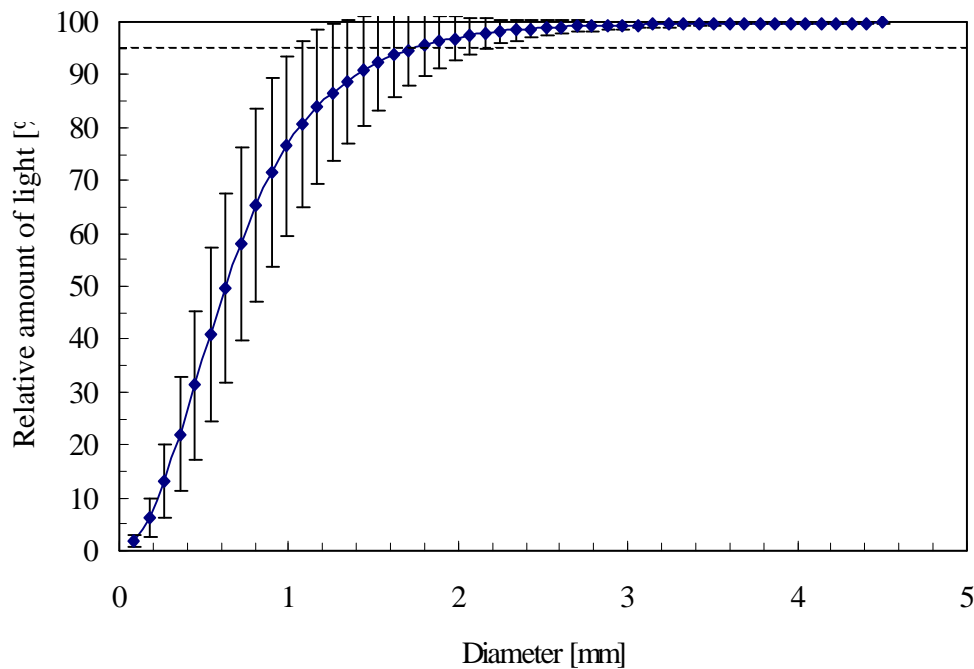
Fig. 4.76: Averaged curve from spot measurements on 78 glass hexagonal mirrors (COMPASS RICH-1) with confidence interval at 1 σ.
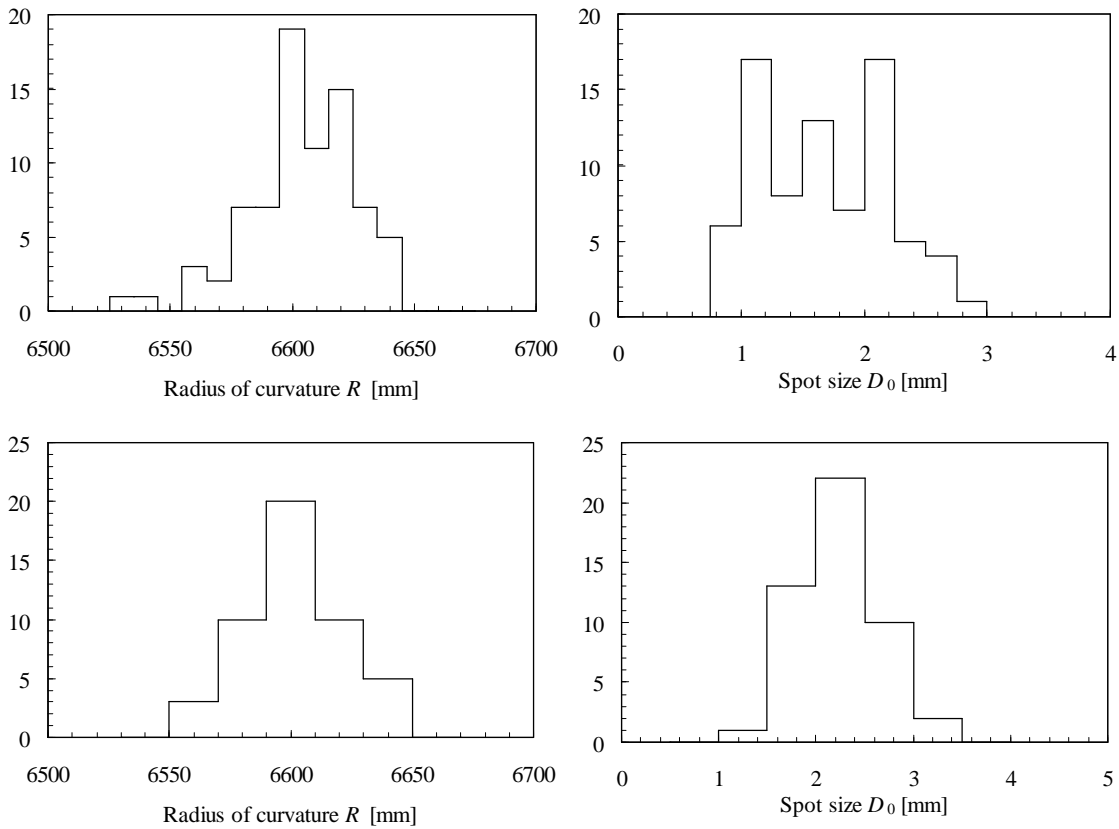
Fig. 4.77: Histograms representing distribution of values of radius of curvature and spot size for 78 hexagonal (top) and 48 pentagonal (bottom) COMPASS RICH 1 mirrors.
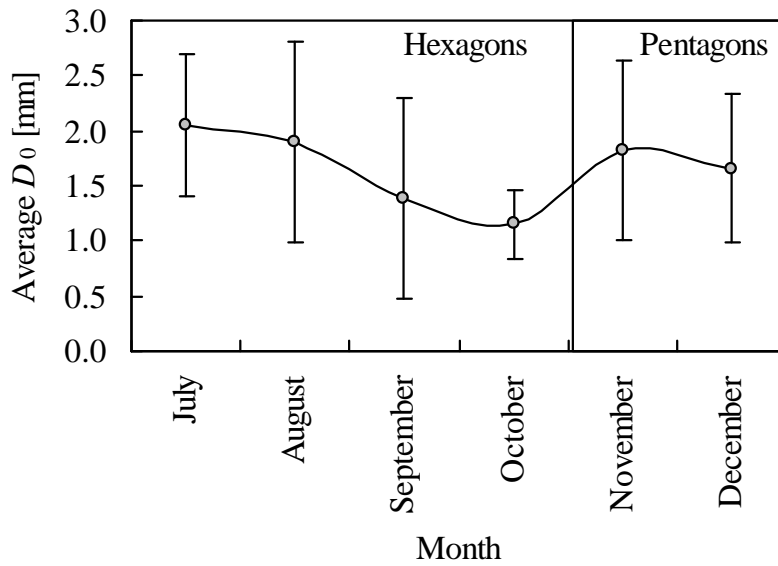
Fig. 4.78: Relation between the average quality and month of manufacture for COMPASS RICH 1 mirrors, together with confidential interval at 2 σ. Hexagonal mirrors were made in the first four, pentagonal mirrors in the last two batches.

4.2.6.3 Long-term stability of thin glass substrates

Mirrors fixed on adjustable mounts are exposed to gravity. Effect of creep could after certain time period eventually affect their reflecting surface geometry. The creep effect is imposed by static stresses in the material and its extent depends on a mirror weight, thickness, Young's Modulus of the glass and a distribution of forces in the substrate structure.

We measured long-term stability of two thin glass substrates. Both of them were COMPASS RICH 1 prototypes with the same parameters. To study an influence of the mirror mount design on the mirror substrate stability, we glued the first mirror on the final COMPASS mount. This had the interface in form of a ring with a diameter 20 mm and width 5 mm. Such a small surface induced relatively high local stresses in the glass in a vicinity of the ring. The other mirror was glued on a large conical interface with a diameter 250 mm and width 7 mm. In this case, stresses were much lower, spread over a large area. Both mirrors have been hung in the same position, as it would be inside the detector vessel.

We have measured the spot size parameter D_0 over period of nine months. The mirror fixed on the large ring has not exhibited any changes beyond the resolution of the measurement method, which was $s_{Do} = 0.02$ mm (see Table 4.4). Contrary, the mirror glued on the small ring has showed small but clear degradation of the reflecting surface quality. The spot size increased from 1.98 mm to 2.14 mm after nine months, which represents 8 %. The performed measurement indicates that the creep effect can affect the long-term stability of large and thin glass mirror substrates in a case of an inconvenient distribution of stresses in the material.

4.3   Mirror adjustable mounts

Precision of the Cherenkov ring pattern recognition and reconstruction relies, apart from the quality of mirrors, on their highly precise and stable positioning. The requirement for a high precision of the mirror positioning inside RICH detectors assumes that every mirror is fixed on the support structure by means of a fine adjustable mount. As discussed in Sect. 4.2, the mirrors are usually made of glass and have hexagonal shape with an area of order of 0.1 m^2. Their thickness is typically less than 7 mm, as the fraction of radiation length represented by the mirror has to be kept as low as possible. Their weight amounts to ~ 2 ÷ 3 kg. The mounts have to represent a low fraction of the radiation length as well, see Sect. 4.1.

4.3.1   Given parameters and requirements

In general, a three-dimensional object in the space has six degrees of freedom. These are three rotations and three translations. In our case, the position of the spherical mirror has to be adjusted through two rotations about axes perpendicular to the optical axis of the mirror (see Fig. 4.79). This adjustment is critical, because a small angle deviation produces over a distance of several metres a big displacement of the

reflected light. The other degrees of freedom are fixed with rough adjustments or their values are obtained by careful mechanical construction.
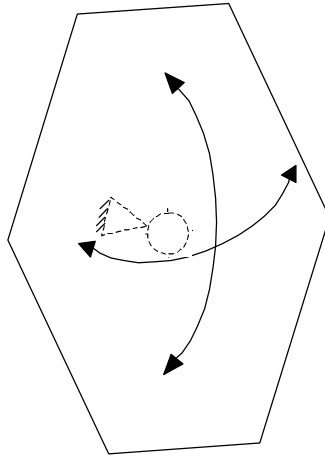

Fig. 4.79: Positions of the RICH mirrors have to be adjusted in rotations around two axes. The adjustment is provided by fine adjustable mounts. Other degrees of freedom are fixed.

The adjustments have to be fine and smooth, with a sufficient range, without hysteresis and with minimum parasitic deviations orthogonal to the adjustment direction (crosstalk). This means that backlashes and frictions in the mechanism must be minimised. To make the adjustment as simple as possible, the adjustment characteristics should be linear. The mount together with its mechanical support has to attenuate mechanical vibrations transferred from engines, vacuum pumps and other sources.

The requirement for a high resolution of the RICH detector means that each single spherical mirror has to be precisely directed to the common focal point at the photodetector plane. The value of the required positioning angular precision s_p was set to $s_p = s_{comp} = 0.03$ mrad for the LHCb RICH 2 detector, see Sect. 4.1. It is necessary not only to adjust the tilt of all mirrors to this precision, but also to conserve adjusted positions during a large fraction of the detector operational lifetime, this being several years. The situation is complicated by the fact that apart from the adjustment precision requirements, only a small amount of material, representing a low fraction of the radiation length of ∼ 3 %, can be used in the mount design. It is evident that an adjustable mount design has to fulfil quite strict mechanical criteria.

4.3.2   Mechanical principles of adjustable mounts

Because of the low weight and fraction of the radiation length requirement, it is not convenient to use a classical precision-mechanics approach. Nevertheless, basic principles stay valid. To generate a fine adjustment angular movement, the simplest way is to transform a linear movement of a screw into a rotation of another

mechanical element around a kind of pivot. Flexible joints are very convenient because they exclude backlashes. For the required precision, it is necessary to design a proper transmission. It can be based on the principle of the lever or of the wedge. Another possibility is to apply the principle of the long arm. All the mentioned principles of fine movement transmission are shown in Figs. 4.80 - 4.82.
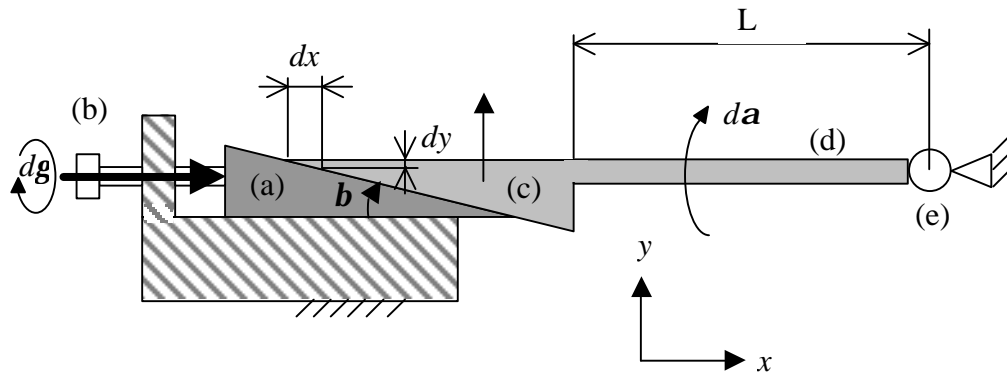
Fig. 4.80: The principle of the wedge (not to scale).

The wedge (a) (Fig. 4.80) is pushed by a screw (b) in direction x. Another wedge (c) can move only in direction y. This movement causes a rotation $d\boldsymbol{a}$ of an arm (d) around a joint (e). The joint can be replaced by a flexible element. Corresponding relations for the movement transformation are:

$$dy = dx \cdot \tan \boldsymbol{b} \qquad (4.50)$$

$$\sin d\boldsymbol{a} = \frac{dy}{L}, \qquad (4.51)$$

where the displacement $dx = s \cdot d\boldsymbol{g}$ of the wedge (a) is produced by turning the screw with pitch s by angle $d\boldsymbol{g}$. If angle $\boldsymbol{b}$ of the wedge has value $\boldsymbol{b} \leq \boldsymbol{j}$, where $\boldsymbol{j}$ is given by $\boldsymbol{j} = \arctan f$ (f is a coefficient of friction), then the system is self-locking.

The lever can be of an inverting - or first order - (Fig. 4.81a) and of a non-inverting - or second order - (Fig. 4.81b) type. The lever (a) is pushed by a screw (b) and turns around a support (c). An arm (d) then turns around a joint (e). Parts (a), (c), (d) and (e) can be connected and replaced by flexible joints. The first order- and second order- levers differ only by the sense of the resulting movement. The corresponding formulas are:

$$dy = dx \cdot \frac{b}{a} \qquad (4.52)$$

$$\sin d\boldsymbol{a} = \frac{dy}{L} \qquad (4.53)$$
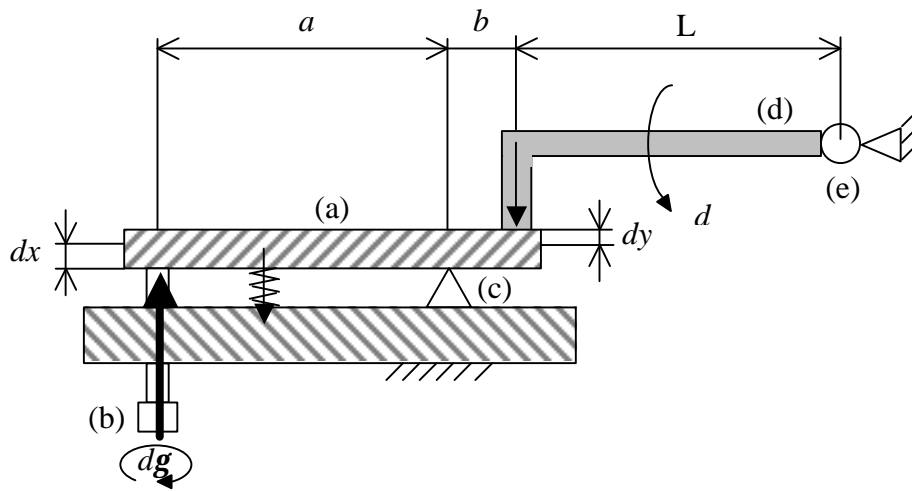
Fig. 4.81a: The inverting type lever (not to scale).
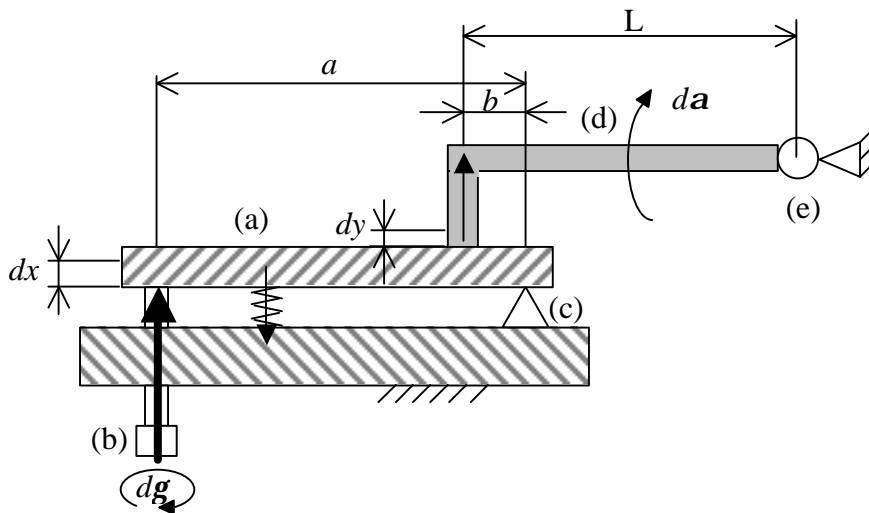
Fig. 4.81b: The non-inverting type lever (not to scale).

The principle of the long arm option (Fig. 4.82) is simple: the long arm (a) is turned around a joint (c) by movement of a screw (b). To get a fine and precise transmission, the arm has to be long and rigid. This solution is acceptable if the design offers sufficient space for long arms. The angular adjustment $d\mathbf{a}$ is given by:

$$\tan d\mathbf{a} = \frac{dx}{L} \tag{4.54}$$
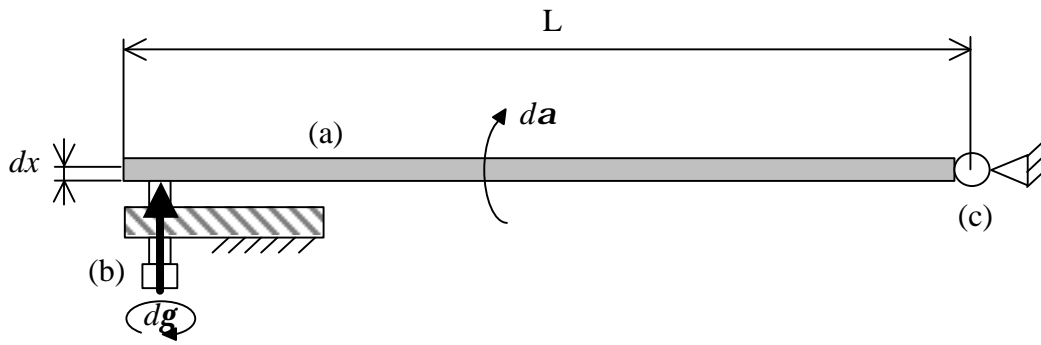
Fig. 4.82: The principle of the long arm (not to scale).

The most representative prototypes, based on the principles shown above, will be presented in Sect. 4.3.6.

4.3.3   Mechanical properties of Polycarbonate

The requirement of robust, stable mirror mounts, with a favourable material budget, resulted in a decision to use Polycarbonate (PC) as material for the basic components of the adjustable mount for the LHCb RICH 2 detector.

Polycarbonate is a thermoplastic polymer with the radiation length of $X_0 = 346$ mm. It has good mechanical properties, high resistance to impact damage, good creep resistance up to 115 $\Diamond$C and it can easily be machined. Although the mechanical properties are generally well known, it is not proven that Polycarbonate has a long-term stability that would fulfil the requirements for the mirror mount. Creep, stress relaxation and the effect of strain rate on yielding are generally much more significant to polymers than they are to metals.

The following figures show some of the long-term characteristics of Polycarbonate [4.25]. Fig. 4.83a represents the creep modulus as a function of time. The modulus decreases from 2233 MPa to 1645 MPa over 10^4 hours at 23 °C, the applied stress being 5.2 MPa. In the designed mount prototype, stresses caused by the mirror weight are approximately an order of magnitude lower. An approximate calculation was made with a mount model in form of a simple cylindrical beam of diameter D and length l as illustrated in Fig. 4.84. The bending stress in the model is given by:

$$\boldsymbol{s}_{max} = \frac{M_{b\,max}}{W_b},\qquad\qquad(4.55)$$

where the maximum moment of deflection $M_{b\,max} = F \cdot l$ and the modulus $W_b = \pi D^3/32$. For $F = 30$ N, $D = 30$ mm and $l = 50$ mm we get $\sigma_{max} \cong 0.6$ MPa. The deformation of the beam is described by formula:

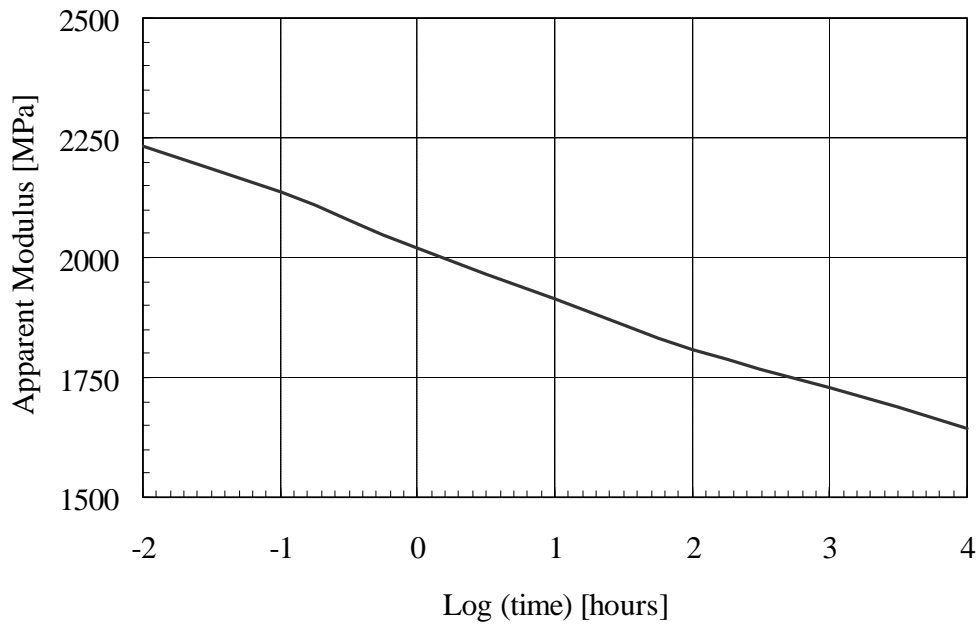**Fig. 4.83a**: Creep Modulus vs. Time at 23 °C and 5.2 MPa for Mobay Makrolon 3200 Polycarbonate. From [4.25].
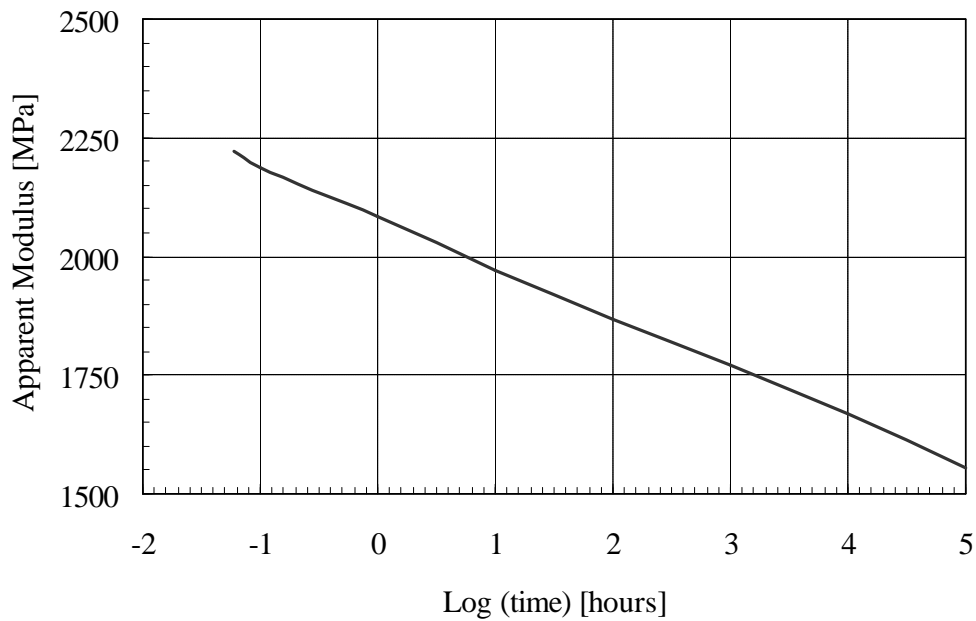

Fig. 4.83b: Creep Modulus vs. Time at 21°C and 20.6 MPa for GE Plastics Lexan Polycarbonate.

$$y(x) = \frac{F \cdot x^3}{3E \cdot I_z},$$ (4.56)

where x is a distance from the fixation point, E is Young's modulus, and modulus $I_z = \pi D^4/64$. The bending angle α is given by:

$$\tan \mathbf{a} = y' = \frac{dy}{dx} = \frac{F \cdot x^2}{E \cdot I_z}$$

(4.57)

For boundary conditions $y(0) = 0$ and $y'(0) = 0$ we get the angular displacement $\Delta\mathbf{a}(l) \cong 0.3$ mrad after 10^4 hours. This is three times worse than the requirement. However, if we take in account ten times lower bending stress and much higher rigidity of the real mount we are still within the specified limit after 10^4 hours.
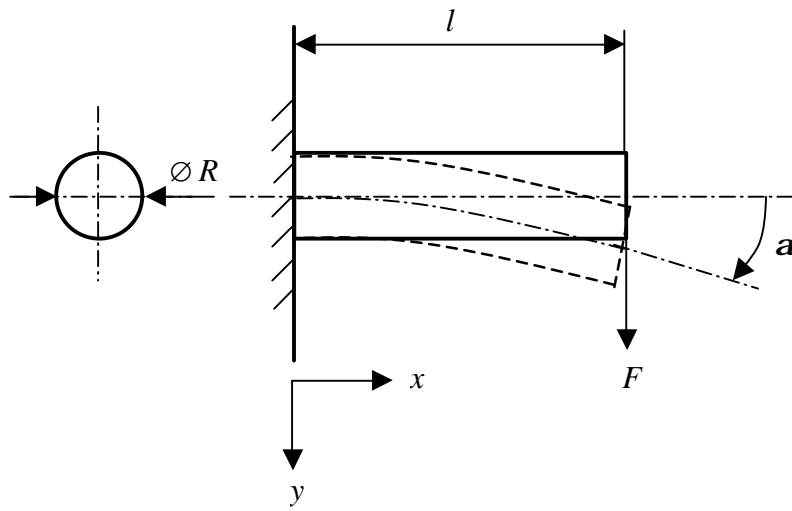
Fig. 4.84: Bending of a simple beam.

More data on Polycarbonate (Fig. 4.83b) from another brand do not show any unexpected change of the creep modulus at least up to 10^5 hours. Data for such a wide time scale are usually obtained by performing experiments at different temperatures and by synthesising the resulting curve by applying the time-temperature superposition rule [4.26].

4.3.4 Analysis of possible measurement methods

In order to provide a feedback to designers and to verify characteristics of adjustable mount prototypes, it was necessary to prepare convenient measurement facilities. Each prototype of the adjustable mount has to be measured on the adjustment range and precision, the presence of hysteresis and of crosstalk, and linearity. An ease of use and time consumption of the adjustment and transmission of vibrations are estimated too. The long-term stability should be verified experimentally as well, especially in the case of materials like Polycarbonate. We prepared set ups for measurements of these characteristics.

To determine the angular displacement of adjustable mount prototypes [4.6], the best method is to measure the corresponding transversal displacement of a laser beam reflected from a small mirror fixed on the prototype, see Fig. 4.85. Precision of the
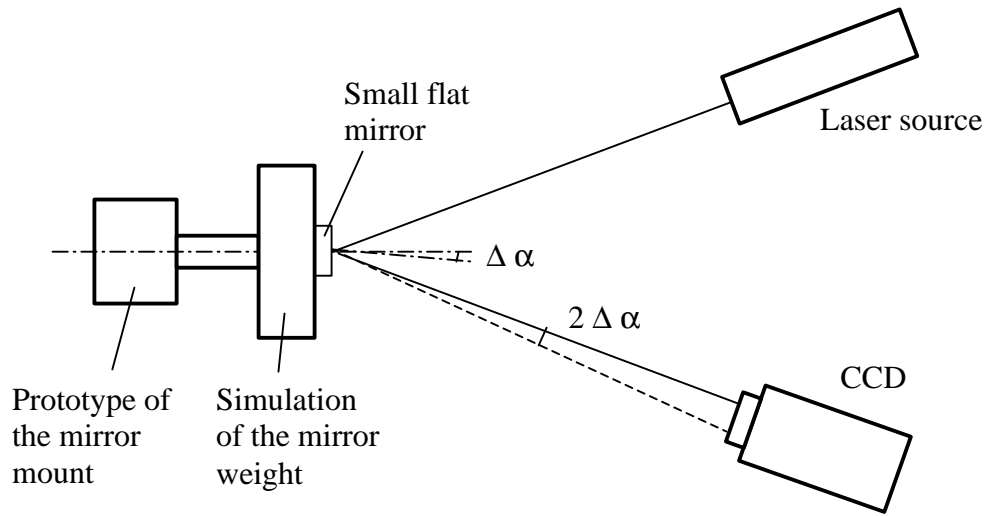
Fig. 4.85: Principle of the measurement of the mirror mount tilt. The CCD detects any angular deviation $2 \Delta \alpha$ of the laser beam reflected on the small mirror. This quantity is double of the mirror mount tilt $\Delta \alpha$.

measurement depends on resolution of the beam displacement measurement, and on the distance between the prototype and a plane of the measurement. For the measurement of angular positioning at level $s_p = 0.03$ mrad, the measurement resolution s_m should be ten times higher, which is $s_m = 3$ µrad. Such a resolution can be achieved by detection of the laser beam displacement by a CCD camera. A standard CCD with pixel size $Dx \cong 10$ µm would be placed at minimal distance L:

$$L = \frac{Dx}{2\sqrt{12}\, s_m} = \frac{1 \cdot 10^{-5}}{2\sqrt{12} \cdot 3 \cdot 10^{-6}} \cong 0.5 \ \text{m} \tag{4.58}$$

In reality, the beam-spot has always diameter bigger than pixel size. Then the spot centroid finding precision s_m is given by relation (4.33) in Sect. 4.2.5.1. For the spot with diameter D_s, a pixel size Dx, a dynamic range N of the CCD and a signal noise s_n it becomes:

$$s_m^2 = \left(\frac{Dx}{2\sqrt{p}} \right)^2 + \left(\frac{Dx^2}{\sqrt{3}p\, D_s} \right)^2 + \left(\frac{s_n}{N} \right)^2, \tag{4.59}$$

where the spot is superimposed on n pixels:

$$n = \frac{p\, D_s^2}{4\, Dx^2} \tag{4.60}$$

Angular measurement resolution is then:

$$\boldsymbol{s}_{res} = \frac{\boldsymbol{s}_m}{2L} \qquad\qquad (4.61)$$

The resolution $\boldsymbol{s}_{res}$ depends on the size of the spot, the CCD pixel size, dynamic range and noise, and the distance mount - CCD.

Other measurement principles, based on capacitive, inductive, resistive and other types of transducers, are not convenient for this measurement because their installation is more complicated and measurement resolution and reliability would be lower. In the case of the optical measurement, only a small planar mirror has to be fixed on the prototype. The set up is therefore very adaptable.

4.3.5   Measurements in the optical laboratory

We prepared two independent set ups for measurements of mount characteristics. One of them, devoted to long-term stability measurements [4.5], is installed in the underground optical laboratory described in Sect. 4.2.5. The other set up was established in a smaller optical laboratory, which is convenient only for instant measurements.

4.3.5.1 Bench for measurement of adjustment characteristics

A scheme of the set up is shown in Fig. 4.86. A beam, produced by a He-Ne laser source (a), is expanded and spatially filtered to extract the TEM_{00} mode (b). A spherical mirror with 5-metre focal length (c) then gently focuses the obtained diffraction-limited beam on a CCD (h). The spot size and intensity on the CCD can be changed by means of a diaphragm (d). Half way between the spherical mirror and the CCD, a small planar mirror (g) fixed on the mount prototype (e) is placed. The prototype is loaded with a weight (i) that simulates the weight of the corresponding RICH mirror. Tilts, produced by the prototype adjustment, are measured by detection of beam-spot position on the CCD.

To make the set up adaptable, the measurement procedure is manual. In addition, a low expected number of measurements per year could not justify automation of the set up. The tilt of the prototype is adjusted in regular steps (usually by $\pi/4$ or $\pi/8$ rad turn of the adjustment screw). After every step, the CCD image of the beam-spot is acquired. Dimensions of the CCD active area determine the range of the measurement. For ½ inch CCD with dimensions 8.3×6.4 mm^2 the angular range is:

$$\boldsymbol{d} = \frac{w}{2L} = \frac{8.3 \cdot 10^{-3}}{2 \cdot 2.2} \cong 2 \;\; \mathrm{mrad} \;, \qquad\qquad (4.62)$$

where w is a width of the CCD active area. Actually it is even less because the whole beam-spot has always to be inside the CCD active area. In order to increase the measurement range, the CCD position is changed every few steps, before the beam-

Fig. 4.86: Scheme of the set-up: (a) He-Ne laser, (b) beam expander and spatial filter, (c) 5 m focal length mirror, (d) diaphragm, (e) mount prototype, (f) attenuator, (g) plane mirror, (h) CCD, (i) weight.

spot leaves the CCD active area. The position of the beam-spot has to be consequently transformed into a global co-ordinate system, given by an initial position of the CCD, see Fig. 4.87. A movable holder of the CCD was incorporated. It allows measurement of the beam-spot displacement in arbitrary direction and the range can be extended according to specific needs.
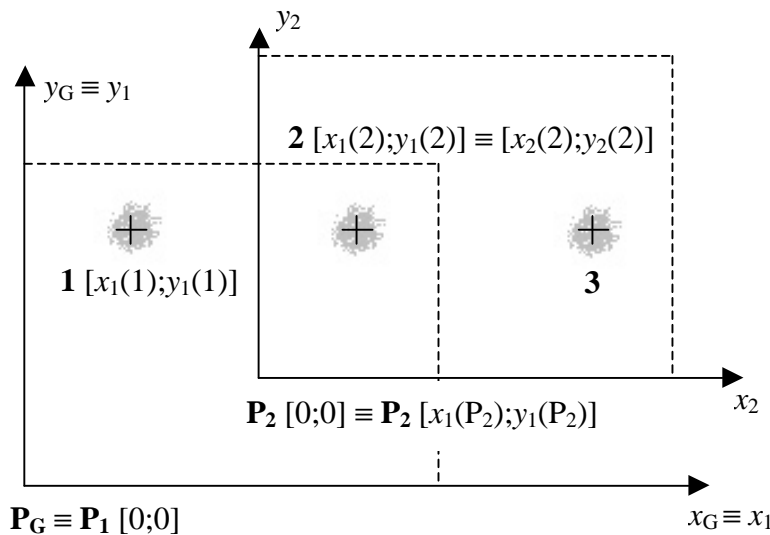
Fig. 4.87: Transformation of local beam-spot co-ordinates to the global co-ordinate system (G). Global co-ordinates of an arbitrary point I $[x_2(I);y_2(I)]$ would be: $x_G(I) = x_1(I) = x_2(I) + x_1(2) - x_2(2)$
$$y_G(I) = y_1(I) = y_2(I) + y_1(2) - y_2(2).$$

The data processing is automatic. We prepared a program to process a sequence of CCD images. For each image, the program first finds the rough location of the spot, then calculates its centre of gravity. The spot has typically diameter of 0.5 mm. For an 8-bit CCD camera with a pixel size $Dx = 11$ μm, placed at $L = 2.2$ m, the

resolution of the spot position measurement is, according to formula (4.61), $s_{res} \cong 1$ μrad. This theoretical value is achievable if errors introduced by vibrations, air turbulence, interaction during adjustment and other outside factors are reduced to acceptable values.

4.3.5.2 Bench for measurement of long-term stability

The principle of the set up is similar to the set up for characterisation of adjustable mounts, but the mirror mount is adjusted before beginning of the measurement and then it stays locked throughout the whole measurement period.

Ambient temperature changes have the strongest effect on the mechanical behaviour of the mount. The temperature monitoring has to be incorporated, allowing checking possible temperature influence on the mount deviations. Temperature changes affect also the stability of the set up itself. The stability of the mount should be measured independent of the set up. Although the optical table, which was used for the set up for measurement of adjustment characteristics, is rather stable it came out from our initial experiments that it is not stable enough for precise long-term stability. We were obliged to install a robust granite bench in the underground optical laboratory. This was essential but not sufficient. Because the mount has to be very stable, even carefully chosen opto-mechanical components of the set up contributed to the measurement result too strongly. The measured signal was overwhelmed by noise caused by the set up. We decided to exclude influence of the set up by making the measurement differential.
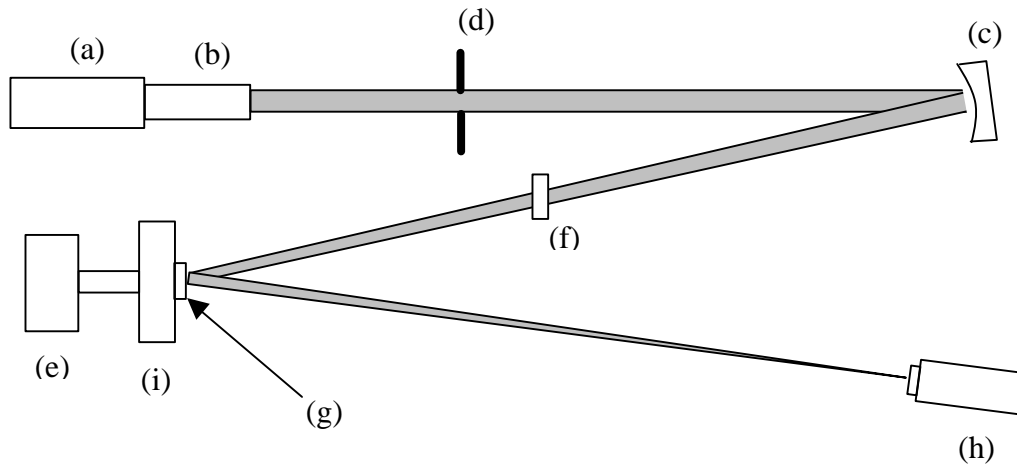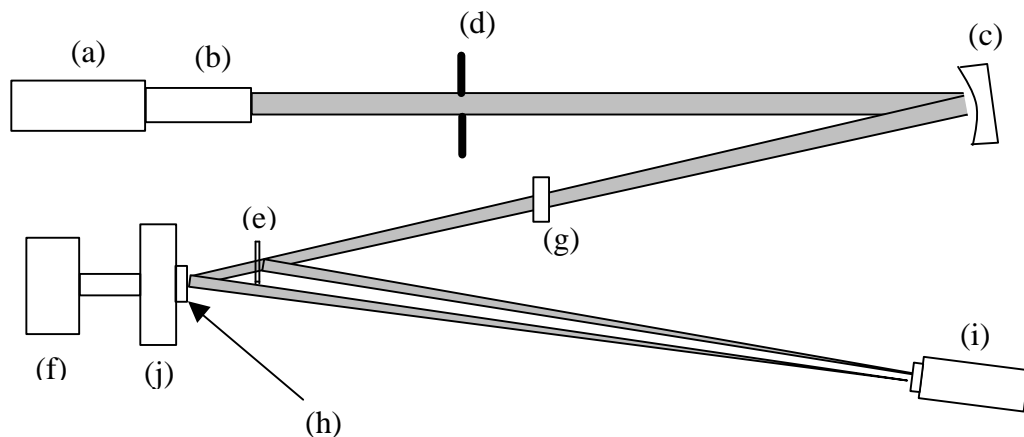

Fig. 4.88: Scheme of the set-up: (a) He-Ne laser, (b) beam expander and spatial filter, (c) 5 m focal length mirror, (d) diaphragm, (e) beam splitter, (f) mount prototype, (g) attenuator, (h) plane mirror, (i) CCD, (j) weight.

The set up is shown in Fig. 4.88. A 3.5 mW He-Ne laser (a) produces a beam, which is first expanded to diameter ~ 20 mm and spatially filtered to extract only the TEM_{00} transverse mode (b). Such a diffraction-limited beam is then gently focused

on a CCD by using a spherical mirror with 5-m focal length (c). Its spot size and intensity on the CCD can be changed by means of a diaphragm (d) inserted between the beam expander and the mirror (c). Half way between this mirror and the CCD, a beam splitter (e) is inserted. The reflected beam (called reference beam) is directed onto the CCD (i). The transmitted beam instead is reflected from a planar mirror (h) mounted on the support prototype (f), loaded with the weight (j), and again directed onto the CCD (sampling beam).

Tilt in the prototype support is probed by measuring the relative position between reference and sampling beam-spots, where the reference beam provides differential compensation for all mechanical movements related to the environment. This includes effects like thermal expansions, stress relaxation, vibrations and laser instabilities. Fig. 4.89a shows the two beam spots on the CCD and Fig. 4.89b displays their diffraction limited profile. For this measurement, the FWHM of the beam profile at the CCD plane was 0.39 mm. For any angle deviation α of the measured mount, the reflected beam direction changes by 2$\boldsymbol{a}$. Therefore, the horizontal and vertical angular deviations (tilt) are given by:

$$\alpha_h = \frac{x_s - x_r}{2L} \quad \text{and} \quad \alpha_v = \frac{y_s - y_r}{2L} \ , \tag{4.63}$$

where $x_{s,r}$ and $y_{s,r}$ are the horizontal (vertical) co-ordinates of the sample and reference beam, respectively, and L is the distance between the planar mirror and the CCD window. The resolution of the measurement is given by formula (4.61) and the measurement range is:

$$\boldsymbol{a}_{Rh} = \frac{w}{2L} \quad \text{and} \quad \boldsymbol{a}_{Rv} = \frac{h}{2L}, \tag{4.64}$$

where $\boldsymbol{a}_{Rh}$ ($\boldsymbol{a}_{Rv}$) is an angular range in horizontal (vertical) co-ordinate and w (h) is a width (height) of the CCD active area.

It is worth noting that the beam splitter (e) has to be more stable than the prototype mount (f). This is not trivial to achieve, as the expected tilts of (f) are already very small. It has been solved by employing the smallest possible beam splitter on a robust and short steel support. We used a standard CCD camera[17] with a 6.4×4.8 mm^2 active area and an 8.5×8.5 μm^2 pixel size. For the distance $L = 2.3$ m between the beam splitter and the CCD window, the measurement resolution $\boldsymbol{s}_{\text{res}}$ should be ≤ 1 μrad for a range $\boldsymbol{a}_{Rv}$ of 1 mrad. Vibration transmission is attenuated by rubber suspension and foam dampers.

The measurement is fully automatic and is controlled by means of a personal computer. We used a frame grabber[18] for image data capturing and a DAQ card[19] for temperature monitoring. The status of the measurement can be checked through the

---

[17] model Philips FTM800
[18] model Scion LG-3
[19] model NI PCI-1200

computer network. Two program macros written in Scion Image programming environment were especially developed for this purpose. One of them controls image data capturing and the other one performs data analysis. Every hour, the frame grabber integrates ten images during five seconds and the resulting image is saved on a disk. Then the image is processed as follows. Every image contains two light spots transmitted by the sampling and reference beams (see Fig. 4.89). The program first finds rough locations of both spots, then calculates their centres of gravity. The precision on spot positions is limited by existence of interference fringes. It was confirmed experimentally to be 5 μrad or better. Finally, absolute and relative horizontal and vertical positions are calculated. Three temperature probes are read and the averaged value is written to a file every minute.
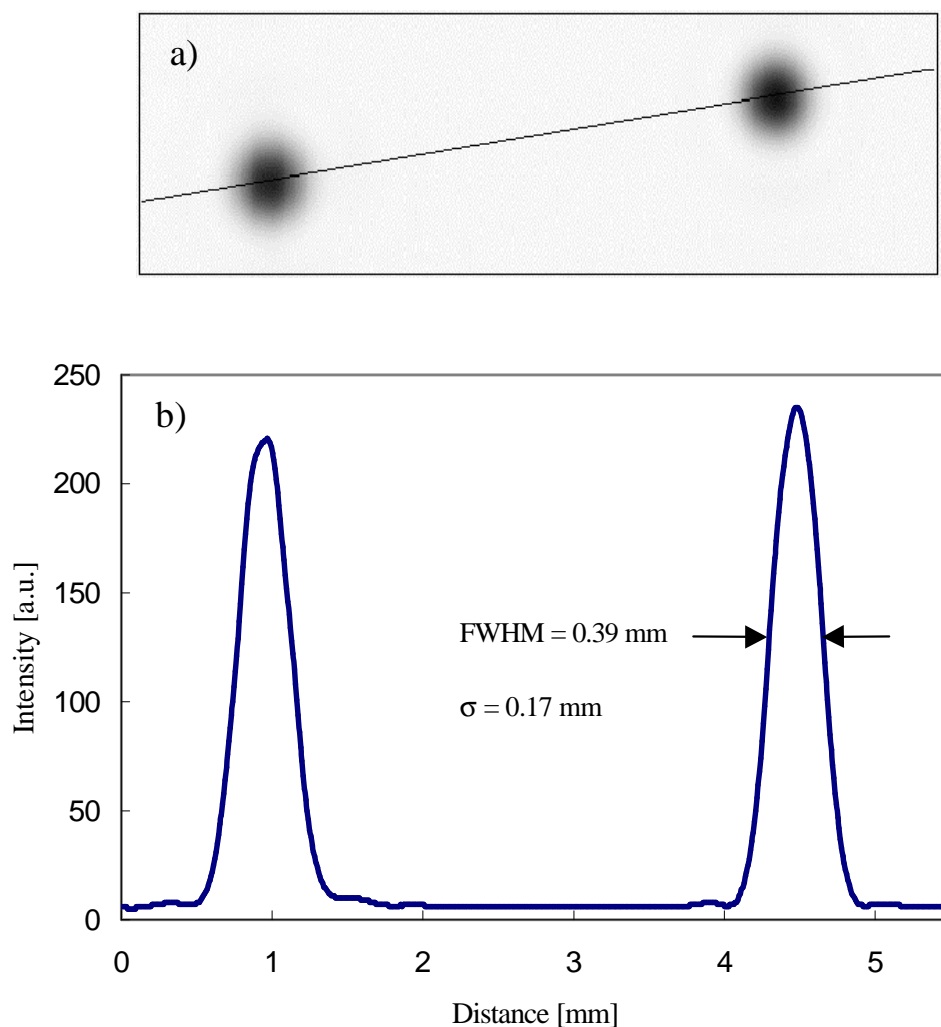
Fig. 4.89: a) Two beam spots on the CCD. The line indicates the cut used to plot the distributions shown in Fig. b): Diffraction limited profile of the beam spots.

4.3.6   Tested mirror mount prototypes

In the following, three prototypes from CERN, INFN and Univ. of Torino, and Tech. Univ. of Prague are described. They are based on the principles shown in Sect. 4.3.2 and are the most representative among several prototypes we have tested.

   A mirror mount prototype A was designed in the EP/TA2 group at CERN for the LHCb RICH 2 detector. It is made of Polycarbonate. The working principle of the prototype is following (Fig. 4.90): The adjustment of the mirror tilt is enabled by a
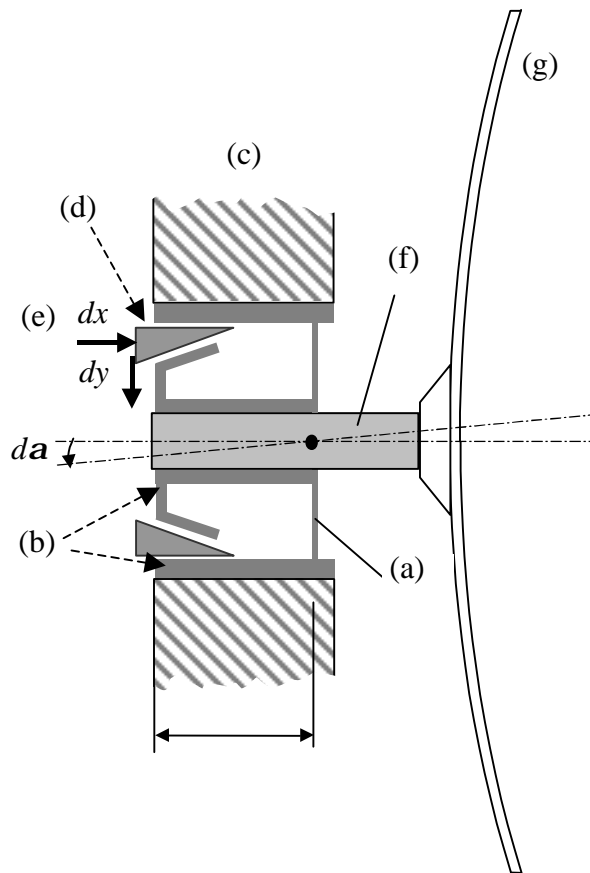
Fig. 4.90: Scheme of the mount prototype A (not to scale).

flexible membrane (a). The whole mount structure (b) is made of one piece of Polycarbonate, eliminating therefore backslashes in the mechanism. It is mounted in a machined hole to a structure (c), which will support all the mirrors fixed by the mirror mounts. A wedge (d) is pressed by a screw (e) into the Polycarbonate structure, consequently pushing the central part of the mount (f) out of the axis position. The flexible membrane deforms elastically, therefore providing the reaction forces necessary to hold the mirror (g) in place. The latter tilts around the centre of the flexible membrane together with the central part of the mount. The angular tilt **a** is given by the formula (4.51), where dy is the displacement due to the wedge and L is the length of the Polycarbonate mount. The same principle is applied for horizontal

and vertical tilts. From equations (4.50) and (4.51) we get the tilt $d\mathbf{a}$ as a function of a screw turn $d\mathbf{g}$ for a chosen screw pitch s, a wedge angle $\mathbf{b}$ and the mount length L:

$$d\mathbf{a} = \arcsin\frac{s\,tg\mathbf{b}}{L}\,d\mathbf{g} \qquad (4.65)$$

To achieve a fine tuning in $\mathbf{a}$, we need to decrease the numerator or/and increase the denominator. However, considerations of increase in X_0 fraction and material stiffness and stability define a range in the possible values for the screw thread, wedge angle and mount length. Moreover, it is desirable to have a self-locking system to ensure a complete blocking of the mount, which defines an upper bound for the $\mathbf{b}$ angle, see Sect. 4.3.2. Therefore, a compromise was found and at present a full turn of the screw means $d\mathbf{a} = 1.0$ mrad for $s = 0.7$ mm, $\mathbf{b} = 5\diamondsuit$ and $L = 60$ mm. The same principle is applied for horizontal and vertical tilts and the average fraction of X_0 represented by the mount is ~ 5 %.

The second mount prototype (prototype B, Fig. 4.91) was developed in INFN and Univ. of Torino for the first RICH detector of the COMPASS experiment. The principle of the long arm discussed in Sect. 4.3.2 was applied. Two perpendicular arms (a) with length $L = 200$ mm turn independently around a ball joint (b). The movement is initiated by two screws (c) with thread pitch $s = 0.5$ mm. The full screw turn makes tilt $d\mathbf{a} = 2.5$ mrad. The design is light, made mostly of aluminium. In comparison with the Polycarbonate prototype, it is less robust and more sensitive to induced vibrations from environmental background.
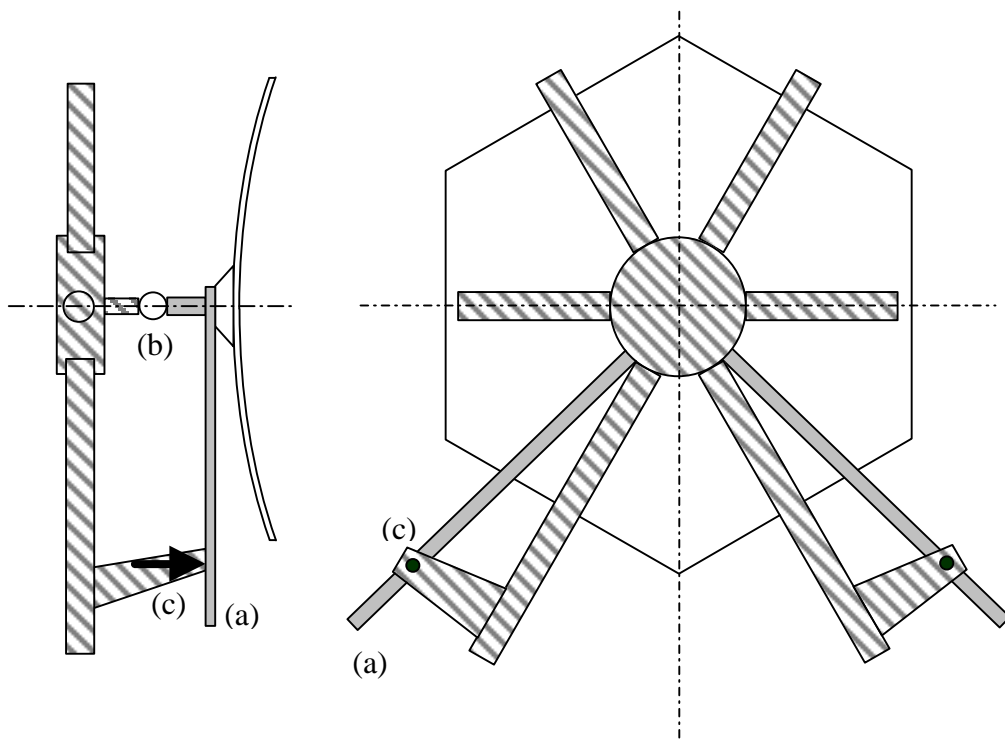
Fig. 4.91: Scheme of the mount prototype B (no to scale).

The prototype from the Technical University in Prague (prototype C, Fig. 4.92) adjusts mirror position by means of three levers of the first order. They are situated under angle 120°. If one of the levers is being adjusted, the mirror turns around the axis that connects the two other levers. The lever (a) is connected by flexible joints (b) with the other parts of the mount. The angle of the lever is controlled by the screw (c). Beside the required angular adjustment, it is possible to equip the mount by an adjustment (flexible structure (d)) in a plane perpendicular to the optical axis of the mirror. The pitch of the screws $s = 1$ mm, transmission 1:10 and $L = 103$ mm provide $d\boldsymbol{a} = 1$ mrad per full screw turn.
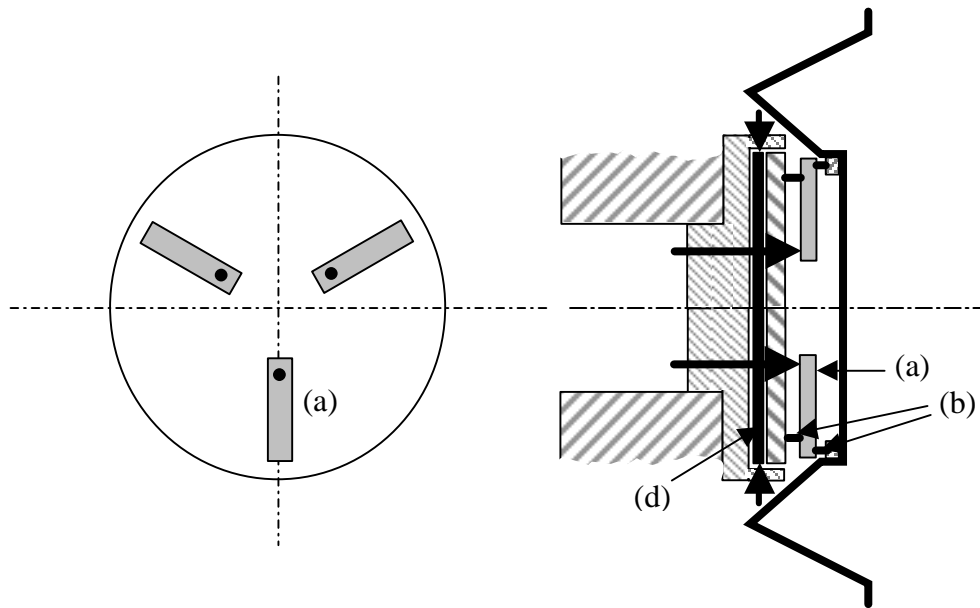
Fig. 4.92: Scheme of the mount prototype C (not to scale).

4.3.7   Measurement results

4.3.7.1   Adjustment characteristics

We measured several prototypes of mirror mounts for the LHCb RICH 2 and COMPASS RICH 1 detectors. The measurement procedure is as following: in precise steps, the corresponding screw adjusts the loaded-mount tilt and for every step a CCD image is acquired and stored. If possible, the whole range is measured. Then, the adjustment sense is reversed and the measurement continues back to the starting position. The same procedure is applied for all two or three adjustment directions. Finally, from the processed data, we get the information about precision, range, linearity, hysteresis and crosstalk.
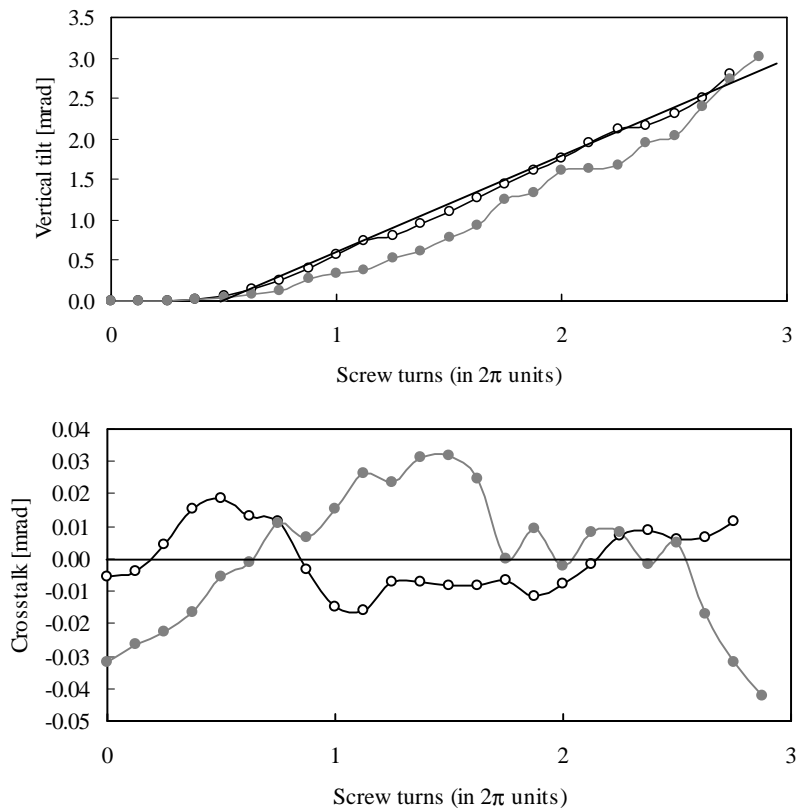
Fig. 4.93a: Results from prototype A with aluminium wedges. Measurement was repeated twice. A linear fit to the measurement is shown. The rms variation for the crosstalk is 0.015 mrad.
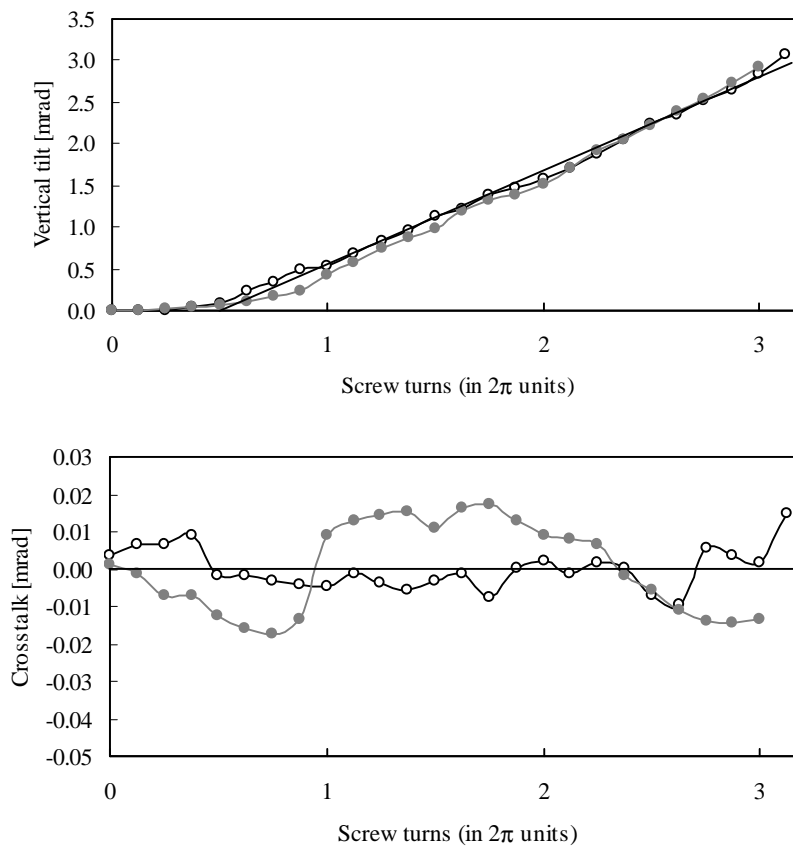
Fig. 4.93b: Results from prototype A with Polyacetal wedges. Measurement was repeated twice. A linear fit to the measurement is shown. The rms variation for the crosstalk is 0.009 mrad.

Fig. 4.93 presents results taken on the prototype A. Two cases were measured: the prototype equipped with aluminium wedges (results in Fig. 4.93a), and the same prototype with plastic wedges, made of Polyacetal (POM) (Fig. 4.93b). Because of self-locking principle, the adjustment in reverse sense is not possible. The adjustment range is 3 mrad, which is small but could be sufficient for carefully machined mounting holes in the supporting structure. Tilt change of 0.1 mrad corresponds to a screw turn of 36°, which enables a sufficiently precise adjustment. The function tilt-screw turn is nearly linear. The rms crosstalk was lower than 0.01 mrad for plastic wedges and less than 0.015 mrad for aluminium wedges. The plastic wedges are more convenient, because of a smaller friction coefficient for the combination Polycarbonate-Polyacetal than for Polycarbonate-aluminium. In Table 4.11 we compare theoretical value of $d\mathbf{a}/d\mathbf{g}$ with the measured values for all tested prototypes, together with their rms crosstalk per full screw turn $d\mathbf{e}/d\mathbf{g}$, regression coefficient R^2, adjustment range and $\mathbf{s}_e$ of crosstalk. Trend of $d\mathbf{a}/d\mathbf{g}$ and $d\mathbf{e}/d\mathbf{g}$ as function of the screw position is displayed in Fig. 4.96a. The wedge principle excludes the possibility of an adjustment in reverse sense. Consequently, if the adjusted tilt passes beyond the set-point value, it is necessary to restart the adjustment procedure.
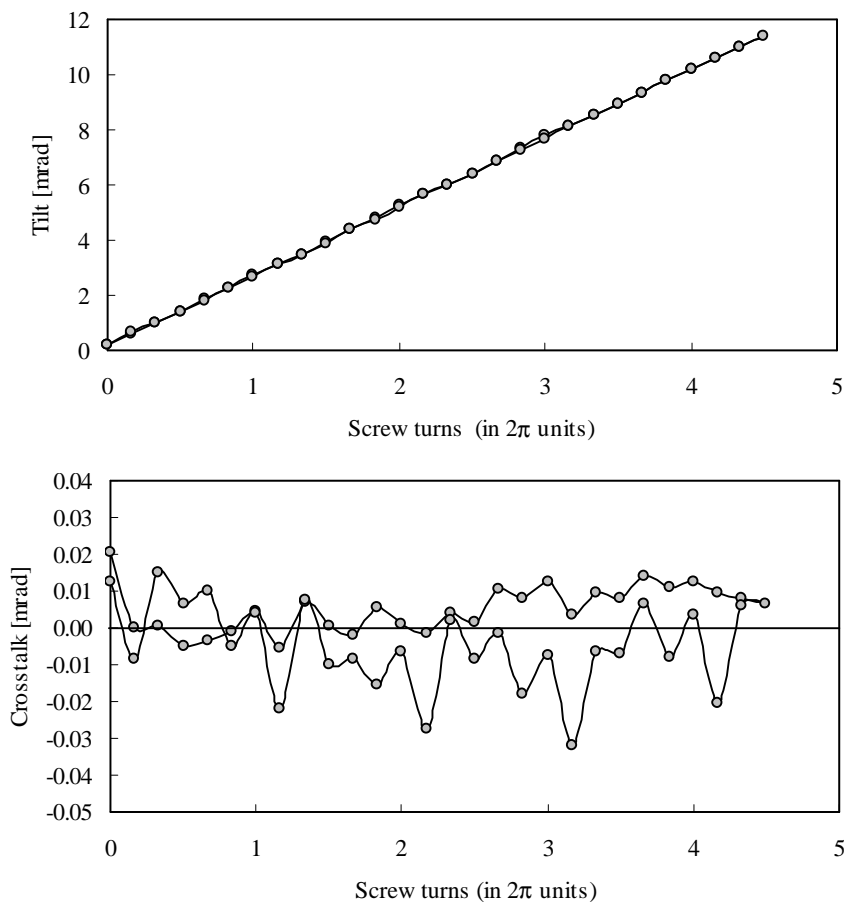
Fig. 4.94: Results from prototype B. The rms variation for the crosstalk is 0.01 mrad.

Results from the prototype B are shown in Fig. 4.94. The total adjustment range is ≥ 12 mrad. A tilt of 0.1 mrad corresponds to a screw turn of 15°. This value is well acceptable for the precision requirement of s_p = 0.06 mrad needed in the COMPASS RICH 1 detector. The adjustment characteristics is linear in the whole measured range and hysteresis-free. The rms value of crosstalk was better than 0.01 mrad. Fig. 4.96b represents a trend of $d\mathbf{a}/d\mathbf{g}$ and $d\mathbf{e}/d\mathbf{g}$. Due to its design and material used, this prototype is vibration sensitive and will need special care in order to minimise vibration errors.

Measurement results from the prototype C are presented in Fig. 4.95. The measurement was done over the whole adjustment range which is 9 to 12 mrad for the three main directions. A tilt of 0.1 mrad is performed by a screw turn of 36°. The adjustment characteristics are linear and without hysteresis. The measured crosstalk was relatively large, its rms value being 0.04 mrad. However, the curve is smooth, as shown in Fig. 4.95, which means that a precise adjustment of the mirror tilt is still achievable. Trend of $d\mathbf{a}/d\mathbf{g}$ and $d\mathbf{e}/d\mathbf{g}$ is shown in Fig. 4.96c. The prototype is vibration insensitive and was equipped with an interface mount–mirror, which was designed to minimise deformations at the thin-mirror rear surface caused by stresses from reaction forces and gravity. A lighter version of the prototype is under development at the Tech. Univ. in Prague.
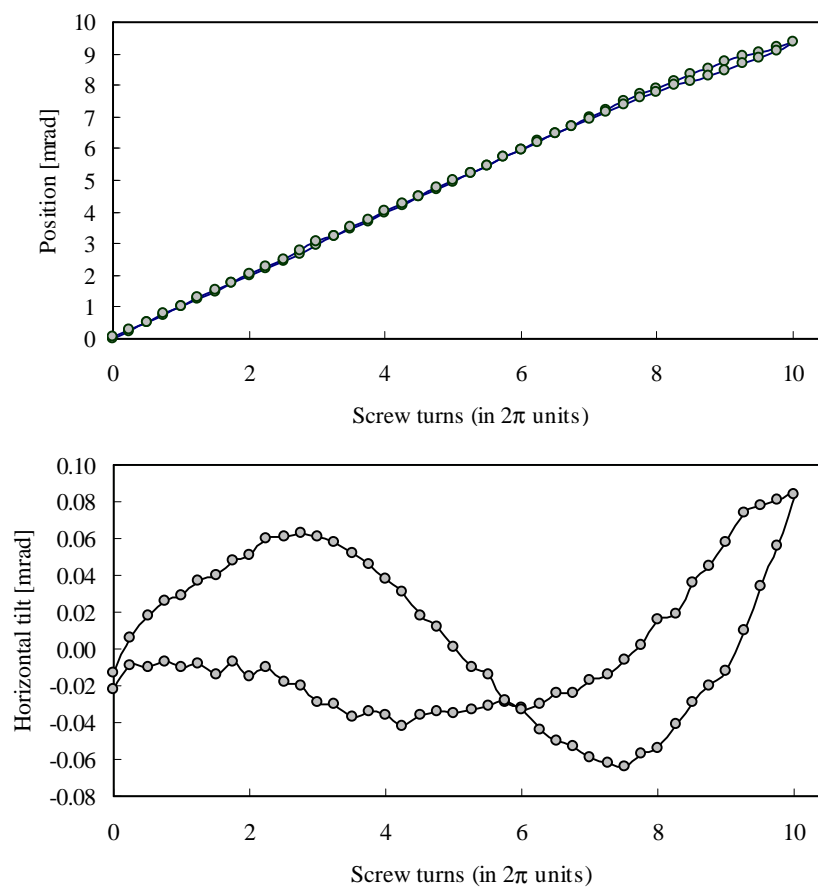
Fig. 4.95: Results from prototype C. The rms variation for the crosstalk is 0.04 mrad.
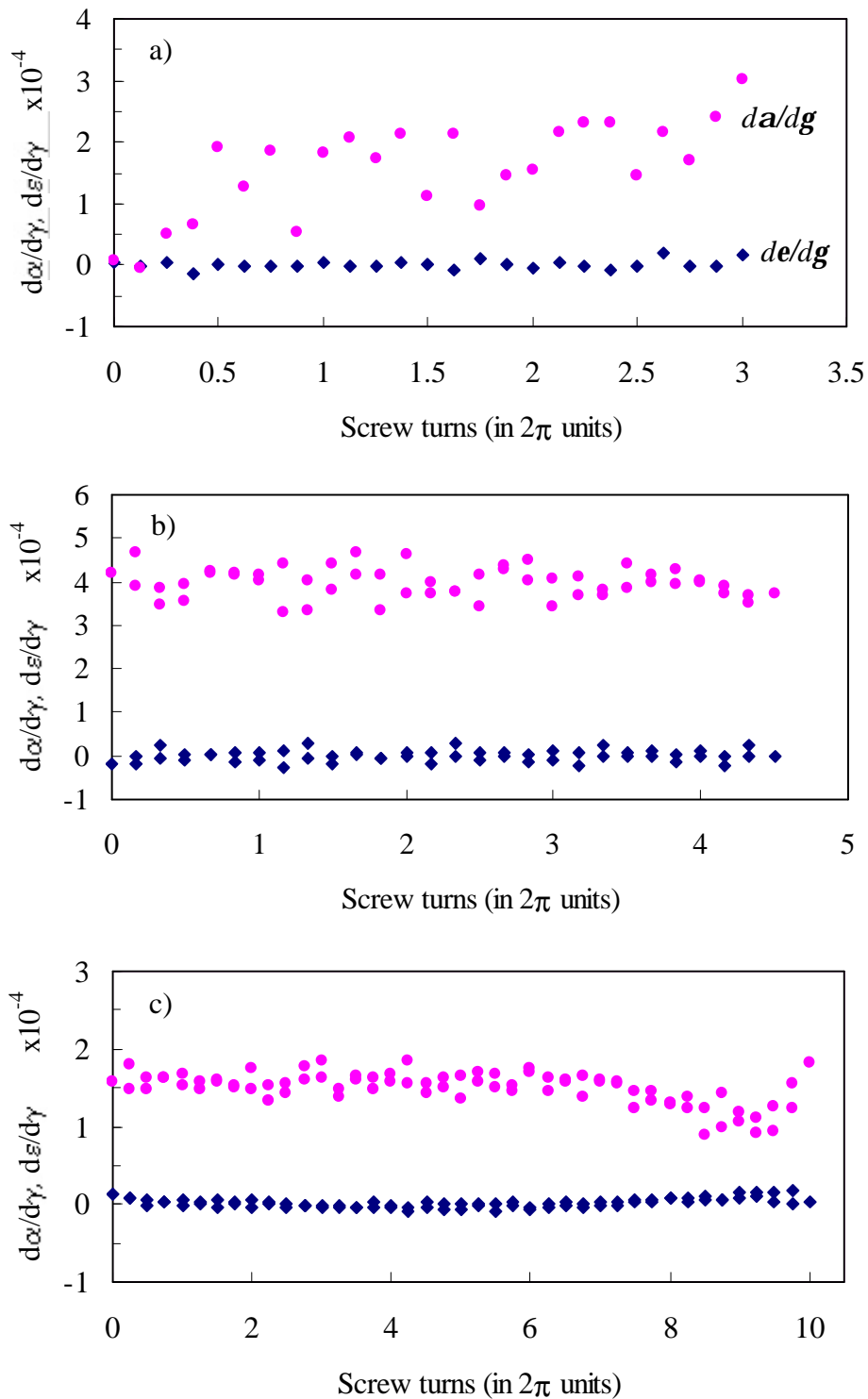
Fig. 4.96: Trend of da/dg (tilt increment per screw turn increment) and de/dg (crosstalk increment per screw turn increment) for mount prototype A, B, C.

Table 4.11: Adjustment characteristics measured on three mount prototypes.

Prototype		Avr. $\dfrac{da}{dg}$		Avr. $\dfrac{de}{dg}$	R^2	Range [mrad]	s_e [mrad]
		Theor.	Meas.				
A	Al	1.6×10^{-4}	1.6×10^{-4}	9.7×10^{-7}	0.975	$\pm\,2.8$	0.01
	POM	1.6×10^{-4}	1.6×10^{-4}	5.6×10^{-7}	0.984	$\pm\,3.1$	0.006
B		4.0×10^{-4}	4.0×10^{-4}	-3.6×10^{-7}	0.9999	Wide (not measured)	0.01
C		1.6×10^{-4}	1.5×10^{-4}	1.6×10^{-6}	0.999	$\pm\,8$	0.04

4.3.7.2 Long-term stability

We measured the prototype of the LHCb RICH 2 mirror mount made of Polycarbonate. The measurement has been taken over a period of more then thirteen months from the beginning of August 1999 to the beginning of September 2000 (9740 hours). Fig. 4.97 shows the temperature changes over the whole measurement time. The temperature range was between 17.6 ◇C and 22.8 ◇C. Between time t = 300 and 1200 hours, temperature varied with a 24 hours period. Absolute changes
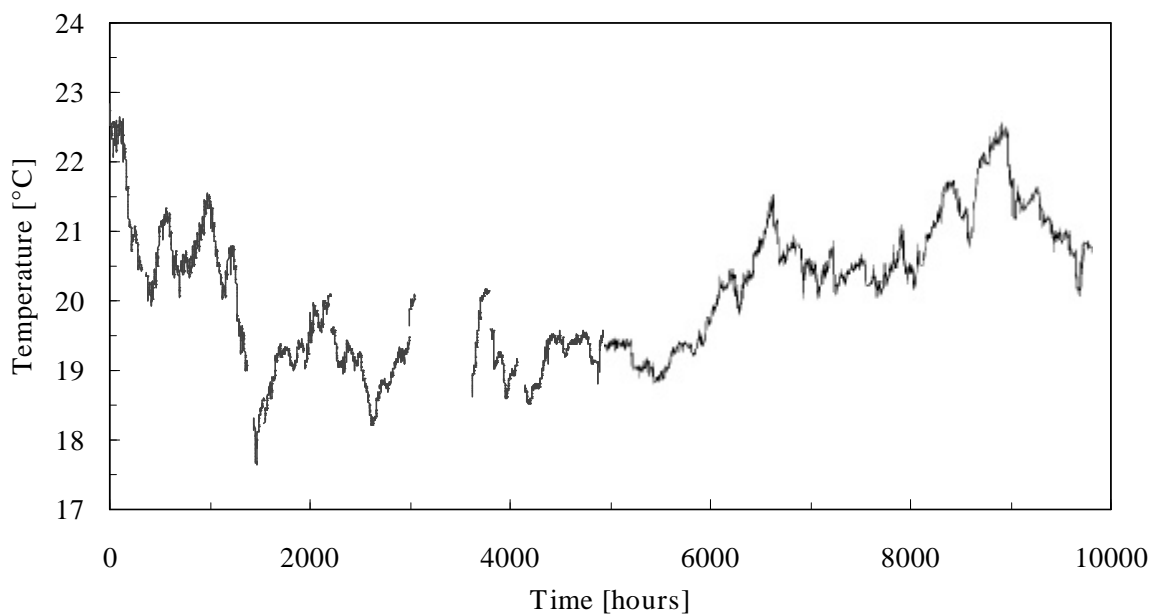
Fig. 4.97: Temperature in the underground optical laboratory. Temperature probe AD590 (Harris Semiconductor) monitored temperature over period of thirteen months.
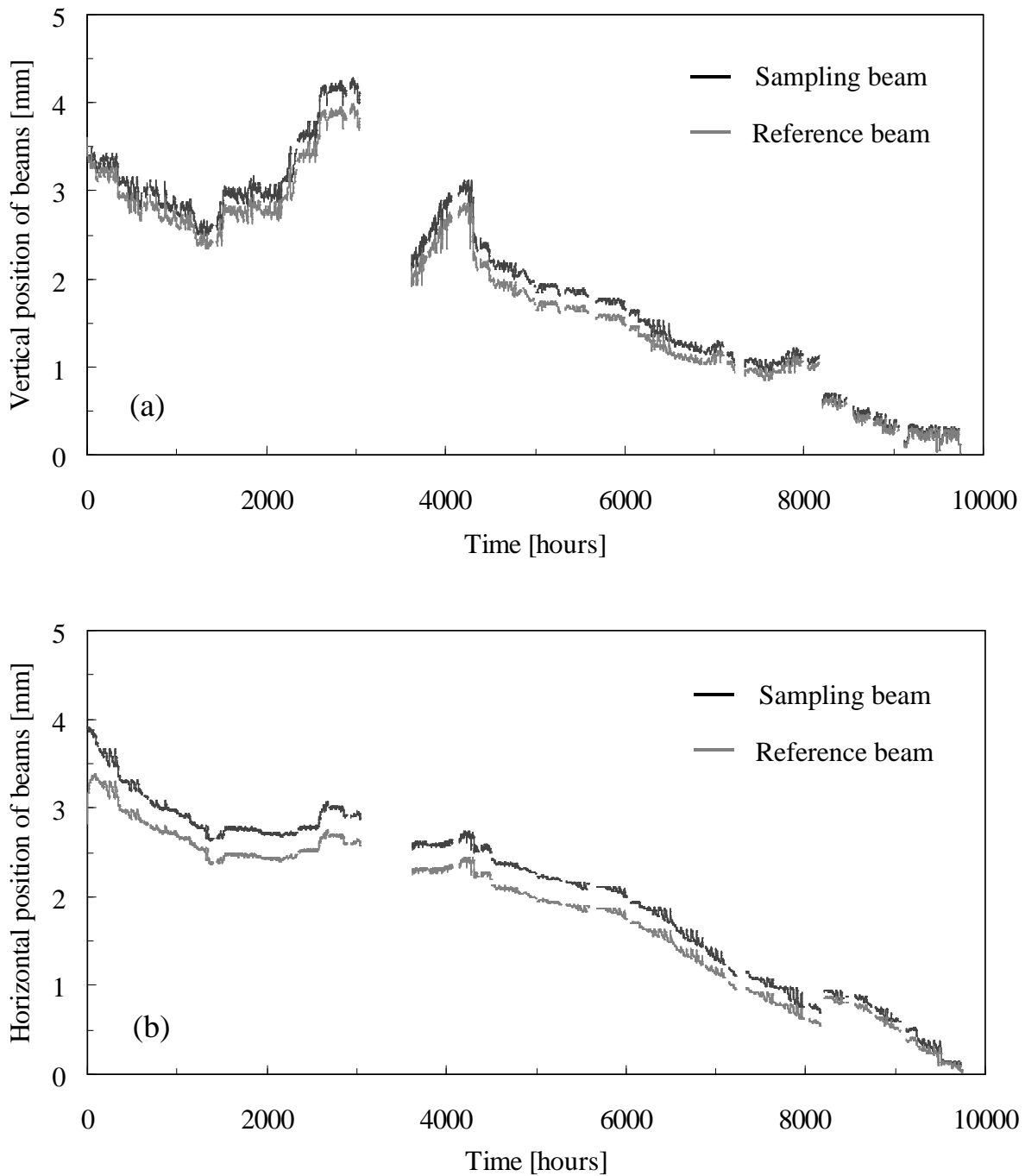
Fig. 4.98: Measurement of the stability of the Polycarbonate mirror mount prototype. Absolute positions of the sampling and the reference beam in vertical (a) and horizontal (b) co-ordinate.

of both beams positions in vertical and horizontal co-ordinates are shown in Fig. 4.98. It is possible to observe a weak correlation between vertical beam movement and temperature variations.

The variations of the relative distance between the two spots in vertical and horizontal co-ordinates provide the tilt changes and therefore the stability properties of the mount. This is shown in Fig. 4.99. A strong relaxation effect is seen during the
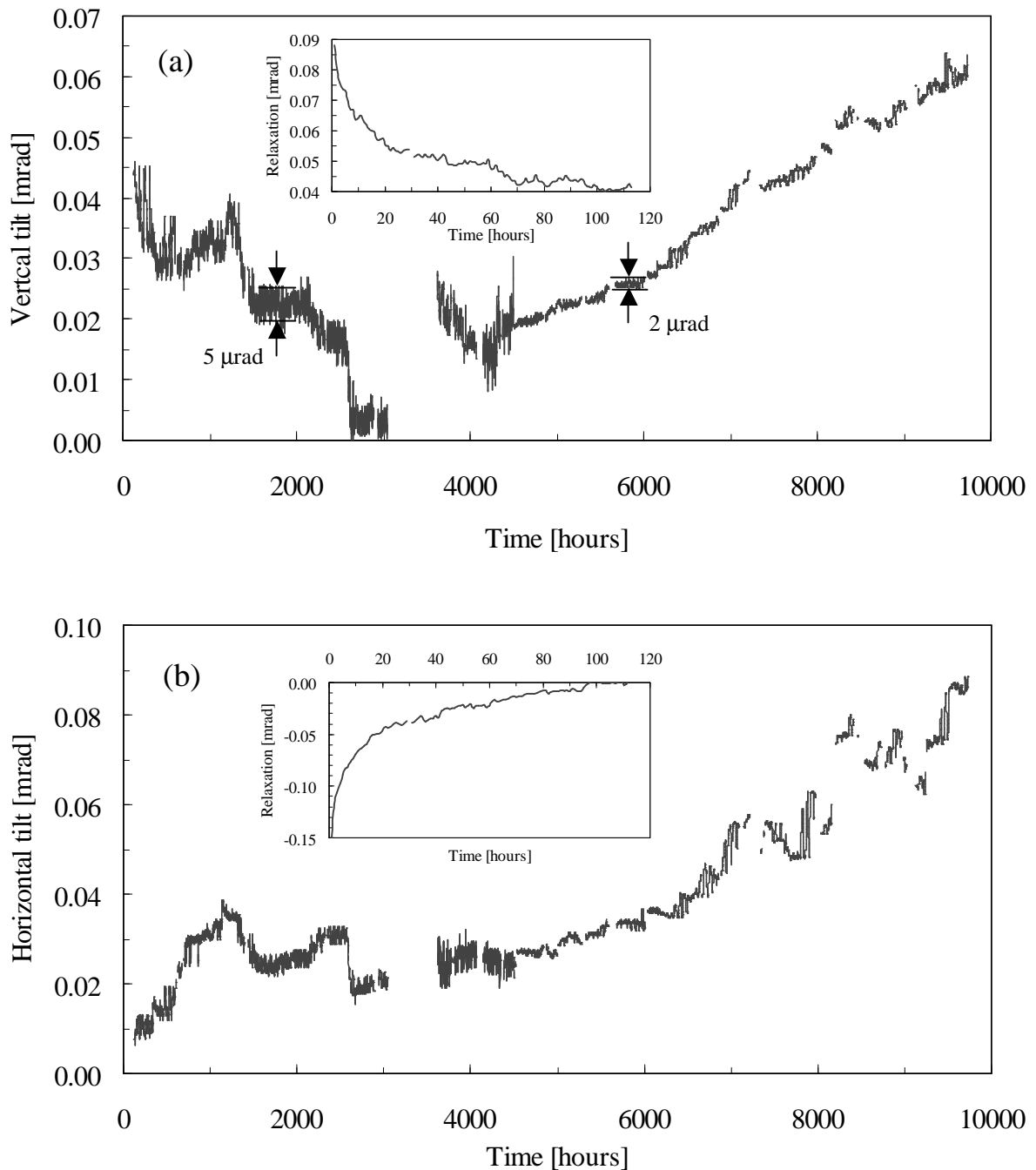
Fig. 4.99: Mirror mount stability in vertical (a) and horizontal (b) co-ordinate. Shown in the insets, it is a strong mechanical relaxation observed at the beginning of the measurement.

first 120 hours in both vertical and horizontal tilt (see insets in Fig. 4.99). It was caused by stress relaxation in the mechanical parts immediately after installation and adjustments. Therefore on the final mirror wall, it will be essential to readjust the mirror positions after the relaxation effect. After removing the initial data affected by this effect, the support becomes stable with a range practically equal for both vertical and horizontal co-ordinates and with a maximum value of 0.08 mrad. The resulting stability is $s_s = 0.02$ mrad. This is inside the final requirement of $s_p = 0.03$ mrad. Moreover, Fig. 4.100 shows the resulting histograms from Fig. 4.99. The

distributions show a fairly central peaked shape probably with a weak correlation with temperature. For the stability histograms (Fig. 4.100), the FWHM of the central peaks range between 10 to 20 μrad. It is also interesting to note the range of variation for the absolute beam positions (up to 4.5 mm) with respect to the relative beam displacements (less than 400 μm). Finally, from Fig. 4.99 we can measure the resolution of the set up to be in any case better than 5 μrad. After elimination of an interference fringes (which did not affect the measurement and was achieved at time t ~ 4500 hours) this resolution went down to 2 μrad. This corresponds well to the theoretical value of $\boldsymbol{s}_{res} \leq 1$ μrad, see Sect. 4.3.5.2.

In agreement with the data found in literature for Polycarbonate, no strong time effect on stiffness has been observed. Temperature effects are more significant than the creep is. However, even with relatively big temperature variations of ± 2.5 °C, the stability of the support was after twelve months well within the requirement $\boldsymbol{s}_p = 0.03$ mrad of the LHCb RICH 2 detector.
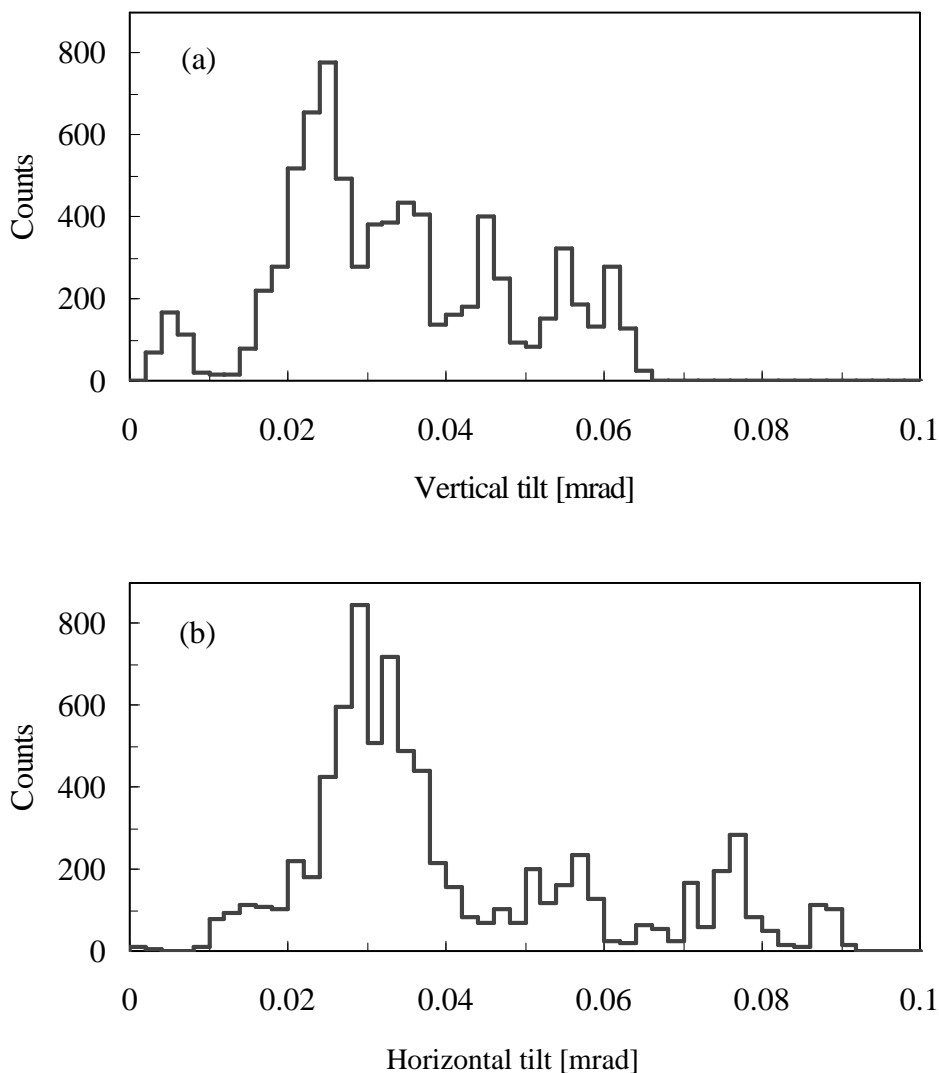
Fig. 4.100: Histograms of vertical tilt (a) and horizontal tilt (b).

5   Conclusions

Development of opto-mechanical tools and procedures, which will contribute to the construction and performance of the new generation of RICH detectors, has been the main subject of this thesis.

Specifications of RICH opto-mechanical components

Specifications for the LHCb RICH 2 mirrors were defined. The hexagonal glass substrates, with diagonal 502 mm and thickness maximum 6 mm satisfy the requirement for precision. It was defined that the maximum size of the spot image of a point source at the centre of curvature has to be smaller than $D_0 = 2$ mm, which corresponds for a radius of curvature $R = 8$ m to the required angular precision of $s_J \leq 0.03$ mrad. Concerning the radius of curvature R, its standard deviation s_R should not exceed 1.9 % of R.

In the case of the RICH 1 detector, the amount of material is more critical and the covered area is smaller. Then, Beryllium mirrors or light composite mirrors could be applicable.

Requirements on the mirror adjustable mounts were defined. They have to provide possibility of a fine adjustment of the mirror angular position, with a maximum error smaller than $s_p = 0.03$ mrad. The mounts should provide easy linear adjustment with a sufficient range, without hysteresis, attenuating mechanical vibrations transferred from external sources. They have to feature long-term stability in order to guarantee precise positions of the mirrors over the whole run time of the detector, this being several years. Basic possible designs were analysed.

Measurements in the optical laboratory

In order to qualify prototypes and final production of the RICH opto-mechanical components, the TA2 optical laboratory was established. After analysis of possible measurement methods, measurement facilities for characterisation of the RICH opto-mechanical components were developed.

Set ups for mirror measurements

To measure the precision of the mirror spherical surface, a fully automatic set up for spot size measurement was developed. This method provides quantitative results with measurement resolution $s_{Do} = 0.02$ mm. The set up simultaneously measures the

value of the mirror radius of curvature with a precision $s_R \cong 1$ mm. The achieved precision of the set up is better than it was required.

For deeper studies of the processes that cause mirror deformations, a set up based on a modified Shack-Hartmann wavefront sensor was developed. This forefront technology enables measurement of a reflective surface topography at a high precision. The sophisticated instrument was prepared and his correct function was verified. The development has not been finished. It will be necessary to calibrate the device and to make it user friendly.

Set ups for mirror mounts measurements

A set up, devoted to the evaluation of adjustment characteristics, was developed. It provides information about precision, range, linearity, hysteresis, sensitivity to vibrations or aging of the adjustment. The angular resolution of the measurement is $s_{\text{res}} \cong 2$ μrad.

A second set up was designed for fully automatic measurement of a long-term stability of the mirror mount. This measurement was especially important to verify the applicability of polymers in the mount design.

Collaboration with industry

Collaboration with several mirror manufacturers was established. The set ups, installed in the optical laboratory, have been used to provide a feedback to the manufacturers and for optimisation of initial specifications. Prototypes of mirrors for the LHCb and COMPASS experiments were qualified. On the base of the provided feedback, manufacturers improved significantly the quality of the mirror prototypes of all three types: glass, Beryllium and composite. In the case of the LHCb RICH 2 glass mirror substrates, a thickness of 4 to 5 mm was found to be feasible. The whole production of the COMPASS RICH 1 glass mirror substrates was successfully tested and qualified.

Long-term stability of a mount prototype, developed at the TA2 group, was tested over a period of more than 13 months. The resulting stability of $s_s = 0.02$ mrad was inside the requirement of $s_p = 0.03$ mrad.

Appendices

Appendix A: A few lines about particles

As introduced in section 2.1, according to the Standard Model [A1], two basic kinds of particles exist: matter particles and force-carrier particles. Matter consists of four fundamental particles: two leptons and two quarks. The leptons are the electron (e) and electron neutrino (v_e), the quarks are the up (u) and down (d). These fundamental particles are declared belonging to the so-called first generation. Two other generations exist, the second and third, which are composed of heavier forms of the first generation particles. The strange (s) and charm (c) quarks and the muon (μ) and muon neutrino (v_μ) belong to the second generation. The top (t) and bottom (b) quarks and the tau lepton (τ) and tau neutrino (v_τ) then fall into the third generation. Table A1 summarises and sorts all the three generations. Matter made of particles from the two heavier generations is unstable and decays into stable matter made of the u and d quarks and the electron. The proton is built of one d and two u quarks and the neutron of one u and two d quarks. Each of particles has an anti-particle with equal mass but opposite charge.

Each type of fundamental force (except for gravity, which is neglected in the Standard Model) is carried by a force-carrier particle. All other particles can be described as composition of fundamental particles and force-carrier particles. For each of the matter particles, there is a corresponding antimatter particle.

Antiparticle has the same properties as the corresponding matter particle (the same mass etc.) except the opposite charge. When a particle and its antiparticle meet, they annihilate into pure energy. This energy may then give rise to neutral force-carrier particles, such as photons, Z bosons, or gluons.

Leptons are either negatively charged (the electron, the muon and the tau) or neutral (three types of neutrinos). Neutrinos have very little, if any, mass. There are a lot of them in the Universe because they are produced in stars and they have a long life time. Because of their little mass, they almost never interact with other particles, which makes them very difficult to detect. Leptons can exist as free particles.

Quarks, in contrast to leptons, are always grouped to form hadrons. We recognise two types of hadrons: baryons are made of three quarks; mesons contain one quark and one antiquark. The most famous representatives of both groups are shown in Table A2 and A3. Individual quarks have fractional electric charges (+2/3 or –1/3) but the sum of the quarks' electric charges in a hadron is always an integer number. Quarks (and gluons) have a type of charge that is not electromagnetic. It is called colour charge. The force between colour-charged particles is very strong, called Strong force. Its carrier particles are called gluons. Hadrons are colour neutral.

Baryons may contain, apart from three quarks, also some gluons and quark-antiquark pairs. They have odd-half-integer (1/2, 3/2, ...) intrinsic angular momentum (spin), measured in units of ←, which is characteristics of fermions.

Mesons are composed of a quark, an antiquark and binding gluons. They are unstable. Since mesons have an integer spin, they belong to bosons.

Each of the fundamental particles has an attribute called "flavour" which can be changed only by the charged weak interaction. There are 6 flavours of quarks and 6 of leptons. Neutral weak interactions with a Z boson do not alter flavour. All the more massive quarks and leptons decay to produce lighter quarks and leptons. This is why stable matter around us contains only electrons and the lightest two quarks (up and down).

Table A.1: Overview of three generations of particles. Masses are given in MeV/c^2 and electric charges in proton units.

Charge	Generation					
	First		Second		Third	
	particle	mass	particle	mass	particle	mass
$+\dfrac{2}{3}$	u	2-8	c	1000-1600	t	~180000
$-\dfrac{1}{3}$	d	5-15	s	100-300	b	4100-4700
-1	e	0.511	μ	106.6	τ	1777
0	ν_e	~ 0	ν_μ	< 0.2	ν_τ	< 25

Table A2: A few representatives of baryons.

Baryons	quarks	Electric charge	Mass [MeV/c^2]	spin
p proton	u u d	+1	938	1/2
$\overline{p}$ antiproton	$\overline{u}$ $\overline{u}$ $\overline{d}$	-1	938	1/2
n neutron	u d d	0	940	1/2
Λ^0 lambda	u d s	0	1116	1/2
Ω^- omega	s s s	-1	1672	3/2
S_C sigma-c	u u c	+2	2455	1/2

Table A3: Mesons.

Mesons	quarks	Electric charge	Mass [MeV/c^2]	spin
π^+ pion	u $\bar{\text{d}}$	+1	140	0
K^- kaon	s $\bar{\text{u}}$	-1	494	0
K^0 kaon	d $\bar{\text{s}}$	0	498	0
ρ^+ rho	u $\bar{\text{d}}$	+1	770	1
D^+ D	c $\bar{\text{d}}$	+1	1869	0
η_C eta-c	c $\bar{\text{c}}$	0	2980	0

Appendix B: Beyond the Standard Model

Although the Standard Model describes very well phenomena observed by experiments, it is an incomplete theory [B1]. It still cannot fully explain the nature of the world, why some particles exist as they do. Arising questions can be listed in three problem classes [B2].

The *Problem of Mass*: why cannot the Standard Model predict a particle's mass? What is the origin of particle mass? Higgs boson?

The *Problem of Flavour*: why are there just six quarks and six leptons? Are quarks and leptons really fundamental? Why is there not equal amount of matter and antimatter in the Universe?

The *Problem of Unification*: are all the gauge interactions combined in a simple group structure that might predict new interactions leading to proton decays and neutrino masses? How will gravity fit into the Standard Model?

One of the major goals of particle physics is to unify strong, weak, and electromagnetic interactions into a single unified theory called "Grand Unified Theory". According to this theory, all forces merge at high energies into one. The advantage of a unified theory over many fragmented theories is that a unified theory would offer a more elegant explanation of data and might point toward future areas of study.

In the later years of his life Einstein tried, but did not succeed, to write a theory which unified gravity with other theories.

In the context of Grand Unified Theory, the theory of supersymmetry attempts to unify the strong, weak, and electromagnetic interactions to help explain why particles have the masses they have. The supersymmetric theory postulates that every particle has a massive "shadow" particle partner. No supersymmetric particle has yet been seen, but experiments underway at CERN beginning in Autumn 1995 have searched for the partner of the W boson, and experiments at Fermilab are looking for the partners of the quarks and gluons. One of the supersymmetric particles (the "neutralino") might make up the missing "dark matter", which is not made up of protons, neutrons, and electrons. The majority of the universe might be made of the dark matter.

Today, one of the basic questions is related to the Universe's absent antimatter [B3]. The existence of antimatter was confirmed at high-energy laboratories like CERN, where pairs of particles and antiparticles are produced and used in accelerators. At LEP, collisions between electrons and positrons have been studied (a positron is the antiparticle of an electron). Showers of particles produced when energetic cosmic rays from space hit the Earth's atmosphere are made up of matter and antimatter.

At the Big Bang, matter and antimatter should have been created in equal amounts, but today the Universe seems to be entirely made of matter. When matter

and antimatter meet, they annihilate leaving behind nothing but energy, so it seems strange that there is anything left at all. It is possible that whole regions of space exist filled only with antimatter, and experiments are planned in space to look for them. But most scientists believe that there is a subtle difference between the way nature treats matter and antimatter, called CP-violation, and that is why a tiny fraction of the matter has survived to build the Universe.

Symmetries and their conservation laws form, together with the elementary particles and their interactions, the basis of the fundamental physical description of nature. The CPT theory describes three basic symmetries of particle interactions. C, charge conjugation, represents replacing a particle by its antimatter counterpart. P, parity, corresponds to looking in a mirror, which reverses all three co-ordinates; this mirror reverses image is not only back-to-front, but also left-right and upside-down. Finally, T is time reversal.

Until approximately 1956 it was assumed that any one of these symmetries applied to any particle interaction would not change the outcome; it was said that the symmetries were conserved. But then experiments showed that in weak interactions, both P and C are broken. C.S. Wu observed that the mirror image of the left-handed neutrino, the right-handed neutrino, does not exist and that therefore the symmetry of the weak interaction is broken by the P operation. The symmetry is restored when the P operator is not applied alone, but when the combined operation CP is applied. CP-transformation converts a left-handed neutrino into a right-handed anti-neutrino, which does exist. Later, it turned out that the combination of C and P was also not conserved. It is this CP-violation, first detected in 1964 at the US Brookhaven laboratory by James Cronin and Val Fitch in the case of the neutral K-meson at a level of 0.2%. Since then accurate measurements have taken place to determine the origin of CP violation in the K-meson system. However, with the K-meson effects due to the strong interaction are too large to draw any conclusion about the origin of CP violation. The expectation is that these effects will be less and better to determine in the case of a heavier meson such as the B-meson.

Scientists still believe that CPT is conserved, or put another way, that an antiparticle is indistinguishable from the mirror-image of a particle moving backwards in time. Bizarre though it may seem, this is one of the most fundamental tenets of modern physics. If it is not true, then physicists will have to take their theories back to the drawing board. Up to now all experiments designed to measure CPT have found no violation.

The problem of CP-violation is now universally recognised as one of the most important ones in modern subatomic physics. Most of high-energy laboratories are setting up programs to study B-mesons. With the LHCb experiment at CERN's LHC accelerator B-meson physics will reach its zenith. The extra energy of the LHC accelerator means that LHCb will be able to measure many more of the CP-violating decays of B mesons than the earlier experiments. This will provide a precise test of the Standard Model, and tell us what it is that nature prefers about matter into the bargain.

Appendix C: Light

It is worth nothing that the most important concept in this thesis is light. Cherenkov detectors are based on light and its particular characteristics deriving by the Cherenkov effect. All described measuring set ups are based on light as well. Light is a very remarkable phenomenon and an extraordinary measurement tool.

This fact has already been recognised in deep history, for example around 230 B.C. by a Greek scholar named Eratosthenes. He used the sunlight to determine the circumference of the earth [C1]. Knowing the distance from Syene to Alexandria (see Fig. C1), he erected a vertical pole in Alexandria and measured the length of the pole's shadow. The measurement was taken at the same precise date and time when the sunlight fell directly down a well in Syene. Assuming that extensions of the well and pole would intersect at the earth's centre, Eratosthenes calculated that the earth's circumference was 40,000 km. This value is remarkably close to today's established value 40,074 km.

Today, majority of all possible physical quantities can be measured by means of light. A big progress came with the invention of the laser source. And, in cases when light cannot directly measure a given quantity, it mediates at least the results. The role of light as a communication tool is undoubtedly even more important than as a measurement tool. Apart from vision, light connects by means of optics fibre cables people around the whole world.

Not by chance, people say that someone "put light in a problem". By means of light, many problems can really be solved. This particle-wave phenomenon deserves a high attention.
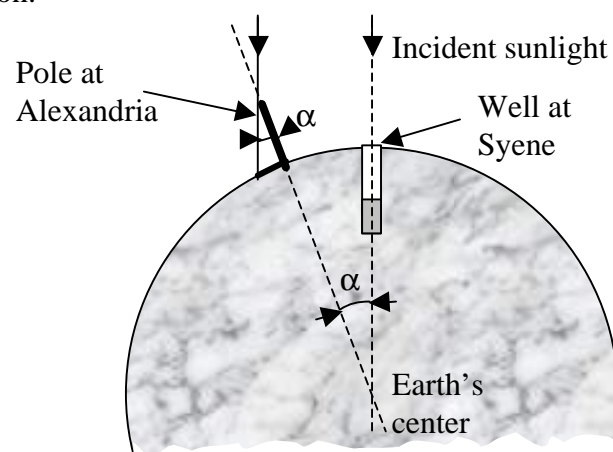

Fig. C1: Principle of the earth's circumference measurement performed around 230 B.C. by Eratosthenes.

References

Chapter 2

[2.1] W. N. Cottingham, D. A. Greenwood, *An Introduction to the Standard Model of Particle Physics*, Cambridge Univ. Press, 1998.
[2.2] B. R. Martin, G. Shaw, *Particle Physics*, John Wiley & Sons, 1992.
[2.3] F. Halzen, A. D. Martin, *Quarks & Leptons: An Introductory Course in Modern Particle Physics*, John Wiley & Sons, 1992.
[2.4] I. S. Hughes, *Elementary Particles*, Cambridge Univ. Press, 1991.
[2.5] P. Ramond, *Beyond the Standard Model*, Addison-Wesley, 1993.
[2.6] *LHC : the large hadron collider*, CERN, 1996.
[2.7] G. Brianti et al., Part. World, Vol. 1, No.4 (1990), 104.
[2.8] The LHCb Collaboration, *Technical Proposal*, CERN/LHCC 98-4, LHCC/P4, 1998.
[2.9] Particle Data Group, *Review of Particle Physics*, Europ. Physic. Jour. C Vol. 3 No. 1-4 (1998) 76.

Chapter 3

[3.1] J Seguinot, *Les compteurs Cherenkov: Applications et limites pour l'identification des particules*, CERN-EP/89-92, LPC/89-25, 1989.
[3.2] T. Ypsilantis, J Seguinot, Nucl. Instr. and Meth. A 343 (1994) 30.
[3.3] P. Gl·ssel, Nucl. Instr. and Meth. A 433 (1999) 17.
[3.4] P. A. Cherenkov, Phys. Rev. 52 (1937) 378.
[3.5] R. H. Dicke, Phys. Rev. 71 (1947) 737.
[3.6] O. Chamberlain, E. Segre, C. Wiegand, T. Ypsilantis, Phys. Rev. 100 (1955) 947.
[3.7] R. Meunier, J. P. Stroot, B. Leontic, A. Lundby, Nucl. Instr. and Meth. 17 (1962) 1 and 20.
[3.8] J. V. Jelley, Proc. Phys. Soc. A 64 (1951) 82.
[3.9] D. Bartlett et al., Nucl. Instr. and Meth. A 260 (1987) 55.
[3.10] A. Roberts, Nucl. Instr. and Meth. 9 (1960) 55.
[3.11] J. Seguinot, T. Ypsilantis, Nucl. Instr. and Meth. 142 (1977) 377.
[3.12] G. Charpak et al., Nucl. Instr. and Meth. 164 (1979) 419.
[3.13] T. Ekelof, J. Seguinot, J. Tocqueville, T. Ypsilantis, Physica Scripta 23 (1981) 718.
[3.14] D. F. Anderson, Nucl. Instr. and Meth. 178 (1980) 125.
[3.15] E. Barrelet et al., Nucl. Instr. and Meth. 200 (1982) 219.
[3.16] J. Vavra, Nucl. Instr. and Meth. A 453 (2000) 262.
[3.17] K. Zeitelhack et al., Nucl. Instr. and Meth. A 433 (1999) 201.

[3.18] J. L. Rosen, Nucl. Instr. and Meth. A 408 (1998) 191.

[3.19] H. W. Siebert et al., Nucl. Instr. and Meth. A 343 (1994) 60.

[3.20] E. Albrecht et al., Nucl. Instr. and Meth. A 433 (1999) 47.

[3.21] S. Stone, Nucl. Instr. and Meth. A 433 (1999) 293.

[3.22] J. Seguinot, T. Ypsilantis, Nucl. Instr. and Meth. A 343 (1994) 1.

[3.23] T. Ekelof, Nucl. Instr. and Meth. A 433 (1999) 372.

[3.24] The LHCb Collaboration, *LHCb RICH Technical Design Report*, CERN LHCC 2000-037, LHCb TDR 3, 2000.

[3.25] The COMPASS Collaboration, *Common Muon and Proton Apparatus for Structure and Spectroscopy*, CERN/SPSLC 96-14, SPSC/P297, 1996.

[3.26] G. Baum et al., Nucl. Instr. and Meth. A 433 (1999) 207.

Chapter 4

[4.1]   M. Bosteels, F. Hahn, S. Haider, R. Lindner, O. Ullaland, *LHCb RICH Gas system proposal*, LHCb 2000-79 RICH.

[4.2]   C. D'Ambrosio, L. Fernandez, M. Laub, D. Piedigrossi, *Precision optical systems for the new generation of Ring Imaging Cherenkov detectors in high energy physics experiments*, Nucl. Instrum. Meth. Phys. Res. A (to be published).

[4.3]   C. D'Ambrosio, L. Fernandez, M. Laub, D. Piedigrossi, *The Optical Systems of LHCb RICHes: a Study of the Mirror Walls and Mirror Specifications*, LHCb 2000-71 RICH.

[4.4]   O. Ullaland et al., *LHCb RICH 2 mechanics*, LHCb 2000-079 RICH.

[4.5]   C. D'Ambrosio, M. Laub, D. Piedigrossi, P. Wertelaers, P. Wicht, *An Experimental Set-up to Measure the Long-term Stability of Large-mirror Supports*, LHCb 2000-020 RICH.

[4.6]   C. D'Ambrosio, M. Laub, D. Piedigrossi, P. Wertelaers, P. Wicht, *Characterization of Mirror Mount Prototypes for RICH Detectors*, LHCb 2000-72 RICH.

[4.7]   D. Malacara, *Optical shop testing*, John Wiley and Sons, Inc., 1978.

[4.8]   M. Born, E. Wolf, *Principles of Optics*, 6th ed., Pergamon Press, Oxford, 1987; S. Solimeno et al., *Guiding, diffraction and confinement of optical radiation*, Academic Press Inc., 1986.

[4.9]   R. Shack, B. Platt, *Optical Science Newsletter*, University of Arizona, 5 (1), 15 (1971).

[4.10] J. Hartmann, *Bemerkungen uber deu Ban und die Justirung von Spectrographen*, Zf. Instrumentenk., 20, 4, (1900).

[4.11] J. Geary, *Introduction to wavefront sensors*, SPIE PRESS, Washington, 1995.

[4.12] R. G. Lane, M. Tallon, Applied Optics, Vol. 31, No. 32 (1992) 6902.

[4.13] J. Pfund et al., *Absolute sphericity measurement: a comparative study on the use of interferometry and a Shack-Hartmann sensor*, Conference on Lasers and Electro-Optics Europe – Technical Digest, 1998, p. 201.

[4.14] V. Ronchi, *Due Nuovi Metodi per lo Studio delle Superficie e dei Sistemi Ottici*, Ann. Sc. Norm. Super Pisa, 15 (1923).

[4.15] I. Adachi, *Quantitative Measurement of Aberration by Ronchi Test*, Atti. Fond. Giorgio Ronchi Contrib. Ist. Naz. Ottica, 15 (1960) 461.

[4.16] J. H. King, J. Opt. Soc. Am., 14 (1934) 250.

[4.17] M. Mansuripur, Optics & Photonics News, July (1997) 42.

[4.18] L. Stutte, J. Engelfried, J. Kilmer, Nucl. Instr. and Meth. A 369 (1996) 69.

[4.19] C. Genrui, Y. Xing, *Study on the Hartmann-Shack Wavefront Sensor*, SPIE Vol. 1752 (1992).

[4.20] J. Pfund, N. Lindlein, J. Schwider, App. Opt. 37 (1998) 22.

[4.21] J. H. Ahlberg et al., *The Theory of Splines and Their Applications*, Academic Press, New York, 1967.

[4.22] M. Atkinson et al., *A proposal to build a ring image Cerenkov detector for use by the Omega Photon Collaboration in WA69 (P140)*, CERN-SPSC-P, 1982.

[4.23] C. D'Ambrosio, M. Laub, D. Piedigrossi, *Optical qualification of the first COMPASS RICH mirrors*, COMPASS 2000-4.

[4.24] C. D'Ambrosio et al., *Characterisation of Optical Components of the COMPASS RICH1 Detector*, Czechoslovak Journal of Physics, Vol. 51 (2001), Suppl. A.

[4.25] Plastics Design Library, *The Effect of Creep and other time related factors on plastics*, Vol. I, Book A (1991), Norwich.

[4.26] A.,I. Goldman, *Prediction of the deformation properties of polymeric and composite materials*, M. Shelef and R.A. Dickie Eds, (1994) Washington Am. Chem. Society.

Appendix A

[A1] http://pdg.web.cern.ch/pdg/cpep/startstandard.html.

Appendix B

[B1] http://pdg.web.cern.ch/pdg/cpep/beyond_start.html.

[B2] J. Ellis, *Perspectives in Physics Beyond the Standard Model*, CERN-TH-98-344.

[B3] http://lhcb-public.web.cern.ch/lhcb-public/html/introduction.htm.

Appendix C

[C1] B. H. Walker, *Optical engineering fundamentals*, McGraw-Hill, Inc., New York, 1994.

.

Acknowledgments

I would like to express my gratitude to all people who supported me during my work on this thesis. I enjoyed the friendly atmosphere in the TA2 group and the feeling of being a member of a team. It has been a great experience!

Namely, I would like to thank Olav Ullaland for his wise leadership, his deep interest and qualified support and for his sense of humour. I thank Wolfgang Klempt and Ettore Rosso for their kind support.

My special thanks belong to Carmelo D'Ambrosio for his excellent supervision, encouragement, qualified advice and friendship. I would like to thank Josef Zicha, my supervisor at the university, for his high interest and invaluable support.

My colleague and friend Didier Piedigrossi deserves my gratitude for his technical support, enthusiasm and a nice atmosphere in our shared office. I enjoyed collaborating with Christophe, Daniel, Erich, Federico, Luis, Patrick, Piet, Robert, Thierry, Tito, Xavier and many others.

I would like to express my sincere thanks and moral support to Didier Puertolas and his family who helped me to find a new home in France.

Last but not least, my personal thanks belong to my dear parents and my two brothers. Without their support, I would never have achieved all I have done.